Università degli Studi di Palermo

AREA QUALITÀ, PROGRAMMAZIONE E SUPPORTO STRATEGICO
SETTORE STRATEGIA PER LA RICERCA
U. O. DOTTORATI

Energia e Tecnologie dell'Informazione
Dipartimento di Ingegneria
ING-IND/32

HYBRID ENERGY STORAGE MODELING AND INNOVATIVE SOLUTIONS FOR ENERGY STORAGE MANAGEMENT SYSTEMS

IL DOTTORE
VINCENZO JUNIOR CASTIGLIA

IL COORDINATORE
MAURIZIO CELLURA

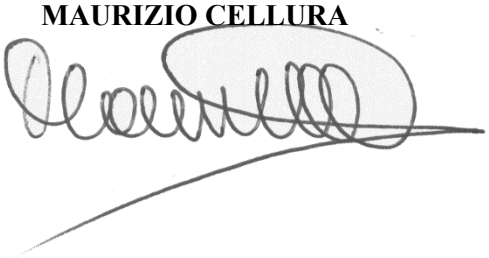

IL TUTOR
ROSARIO MICELI

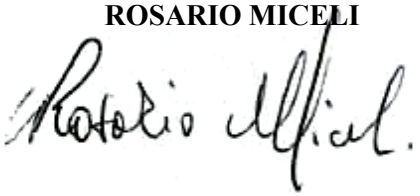

CICLO XXXIII
2022

Preface

The activity of Ph.D. was carried out at the Department of Engineering of the University of Palermo (Italy) from April 2018 to September 2021.

The theoretical development, simulation analysis, implementation and experimental tests has been performed in Sustainable Development and Energy Saving Laboratory (SDESLAB) of the University of Palermo.

Part of the activity was developed during the visiting period in Aalborg (Denmark) at the department of Energy Technology of Aalborg University from July 2019 to January 2020.

Contents

Introduction

The present dissertation concerns about the modeling of different electrical energy storage sources, in particular batteries and supercapacitors (SCs), and of novel configurations of Hybrid Energy Storage Management Systems (HESMS).

This work is developed within the program "PON-FSE Dottorati Innovativi a caratterizzazione industriale AA 2017/2018" and the project "Hybrid energy storage systems and innovative solutions of Energy Storage Management System (ESMS) for electrical vehicles and energy storage facilities".

The worldwide energy policies aimed to reduce CO_2 emissions consider the transport sector strategic for achieving the international objectives of global warming mitigation. This is due to the great potential associated with mobility demand, as the actual state of the art of propulsion systems is fossil fuel-based. Specifically, the 2016 word CO_2 inventory assigned to the entire transport sector a share of 21.4%. As regards the automotive transport sector, multiple national action plans are already in place which aims to replace internal combustion engines vehicles with electric vehicles, setting in 2030 as the ultimate limit for the marketing of private cars powered by fossil fuels. Considering the ambitious targets, the complete electrification of the transportation sector represents a viable solution for improving efficiency and exploiting all the benefits of the expected transition toward renewable energy sources (RES).

One of the main problems to overcome in electric vehicles is the supply of electricity in the forms and ways required by the engines. The high power and torque densities of the electric motors make it possible to reduce the weight of the propulsion systems. However, the energy and power densities of the electrical storage systems fail to reach the levels of fossil fuels, inevitably leading to an increase in the share of weight associated with the propulsion energy. Moreover, electrical energy and power availability must be guaranteed in all possible operative conditions to satisfy the end user.

The growing need for energy demand and the desire to achieve sustainable development, are reflected in the use of RESs-based Distributed Generators (DG). The use of smart supervisory control and local clustering of demand and generation can lead to marked improvements in the efficiency, reliability, and resilience of the electrical system. The main problem of RESs-based DG is the natural variation of

some renewable sources, such as wind and solar. To reduce the impact of intermittent RES generation, the most effective and practical solution is the employment of Energy Storage Systems (ESSs).

From the above, it is clear that transportation sector electrification and distributed generation from renewable sources have one critical issue in common: energy storage and management optimization.

In this scenario, the usage of HESMS can help to address the aforementioned critical issues. This dissertation contributes to different aspect of the topic, starting from the energy storage source modeling, to the problem of managing power and energy provided by multiple energy sources.

The present work is structured in eight chapters organized as follows.

Chapter One presents an analysis of energy storage technologies state of the art, with a focus on the ones considered in the thesis (batteries and supercapacitors), and of the main functionality of the energy storage management system.

In **Chapter Two**, the issues of battery modeling are addressed. Three different battery equivalent circuit models are analyzed and compared, along with the respective parameters estimation methodology. The models are experimentally validated to obtain a comparison between the achievable accuracy.

In **Chapter Three**, the supercacitors modeling is carried out. The three-branches supercapacitor equivalent circuit model is considered and an improved parameter estimation procedure is proposed. The residual charge phenomenon is investigated and integrated in the proposed model. Experimental validations are carried out both on single SCs units and on SCs pack.

In **Chapter Four** a novel grid connected converter with mixed harmonic elimination control and integrated battery balancing algorithm is presented. The theoretical analysis of the system, the component sizing and the system control are presented. The system is simulated in Matlab/Simulink, verifying the correct synchronization, the possibility to exchange energy with the main grid and the capability to maintain equalized battery voltages.

Chapter Five presents a battery/supercapacitors hybrid energy storage management system. The power and the energy required by a generic profile is considered for the sizing of the storage system. A comparison between a battery-only storage system and a hybrid storage system composed of a battery pack and a SCs bank is reported. In particular, a description of the power sharing rule-based algorithm and of the iterative sizing method is provided. The HESMS power electronics converters modeling, control and design is also considered. An experimental validation of the HESMS is carried out on a laboratory prototype, confirming the effectiveness of the proposed control strategy.

Chapter Six, deals with the quasi-Z-Source Inverter (qZSI) modeling and control. First, the small-signal model for the quasi-Z-network is obtained with the state-space averaging method. Then the small-signal transfer functions are used to

design three control schemes: the first one for the input current control, the second one for PI based DC-link voltage and output current control and the third one for PI based DC-link voltage and PR based output current control. Simulation and experimental results are provided to validate the controller design.

In **Chapter Seven** a new topology of qZS-based hybrid energy storage system is presented. The proposed topology uses a battery and a SCs pack as energy sources. The system features a single-stage DC-DC-AC conversion and the integration of battery and SCs without additional converters. The power balance between the battery, the SCs and the grid is achieved by controlling the shoot-through duty cycle and the modulation index. The operation of the system under several different conditions is simulated using PLECS. The simulation results confirm the correct operation of the system and the possibility to use this topology in HESS applications.

In **Chapter Eight** a qZS-based Inductive Power Transfer System (IPT) for electrical vehicle battery charging application is investigated. Taking advantage of the shoot-through states the simultaneous DC voltage regulation and DC/AC conversion is possible. Moreover, thanks to the Z-network, the qZS-IPT system is immune to short-circuits. A new modulator is proposed, capable of making the transition between buck and boost modes in a simple and effective way. The theoretical analysis is validated by means of simulations and experimental results, verifying proper system operation in both buck and boost modes, and ensuring the system's ability to perform the battery charging.

Chapter 1

Energy Storage and Management

1.1 Introduction

The transition to a low-carbon and green economy includes the goals of a 40% reduction in greenhouse gas emissions, 32% of consumption provided by Renewable Energy Sources (RES) and a 32.5% improvement in energy efficiency [1].

In order to achieve these objectives, the development of power generation systems from non-programmable renewable sources, such as eolic and photovoltaic (PV), will be of fundamental importance. Thanks to incentive policies and technological developments, the price of renewable technologies has been significantly reduced in recent years [2], with a 80% reduction for PV panels between 2009-2015, and a 30-40% reduction for wind turbines in the same period. The typical generation profile of a PV panel repeats daily, with a peak around noon and minimum values during the darkest hours. In addition, cloudiness can cause sudden changes in power generation within a few minutes, posing a challenge for balancing the power grid. In the case of wind-based generation, fluctuations in the produced energy usually affect longer periods, typically days or weeks. However, these fluctuations must be balanced by the power grid.

In this scenario, energy storage systems can be a turning point. The use of such systems can lead to:

- improved network management,
- speed of reaction in case of rapid power loss or power surges,
- interfacing of different grid elements for cost-effective balancing of RES over different time windows.

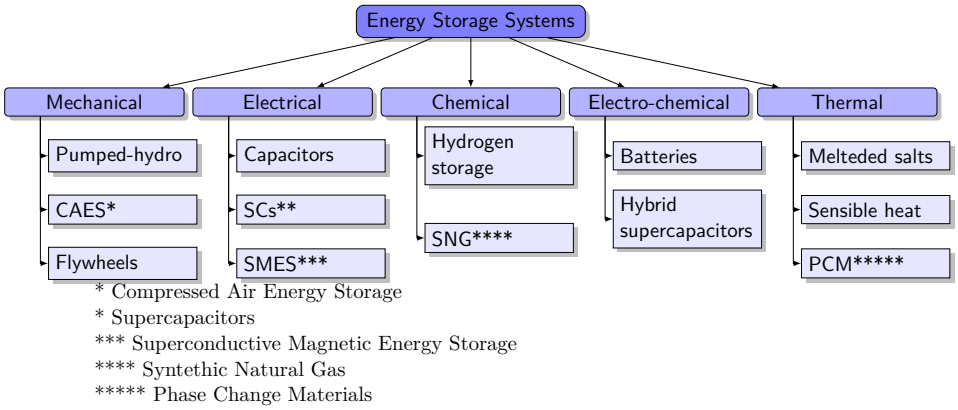

Figure 1.1: Example of energy storage types [3].

1.2 Energy storage technologies

Some fundamental parameters can be defined to compare the energy storage technologies:

- **Energy density** is the energy stored for each cubic meter, or liter, of the device. It is usually measured in Wh/m^3 or Wh/l.
- **Specific Energy**, or **gravimetric energy density**, is the energy stored for each kg of the device. It is usually measured in Wh/kg.
- **Power density** is the maximum amount of power obtained for each cubic meter, or liter, of the device. It is usually measured in W/m^3 or W/l.
- **Specific Power**, or **Power-to-weight ratio (PWR)**, is the maximum amount of power obtained for each kg of the device. It is usually measured in W/kg.
- **Life cycles** represent the useful life of an energy storage system. It can be expressed in terms of years of service or number of possible charge/discharge cycles.
- **Efficiency** is the ratio between the energy "fed" into the storage system and the energy that can be "pulled out" of it. It is usually expressed in percent.
- **Response times** represents the speed of reaction of a storage technology. It is expressed in time units, from ms to hour.

Energy can be stored in different forms, as shown in Fig. 1.1. A brief description of the various storage technologies is provided below.

1. **Mechanical storage** systems store energy in kinetic and/or potential form:

(a) **Pumped-hydro** storage use the gravitational potential energy of the water, pumped from a lower elevation basin to a higher one. This technology represents the major share of storage capacity globally (97%). The response times range from few seconds to minutes.

(b) **Compressed Air Energy Storage (CAES)** uses electricity to compress air, which is then stored in vessels or underground caves. The response times are in the order of minutes.

(c) **Flywheels** store electrical energy as kinetic energy, accelerating a rotor disk. The response times are in the order of milliseconds to seconds.

2. **Electrical storage** systems store energy in electric or magnetic fields form:

   (a) **Capacitors and Supercapacitors (SCs)** store energy in the form of electrostatic potential energy. The latter have a high storage capacity, making it possible to discharge for long periods. They can respond almost instantly in both charging and discharging surges, making them suitable for peak power shaping.

   (b) Superconductive Magnetic Energy Storage (SMES) systems store energy in the magnetic field created by the flow of DC current in a superconducting coil. The response time is in the order of seconds, and due to the high operational cost they are most commonly used to improve power quality.

3. **Chemical storage** systems comes in the form of fuels as biomass, coal or gas.

   (a) **Hydrogen** can be stored in liquid or gas form. Hydrogen can be produced using diverse resources, including nuclear, natural gas and coal, biomass, and other renewable sources. The latter is the most eco-friendly choice for the hydrogen production.

   (b) **Synthetic Natural Gas (SNG)** can be derived from coal, (waste) biomass or synthesized with Power-to-Gas process and then stored.

4. **Electro-chemical** storage store energy in a combination of electrical and chemical form:

   (a) **Batteries** are one of the fastest growing storage technology due to the significant growth of the electric vehicles sector and the develop of grid-connected storage plants. In general they present good energy density and fast response times, making them suitable in a variety of applications.

   (b) **Hybrid-Supercapacitors** are halfway between a battery and a SC. They usually have higher operating voltage, energy density and capacitance than standard SCs. These improved characteristics come at the

expense of service life, which is reduced due to the "chemical" part of the component.

5. **Thermal storage** convert electricity to heat, which is then stored in vaious type of materials.

   (a) **Melted salts** absorbs heat energy altering their chemical bonds. They can be subsequently "discharged" thorough reversed chemical reaction which results in heat. The heat is used to generate steam for a turbine-based electricity generation plant.

   (b) **Sensible heat** can be used to increase a material temperature. The material can be water, rock, earth, etc. A large part of the initial energy can be retrieved cooling the material, while it generate steam for electricity production.

   (c) **Phase Change Materials (PCM)** exploits the latent heat to releases or absorbs energy during a phase transition.

Fig. 1.2 shows two typical graph used to directly compare energy storage systems. Fig. 1.2 (a) illustrates the depending on the needed storage capacity and discharge time for grid-support applications. Regarding the storage flexibility, two extreme requirements should be considered: short term and long term flexibility. Chemical and mechanical storage could absorb almost all excess variable renewable energy, covering the long term flexibility for the electricity system. Meanwhile, electrical and electro-chemical storage, linked to PV and wind plants can cover short term needs.

Fig. 1.2 (b) shows a graph called "Ragone" plot. It shows some energy technologies in a Specific Power - Specific Energy graduated axes. The vertical axis describes how much energy is available per unit mass, while the horizontal axis shows how quickly that energy can be released. As it can be noticed, capacitors and SCs have high specific power, comparable to the one of an internal combustion engine. On the contrary, fuel cells and batteries presents low specific power but high specific energy. By integrating different energy storage technologies, the best performance can be achieved in various applications.

In the following sections, a focus on batteries and supercapacitors is carried out, as they represent the most used technologies in this thesis work.

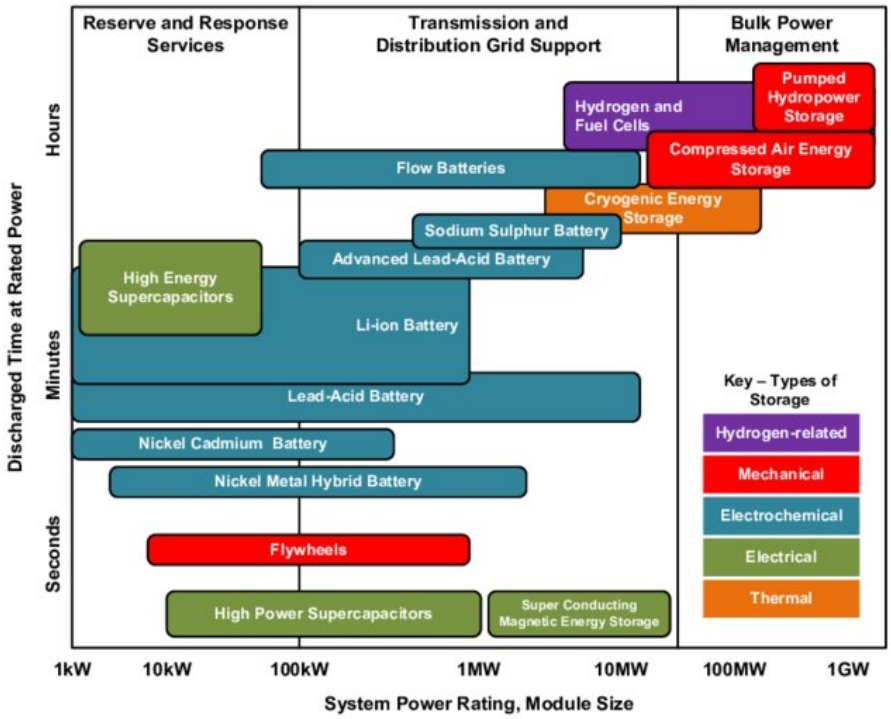

(a)

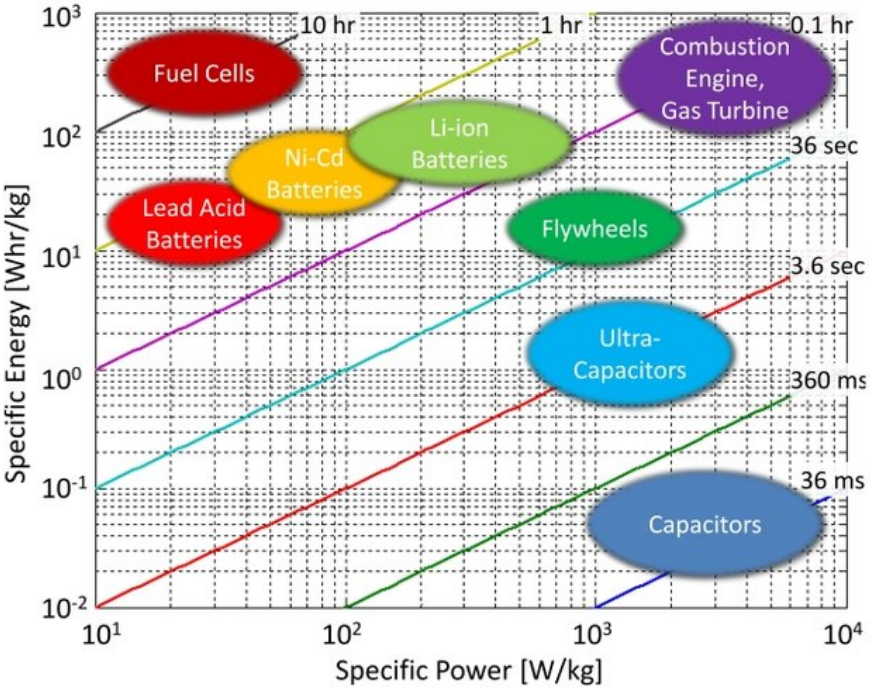

(b)

Figure 1.2: (a) Applicable power ranges and discharge power duration of different energy storage technologies [4]. (b) Ragone Plot of energy storage technologies [5].

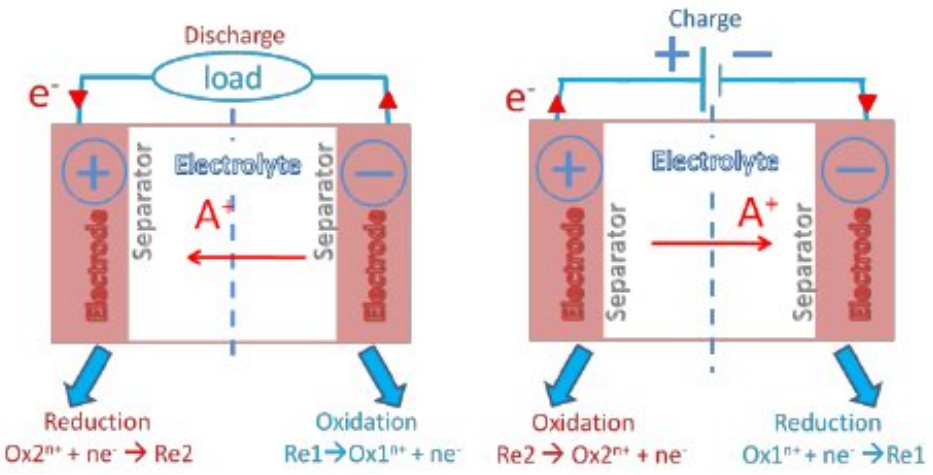

Figure 1.3: Schematic of the working principle of a battery [6].

1.2.1 Batteries

Batteries convert chemical energy in electrical energy in form of direct current. An elementary battery cell is composed of:

- **Positive electrode (cathode)**: typically an oxide or sulfide in which the reduction reaction takes place during discharge.
- **Negative electrode (anode)**: metal or alloy in which the oxidation reaction takes place during discharge.
- **Electrolyte**: medium in which the electrodes are immersed, through which ionic conduction takes place. It can be liquid, solid or gel.

Fig. 1.3 shows the working principle of a battery. The direct current is generated thanks to the chemical reaction that takes place between the electrodes and the electrolyte. In the case of rechargeable batteries this chemical reaction is reversible, reversing the direction of the current circulating on the battery.

Considering energy management applications, it is not important to study what is happening at the chemical level, rather what is happening at the macroscopic level. For this reason, the battery can be treated as a 'black box' with specific operating parameters. These parameters include specific energy, energy density, specific power, rated voltages, charging efficiency, energy efficiency, operating temperatures, number of charging cycles etc. Some of these parameters will be described in more detail below.

Nominal voltage

The battery voltage varies from a maximum value, when it is fully charged, to a minimum value when it is fully discharged. The nominal voltage is a kind of average

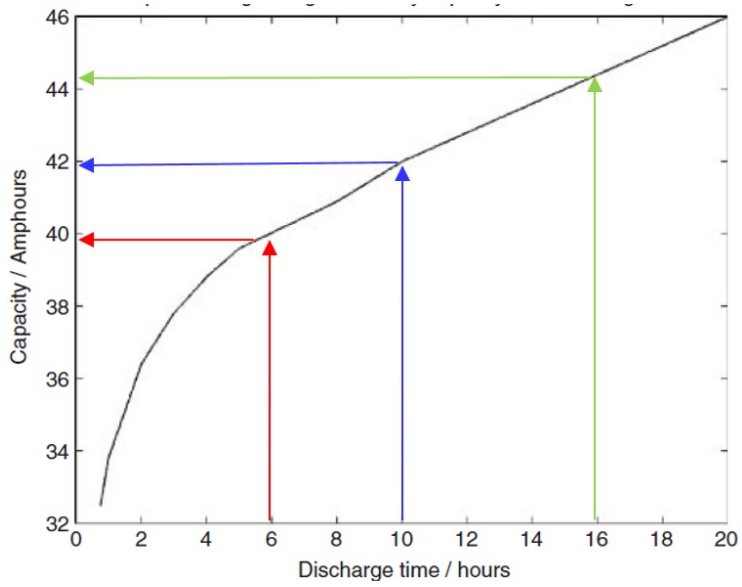

Figure 1.4: Graph showing change in battery capacity with discharge time.

value between the two. A typical voltage range is 4.2-3 V with a nominal voltage of 3.7 V. Due to the low voltage of each cell, in order to reach a voltage sufficient for most applications (200 - 800 V), several battery cells are connected in series.

Nominal Capacity

The battery nominal capacity is the amount of electric charge a battery can deliver at nominal voltage. It is usually measured in ampere-hour (Ah). Capacity scales-up with the dimensions of the battery cell: larger cells have greater capacity, but develop the same nominal voltage.

Assuming a 10 Ah battery capacity, this means that, theoretically, it can provide 10 A for 1 hour or 2 A for 5 hours or, theoretically, 1 A for 10 hours. In practice, faster discharging rates lead to a loss of capacity. For example, Fig. 1.4 shows the capacity variation for a battery with a nominal capacity of 42 Ah and a nominal discharge time of 10 hours. The faster the battery is discharged, the lower the actual capacity it presents.

C-rate

The C-rate represents the rate at which the battery is being charged or discharged. It is defined as ratio between the battery current the the theoretical current which would completely discharge the battery in one hour. It has the unit $h^{-}1$.

Stored Energy

The energy stored in a battery depends on the voltage and the stored charge. The battery energy is usually expressed in Wh and calculated considering the nominal

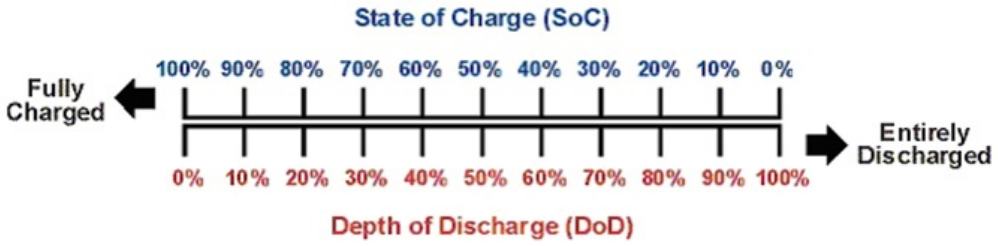

Figure 1.5: SoC and DoD representation.

battery voltage V_n and the nominal capacity C_n:

$$E = V_n \cdot C_n \tag{1.1}$$

State of Charge and Depth of Discharge

The battery State of Charge (SoC) is defined as the battery remaining capacity divided by the battery nominal capacity. It is usually expressed in percent points.

The battery Depth of Discharge (DoD) is defined as the battery supplied capacity divided by the battery nominal capacity.

SoC and DoD tied by the following equation:

$$SoC = 100\% - DoD \tag{1.2}$$

as it can be appreciated in Fig. 1.5.

State of Health

The battery State of Health (SoH) is a qualitative measure of the actual condition of a battery compared to its ideal (or initial) conditions. Several parameters effects the battery performances over time:

- internal resistance/impedance;
- capacity;
- voltage;
- temperature;
- self-discharge;

As an example, Fig. 1.6 shows the parameter variation with the battery number of cycles. In particular, the battery capacity, internal resistance and self discharge are evaluated at the battery Beginning of Life (BoL) and after a certain number of cycles. As it can be noticed, the battery capacity tend to decrease while the self-

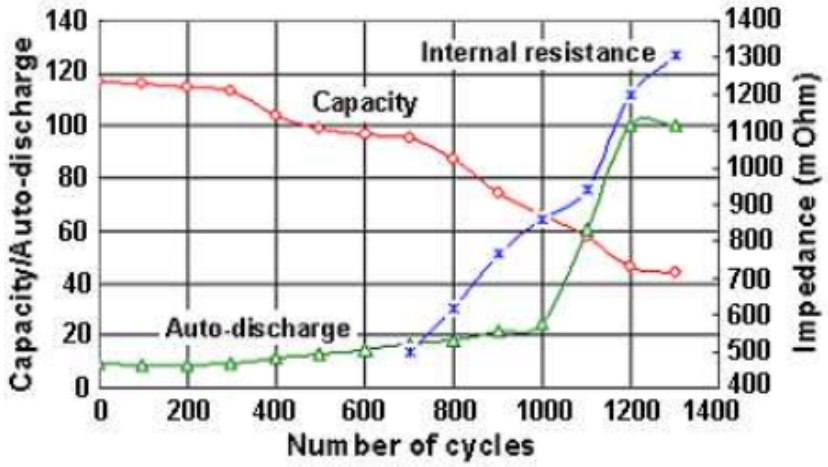

Figure 1.6: Parameters variation with battery number of cycles.

discharge and internal resistance tend to increase with time. Considering the above, the SoH can be estimated in different ways, i.e.

$$SoH_R = \frac{actual\,internal\,resistance}{BoL\,internal\,resistance} \cdot 100 \tag{1.3}$$

$$SoH_C = \frac{actual\,capacity}{BoL\,capacity} \cdot 100 \tag{1.4}$$

There is not a standard way to evaluate when a battery reaches its End of Life (EoL). Depending on the application, reaching $SoH_C = 80\%$ means the battery needs to be replaced (i.e. automotive application). Other application may accept a battery $SoH_C = 50\%$ (low power profile, grid-connected applications) [7].

Coulombic efficiency

The Couloumbic Efficiency (CE), or Faradaic Efficiency, represents the efficiency with which electrons are transferred into the battery. The charging efficiency is the ratio of the total charge extracted from the battery to the charge fed into the battery, considering a complete cycle.

$$\eta_c = \frac{\text{total extracted charge}}{\text{total supplied charge}} \cdot 100 \tag{1.5}$$

Theoretically a battery should return the total charge supplied, thus CE = 100%. For lithium-ion batteries CE is about 99%, for lead-acid is around 90%.

Energy efficiency

Batteries are not always totally charged and discharged. Actually, they are usually cycled between a maximum and a minimum SoC level. In this case we are not talking about charge efficiency, rather about energy efficiency of the battery. The

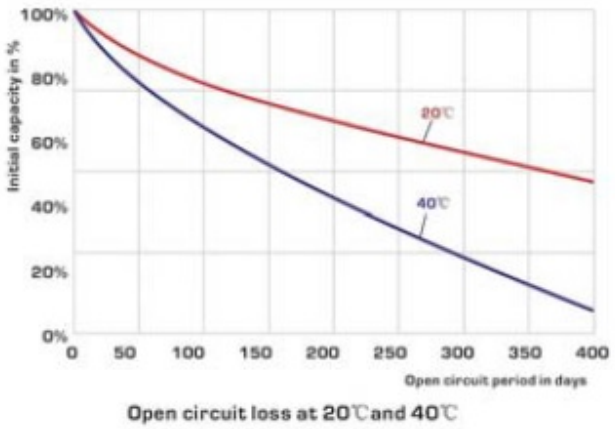

Figure 1.7: Self-discharge of a lead-acid battery for different temperatures [8].

battery energy efficiency is defined as the ratio of the charge drawn from the battery from a SOC Y to a SoC X the charge supplied to the battery from a SoC X to a SoC Y:

$$\eta_e = \frac{\text{charge drawn from SoC Y to SoC X}}{\text{charge supplied from SoC X to SoC Y}} \cdot 100 \tag{1.6}$$

Self-discharge

When they are not in use, batteries tend to discharge. This phenomenon is called self- discharge or auto-discharge and its extent depends on several factors such as battery chemistry and temperature. The self- discharge is mainly caused by:

- local corrosion effects at the contact between electrodes and electrolyte (intergranular corrosion);
- Presence of impurities in the electrodes or electrolyte;
- insulation defects between electrodes of opposite polarity.

Fig. 1.7 shows the self-discharge of a lead-acid battery for different temperatures [8]. High temperatures cause high self-discharge values.

Battery temperature

Most batteries operate at room temperature. Some batteries require high temperatures for the start-up operations. Others need a cooling system to keep them to a controlled temperatures. Others require an heating system, because their performances deteriorates at low temperatures. The battery temperature impacts several parameters such as capacity and open circuit voltage [9]. As an example, Fig. 1.8 shows the temperature effect on the open circuit voltage of typical Li-Ion cell.

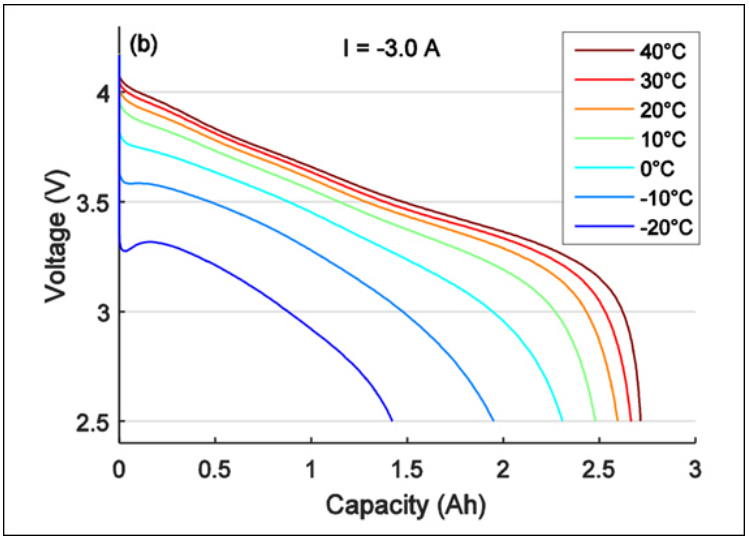

Figure 1.8: Temperature effect on the battery open circuit voltage [9].

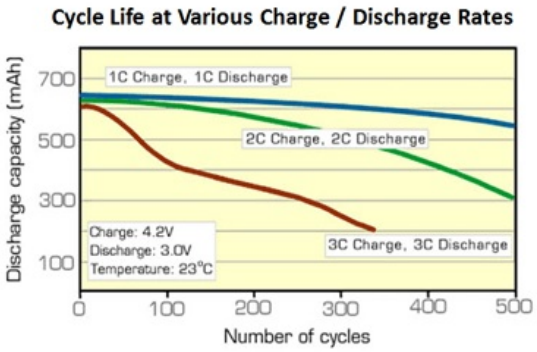

(a)

Depth of discharge	Discharge cycles
100% DoD	300 – 500
50% DoD	1,200 – 1,500
25% DoD	2,000 – 2,500
10% DoD	3,750 – 4,700

(b)

Figure 1.9: (a) C-rate effect on the battery life cycle. (b) DoD effect on the battery life cycles.

Battery life cycles

Modern batteries can handle several hundred full charge/discharge cycles. The exact number depends on "how" the battery is used. Fig. 1.9 (a) shows the effect of the C-rate on the battery capacity as a function of the battery number of cycles. It can be noticed that running the battery with higher C-rates leads to a faster performance deterioration.

Another important parameter in the life cycles number determination is the DoD level. As already mentioned, a battery can usually handles several hundred of full charge/discharge cycle. However, cycling the battery with smaller DoDs leads to much slower aging of the battery, allowing for extended use, up to thousands of cycles. A typical relation of DoDs levels and discharge cycles is shown in Fig. 1.9 (b).

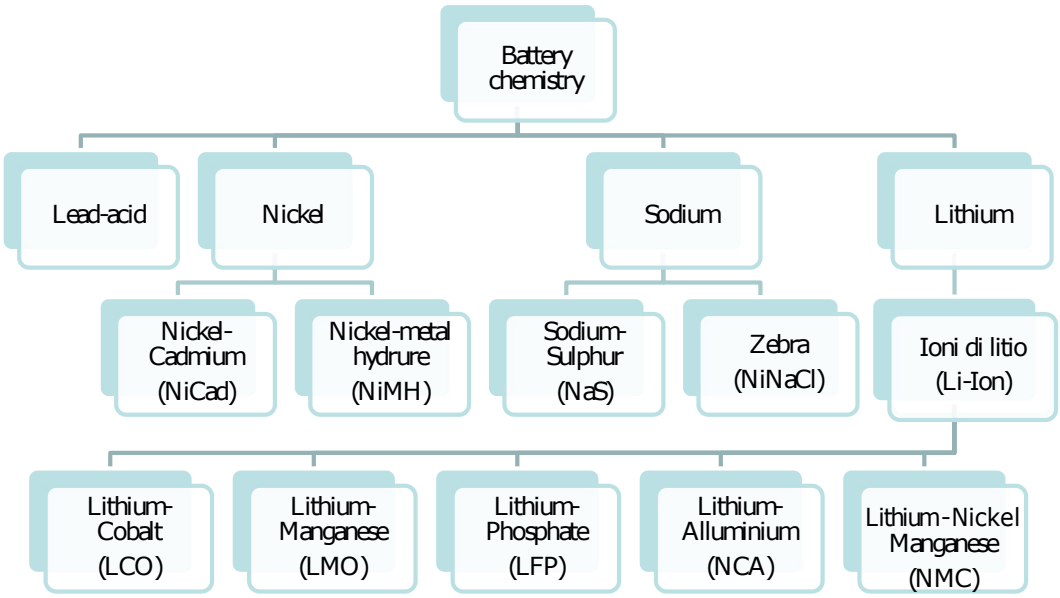

Figure 1.10: Battery chemistry types.

Table 1.1: Li-Ion batteries specifications for different chemistries [10].

Material -	**Nominal voltage** (V)	**Specific energy** (Wh/kg)	**Life cycles** -
LCO	3.7	110-190	500-1000
LMO	3.8	100-120	500-1000
NCA	3.6	100-150	2000-3000
NMC	3.6	100-170	2000-3000
LFP	3.3	90-115	>3000
LTO	2.2	60-75	>5000

Battery chemistry

Several battery chemistry are commercially available, each one with their own advantages and disadvantages. Fig. 1.10 shows a small round-up of the main battery chemistry types.

Focusing on the Li-Ion type, Table 1.1 gives some specifications for each technology. LCO Battery have the highest specific energy, but the lowest life cycles. LMO batteries have the highest nominal voltage. NCA batteries are a good compromise between specific energy and life cycles and are usually employed for EVs. NMC batteries can achieve a wide range of performances depending on the percentage of Ni, Mn and Co employed. LTO batteries have the lowest specific energy, on the other hand they present the higher life cycles. From the above, it is clear that there is no battery chemistry suitable for all applications. From time to time it is necessary to choose the technology that allows the best performances.

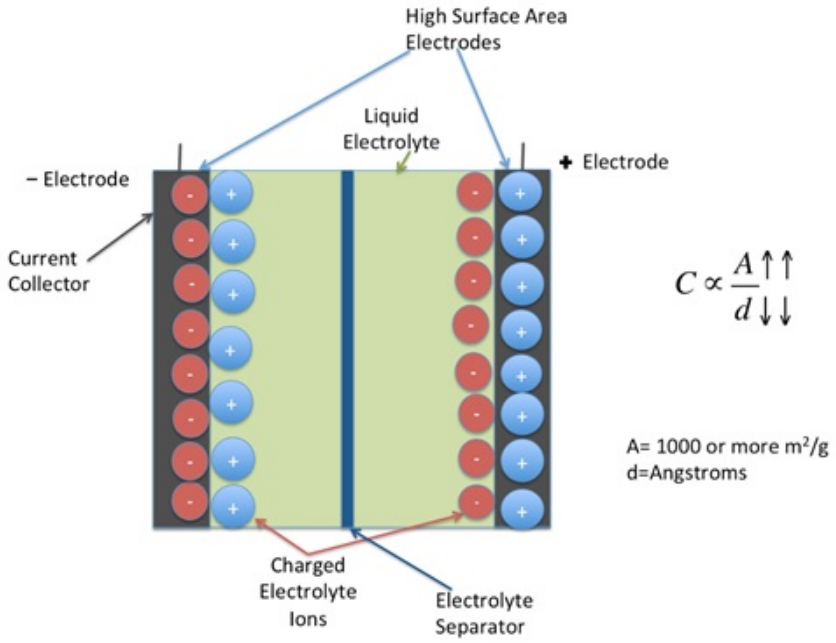

Figure 1.11: Operation principle of a SCs.

1.2.2 Supercapacitors

SCs store the energy using the electric field created between the electrodes and the electrolyte, as shown in Fig. 1.11. The SC differs from the traditional capacitor for mainly two reason:

1. The plates are made of metals coated with a porous substance that increases the surface area on which charge can be accumulated.

2. The dielectric is replaced by an electrolyte solution, and the plates are separated by a very thin layer of insulation. In this way, the distance between the plates is minimized.

When the plates are charged, opposite charges are formed on each face of the separator, creating what is called an "electric double-layer capacitor" (EDLC). Thanks to this double layer of charges, separated by a very small thickness, and to the porous material that increases the surface available for the accumulation of charges, it is possible to obtain very high capacitance values.

As already said for the batteries, we will not focus on the chemical composition and related phenomena, rather we will analyze the macroscopic behavior of the SC by referring to certain operating parameters that will be described in the following sections.

Nominal voltage

The nominal voltage is the maximum DC or peak voltage that can be applied continuously to the SC without damaging it. This value already includes a safety margin to prevent the breakdown voltage, above which the electrolyte decomposes. SCs are low voltage device, like batteries, are low voltage devices with a nominal voltage ranging from 2 to 4 V. In order to reach the voltage ratings of normal applications, several SCs are connected in series in the same way of a battery pack.

Capacitance

The capacitance value C of a SC, measured in F, is:

$$C = \epsilon \frac{A}{d} \tag{1.7}$$

where ϵ is the electric permittivity of the material interposed between the plates of the capacitor, A is the surface area of the plates and d is the distance between the plates. The peculiarity of SCs is that they have a very small plate spacing and a very high plate surface area. As a result, SCs present higher capacitance values than conventional capacitors, arising from the extremely large surface area of electrodes and the extremely thin double-layer distance. SCs capacitance range from 100 F to 10000 F, depending on the SC type.

Stored energy

The energy stored in a SC depends on its capacitance and voltage. The maximum energy stored in a capacitor, in Wh, can be expressed as

$$E_{max} = \frac{1}{2} \frac{C \cdot V_n^2}{3600} \tag{1.8}$$

The energy density and specific energy of a SC is much smaller than batteries. On the other hand, they have higher power density and specific power.

Internal DC and AC resistance

As the ions move within the electrolyte, through the separator to the electrodes, losses occur that are attributed to an internal DC resistance. The internal AC resistance, often referred to as Equivalent Series Resistance (ESR), is measured at a specified frequency range, between 1-100 kHz. The ESR is typically much smaller than the DC internal resistance. Considering the high power usually handled by SCs, it is important to have low DC and AC resistance value, in order to keep the losses as low as possible.

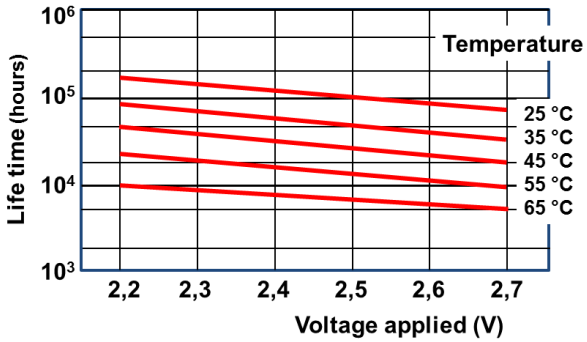

Figure 1.12: Lifetime of a SCs as a function of voltage and temperature [12].

Self-discharge

Due to irregularities in the structure of the SC, a leakage current can occur, leading to self-discharge. The leakage current depends on several factors such as capacitance, voltage, temperature, and the chemical stability of the electrode and electrolyte. Self-discharge is usually indicated in terms of time and can range from hours to weeks.

Supercapacitors life cycles

Compared to batteries, SCs have a very high number of life cycles (100 000 - 1 000 000 cycles). SCs are not chemical-based storage system (except some particular types), and their lifetime depends mainly on the evaporation rate of the liquid electrolyte [11]. Higher temperatures voltages accelerate the evaporation process, affecting the SCs life cycles, as reported in Fig. 1.12.

Supercapacitor types

SCs can be classified into three categories, depending of the way they store the electrical energy:

- **EDCL** - energy stored in electrostatic form;
- **Pseudocapacitors** - energy stored in electrochemical form;
- **Hybrid capacitors** - energy stored in both electrostatic and electrochemical forms.

For each of the above categories, the combinations of the electrode and electrolyte material results in different SCs performance and characteristics. In general EDLCs have smaller energy density compared to Pseudocapacitors. However EDLCs have higher life cycles. The hybrid types are usually a compromise between the other two types.

1.3 Energy Storage Management System

All applications where one or more storage technologies are installed need a "supervisor" that takes care of the safe and efficient operation of the overall system. For battery-power , this supervisor is called Battery Management System (BMS), whereas in general can be referred to as Energy Storage Management System (ESMS). The main features of an ESMS are:

1. Storage system monitoring - voltage, current, temperature measurement and SoC, SoH estimation;
2. Storage system protection and safety - avoid overload, over-voltage and over-temperature conditions;
3. Storage system charge and discharge management - for batteries and SC also charge equalization and cell balancing.
4. Storage system thermal management;
5. Data communications;

The "brain" of an ESMS consists of one or more Electronic Control Unit (ECU). This unit has the task of making the most appropriate decisions based on the situation of the system, which is evaluated from the measured quantities and the estimated parameters.

1.3.1 ESMS functionalities

ESMS architectures

Several ESMS architectures can be used, as shown in Fig. 1.13 [13]. The main difference between the architectures are the following:

- **Centralized**: a single controller connected to the battery cells with several wires. They are the cheapest, not very expandable and have complex wiring.
- **Modular**: several controllers, each managing a certain number of cells, communicate with each other. They are more easily expandable.
- **Distributed**: a micro-controller is installed for each cell, with a single communication cable running from the battery to the central controller. They are the most expensive, but are the easiest to install and assemble.

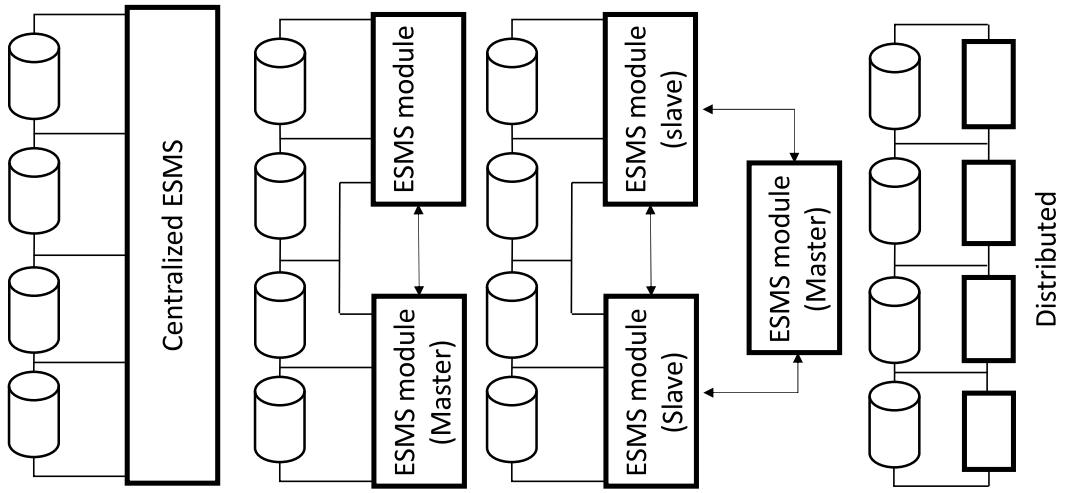

Figure 1.13: ESMS architectures.

Storage system monitoring

One of the most important activities of the ESMS is the monitoring of different parameters such as voltages, currents and temperatures. The correct evaluation of these quantities is of utmost importance, because on the basis of these data the ESMS makes certain decisions.

Measurements are usually carried out using transducers, to converter different parameters in voltage signal, and some conditioning circuits, to adapt the voltage value to the one supported by the ECU. The analog-to-digital (A/D) converters transform the analogue data to a digital value, allowing the ECU to process it.

The main parameters monitored by the ESMS are:

- **Pack Voltage and current** - when batteries or SCs pack are used, the total voltage and current of the pack need to be measured;
- **Cell voltage** - the voltage of each series connected cells is measured for balancing purposes, as will be described later;
- **Temperatures** - several sensors are needed to evaluate the average storage system temperature;
- **Isolation** - low voltage (<48 V) batteries are earth grounded; large High-Voltage (HV) batteries are floating systems.
- **Interlocks** - the status of several switch/relay is monitored to ensure the correct operation of the system.

Storage system protection and safety

The ESMS should detect the most appropriate mode of operation, based on the system conditions. The management system main activities for the protection and

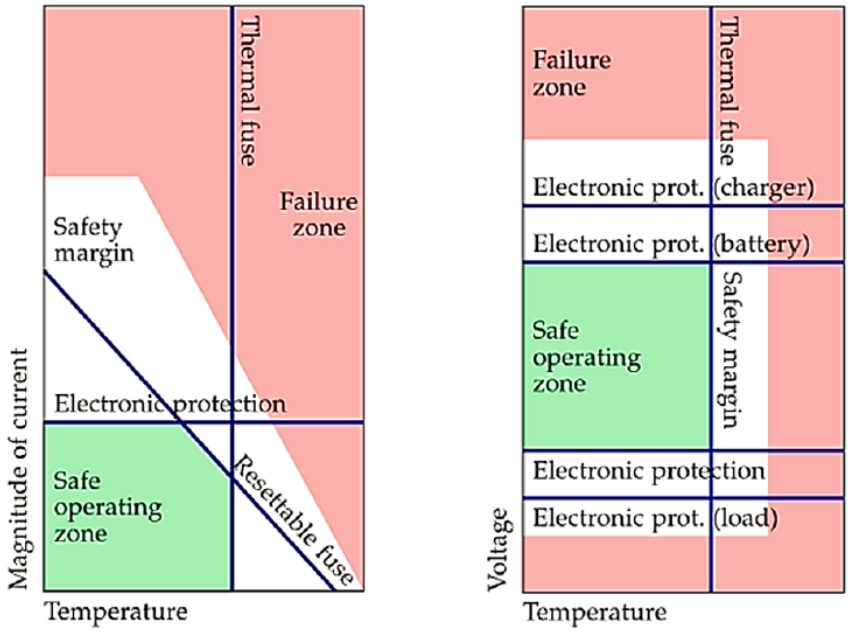

Figure 1.14: Operating zone of an ESMS.

safety of the storage system are:

- **Manage system setting** - The possible operation modes of a storage systems are usually represented as in Fig. 1.14. The green zone represents the Safe Operating Area (SOA), the white zone represents the safety margins and the red zone represents the failure of the system [14]. The ESMS set the SOA, the fault criteria and authenticate and identify the system.
- **Detect or predict hazardous events** - hazardous event can be external or internal to the battery/SCs pack. Over-voltage, over-current, short circuit, isolation faults or high/low temperatures are detected or predicted by the ESMS.
- **Respond to hazardous event** - if an abnormal state is detected, the ESMS run the fault tolerance routines, manage the heating/cooling, the charge/discharge and the interlock loop, and gives external communication of the fault.

Storage system charge and discharge management

The charge/discharge management requires various actions as summarized below [15].

- **Control of the current path** - this is achieved by means of passive (fuses) or active devices (switch/relays). A relay between pack and load/charger is used to connect/disconnect the storage from the rest of the system. Relays between

pack modules are used to exclude a possible faulty module. A pre-charge circuit with its own relay is usually needed for the start-up operations.

- **Perform energy management** - this is achieved controlling the electronic power converters connected to the storage systems, in order to regulate the charging/discharging current, to enable/disable the charging/discharging process or to set the dynamic power or current limits.
- **Balance the pack** - as it will be discussed in a separate section, the batteries/SCs cells voltages in a pack need to be equalized, in order to maximize the lifetime, efficiency and capacity of the storage system.

Storage system thermal management

The ESMS thermal management has several purposes [16]:

- keep the temperature below a desired value, in order to prevent thermal runaway;
- keep the temperature above a certain level to increase capacity;
- to uniform the temperature to increase the life cycles of the storage system.

So the main functions of the thermal management are the cooling and heating of the storage system. As far as cooling is concerned, it can be realized with:

- **Liquid** - liquid cooling usually takes less pace and is more effective, so higher loads are possible. On the other hand, they have higher cost, weight and require more maintenance. The liquid can be in direct or indirect contact with the storage system.
- **Air** - air cooling can be obtained with forced convection, using fans, or with natural convection. This method is less complicated and has lower cost however it causes a less uniform temperature distribution.
- **Phase Change Materials (PCM)** - PCM-based cooling system are very simple and can be used to smooth and damp the storage system temperature. PCM alone has limited heat removal and should be paired with an additional cooling system, increasing the needed volume.

For the storage system heating, the IC engine heat of an electric or fuel fired heater can be used.

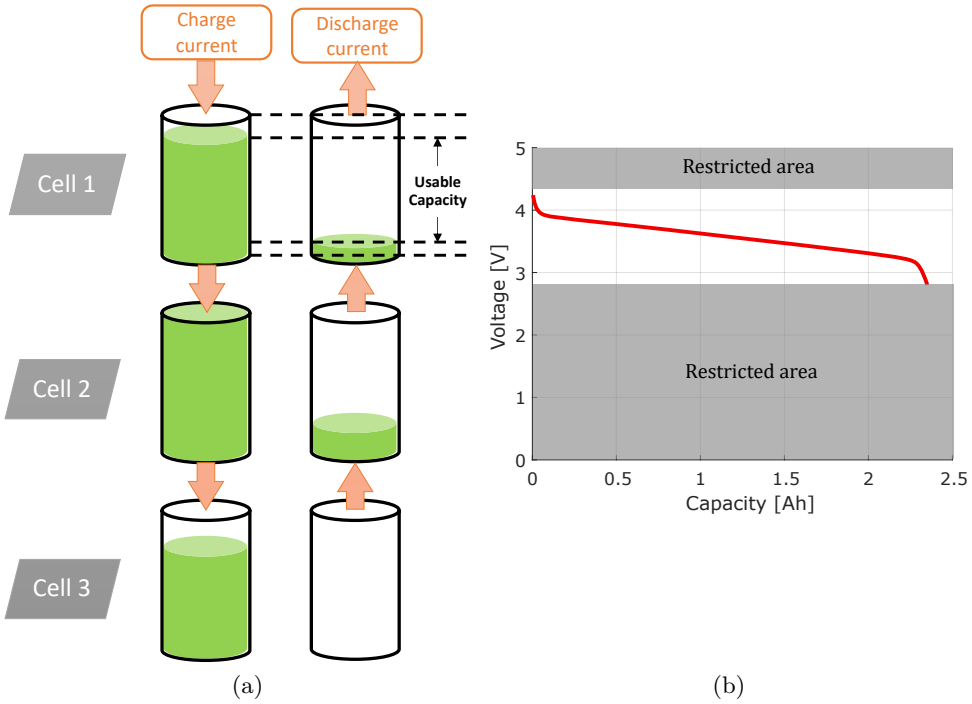

(a) (b)

Figure 1.15: Operation principle of a SCs.

1.3.2 Cell balancing

Batteries and SCs are low voltage devices. To reach the voltage rating of automotive or grid connected applications (200-800 V) several elementary cells (batteries or SCs) are connected in series. Theoretically, each cell of the whole pack have the exact same parameters. Therefore the voltage across them should be uniformly distributed. This is not the case for practical energy storage cells, which presents differences due to:

- Manufacturing and environment variance;
- Degradation with aging;
- Differences in thermal conditions;
- Differences in internal impedance;
- Unequal self-discharge.

These mismatches reduce the lifetime, efficiency and capacity of the battery.

Considering Fig. 1.15 (a), three battery cells are connected in series. Batteries can work in a specified range (usually 3-4.2 V as in Fig. 1.15 (b)), to avoid damages. The charging process is interrupted when a cell reaches the maximum voltage value. Considering Fig. 1.15 (a), Cell 2 is the first to reach the maximum voltage, thus the charge process is interrupted. However Cells 1 and 3 are not fully charged. The discharging process is interrupted when a cell reaches the minimum voltage value.

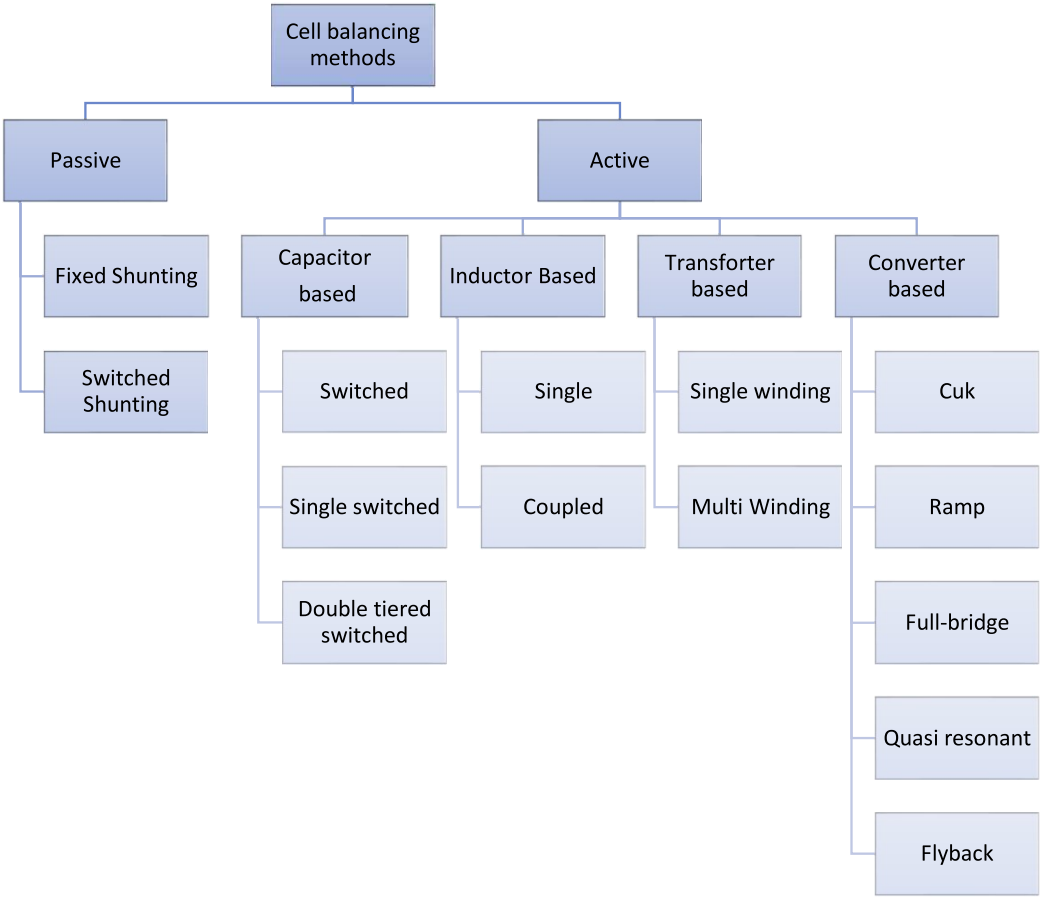

Figure 1.16: Classification of cell balancing methods.

Considering Fig. 1.15 (a), Cell 3 is the first to reach the minimum voltage value, however Cells 1 and 2 still have available capacity. To avoid the over-discharge or Cell 3, the discharge process in interrupted. If no actions are taken, the usable capacity of the battery packs is therefore reduced.

For this reason, ESMS must provide cell balancing, monitoring the voltage on each cell and reacting when necessary. Cell balancing techniques are divided into two categories: passive and active balancing, as illustrated in Fig. 1.16.

Passive balancing

Passive balancing, or dissipative balancing, techniques draws the energy from the most charged cell and dissipates it as heat, usually though resistors. Passive balancing methods have the following characteristics:

- low-cost;
- simple and reliable;
- long balancing times;
- heat generation due to energy dissipation;

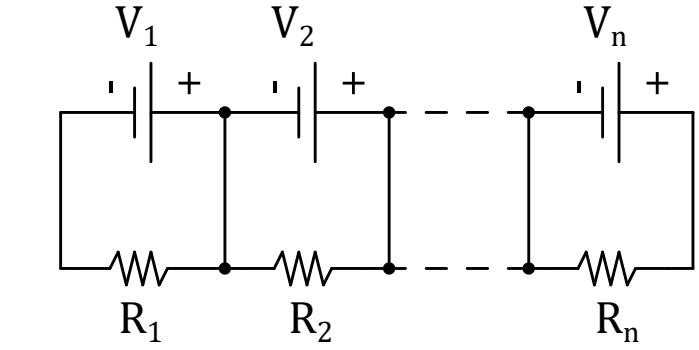

(a)

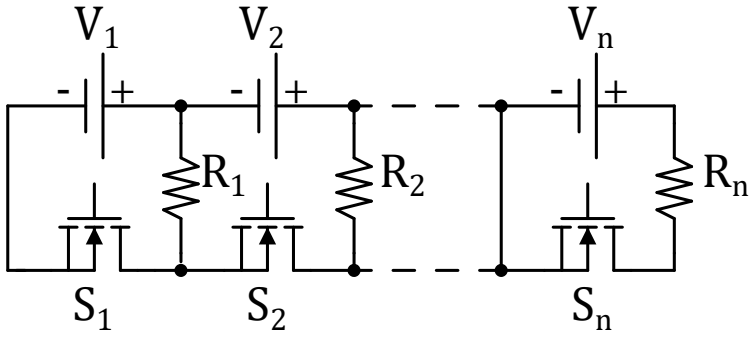

(b)

Figure 1.17: Passive balancing: (a) Fixed shunting resistor and (b) switched shunting resistore.

- balancing only during charging.

Two main methods can be used for passive balancing:

1. **Fixed shunt resistors**: a balancing resistor is permanently added in parallel to each cell, as shown in Fig 1.17 (a). Cells with higher energy dissipates more energy as heat, until charge levels match with cells of lower energy level. This is the simplest and cheapest method but comes with permanent energy losses. This method is suitable for nickel and lead-acid batteries for low power applications.

2. **Switched shunt resistor**: a balancing resistor and a controlled switch are connected in parallel to each cell, as shown in Fig 1.17 (b). When a cell need to be balanced, the respective switch is controlled to connect the balancing resistor.

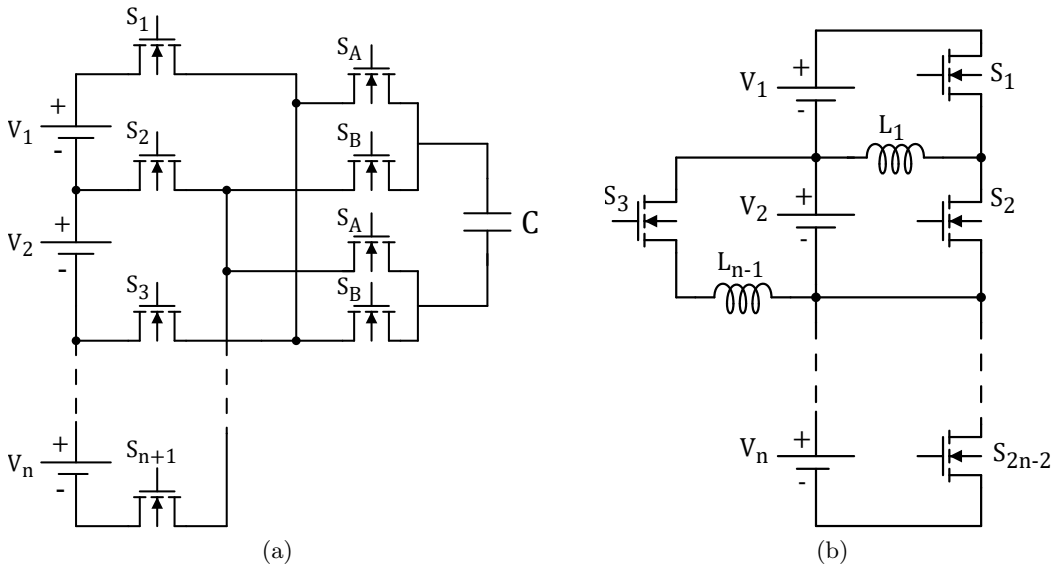

Figure 1.18: Active balancing circuits: (a) Single switched capacitor circuit; (b) Coupled inductor.

Active balancing

Active balancing techniques transfer the energy from the most charged cell to the least charged cell. Therefore no energy is dissipated, increasing the balancing efficiency and allowing for higher balancing current. Active balancing methods have the following characteristics:

- higher cost;
- fast balancing;
- allow bigger cell-to-cell variations;
- less heat generation;
- balancing in both charging and discharging mode.

Active equalization circuits can be classified with respect to the device used as temporary storage:

1. **Capacitor-based:** these methods use capacitors to transfer energy among the cells in a battery pack. Different architectures can be found in literature, including the switched capacitor [17]-[18], the single switched capacitor [19]-[20] and the double tiered capacitor [21]-[22].

   As an example, the single switched capacitor circuit is shown in Fig. 1.18 (a). It consists of a single capacitor and n+5 switches. The most and the least charged cells are identified, and the appropriate switches are enabled to perform the energy transfer.

2. **Inductor-based:** these methods use inductors to transfer energy between the battery cells. Two main architectures can be identified, i.e. single inductor o coupled inductor [23]. The inductor-based balancing circuits can achieve very high balancing current, therefore high equalization speed.

   As an example, the coupled inductor circuit is shown in Fig. 1.18 (b). It consists of *n-1* inductors and *2n-2* switches, for n series-connected cells. Also in this case a control algorithm is needed to sense the cells voltages and turn on and off the appropriate switches for a proper energy transfer.

3. **Transformer-based:** these methods use transformers to transfer energy between the cells in a battery pack. Two main architectures can be identified: the single winding transformer [24] and multi-wingdings transformer [25].

4. **Converter-based:** these methods use power electronics converters to transfer energy between the cells in a battery pack. The architectures available in literature can be classified in five categories: cúk [26], ramp, full-bridge, resonant and fly-back converters [27]. This kind of balancing circuits achieve the greatest flexibility, higher balancing current and speed. On the other hand, they are quite costly and complex.

1.3.3 Hybrid Energy Storage Systems

In automotive and grid connected applications, the Energy Storage Systems (ESSs) usually experiences irregular and frequent discharging/charging pattern which truncates the ESS lifespan, therefore the replacement cost of the ESS increase significantly.

High energy density storage technologies such as batteries and fuel cells have limited power capability. On the other hand, high power density technologies such as supercapacitors or flywheels have limited energy storage capability. The drawback of each technology can be overcome with the so-called Hybrid Energy Storage Systems (HESSs). Depending on the purpose of the hybridization, different energy storages can be used as a HESS. Generally, the HESS consists of high-power storage (HPS) and high-energy storage (HES) where the HPS absorbs or delivers the transient and peak power while the HES meets the long-term energy demand. HESSs provide many benefits: improving the total system efficiency, reducing the system cost, and prolonging the lifespan of the ESS. Due to the various types of energy storage technologies with different characteristics, a wide range of energy storage hybridization can be realized.

Fig. 1.19 shows an example HESS composed of batteries (high specific energy storage) and supercapacitors (high specific power storage), and three possible power flow management strategies. Fig. 1.19 (a) shows the case of high power demand from the load. Both energy storage sources supply power to the load. Fig. 1.19 (b)

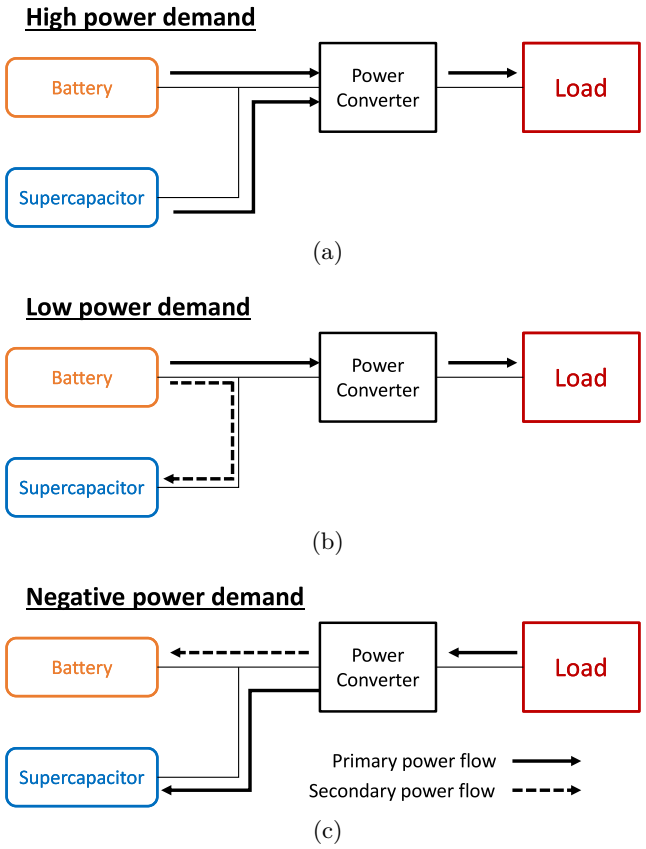

Figure 1.19: Hybrid energy storage system power flow in case of (a) high power demand, (b) low power demand, (c) negative power demand.

shows the case of low power demand. The battery supplies power both to the load (continuous arrow) and the supercapacitors (dashed arrow). Fig. 1.19 (c) shows the case of negative power. The peak power is absorbed by the supercapacitors, the remaining power can be supplied to the batteries.

HESSs can be classified into three categories:

- **Passive HESS**: Passive HESSs interface the different storage systems directly, without using additional converters. These solutions have the advantage of ease of implementation, efficiency and cost-effective. On the other hand, since the terminal voltage of the storages is not regulated, the power flow management is determined by internal resistance and voltage-current characteristics. As a result, the available energy from the HPS is very limited and it acts as a low pass filter for the HESS. Figs. 1.20 (a), (b) show two possible passive HESS structures, with batteries and supercapacitors directly connected in parallel and a single or two-stage conversion respectively.

- **Semi-active HESS**: in the semi-active topology, a power converter is inserted at the terminal of one storage, while the other is directly connected to the dc bus. Using one extra converter requires space and increase the cost of the

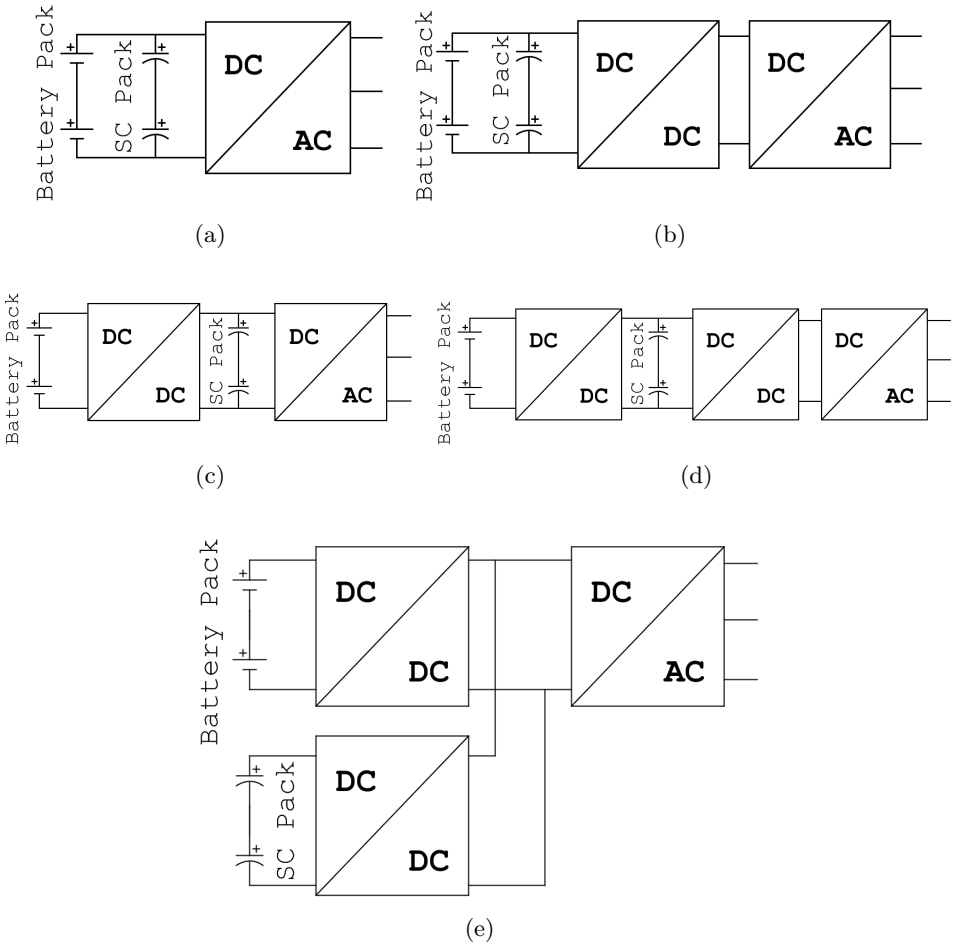

Figure 1.20: Passive HESS (a),(b); Semi-active HESS (c); Active HESS (d), (e).

system but improves the power flow management. Fig. 1.20 (c) shows a semi-active HESS structure, in which the battery pack is connected to a DC/DC converter and the SCs pack is connected to the input of the DC/AC converter. The battery and the SCs pack can also be swapped to obtain another structure. In this case, the power flow of one only source can be directly controlled.

- **Active HESS**: in Active HESSs each energy source is connected through a power converter to the system. Complexity and cost of the system increase but the power flow is fully controllable. Figs. 1.20 (d) and (e) show two possible active HESS structures. In (d) two cascaded DC/DC converters are used, one controls the battery pack power flow, the other one controls the SCs pack power flow. The voltage levels are still tied-up together. In (e) two DC/DC converters are connected in parallel output configuration. This solution presents the best possible power flow management, with total control over voltages and currents.

References

[1] European Commission. "2030 climate & energy framework." (2021), [Online]. Available: https://ec.europa.eu/clima/policies/strategies/2030_it#:~:text=Obiettivi%20chiave%20per%20il%202030,5%25%20dell'efficienza%20energetica..

[2] International Renewable Energy Agency, *The power to change: Solar and wind cost reduction potential to 2025*, 2016.

[3] World Energy Council, *Five steps to energy storage*, 2020.

[4] D. Sprake, Y. Vagapov, S. Lupin, and A. Anuchin, "Housing estate energy storage feasibility for a 2050 scenario," Sep. 2017. DOI: 10.1109/ITECHA.2017.8101925.

[5] M. Farag, "Lithium-ion batteries: Modelling and state of charge estimation," Ph.D. dissertation, Jun. 2013.

[6] T. Hordé, P. Achard, and R. Metkemeijer, "Apache: Integrated hybrid fuel cell system for 2-seat all electric aircraft propulsion," *28th Congress of the International Council of the Aeronautical Sciences 2012, ICAS 2012*, vol. 5, Sep. 2012.

[7] S. M. Rezvanizaniani, Z. Liu, Y. Chen, and J. Lee, "Review and recent advances in battery health monitoring and prognostics technologies for electric vehicle (ev) safety and mobility," *Journal of Power Sources*, vol. 256, pp. 110–124, 2014, ISSN: 0378-7753. DOI: https://doi.org/10.1016/j.jpowsour.2014.01.085. [Online]. Available: https://www.sciencedirect.com/science/article/pii/S0378775314001098.

[8] T. Utsunomiya, O. Hatozaki, N. Yoshimoto, M. Egashira, and M. Morita, "Self-discharge behavior and its temperature dependence of carbon electrodes in lithium-ion batteries," *Journal of Power Sources*, vol. 196, no. 20, pp. 8598–8603, 2011, ISSN: 0378-7753. DOI: https://doi.org/10.1016/j.jpowsour.2011.05.066. [Online]. Available: https://www.sciencedirect.com/science/article/pii/S0378775311010925.

[9] A. Farmann and D. U. Sauer, "A study on the dependency of the open-circuit voltage on temperature and actual aging state of lithium-ion batteries," *Journal of Power Sources*, vol. 347, pp. 1–13, 2017, ISSN: 0378-7753. DOI: https://doi.org/10.1016/j.jpowsour.2017.01.098. [Online]. Available: https://www.sciencedirect.com/science/article/pii/S0378775317301088.

[10] A. Stan, M. Świerczyński, D. Stroe, R. Teodorescu, and S. J. Andreasen, "Lithium ion battery chemistries from renewable energy storage to automotive and back-up power applications — an overview," in *2014 International*

Conference on Optimization of Electrical and Electronic Equipment (OPTIM), 2014, pp. 713–720. DOI: 10.1109/OPTIM.2014.6850936.

[11] P. Kreczanik, P. Venet, A. Hijazi, and C. Guy, "Study of supercapacitor aging and lifetime estimation according to voltage, temperature, and rms current," *Industrial Electronics, IEEE Transactions on*, vol. 61, pp. 4895–4902, Sep. 2014. DOI: 10.1109/TIE.2013.2293695.

[12] Elcab. "Own work." (2021), [Online]. Available: https://commons.wikimedia.org/w/index.php?curid=25527628.

[13] D. Andrea, *Battery Management Systems for Large Lithium-ion Battery Packs*, ser. EBL-Schweitzer. Artech House, 2010, ISBN: 9781608071050. [Online]. Available: https://books.google.it/books?id=o-QpFOR0PTcC.

[14] G. L. Plett, *Battery Management Systems, Volume II: Equivalent-Circuit Methods*, ser. Norwood. Artech House, 2015.

[15] J. V. Barreras, T. Kalogiannis, C. Fleischer, A. Christensen, E. Schaltz, and D. U. Sauer, "Fuse and switch box design, modeling and characterization in hil simulation environment for bms testing," in *International Conference on Sustainable Mobility Applications(SMART2015)*, 2015.

[16] S. S. Madani, E. Schaltz, and S. Knudsen Kær, "Simulation of thermal behaviour of a lithium titanate oxide battery," *Energies*, vol. 12, no. 4, 2019, ISSN: 1996-1073. [Online]. Available: https://www.mdpi.com/1996-1073/12/4/679.

[17] Y. Ye and K. W. E. Cheng, "An automatic switched-capacitor cell balancing circuit for series-connected battery strings," *Energies*, vol. 9, no. 3, 2016, ISSN: 1996-1073. [Online]. Available: https://www.mdpi.com/1996-1073/9/3/138.

[18] Y. Shang, C. Zhang, N. Cui, and C. C. Mi, "A delta-structured switched-capacitor equalizer for series-connected battery strings," *IEEE Transactions on Power Electronics*, vol. 34, no. 1, pp. 452–461, 2019. DOI: 10.1109/TPEL.2018.2826010.

[19] M. Daowd, M. Antoine, N. Omar, P. Van den Bossche, and J. Van Mierlo, "Single switched capacitor battery balancing system enhancements," *Energies*, vol. 6, no. 4, pp. 2149–2174, 2013, ISSN: 1996-1073. [Online]. Available: https://www.mdpi.com/1996-1073/6/4/2149.

[20] Y. Shang, F. Lu, B. Xia, C. Zhang, N. Cui, and C. Mi, "A switched-coupling-capacitor equalizer for series-connected battery strings," in *2017 IEEE Applied Power Electronics Conference and Exposition (APEC)*, 2017, pp. 1425–1429. DOI: 10.1109/APEC.2017.7930884.

[21] A. C. Baughman and M. Ferdowsi, "Double-tiered switched-capacitor battery charge equalization technique," *IEEE Transactions on Industrial Electronics*, vol. 55, no. 6, pp. 2277–2285, 2008. DOI: 10.1109/TIE.2008.918401.

[22] R. Fukui and H. Koizumi, "Double-tiered switched capacitor battery charge equalizer with chain structure," Nov. 2013, pp. 6715–6720. DOI: 10.1109/IECON.2013.6700244.

[23] A. Farzan Moghaddam and A. Van den Bossche, "An efficient equalizing method for lithium-ion batteries based on coupled inductor balancing," *Electronics*, vol. 8, p. 136, Jan. 2019. DOI: 10.3390/electronics8020136.

[24] S.-H. Park, K.-B. Park, H.-S. Kim, G.-W. Moon, and M.-J. Youn, "Single-magnetic cell-to-cell charge equalization converter with reduced number of transformer windings," *IEEE Transactions on Power Electronics*, vol. 27, no. 6, pp. 2900–2911, 2012. DOI: 10.1109/TPEL.2011.2178040.

[25] Y. Chen, X. Liu, Y. Cui, J. Zou, and S. Yang, "A multiwinding transformer cell-to-cell active equalization method for lithium-ion batteries with reduced number of driving circuits," *IEEE Transactions on Power Electronics*, vol. 31, no. 7, pp. 4916–4929, 2016. DOI: 10.1109/TPEL.2015.2482500.

[26] R. Ling, Q. Dan, L. Wang, and D. Li, "Energy bus-based equalization scheme with bi-directional isolated cuk equalizer for series connected battery strings," in *2015 IEEE Applied Power Electronics Conference and Exposition (APEC)*, 2015, pp. 3335–3340. DOI: 10.1109/APEC.2015.7104831.

[27] Y. Shi and R. Song, "A novel high-efficiency double-input bidirectional dc/dc converter for battery cell-voltage equalizer with flyback transformer," *Electronics*, vol. 8, p. 1426, Nov. 2019. DOI: 10.3390/electronics8121426.

Chapter 2

Batteries

2.1 Introduction

The strong development of electric vehicles (EVs) moves the research actions on new solutions for the automotive field. First, batteries and storage systems represent the burning issues of this sector. Among them, lithium ion batteries represent the main technology that is catching on for different purposes. These kinds of batteries are used for both stationary and mobile applications because of their high-energy density and high-power density. Great performances and innovative designs are asked for by the electric transportation market [1]; for this reason, accurate and reliable models are needed. Knowing SoC (State of Charge) [2], [3], SoH (State of Health) [4], OCV (Open Circuit Voltage) [5], currents, and voltages is absolutely necessary in order to have well designed and efficient energy storage systems, because non-linear physical effects in batteries strongly influence battery lifetime [6]. An accurate battery model allows, in the design phase, to consider several factors such as charging strategies or extreme operating conditions [7]. The main difficulty in is related to the need to make models as simple as possible [8]. Actually, in most cases, accurate models need complex solutions. In literature, a lot of different modeling methods are available and these can be mainly classified into three categories: electrochemical, mathematical or electrical [9], [10].

Electrochemical models are the more accurate but also more complex. They consider the chemical reactions happening through the electrodes to estimate the external parameters and are useful specially to describe thermodynamic and kinetic phenomena occurring in the cell. The first models were introduced by Fuller, Doyle and Newman [11]-[13] developing the porous electrode theory. They provide insight into batteries' internal dynamics such as electrochemical reactions, mass transportation, diffusion, concentration distribution, and ion distribution. They can relate the constructive parameters (material used for electrode, thickness of separator, dimensions of the cell) to the electrical parameters (voltage, current, capacity) and thermal behavior. An electrochemical model is made of a system of coupled time-variant spa-

tial partial differential equations. To solve these models, high computational efforts are needed and, in addition, several parameters that are difficult to measure or obtain, are needed. In [14], Kandler et al. considered a 1-dimensional model, in which the x coordinate is used to define the thickness of each component of the cell (current collectors, electrodes, separator). Many parameters are needed to fully parametrize the model, and most of them require a deep knowledge of the cell chemistry, production process, etc. The complexity and difficulty of finding all the necessary parameters make these models suitable only in the battery design phases. In order to decrease the electrochemical model complexity, Model Order Reduction (MOR) techniques can be applied. In [15], [16], the reduced order model equations and the model parameters identification for a lithium-iron phosphate battery is presented. The maximum Root Mean Square Error (RMSE) between the measured voltage and the electrochemical reduced order model output is within 55 mV for a single cell. In [17], a reduced order model based on a Galerkin projection method is developed for Lithium-Iron-Phosphate (LFP) and Nickel-Manganese-Cobalt (NMC) batteries, achieving a maximum RMSE equal to 15.5 mV.

Mathematical models can be further divided into two categories: empirical and stochastic [18]. The first ones are used to describe a specific behavior of the battery using simple equations. These models can only be used for specific applications, making errors of the order of $5 - 20\%$. The advantages of the empirical models are the low complexity and the possibility to achieve real-time parameter identification. The second category of mathematical models, the stochastic models, are based on the principle of the discrete-time Markov chain. They can achieve higher accuracy with respect to the empirical model while keeping low complexity and fast simulation. In[19], a mathematical method based on the least square algorithm is used for the dynamic parameters identification by modifying the Shepherd battery model. Hybrid method can be also applied, such as that used in [20] in which both static and dynamic parameters are estimated thanks the an extended Kalman Filtering Algorithm-based method.

Equivalent circuit battery models are developed by using resistors, capacitors and voltage sources in various combinations [21]-[24]. In [25], three equivalent circuital models, the *Rint* model, the *Thevenin* model and the Double Polarization (DP) model, are compared. The DP model gives the best results, with a maximum RMSE of 10 mV, but requires a more complex procedure for the parameter estimation.

Most of the battery models proposed in the previously cited literature require time-consuming experimental tests and costly equipment for their parametrization [26]. In the first design phase of a battery powered application, it is important to quickly evaluate the performances considering different kinds of batteries, different configurations, etc. The possibility to easily obtain battery models parameters from the technical data-sheets and to readily implement the model becomes of great importance [27].

The aim of this chapter is to compare three different parameter identifications and the modelling approaches. In particular, the modified *Shepherd* model, the *Rint* model and the *Thevenin* model are considered. The first two models are parametrized using just the information. For the *Thevenin* model, a pulse discharge test is executed for parametrization. The models are then validated at steady state, comparing the simulation results with the data-sheet discharge curves, and in transient operation, comparing the simulation results with experimental results. The test-bench used for the parametrization and validation of the models is extensively described, considering the accuracy of each employed instrument. The three modeling and parametrization approaches are systematically applied to the LG 18650HG2 lithium-ion cell, and the results are presented, compared and discussed. Section 2.2 presents the three different battery models. Sections 2.3 describes the parametrization procedures and the test-bench. Section 2.4 faces the validation of models, and Section 2.5 presents the discussion.

2.2 Batteries Modeling

In this section, the three considered battery models are analyzed, considering the governing equations. Then, the parametrization procedures are explained in detail and applied to the LG 18650HG2 cell.

2.2.1 *Sheperd* Model

One of the best-known mathematical models for constant-current discharge is the Shepherd model [28], [29]:

$$V = E_0 - K\left(\frac{Q}{Q - it}\right) i - R_0 \cdot i + A \cdot e^{(-B \cdot it)} \tag{2.1}$$

where:

- E_0 represents the open circuit voltage of a battery at full capacity (V);
- K is the polarization resistance coefficient (Ω);
- Q is the battery capacity (Ah);
- i is the battery current (A);
- R_0 is the internal resistance (Ω);
- $it = \int idt$ is the removed charge (Ah);
- A, B are empirical constants (V), (1/Ah).

Several mathematical models take the Shepherd model and try to improve it, adding or modifying some terms. In [30], a term to consider the polarization voltage

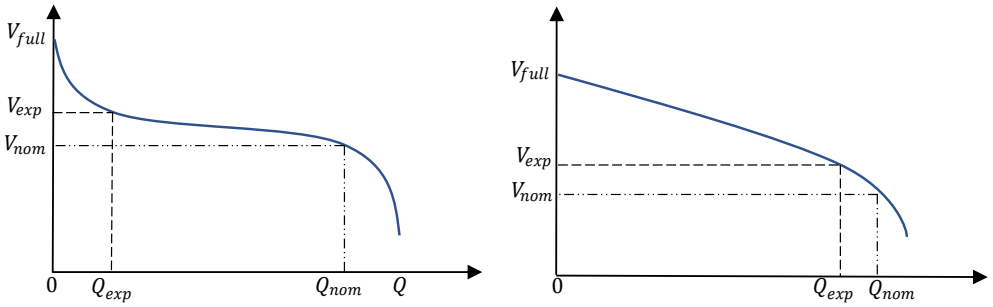

Figure 2.1: Typical discharge curves of: (a) LFP cell; (b) NMC cell

is added to the discharge model and the polarization resistance effect is slightly modified, resulting in the following equation

$$V = E_0 - \underbrace{K\left(\frac{Q}{Q-it}\right)i^*}_{\substack{\text{Polarization}\\ \text{resistance term}}} - \underbrace{K\left(\frac{Q}{Q-it}\right)it}_{\substack{\text{Polarization}\\ \text{voltage term}}} - R_0 \cdot i + A \cdot e^{(-B \cdot it)} \tag{2.2}$$

where i^* is the filtered current.

Furthermore, a different equation is given for the battery charging:

$$V = E_0 - K\left(\frac{Q}{it - 0.1 \cdot Q}\right)i^* - K\left(\frac{Q}{Q-it}\right)it - R_0 \cdot i + A \cdot e^{(-B \cdot it)}. \tag{2.3}$$

An important feature of this model is the possibility to easily find all the model parameters without the need of experimental tests. Starting from a typical discharge curve given in the manufacturer's data-sheet, four points are identified:

1. fully charged voltage V_{full}, first point of the characteristic;
2. end of the exponential zone Q_{exp}, V_{exp};
3. end of the nominal zone Q_{nom}, V_{nom} (when the voltage starts to decrease quickly);
4. maximum capacity Q, last point of the characteristic.

Depending on the cell's chemistry, the discharge curves can be slightly different and the points are shifted accordingly, as can be seen in Figure 2.1 (a) and (b).

In addition, the cell internal resistance R_0 is needed, which is generally given in the data-sheet. It should be noted that the discharge curves are obtained with a constant current discharge. Once all the data has been obtained, Equation 2.2 can be rewritten for each of the identified points to write a set of three equations with three unknowns $E_0,\ K,\ A$.

At the start of the characteristic $V = V_{full}$, the supplied charge is $it = 0$, the filtered current is $i^* = 0$, and the cell current is $i = I$. Equation 2.2 gives:

$$V_{full} = E_0 - R_0 \cdot I + A \tag{2.4}$$

The parameter B, which represents the time constant of the exponential term, depends on the shape of the discharge curve. For the discharge curve of 2.1 (a), it can be noticed that the exponential term energy is almost zero and can be approximated to $4/Q_{exp}$. For the discharge curve of 2.1 (b), the exponential term is still predominant and the parameter B can be approximated to $2/Q_{exp}$. For the exponential point, the voltage is $V = V_{exp}$, the supplied charge is $it = Q_{exp}$, and the filtered current is $i^* = 0$ because it is assumed that steady state has been reached. With the previous assumption, 2.2 gives:

$$V_{exp} = E_0 - K\frac{Q}{Q - Q_{exp}}\left(Q_{exp} + I\right) - R_0 \cdot I + A \cdot e^{(-B \cdot Q_{exp})}. \tag{2.5}$$

For the end of the nominal zone, the voltage is $V = V_{nom}$, the supplied charge is $it = Q_{nom}$ and 2.2 gives:

$$V_{nom} = E_0 - K\frac{Q}{Q - Q_{nom}}\left(Q_{nom} + I\right) - R_o \cdot I + A \cdot e^{(-B \cdot Q_{nom})}. \tag{2.6}$$

Solving the set of Equations 2.4-2.6 gives the models parameters, which can be expressed as

$$E_0 = \frac{E_{exp}C_{nom} - E_{nom}C_{exp}}{\left[\left(1 - e^{(-B \cdot Q_{nom})}\right)C_{exp} - \left(1 - e^{-3}\right)C_{nom}\right]} \tag{2.7}$$

where:

- $C_{exp} = \frac{Q}{Q - Q_{exp}}\left(Q_{exp} + I\right)$;
- $C_{nom} = \frac{Q}{Q - Q_{nom}}\left(Q_{nom} + I\right)$;
- $E_{exp} = -V_{exp} - R_0 \cdot I + \left(V_{full} + R_0 \cdot I\right) \cdot e^{-BQ_{exp}}$;
- $E_{nom} = -V_{nom} - R_0 \cdot I + \left(V_{full} + R_o \cdot I\right) \cdot e^{-B \cdot Q_{nom}}$.

$$K = E_0\left(\frac{1 - e^{-B \cdot Q_{exp}}}{C_{exp}}\right) + \frac{E_{exp}}{C_{exp}} \tag{2.8}$$

$$A = V_{full} - E_0 + R \cdot i \tag{2.9}$$

$$B = \begin{cases} \dfrac{2}{Q_{exp}}, & \text{for LFP cell} \\ \dfrac{4}{Q_{exp}}, & \text{for NMC cell} \end{cases} \tag{2.10}$$

2.2.2 *Rint* Model

A basic equivalent circuit battery model is shown Figure 2.2, and it is known as *Internal Resistance Model* or *Rint* model. This model describes the battery behavior

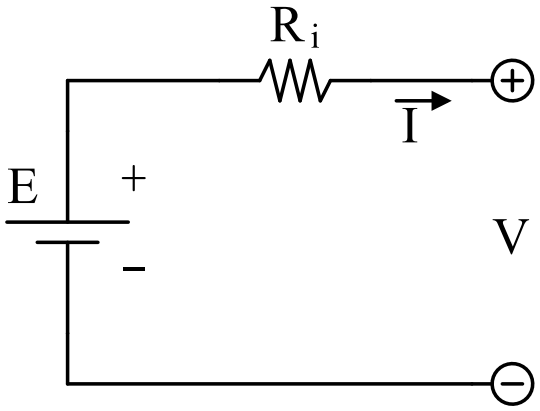

Figure 2.2: Schematic representation of the *Rint* equivalent circuit model.

using an ideal voltage source E, whose purpose is to simulate the battery open circuit voltage, and a resistor R_i that takes into account the battery internal resistance due to the electrodes. The battery terminal voltage can be expressed as:

$$V = E - R_i \cdot I \tag{2.11}$$

In this model, E and R_i are considered constant and the battery capacity is considered infinite. It can be used in simulation where the variation of the SoC is negligible.

Higher accuracy can be achieved by adding the SoC dependence for the open circuit voltage and the internal resistance.

$$V\left(SoC\right) = E\left(SoC\right) - R_i\left(SoC\right) \cdot I \tag{2.12}$$

To fully parametrize the model, $E\left(SoC\right)$ and $R_i\left(SoC\right)$ are needed. One of the advantages of this model is the possibility to parametrize it taking only the information from a typical cell manufacturer's data-sheet. Moreover, to consider the dependency of the battery capacity with the discharge current, the Peukert equation is used.

2.2.3 *Thevenin* Model

The *Rint* model does not consider the transient behavior of the battery. The insertion of a parallel Resistor-Capacitor (RC) branch, as shown in Figure 6, allows considering the short-term transient due to the electrolyte polarization. Similarly to *Rint* model,E and R_0 represent respectively the battery open circuit voltage and the electrode resistance, R_1 represents the polarization resistance and C_1 represents the polarization capacitance [33]. To enhance the model accuracy and consider transient phenomenon with different time constants, other RC branches can be included in series with Thevenin's model. However, the parametrization process of the model

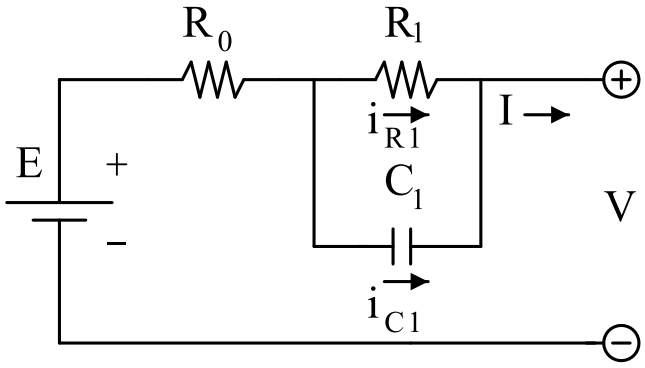

Figure 2.3: Schematic representation of the *Thevenin* equivalent circuit model.

becomes even more complicated. If the model is employed to simulate the battery behavior in one operating condition at a given SoC, the model's parameters can be counted as constants. Otherwise, if wide SoC operating range has to be simulated, the parameters can be considered dependent on temperature and SoC. The model is defined by the next equations:

$$\begin{cases} V\left(SoC\right) = E\left(SoC\right) - I \cdot R_0\left(SoC\right) - i_{R_1} \cdot R_1\left(SoC\right) \\ I = i_{R_1} + i_{C_1} \end{cases} \tag{2.13}$$

2.3 Batteries Parametrization

2.3.1 *Sheperd* Model

The parameter estimation procedure described above is now applied to the LG 18650HG2 cell. Figure 2.4 (a) shows the extracted points from the datasheet discharge curves. Among the four characteristics, the one at 0.2 C was chosen for the parameter estimation procedure. Figures 2.4 (b)–(d) show the point identification on the 0.2 C discharge curve. Figure 2.4 (a) depicts the maximum charge voltage V_{full} and the maximum capacity Q. Figure 2.4 (b),(c) represent respectively the exponential zone and the nominal zone detection.

Table 2.1 summarizes the identified points and the cell internal resistance R_0 given in the manufacturer's data-sheet. To estimate the other parameters, first a value for B must be chosen looking at the shape of the discharge curve, as described in Section 2.1. In this case, $B = 2/Q_{exp}$ was chosen. Using the data from Table 2.1 and the Equations (2.7)-(2.10), the model parameters, summarized in Table 2.2, were obtained.

2.3.2 *Rint* Model

To fully parametrize the model, $E(SoC)$ and $R_i(SoC)$ are needed. One of the advantages of this model is the possibility to parametrize it taking only the information

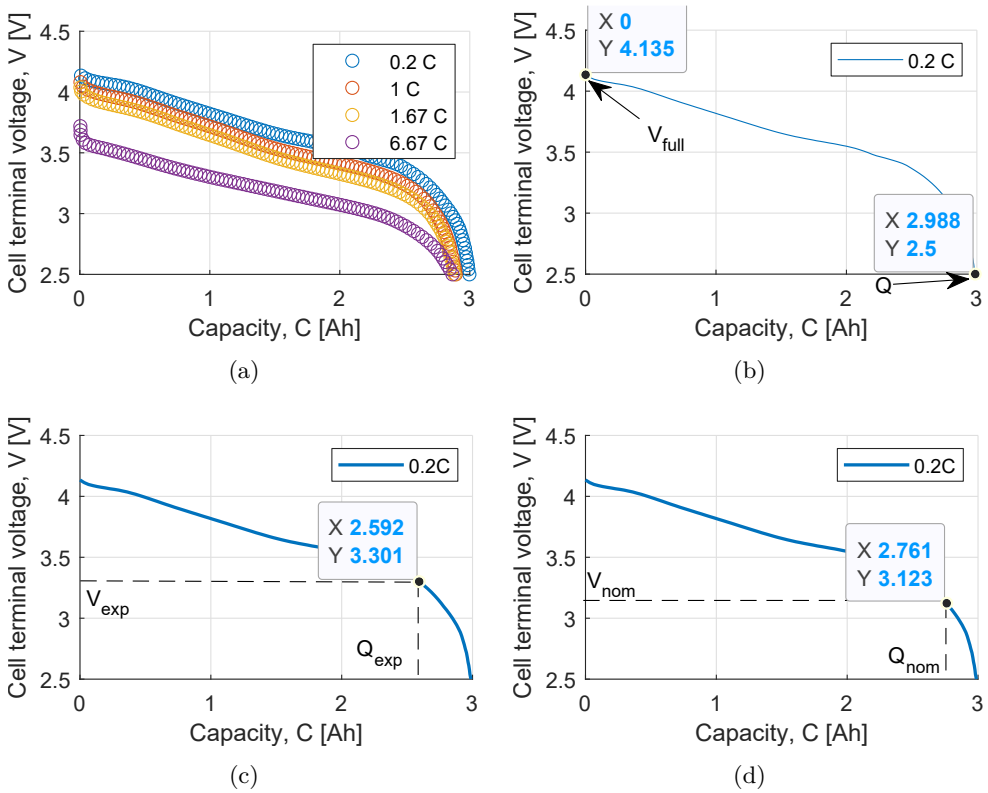

Figure 2.4: (a) Points extracted from the data-sheet discharge curves, at four different C rates (0.2 C, 1 C, 1.67 C, 6.67 C); Point identification for: (b) fully charged voltage V_{full} and maximum cell capacity Q; (c) Exponential zone voltage V_{exp} and capacity Q_{exp} identification; (d) Nominal zone voltage V_{nom} and capacity Q_{nom} identification.

Table 2.1: Identified points for the parameter estimation procedure.

V_{full} (V)	Q (Ah)	V_{exp} (V)	Q_{exp} (Ah)	V_{nom} (V)	Q_{nom} (Ah)	R_0 (Ω)
4.135	2.998	3.30	12.592	3.123	2.761	0.025

Table 2.2: *Shepherd* model parameters.

E_0 (V)	K (mΩ)	A (V)	B (Ah)
3.488	8.5000	0.6612	0.7716

from a typical cell manufacturer's data-sheet. Moreover, to consider the dependency of the battery capacity with the discharge current, the Peukert equation is used.

Normalization

The first step to parametrize the model is the extraction of the discharge curves from the data-sheet. The discharge curves give the cell terminal voltage as a function of the supplied capacity, expressed in Ah, for different values of the discharge current. The discharge curves are then normalized and interpolated to have datasets with equally spaced grids. To achieve normalization, the capacity values are divided by their maximum values:

$$DoD = \frac{Q_X}{Q_{X,max}} \tag{2.14}$$

where the subscript X is the considered discharge curve C-rate, and $Q_{X,max}$ is the maximum capacity of the considered discharge curve. In this way, the discharge curves are represented as function of the Depth of Discharge (DoD).

Internal Resistance

The internal resistance as function of DoD can be derived from the normalized discharge curves, considering two different characteristics

$$\begin{cases} E(DoD) = V_X(DoD) + R_{i,j}(DoD) \cdot I_X \\ E(DoD) = V_Y(DoD) + R_{i,j}(DoD) \cdot I_Y. \end{cases} \tag{2.15}$$

If the internal resistance $R_i(DoD)$ does not depend on the discharge current, it can be calculated as

$$R_{i,j}\left(DoD\right) = \frac{V_X\left(DoD\right) - V_Y\left(DoD\right)}{I_Y - I_X} \tag{2.16}$$

Since usually N discharge curves are available in the data sheets, Equation (2.16) can be applied to all the curves combination. The internal resistance used in the model is finally calculated as the average value

$$R_i\left(DoD\right) = \frac{\sum_{j=1}^{J} R_{i,j}\left(DoD\right)}{J} \tag{2.17}$$

where J is the number of possible combinations, given by

$$J = \frac{N!}{(N-2)! \cdot 2} \tag{2.18}$$

Open Circuit Voltage

The open circuit voltage as a function of DoD can be estimated as

$$E_X\left(DoD\right) = V_X\left(DoD\right) + R_i\left(DoD\right) \cdot I_X \tag{2.19}$$

Applying Equation (2.19) to all the discharge curves available in the data-sheet, the average open circuit voltage as a function of the DoD is derived as

$$E\left(DoD\right) = \frac{1}{N}\sum_{X=1}^{N} E_X(DoD) \tag{2.20}$$

Capacity

The cell capacity depends on the discharge current, and to consider this phenomenon, the Peukert Capacity is considered [31], [32]. If the battery supplies a current I_X to the load, from the point of view of the battery capacity, it is as if a current equal to I_X^k was supplied. If the battery is recharged, the phenomenon is negligible, therefore $k = 1$. Accordingly, an equivalent battery capacity, defined as Peukert capacity, can be calculated as

$$C_P = I_X^k \cdot T_X \tag{2.21}$$

where:

- C_P is the Peukert Capacity (Ah);
- k is the Peukert coefficient (-);
- I_x is the discharge current (A);
- T_X is the discharge time for discharge current I_x (h).

To estimate the Peukert coefficient for a given cell, the discharge times at two different discharge currents are needed. From the manufacturer data-sheet, the actual supplied capacity and the discharge current can be extrapolated, and the discharge time can be calculated as

$$T_X = \frac{Q_X}{I_X} \quad , \quad T_Y = \frac{Q_X}{I_Y} \tag{2.22}$$

and the Peukert coefficient is given by

$$k_i = \frac{(\log T_Y - \log T_X)}{(\log I_X - \log I_Y)} \tag{2.23}$$

From (2.23), the Peukert coefficient can be derived for any different discharge curves included in the data-sheet. Usually, X is chosen equal to the minimum

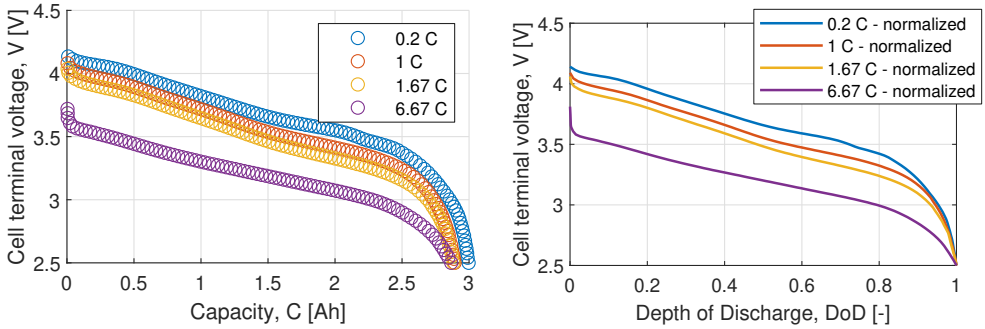

(a) (b)

Figure 2.5: Data-sheet discharge curves: (a) extracted point from data-sheet; (b) interpolated and normalized discharge curves.

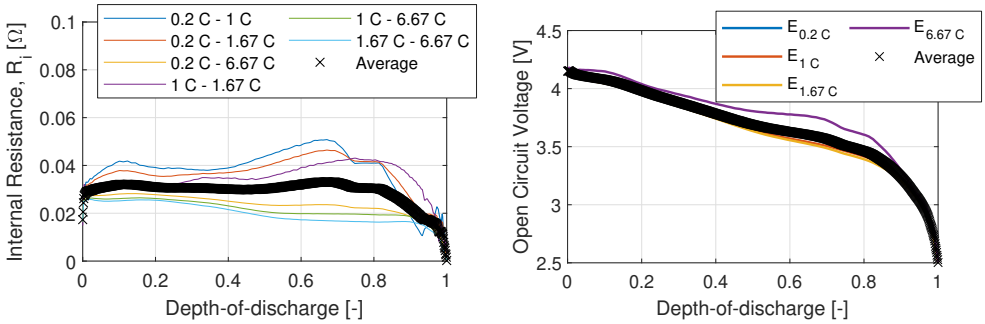

(a) (b)

Figure 2.6: Model parameter identification: (a) internal resistance and (b) open circuit voltage as a function of the Depth of Discharge.

discharge current while Y is varied to consider all the discharge profiles. The Peukert coefficient used for the simulation is then given by the average value as

$$k = \frac{\sum_{i=1}^{N-1} k_i}{N-1} \tag{2.24}$$

The parameter estimation procedure described above is now applied to the LG18650HG2 cell. Figure 2.5 (a) shows the data-sheet discharge curve, which is given as a function of the supplied capacity. The curves are then normalized, using Equation (2.14), and interpolated as shown in Figure 2.5 (b). The internal resistance is estimated for each possible curve combination using Equation (2.16), obtaining the solid curves represented in Figure 2.6 (a). Finally, using Equation (2.17), the average internal resistance, represented in Figure 2.6(b) with the crossed line, is obtained.

The open circuit voltage is calculated for each discharge curve using Equation (2.19), represented in Figure 2.6(b) with the solid lines. The average open circuit voltage, shown in Figure 2.6(b) with the crossed line, is then obtained with Equation (2.20). Table 2.3 summarizes the *Rint* model parameters.

Table 2.3: *Rint* model parameters.

DoD	0	0.1	0.2	0.3	0.4	0.5	0.6	0.7	0.8	0.9	1
E_0 (V)	4.18	4.08	3.98	3.88	3.78	3.69	3.63	3.57	3.46	3.24	2.58
R_0 (mΩ)	17.3	32.0	31.0	30.7	30.1	30.2	32.0	32.8	30.4	22.4	17.1

Peukert Capacity	
C_P (Ah)	2.97
k (-)	1.02

2.3.3 *Thevenin* Model

To fully parametrize the model, four parameters are needed: E, R_0, R_1, C_1 and they are all SoC dependent. For this model, the manufacturer's specifications do not provide enough information to proceed with the parametrization procedure. Thus, some experimental tests must be performed, in particular a Pulse Discharge Test (PDT) [33]. The PDT consists in discharging a fully charged cell with a current pulse of specified amplitude and duration. At the end of the pulse, the cell is left in open circuit to stay at rest. At the end of the rest period, another current pulse is applied, and the procedure is repeated until the cell reaches the cut-off voltage.

The test starts charging the cell to its maximum voltage using the Constant Current/Constant Voltage procedure. After a rest period, the Pulse Discharge test is performed. The cell voltage is continuously acquired, and a pre-defined current pulse is applied. The removed charge in Ah can be calculated as:

$$\Delta Q = \frac{t_p \cdot I_p}{3600}. \tag{2.25}$$

Figure 2.7 illustrates the current pulse and the cell voltage, with all the equations used for the parameter estimation. At the start of the test, the acquired voltage corresponds to the cell open circuit voltage at 0% Depth of Discharge, due to the rest period after the full charge. The acquired voltage at the end of the rest period of the first current pulse, corresponds to the cell open circuit voltage at $\frac{\Delta Q}{Q_n} \cdot 100\%$ Depth of Discharge, where Q_n is the nominal capacity of the cell.

The immediate voltage reduction after the start of the current pulse is

$$\Delta V_0 = R_0 \cdot I_p \tag{2.26}$$

and the internal resistance can be estimated as

$$R_0 = \Delta V_0 / I_p \tag{2.27}$$

Then, the cell is left open circuit for as long as it takes for the electrolyte polarization phenomenon to complete. The voltage rise, from end of the current pulse to

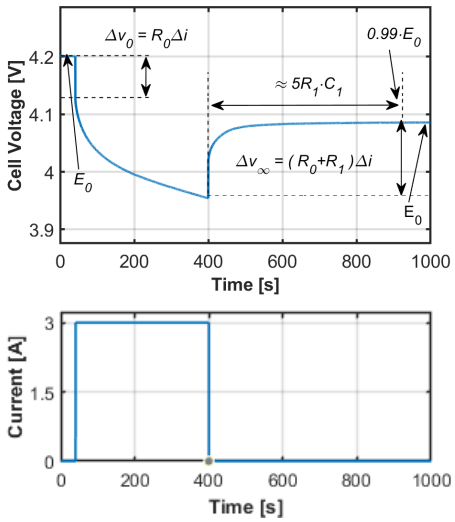

Figure 2.7: Current pulse and battery terminal voltage response.

the end of the rest period, is:

$$\Delta V_\infty = (R_0 + R_1) \cdot I_p \tag{2.28}$$

From the Equations 2.27 and 2.28, R_1 can be computed as:

$$R_1 = \frac{\Delta V_\infty}{I_p} - R_0 \tag{2.29}$$

Finally, the polarization capacitance is estimated considering that, after approximately five time constants, the cell terminal voltage is equal to $0.99 \cdot E_0$, thus

$$\Delta t_\infty \cong 5 R_1 C_1 \tag{2.30}$$

and C_1 can be estimated as:

$$C_1 = \frac{\Delta t_\infty}{5 R_1} \tag{2.31}$$

The parameter estimation procedure described above is now applied to the LG 18650HG2 cell. First, the characteristics of the current pulse are chosen. The pulse starts after 40 s from the beginning of the test, with an amplitude $I_p = 3$ A for $t_p = 360$ s. The removed charge is therefore

$$\Delta Q = \frac{360 \cdot 3}{3600} = 0.3 \text{ Ah} \tag{2.32}$$

corresponding to approximately 10% of the nominal capacity of the battery. Figure 2.8 shows the experimental cell terminal voltage, acquired during the PDT, and used for the parameter estimation procedure. A MATLAB application was created to programmatically estimate all the parameters. The application considers each

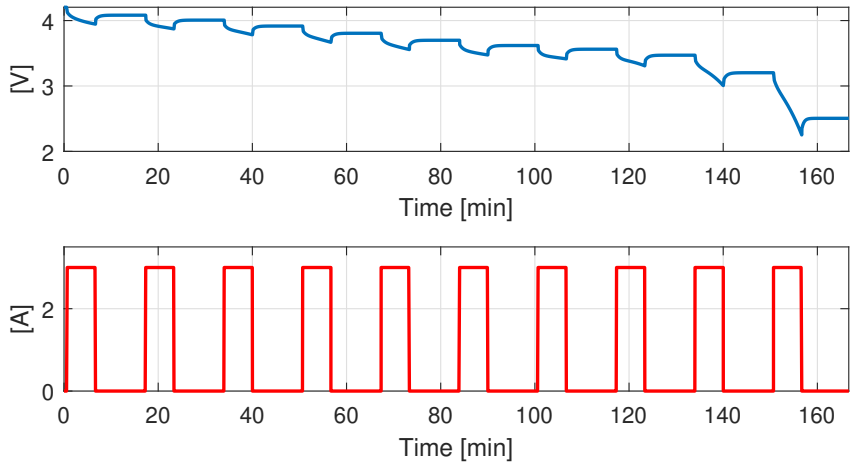

Figure 2.8: Cell terminal voltage and battery current during the experimental PDT.

Table 2.4: *Thevenin* model parameters.

DoD	0	0.1	0.2	0.3	0.4	0.5	0.6	0.7	0.8	0.9	1
E_0 (V)	4.20	4.08	4.01	3.89	3.80	3.70	3.63	3.55	3.46	3.22	2.5
R_0 (mΩ)	25.6	23.9	22.4	22.0	21.9	21.9	22.0	22.1	22.7	26.2	28.7
R_1 (mΩ)	16.9	20.0	25.2	22.3	22.1	25.0	30.0	25.7	29.9	43.3	56.7
C_1 (kF)	2.05	2.00	1.59	1.79	1.81	1.60	1.31	1.55	1.33	0.92	0.51

pulse individually and applies Equations (2.25)-(2.32) to calculate E_0, R_0, R_1, C_1. The results are reported in Figure 2.9, in which the red crosses are the estimated points and the blue solid line is a polynomial function, obtained with a least square approximation procedure. Table 2.4 summarizes the *Thevenin* model parameters.

2.3.4 Test-bench description

With the aim to validate experimentally the described models, a test bench (Figure 2.10), was implemented, composed by:

- a LG18650HG2 cell, whose characteristics are reported in Table 2.5,
- a Fluke PM2812 Programmable Power Supply, whose characteristics are reported in Table 2.6, used to charge the cells;
- an Agilent 6060B Single Input Electronic Load, whose characteristics are reported in Table 2.7, used on the discharge phase of the cell;
- a NI 9215 16-Bit Data Acquisition Board (placed in a NI cDAQ 9172 chassis), whose characteristics are reported in Table 2.8, used to acquire the cell voltage signal;
- a SRD05VDCSl-C 4-Channels Optical Isolated Relay;
- a NI 9401 Digital Module (placed in the NI cDAQ 9172 chassis), used to control the relay.

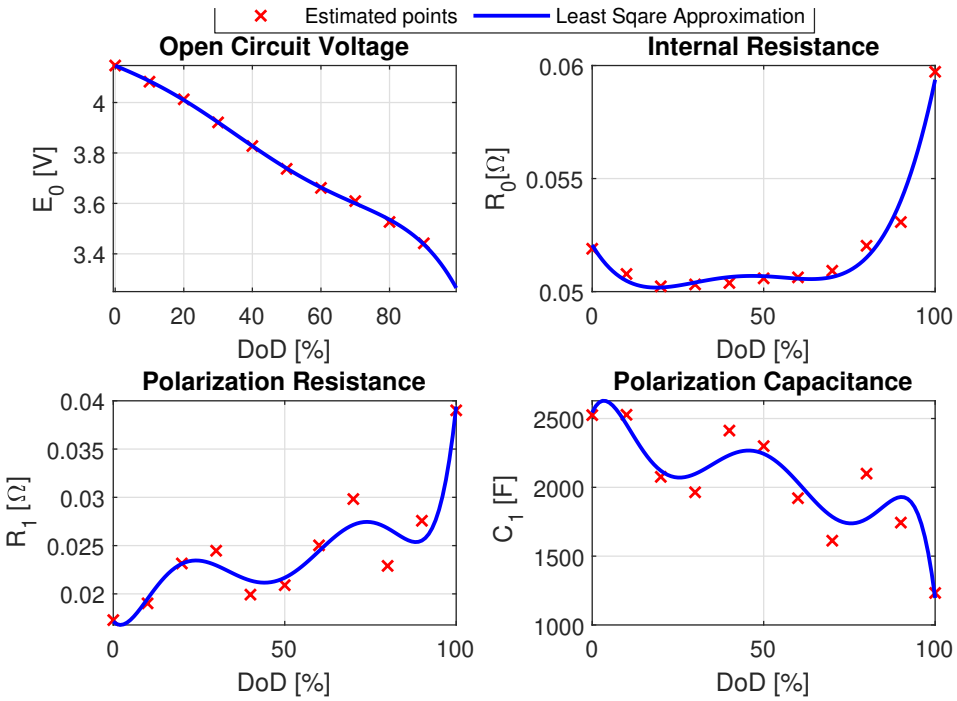

Figure 2.9: Estimated parameters for the LG HG2 cell.

All the instrumentation is controlled by a PC connected to the power supply and the electronic load via GPIB and to the NI chassis via USB.

The cell voltage signal is acquired at a 10 kS/s sampling frequency and then scaled at a 10 S/s sampling frequency calculating the average value in a 0.1 s time window. All the acquisitions were carried out after the calibration of the board.

The battery current is not directly measured and its values are taken from the values settled in the power supply (during the charge phase) or in the electronic load (during the discharge phase).

The battery capacity is estimated using the Coulomb Counting method, as:

$$Q = \sum_{i=1}^{N} I \cdot \Delta T_s \tag{2.33}$$

where I is the battery current and ΔT_s is the sampling period.

Measurement Uncertainty Evaluation

In order to assess the accuracy of the parameters estimation for the *Thevenin* model, the uncertainty evaluation was performed, strictly following the rules prescribed by [34], for the measurements of the four parameters E_0, R_0, R_1 and C_1. The acquired voltage is affected by three main error sources, namely offset error, gain error and noise. The first step is to evaluate the uncertainty associated with each error source starting from the data acquisition board specifications:

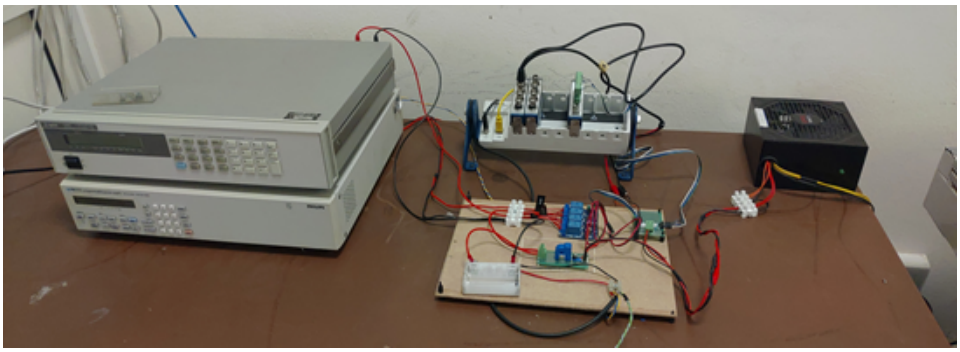

Figure 2.10: Test-bench used for parameter estimation and model validation.

Table 2.5: LG 18650HG2 cell specification.

Nominal voltage (V)	3.7
Nominal capacity (Ah)	3
Continuous discharge current (A)	20
Internal resistance (mΩ)	24-26
Standard charge current (A)	1.5
Fast charge current (A)	4
Max voltage (V)	4.2

Table 2.6: Power supply Fluke PM2812 specifications.

Output voltage range (V)	0-60
Output current range (A)	0-5
Readback current accuracy (A)	±(0.1%+15 mA)
Current noise (mA)	10

Table 2.7: Electronic load Agilent 6060B specifications.

Input voltage range (V)	0-60
Input current range (A)	0-5
Maximum power (W)	300
Readback current accuracy (A)	±(0.05%+65 mA)
Current noise (mA)	4

Table 2.8: Data Acquisition Board NI 9215 Specifications.

Signal level (V)	± 10
Type of ADC	16-Bit successive approximation
Channels	4 differential (simultaneously acquired)
Sample rate (kS/s/ch)	100
Accuracy (after calibration) (mV)	±(0.02%+1.5 mV)
Noise (peak-to-peak) (mV)	2.2

- considering a rectangular distribution for the offset error;

$$u_{offset} = \frac{1.5}{\sqrt{3}} = 0.87 \text{ mV} \tag{2.34}$$

- considering a rectangular distribution for the gain error and considering the worst case that corresponds to the maximum measured value (4.2 V);

$$u_{gain} = \frac{0.02 \cdot 4200}{100\sqrt{3}} = 0.49 \text{ mV} \tag{2.35}$$

-

$$u_{noise} = \frac{2.2}{3\sqrt{1000}} = 0.02 \text{ mV} \tag{2.36}$$

Therefore, the voltage standard uncertainty is

$$u_V = \sqrt{u_{offset}^2 + u_{gain}^2 + u_{noise}^2} = 1 \text{ mV} \tag{2.37}$$

and the expanded uncertainty with a 99% confidence level (coverage factor $k = 2.58$) is equal to 2.6 mV.

Actually, for the estimation of R_0, R_1 and C_1, only the differential voltage value ΔV is needed. In this case, the offset errors do not generate uncertainty, and, therefore:

$$u_{\Delta V} = \sqrt{u_{gain}^2 + u_{noise}^2} = 0.49 \text{ mV} \tag{2.38}$$

and the expanded uncertainty is equal to 1.3 mV.

With regard to the current measurement, starting from the electronic load specifications, three error sources have to be considered:

- considering a rectangular distribution for the offset error

$$u_{offset} = \frac{60}{\sqrt{3}} = 35 \text{ mA} \tag{2.39}$$

- considering a rectangular distribution for the gain error and considering the

worst case that corresponds to the maximum measured value (5 A);

$$u_{gain} = \frac{0.05 \cdot 5000}{100\sqrt{3}} = 1.4 \text{ mA} \tag{2.40}$$

- the noise error is expressed as rms value

$$u_{noise} = 4 \text{ mA} \tag{2.41}$$

Therefore, the current standard uncertainty is

$$u_I = \sqrt{u_{offset}^2 + u_{gain}^2 + u_{noise}^2} = 35 \text{ mA} \tag{2.42}$$

and expanded uncertainty with a 99% confidence level is equal to 91 mA.

Regarding the R_0 measurement, applying the uncertainty propagation low to Equation (2.27) and considering that the current during the parametrization process is set at 3 A, and considering the worst case, which corresponds to the maximum observed $\Delta V (\Delta V = 0.1\ V)$

$$u_{R_0} = \sqrt{\frac{1}{I^2} u_{\Delta V}^2 + \frac{\Delta V^2}{I^4} u_I^2} = 1.1\ \mu\Omega \tag{2.43}$$

The expanded uncertainty with a 99% confidence level is, therefore, equal to 2.8 $\mu\Omega$.

About the R_1 measurement, applying the uncertainty propagation law to Equation (2.29)

$$u_{R_1} = \sqrt{\frac{1}{I^2} u_{\Delta V}^2 + \frac{\Delta V_\infty^2}{I^4} u_I^2 + u_{R_0}^2} = 2.3\ \mu\Omega \tag{2.44}$$

and the expanded uncertainty is therefore equal to 6 $\mu\Omega$.

Regarding the C_1 measurement, applying the uncertainty propagation law to Equation (2.31)

$$u_{C_1} = \sqrt{\frac{1}{R_1^2} u_{\Delta t}^2 + \frac{\Delta t^2}{5R_1^4} u_{R_1}^2} \tag{2.45}$$

However, considering the low value of time jitter of the data acquisition board, the uncertainty of the ΔT measurement can be safely neglected. Therefore:

$$u_{C_1} = \frac{\Delta t}{\sqrt{5} R_1^2} u_I = 0.96 \text{ F} \tag{2.46}$$

and the expanded uncertainty is therefore equal to 2.5 F.

With regard to the SoC measurement, referring to Equation (2.33)

$$u_{SoC} = \sum \left(\Delta T_i u_I + I_I u_{\Delta T} \right) \tag{2.47}$$

that, neglecting the ΔT uncertainty and considering that the ΔT_j are constant (0.1

s) and considering N steps, becomes

$$u_{SoC} = N\Delta T u_I \tag{2.48}$$

2.4 Models Validation

The considered models are first validated by superimposing simulation results to the data-sheet curves for the LG 18650HG2 Li-ion cell in Section 2.4.1. The models are then validated with respect to experimental results in different operating conditions in Sections 2.4.2–2.4.4. In particular, the constant current/constant voltage (CC/CV) recharge, the Pulse Discharge Test (PDT) and the Dynamic Discharge Test (DDT) of the cell are considered. In order to compare the models, the instantaneous error and the Root Mean Square Error (RMSE) expressed are considered. The instantaneous error is calculated as

$$Err(t_i) = \left[\frac{A(t_i) - S(t_i)}{A_{max}}\right] \cdot 100 \quad [\%] \tag{2.49}$$

where:

- $A(t_i)$ is the actual value at the considered instant t_i;
- $S(t_i)$ is the simulated value at the considered instant t_i;
- A_{max} is the maximum observed value.

The Root Mean Square Error (RMSE) is calculated as

$$RMSE = \sqrt{\frac{\sum_{i=1}^{N} \left[A(t_i) - S(t_i)\right]^2}{N}} \text{ [V]} \tag{2.50}$$

where N is the number of samples of the experimental and simulated data.

2.4.1 Data-sheet Discharge Curves

In the following sections, the described models are validated at steady state, comparing the discharge curves extracted from the manufacturer's data-sheet and the simulation results for the LG HG2 18650 cells.

Sheperd Model Validation

Figure 2.11 shows the simulation results for the *Shepherd* model superimposed on the data-sheet curves for different C-rates. The dotted curves represent the data-sheets extracted points; the solid line represents the simulation results. It can be noted that, for lower C-rates (0.2 C, 1 C, 1.67 C), the simulated curves fit well to the data-sheet curves during almost 85% of the discharge. For higher C-rate (6.67 C) this model

does not give a good approximation of the cell voltage. The parameter estimation was done for the 0.2 C discharge curve, considering the parameters independent of the discharge current. In practice, the parameters also depend on the discharge current, and this can cause the accuracy problem.

Figure 2.12 shows each discharge curve individually and the related instantaneous error calculated with Equation (2.49), and RMSE calculated with Equation (2.50). For 0.2 C, 1 C, 1.67 C discharge rates represented respectively in Figure 2.12 (a)–(c), the error is within 0–5% for SoC and within 100–20%. For SoC below 20%, the accuracy of the model decreases significantly. For 6.67 C discharge rate, represented in Figure 2.12 (b), the error starts at 4% and ramps up to 12%, hence this model is not suitable for high discharge rate.

Rint Model Validation

Figure 2.13 shows the simulation results for the *Rint* model superimposed on the data-sheet curves for different C-rates. Differently from the *Sheperd* model, the *Rint* model shows good accuracy for all C-rates (0.2 C, 1 C, 1.67 C 6.67 C), predicting with appropriate precision the cell terminal voltage.

Figure 2.14 shows each discharge curve individually and the related error. For the 0.2 C discharge curve, Figure 14a, the error is below 1% for all the SoC range. For the 1 C discharge curve, Figure 2.14(b), the error is below 5% for SoC between 100 to 2% but then starts to increase. For the 1.67 C discharge curve, Figure 2.14(c) is always below 2%. Finally, for the 6.67 C discharge curve, Figure 2.14(d), the error is below 5%.

Thevenin Model Validation

Figure 2.15 shows the simulation results for the Thevenin model superimposed on the data-sheet curves for different C-rates. Again, the model has better accuracy for lower C-rates.

Figure 2.16 shows each discharge curve individually and the related error, calculated again with Equation (2.49). For the 0.2 C, 1 C and 1.67 C discharge curves, Figure 2.16(a)–(c), similar results are obtained with an error below 2.5% for SoC between 100 to 20%. Finally, for the 6.67 C discharge curve, Figure 2.16(d), the error continuously increases, thus this model is not suited for higher C-rates.

2.4.2 Battery CC/CV Charge

Figures 2.17, 2.18 and 2.19 (a) show the experimental cell voltage and current (solid blue and orange line respectively) superimposed to the simulated cell voltage and current (dashed blue and orange line respectively) obtained with the Shepherd, Rint and Thevenin model respectively. Figures 2.17, 2.18 and 2.19 (b) show the instantaneous percentage error (solid blue line) and report the RMSE. The best

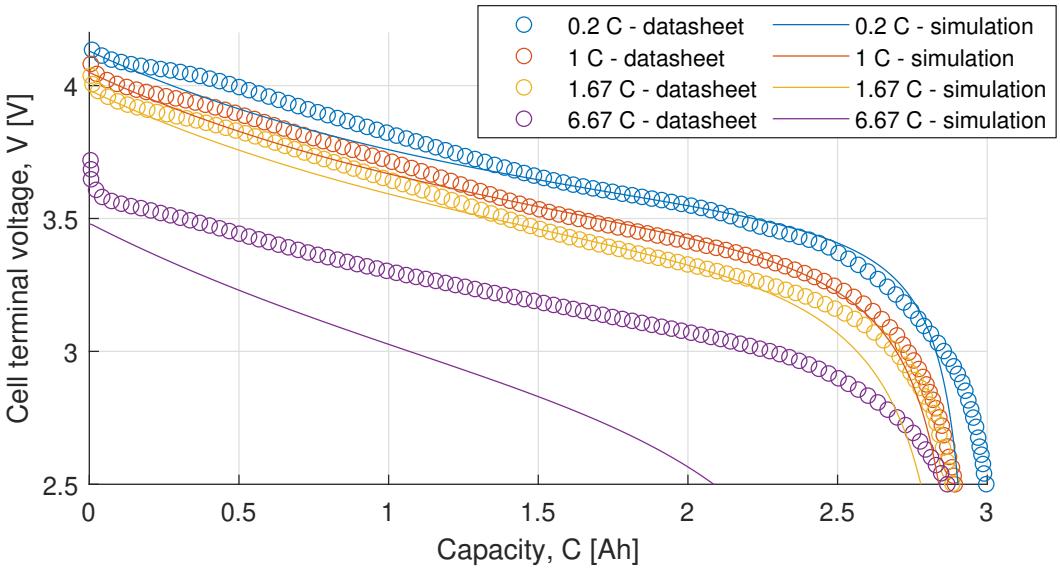

Figure 2.11: Data-sheet discharge curves vs. simulation results for the *Shepherd* model.

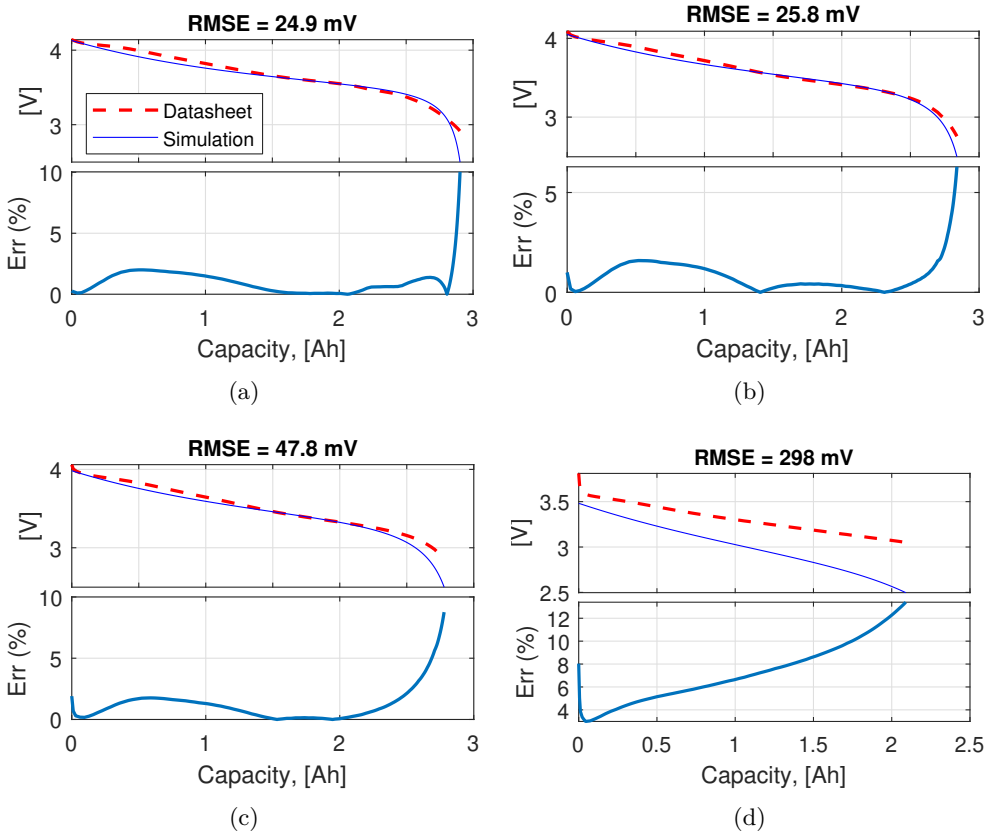

Figure 2.12: *Shepherd* model data-sheet vs. simulation curves and error: (a) 0.2 C discharge; (b) 1 C discharge; (c) 1.67 C discharge; (d) 6.67 C discharge.

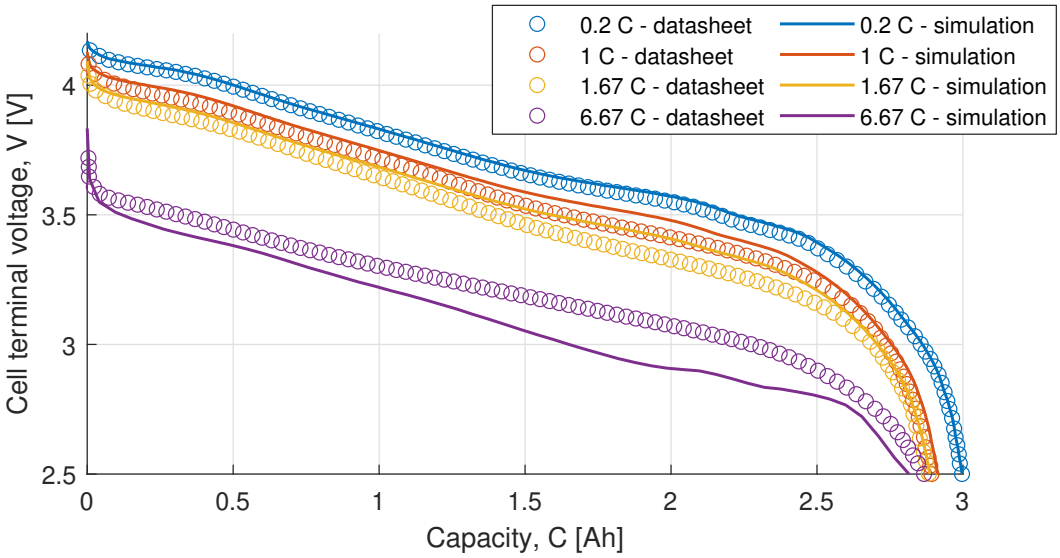

Figure 2.13: Data-sheet discharge curves vs. simulation results for the *Rint* model.

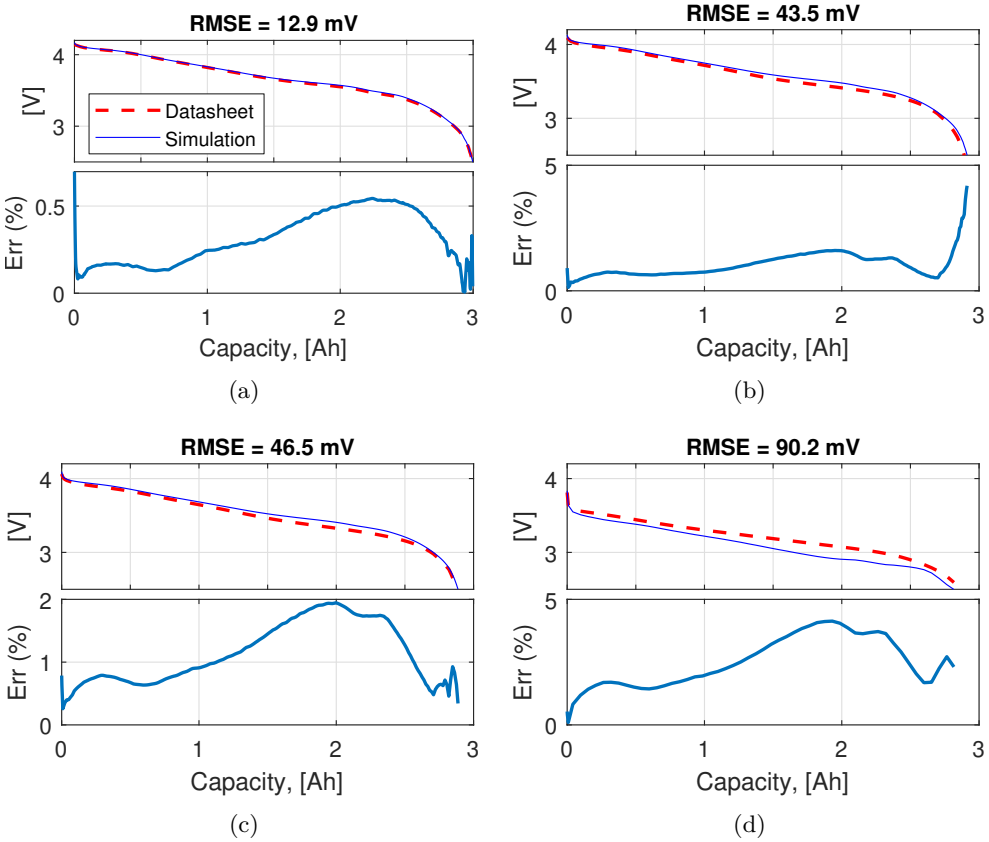

Figure 2.14: *Rint* model data-sheet vs. simulation curves and error: (a) 0.2 C discharge; (b) 1 C discharge; (c) 1.67 C discharge; (d) 6.67 C discharge.

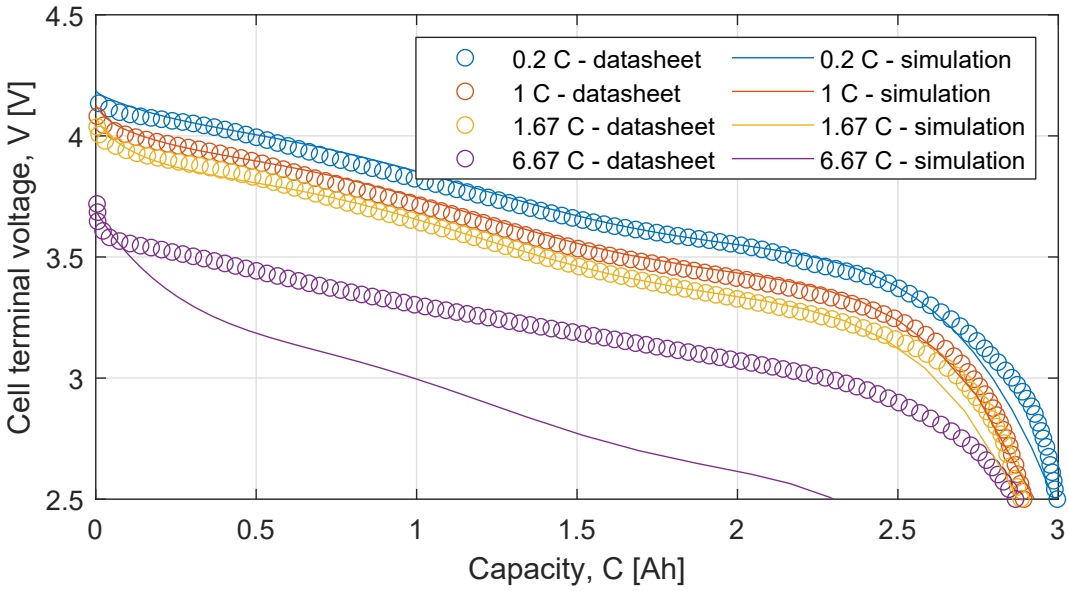

Figure 2.15: Data-sheet discharge curves vs. simulation results for the *Thevenin* model.

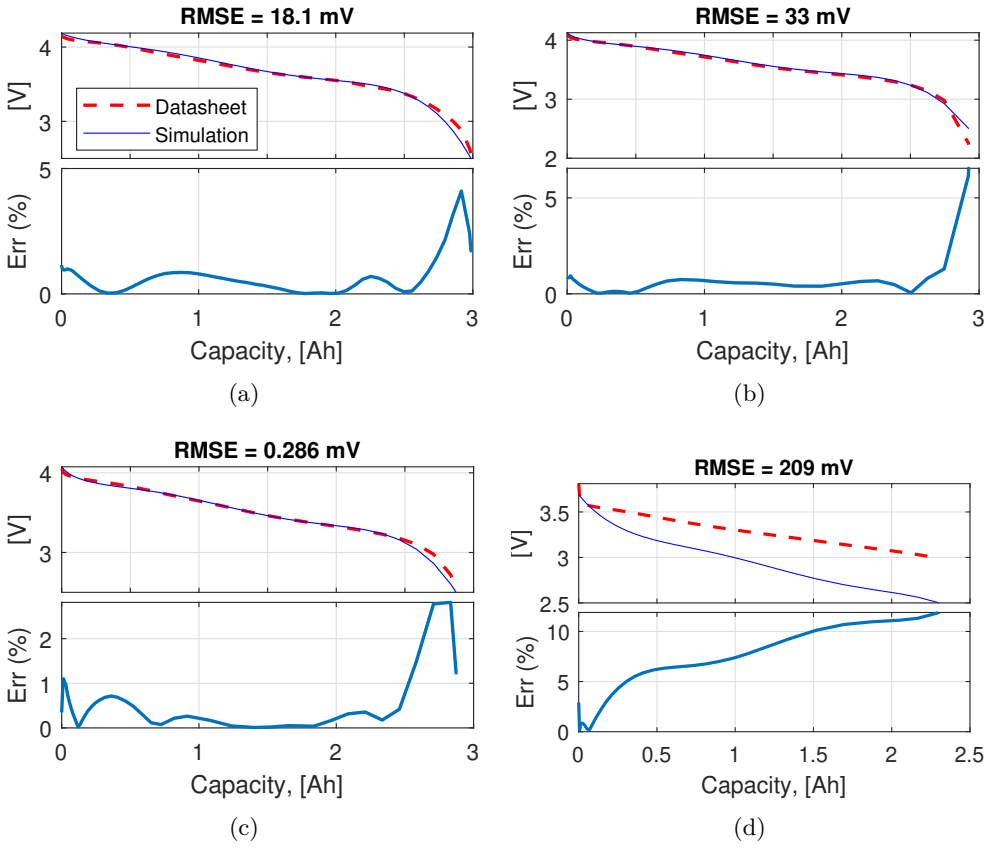

Figure 2.16: *Thevenin* model data-sheet vs. simulation curves and error: (a) 0.2 C discharge; (b) 1 C discharge; (c) 1.67 C discharge; (d) 6.67 C discharge.

results were obtained with the *Thevenin* model with a RMSE equal to 69 mV and an instantaneous error between ± 1% most of the time.

2.4.3 Battery Pulse Discharge

Figures 2.20, 2.21 and 2.22 (a) show the experimental cell voltage (solid blue line) and the simulated cell voltage (dashed orange line) obtained with the *Shepherd*, *Rint* and *Thevenin* model respectively for the Pulse Discharge Test. Figures 2.20, 2.21 and 2.22 (b) show the instantaneous percentage error (solid blue line) and report the RMSE. Once again, the model that best fits the experimental results is the Thevenin model, with a RMSE equal to 15 mV and an instantaneous error between ± 2%.

s

2.4.4 Battery Dynamic Discharge

Figures 2.23, 2.24 and 2.25 (a) show the experimental cell voltage (solid blue line) and the simulated cell voltage (dashed orange line) obtained with the *Shepherd*, *Rint* and *Thevenin* model respectively for the Dynamic Discharge Test. Figures 2.23, 2.24 and 2.25 (b) show the instantaneous percentage error (solid blue line) and report the RMSE. In this case too, the *Thevenin* model gives the best results with a RMSE equal to 44 mV and instantaneous error less than 3%.

2.5 Discussion

This chapter carried out a comparison study of battery modeling and parameter identification techniques. Three models were considered: the *Shepherd*, the *Rint* and the *Thevenin* battery models.

The *Shepherd* model belongs to the category of mathematical models. It can simulate the battery behavior both in static and transient operations thanks to the filtered current term. The parametrization procedure is quite simple, because all the necessary information can be found in the battery data-sheet. The parametrization was carried out considering the 0.2 C discharge curve characteristic and considering the parameters current-independent.

The *Rint* model belongs to the category of equivalent circuit models and it does not consider the short-term battery dynamics. The parametrization procedure is a bit more complex than the Shepherd model one, but all the information can still be found in the manufacturer's data-sheet. The parametrization procedure considers different discharge curves, thus obtaining parameters that are somehow current dependent.

The *Thevenin* model belongs to the category of equivalent circuit models and, thanks to the RC branch, it can simulate the short-term battery dynamics. To parametrize the model, costly and time-consuming tests are required.

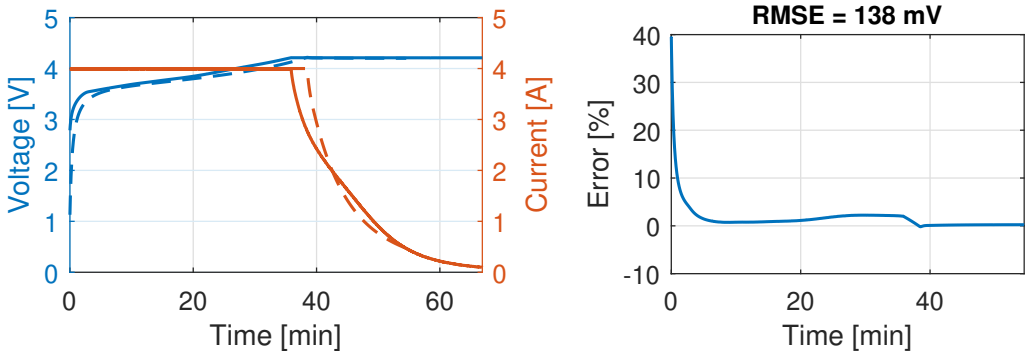

(a) (b)

Figure 2.17: *Shepherd* model CC/CV recharge: (a) experimental (solid line) and simulated (dashed line) voltage and current; (b) Error trend and RMSE.

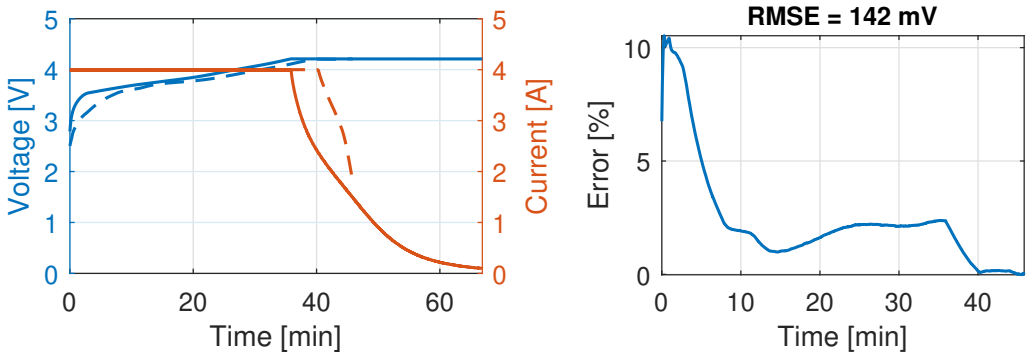

(a) (b)

Figure 2.18: *Rint* model CC/CV recharge: (a) experimental (solid line) and simulated (dashed line) voltage and current; (b) Error trend and RMSE.

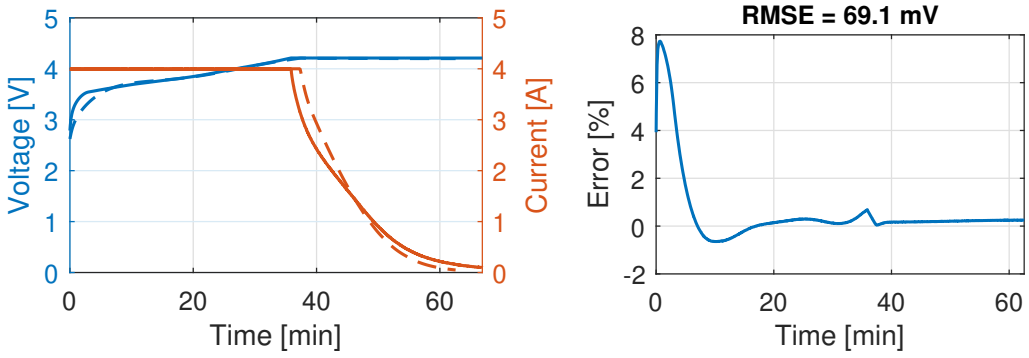

(a) (b)

Figure 2.19: *Thevenin* model CC/CV recharge: (a) experimental (solid line) and simulated (dashed line) voltage and current; (b) Error trend and RMSE.

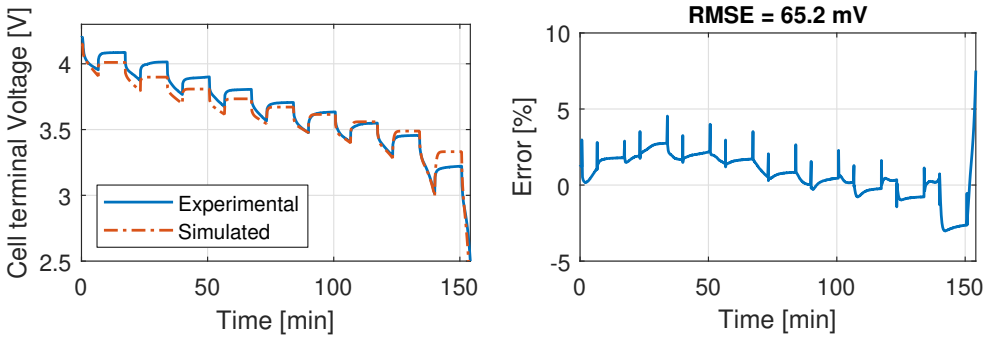

(a) (b)

Figure 2.20: *Shepherd* model Pulse Discharge Test: (a) experimental and simulated cell voltage; (b) Error trend and RMSE.

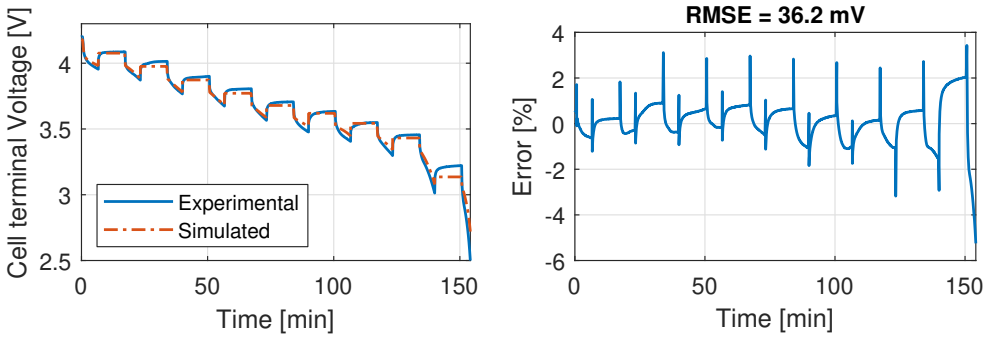

(a) (b)

Figure 2.21: *Rint* model Pulse Discharge Test: (a) experimental and simulated cell voltage; (b) Error trend and RMSE.

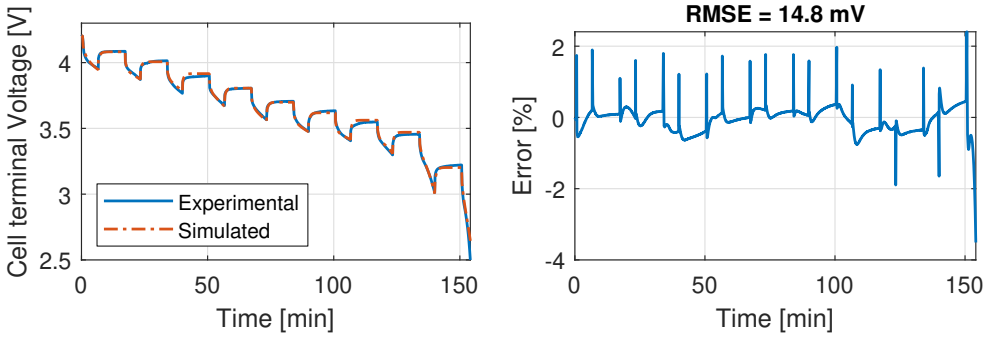

(a) (b)

Figure 2.22: *Thevenin* model Pulse Discharge Test: (a) experimental and simulated cell voltage; (b) Error trend and RMSE.

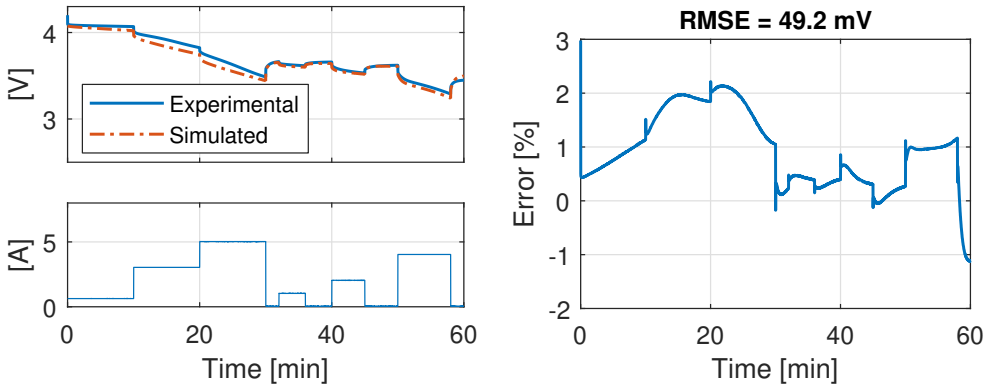

(a) (b)

Figure 2.23: *Shepherd* model Pulse Discharge Test: (a) experimental and simulated cell voltage; (b) Error trend and RMSE.

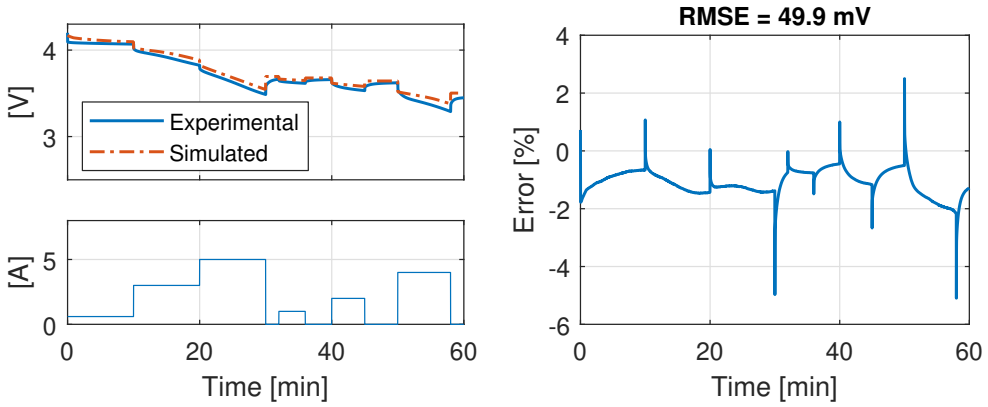

(a) (b)

Figure 2.24: *Rint* model Pulse Discharge Test: (a) experimental and simulated cell voltage; (b) Error trend and RMSE.

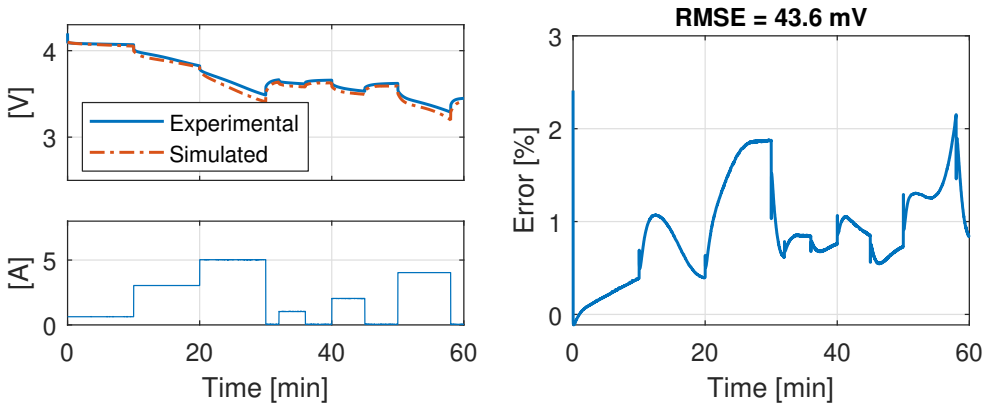

(a) (b)

Figure 2.25: *Thevenin* model Pulse Discharge Test: (a) experimental and simulated cell voltage; (b) Error trend and RMSE.

Table 2.9: RMSE [mV] comparison.

Model	**Data-sheet**				**Experimental Test**		
	0.2 C	1 C	1.67 C	6.67 C	CC/CV	PDT	DDT
Sheperd	24.9	**25.8**	47.8	298.4	137.6	65.2	49.2
Rint	**12.9**	43.5	46.54	**90.2**	141.6	36.2	49.9
Thevenin	18.1	33.0	**0.3**	208.9	**69.1**	**14.8**	**43.6**

Table 2.9 summarizes the RMSE, expressed in mV, for all the model and test combinations. The bold numbers highlight the minimum obtained RMSE. It can be noticed that, considering the data-sheet curves, the models can describe well the behavior of the battery for 0.2, 1 and 1.67 C. For 6.67 C (20 A), the best results were obtained with the *Rint* model. The *Thevenin* model gives the best results in all the experimental tests in terms of RMSE, but both the *Sheperd* and *Rint* models give adequate simulation results.

The *Sheperd* and *Rint* models can be therefore used in early design phase, for example for a rough comparison between different types of cells, considering nominal voltage, weight, cost, overall dimensions, and quickly evaluating the performance of the battery pack. Once the cell type for the application is defined, the PDT can be performed to obtain the parameters for the *Thevenin* model, which gives better results in terms of accuracy. Moreover, the accuracy of the *Thevenin* model can be further improved by considering the parameters variable with current, temperature, age etc. by performing appropriate tests.

2.6 Conclusion

In this chapter, three battery equivalent circuit models (*Shepherd*, *Rint*, *Thevenin*) selected from the literature were presented and the parameters estimation procedures for each model were described. The parameters estimation procedures were systematically applied to the LG 18650HG2 battery cell. It should be noted that, for the *Shepherd* and *Rint* models, the parametrization can be carried out using just the information on manufacturer's data-sheets. However, their accuracy is limited by the veracity and precision of the curves and parameters in the data-sheets. On the other hand, the *Thevenin* model requires a costly test-bench and time-consuming experimental test for its parametrization. The advantage, in this case, is the possibility to have a perfect knowledge of measurements and parameters estimation uncertainties. The comparison of the three models showed that *Thevenin* model, whose parameters were obtained from experimental tests, gave the best results as expected. However, the *Shepherd* and *Rint* models gave adequate simulation results, proving to be suitable for the early design stages of a battery-powered system. In this work, the temperature, battery current and aging effect on the parameters were not considered, as this information would require expensive equipment and extensive testing. The aim of the work was to identify three easy-to-implement battery models, suitable for the early stages simulation and design of a battery-powered system. In the optimization phase of such systems, more accurate models should be used instead.

References

[1] G. Saldaña, J. I. San Martín, I. Zamora, F. J. Asensio, and O. Oñederra, "Analysis of the current electric battery models for electric vehicle simulation," *Energies*, Jan. 2019.

[2] H. He, H. Qin, X. Sun, and Y. Shui, "Comparison study on the battery SoC estimation with EKF and UKF algorithms," *Energies*, Oct. 2013.

[3] D. Wang, Y. Bao, and J. Shi, "Online lithium-ion battery internal resistance measurement application in state-of-charge estimation using the extended kalman filter," *Energies*, Sep. 2017.

[4] H. Yang, Y. Qiu, and X. Guo, "Prediction of state-of-health for nickel-metal hydride batteries by a curve model based on charge-discharge tests," *Energies*, Nov. 2015.

[5] A. Gismero, E. Schaltz, and D.-I. Stroe, "Recursive state of charge and state of health estimation method for lithium-ion batteries based on coulomb counting and open circuit voltage," *Energies*, Jan. 2020.

[6] S. E. Samadani, R. A. Fraser, and M. Fowler, "A review study of methods for lithium-ion battery health monitoring and remaining life estimation in hybrid electric vehicles," in *SAE 2012 World Congress & Exhibition*, 2012.

[7] E. Raszmann, K. Baker, Y. Shi, and D. Christensen, "Modeling stationary lithium-ion batteries for optimization and predictive control," in *2017 IEEE Power and Energy Conference at Illinois (PECI)*, Feb. 2017.

[8] M. R. Jongerden and B. R. H. M. Haverkort, "Battery modeling," Jan. 9, 2008.

[9] A. Fotouhi, D. J. Auger, K. Propp, S. Longo, and M. Wild, "A review on electric vehicle battery modelling: From lithium-ion toward lithium–sulphur," *Renewable and Sustainable Energy Reviews*, Apr. 1, 2016.

[10] S. Barcellona and L. Piegari, "Lithium ion battery models and parameter identification techniques," *Energies*, Dec. 2017.

[11] M. Doyle, T. F. Fuller, and J. Newman, "Modeling of galvanostatic charge and discharge of the lithium/polymer/insertion cell," *J. Electrochem. Soc.*, Jun. 1, 1993.

[12] T. F. Fuller, M. Doyle, and J. Newman, "Simulation and optimization of the dual lithium ion insertion cell," *J. Electrochem. Soc.*, Jan. 1, 1994.

[13] J. Newman and W. Tiedemann, "Porous-electrode theory with battery applications," *AIChE Journal*, 1975.

[14] K. Smith and C.-Y. Wang, "Solid-state diffusion limitations on pulse operation of a lithium ion cell for hybrid electric vehicles," *Journal of Power Sources*, Oct. 20, 2006.

[15] R. Ahmed, M. E. Sayed, I. Arasaratnam, J. Tjong, and S. Habibi, "Reduced-order electrochemical model parameters identification and SOC estimation for healthy and aged li-ion batteries part I: Parameterization model development for healthy batteries," *IEEE Journal of Emerging and Selected Topics in Power Electronics*, Sep. 2014.

[16] ——, "Reduced-order electrochemical model parameters identification and state of charge estimation for healthy and aged li-ion batteries—part II: Aged battery model and state of charge estimation," *IEEE Journal of Emerging and Selected Topics in Power Electronics*, Sep. 2014.

[17] G. Fan, X. Li, and M. Canova, "A reduced-order electrochemical model of li-ion batteries for control and estimation applications," *IEEE Transactions on Vehicular Technology*, Jan. 2018.

[18] M. Doyle and J. Newman, "The use of mathematical modeling in the design of lithium/polymer battery systems," *Electrochimica Acta*, Oct. 1, 1995.

[19] R. Li, Z. Wang, J. Yu, Y. Lei, Y. Zhang, and J. He, "Dynamic parameter identification of mathematical model of lithium-ion battery based on least square method," in *2018 IEEE International Power Electronics and Application Conference and Exposition (PEAC)*, Nov. 2018.

[20] L. Haoran, L. Liangdong, Z. Xiaoyin, and S. Mingxuan, "Lithium battery SOC estimation based on extended kalman filtering algorithm," in *2018 IEEE 4th International Conference on Control Science and Systems Engineering (ICCSSE)*, Aug. 2018.

[21] S. Li and B. Ke, "Study of battery modeling using mathematical and circuit oriented approaches," in *2011 IEEE Power and Energy Society General Meeting*, Jul. 2011.

[22] H. Hinz, "Comparison of lithium-ion battery models for simulating storage systems in distributed power generation," *Inventions*, Sep. 2019.

[23] A. Nikolian, Y. Firouz, R. Gopalakrishnan, *et al.*, "Lithium ion batteries—development of advanced electrical equivalent circuit models for nickel manganese cobalt lithium-ion," *Energies*, May 2016.

[24] T. R. B. Grandjean, A. McGordon, and P. A. Jennings, "Structural identifiability of equivalent circuit models for li-ion batteries," *Energies*, Jan. 2017.

[25] H. He, R. Xiong, H. Guo, and S. Li, "Comparison study on the battery models used for the energy management of batteries in electric vehicles," *Energy Conversion and Management*, Dec. 1, 2012.

[26] J. V. Barreras, E. Schaltz, S. J. Andreasen, and T. Minko, "Datasheet-based modeling of li-ion batteries," in *2012 IEEE Vehicle Power and Propulsion Conference*, Oct. 2012.

[27] S. Potrykus, F. Kutt, J. Nieznański, and F. J. Fernández Morales, "Advanced lithium-ion battery model for power system performance analysis," *Energies*, Jan. 2020.

[28] C. M. Shepherd, "Design of primary and secondary cells: II . an equation describing battery discharge," *J. Electrochem. Soc.*, Jul. 1, 1965.

[29] B. Enache, E. Lefter, and C. Stoica, "Comparative study for generic battery models used for electric vehicles," in *2013 8th Internation Symposium on Advanced Topics in Electrical Engineering (ATEE)*, May 2013.

[30] O. Tremblay and L.-A. Dessaint, "Experimental validation of a battery dynamic model for EV applications," *World Electric Vehicle Journal*, Jun. 2009.

[31] D. Doerffel and S. A. Sharkh, "A critical review of using the peukert equation for determining the remaining capacity of lead-acid and lithium-ion batteries," *Journal of Power Sources*, Apr. 21, 2006.

[32] N. Omar, P. V. d. Bossche, T. Coosemans, and J. V. Mierlo, "Peukert revisited—critical appraisal and need for modification for lithium-ion batteries," *Energies*, Nov. 2013.

[33] G. L. Plett. "Modeling, simulation, and identification of battery dynamics." (), [Online]. Available: `http://mocha-java.uccs.edu/ECE5710/index.html`.

[34] *JCGM 100 – evaluation of measurement data – guide to the expression of uncertainty in measurement (ISO/IEC guide 98-3).*

Chapter 3

Supercapacitors

3.1 Introduction

Transitioning to sustainable, green transportation, along with the constant growth of renewable energy source generation plants, is essential to decrease air pollution and CO2 emissions. In conjunction with the development of the above applications, the research of increasingly efficient and high-performing energy storage systems is of utmost importance [1].

The needs related to the sustainable energy management focus the research activities on the storage systems technologies and their applications. Supercapacitors (SCs) represent an enabling technology introducing advantages both from technical and economic points of view. Thanks to their construction, SCs are particular caps able to store a greater amount of electric charge, if compared to the traditional ones [2]. SCs can be charged and discharged almost instantly, guaranteeing high specific power. Besides, the number of charge/discharge cycles are much higher than the traditional storage systems ones. SCs find their application in different fields. As a matter of fact, they can be employed in grid-connected applications, in which the combination of SCs and large electrochemical batteries enables the implementation of new grid-services such as the inertia simulation, the power oscillation damping and so on [3] or in particular cases as adaptive protection against communication outages in microgrids [4]. Even though the SCs applications in grid-connected field are manifold, their main use is in the automotive field. They can be used as energy storage devices alongside traditional Li-ion batteries [5]-[6] or Fuel Cells [7]. One of the main aspects that cannot be neglected in the study of the SCs applications is their modelization. Literature shows different approaches that can be summarized into three main areas: electrochemical, thermal and circuital modelization. Electrochemical models are mainly based on the impedance spectroscopy. They are mostly used to investigate the aging effect due to a cycling use of the SCs [8]. Despite being extremely accurate, an electrochemical approach implies the analysis of several internal parameters such as the equivalent distributed resistance, the time taken by a

reactant to diffuse from one side of the SC layer to the other and so on, resulting in very high computational effort. Thermal models, starting from the governing equations of the SCs working are used to detect the temperature distribution during the charging/discharging operations by taking into account several factors such as the current density, the collector and the separator materials [9]. Even though a thermal approach is very useful to estimate the main parameters of a SC, with such type of model it is possible to characterize the SC behavior only for specific boundary conditions. Besides, the heat conduction model has to be chosen on the base of the construction geometry. For example, the stacked-type capacitors and the rolled-type capacitors, which are the main typologies of commercial SCs, cannot be modelized with the same approach, making the analysis method not very versatile. The most used modelization approach in model-based design of engineering applications is the circuital one.

In its simplest form, the SC equivalent circuit model is composed of a resistor, representing the Equivalent Series Resistance (ESR) of the component, connected in series with a parallel RC branch, ,representing the capacitance effect of the SC and the self-discharge phenomenon, as proposed in [10]. This kind of equivalent circuit can describe the SC behavior in the range of seconds. The applicability of the model could be, for example, the simulation of the converter/control stage considering the PWM frequencies. If a larger time window is needed, further elements can be added to the equivalent circuit to model different dynamics. Focusing on an operating time ranging from minutes to hours, the so called three-branches model, first proposed in [11], is one of the most employed. Main drawbacks of the model presented in [11] are two: 1) the model does not consider the residual charge phenomenon, 2) the model is validated for a single SC. Considering that the nominal voltage of a single SC is in general around 2.7 V , and considering that almost every SCs application need greater voltage, it is essential to verify if the model can be easily up-scaled to simulate the behavior of a SCs bank composed of several component connected in series and parallel.

This chapter is organized as follows. Section 2.2 presents the three-branches model of the SC. Section 2.3 describes the parameter estimation procedure and the test-bench used for the characterization of the Vinatech 2.7 V 100 F SC. In Section 2.4 the parameter optimization procedure is explained. Section 2.5 describes the residual charge phenomenon and how it is implemented in the proposed three-branches model. In Section 2.6 the simulation results, obtained in MATLAB/Simulink environment, for the single SC and the SCs bank are validated with experimental tests to assess the model accuracy.

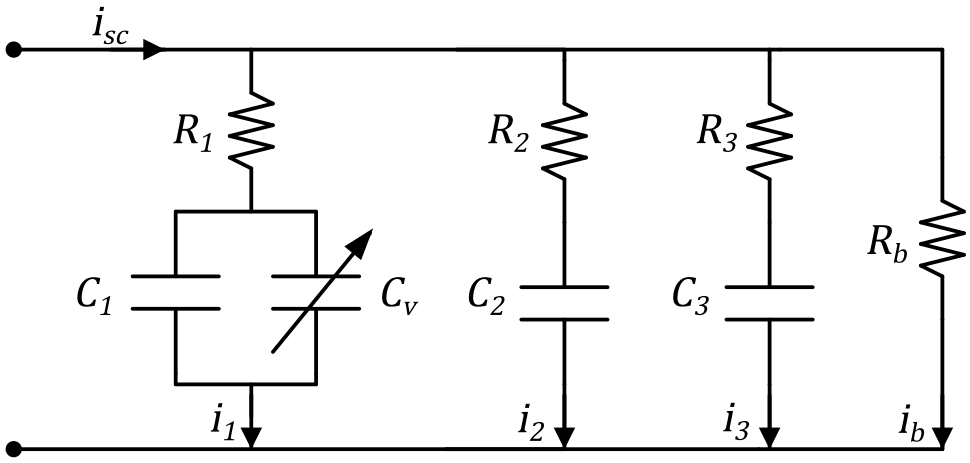

Figure 3.1: Three-branches equivalent circuit model.

3.2 Three-branches Model Description

The three-branches model was first proposed in [11]. The equivalent circuit schematic is depicted in Fig. 3.1.

The equivalent circuit features three RC series branches, each one with different time constant. The first branch, known also as immediate branch, describes the SC instantaneous behavior. It is composed of a fixed resistor R_1, a fixed capacitor C_1 and a voltage dependent capacitor C_v. The time constant is in the range of seconds. The voltage across the first branch fixed capacitor, v_{C_1} can be expressed as

$$v_{C_1} = v_{sc} - i_1 R_1 \tag{3.1}$$

where:

- v_{sc} is the voltage at the SC terminal,
- i_1 is the first branch current.

The current in the first branch, considering the voltage dependent capacitor, can be expressed as

$$i_1 = (C_1 + C_v v_{C_1}) \frac{dv_{C_1}}{dt} \tag{3.2}$$

The second branch, or delayed branch, consists of a fixed resistor R_2 and a fixed capacitor C_2 and has a time constant of a few minutes. The voltage across the second branch fixed capacitor, v_{C_2}, can be expressed as

$$v_{C_2} = v_{sc} - i_2 R_2 \tag{3.3}$$

where i_2 is the second branch current expressed as:

$$i_2 = C_2 \frac{dv_{C_2}}{dt} \tag{3.4}$$

The third branch, also called long-term branch is composed of a fixed resistor R_l and a fixed capacitor C_l and has time constant of hours. The voltage across the third branch fixed capacitor can be expressed as

$$v_{C_3} = v_{sc} - i_3 R_3 \tag{3.5}$$

where i_3 is the second branch current expressed as:

$$i_3 = C_3 \frac{dv_{C_3}}{dt} \tag{3.6}$$

In Fig. 3.1 equivalent circuit, a fourth branch is added to consider the possibility to add an external balancing resistor R_b. The total current flowing in the SC terminal can finally be expressed as:

$$i_{sc} = i_1 + i_2 + i_3 + i_b \tag{3.7}$$

3.3 Three-branches Model Parametrization

To parametrize and validate the SC model, an experimental set-up has been implemented composed of:

- Vinatech supercapacitors, whose characteristics are reported in Table 3.1;
- a Fluke PM2812 Programmable Power Supply, whose characteristics are reported in Table 3.2, used to charge the SC;
- an Agilent 6060B Single Input Electronic Load, whose characteristics are reported in Table 3.3, used on the discharge phase of the SC;
- a NI 9215 16-Bit Data Acquisition Board (placed in a NI cDAQ 9172 chassis), whose characteristics are reported in Table 3.4, used to acquire the SC voltage and current signal.

Fig. 3.2 shows a block diagram illustration of the implemented test-bench. The PM1812 and HP6060B are connected to a PC using GPIB, while the CompactRIO system with the NI9215 Analog Input is connected using USB. Both electronic load and programmable power supply are connected in remote sensing operation, so the voltage drop across the leads can be eliminated. The SC voltage is directly acquired using the differential input of the NI9215 module, with 10 kS/s sampling frequency. The obtained samples are then averaged over a 0.1 s time window. All the experiments were carried out after the calibration of the acquisition board.

To estimate the model parameters, the procedure outlined in [12] has been used. Briefly, the procedure consists of:

- a constant current charge phase, till the SC reaches its rated voltage,

- a rest phase, during which the SC is left in open circuit for half an hour,
- a post-processing phase, during which the SC acquired voltage response is employed for an event recognition analysis.

In order to repeat the test several time, the procedure has been automated by creating a virtual instrument in LabView 2016, performing the following tasks:

1. the SC is charged to the desired voltage, using the PM2812 programmable power supply in current mode with a fixed value I_{ch},
2. when the SC reaches the desired voltage, the power supply is disconnected and the SC is left in open circuit,
3. the voltage across the SC is acquired continuously for the desired time window,
4. the SC is discharged using the Agilent 6060B electronic load and can be left in short-circuit for the desired amount of time,
5. the acquired voltage is saved into a .xlsx file and exported to MATLAB for the parameter estimation procedure.

A MATLAB script was implemented to automatically find all the event and to estimate the model parameters as reported in the following paragraphs.

The parameter estimation procedure was then performed on several new SCs. Table 3.5 summarizes the estimated parameters for four different SCs, as well as the calculated average values.

3.3.1 Immediate Branch Parameters

Event n. 0

the test start ($t_0 = 0$) with a fully discharged SC ($V_0 \cong 0$). The current source is switched on going from 0 to $I_{ch} = 5$ A.

Event n. 1

the first voltage drop is mainly due to the resistor R_1. The immediate branch fixed resistor value can be estimated as:

$$R_1 = \frac{V_1 - V_0}{I_{ch}} \tag{3.8}$$

where V_1 is the voltage value after the initial voltage drop.

Event n. 2

find the point where $V_2 = V_1 + \Delta$ V, with $\Delta V = 50$ mV and measure the elapsed time t_2. The fixed capacitance C_1 can be estimated as:

$$C_1 = \frac{I_{ch}\Delta t}{\Delta V} \tag{3.9}$$

where $\Delta t = t_2 - t_1$.

Event n. 3

Find the point where $V_3 = V_{max}$ and measure t_3. The current source is switched off ($I_{ch} = 0$).

Event n. 4

Take the voltage V_4 at time $t_4 = t_3 + t_{sd}$ where t_{sd} is the shut-down time of the current source. The voltage dependent capacitance C_v can be estimated as:

$$C_v = \frac{2}{V_4} \cdot \left(\frac{I_{ch} \cdot (t_4 - t_1)}{V_4} - C_1 \right) \tag{3.10}$$

3.3.2 Delayed Branch Parameters

Event n.5

Find the point where $V_5 = V_4 - \Delta V$. Measure $\Delta t = t_5 - t_4$. The delayed branch fixed resistance can be estimated as:

$$R_2 = \frac{\left(V_4 - \frac{\Delta V}{2}\right) \cdot \Delta t}{\left[C_1 + C_v \left(V_4 - \frac{\Delta V}{2}\right)\right]} \tag{3.11}$$

Event n.6

Take the point at the time $t_6 = t_5 + 3R_2C_2$. Supposing a typical time constant of 100 seconds, measure V_6.

$$C_2 = \ I_{ch} \cdot \frac{t_4 - t_1}{V_6} - \left(C_1 + \frac{C_v}{2} \cdot V_6 \right) \tag{3.12}$$

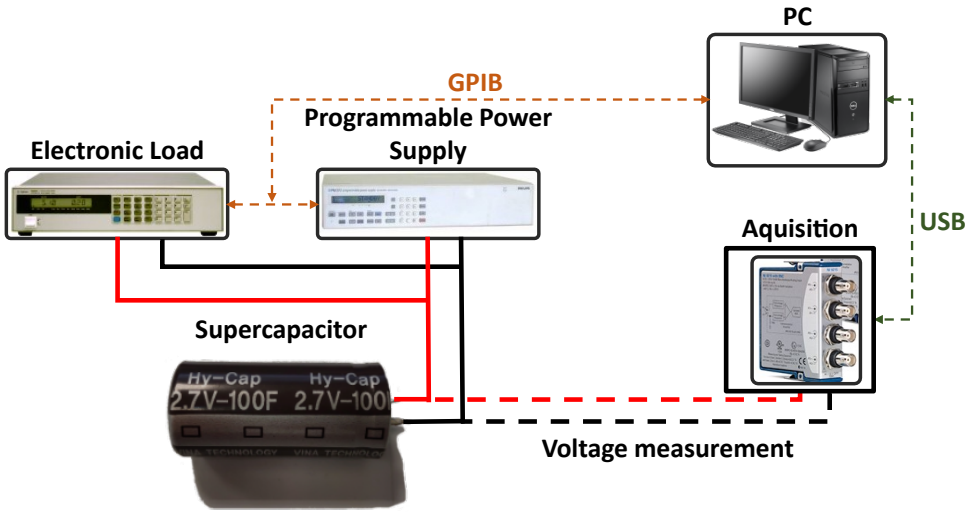

Figure 3.2: Block diagram of the experimental set-up.

Table 3.1: Supercapacitor Data-sheet Specifications

Specification	Unit	Value
Rated voltage	V	2.7
Rated capacitance	F	100
AC impedance (1 kHz)	mΩ	6
DC resistance	mΩ	10
Maximum current	mA	65
Leakage current	mA	0.2
Stored energy	J	364.5

3.3.3 Long-term Branch Parameters

Event n.7

Find the point where $V_7 = V_6 - \Delta V$ and measure $\Delta t = t_7 - t_6$. The fixed resistance of the long-term branch can be estimated as:

$$R_3 = \frac{\left(V_6 - \frac{\Delta V}{2}\right)\Delta t}{(C_1 + C_v)\left(V_6 - \frac{\Delta V}{2}\right)\Delta V} \tag{3.13}$$

Event n.8

Wait the end of the test $t_8 = 30$ min and measure V_8

$$C_3 = I_{ch} \cdot \frac{t_4 - t_1}{V_8} - \left(C_1 + \frac{C_v}{2} \cdot V_8\right) - C_2 \tag{3.14}$$

Table 3.2: PM2818 Programmable Power Supply Specifications

	Current	**Voltage**
Ratings	$0 \div 10$ A	$0 \div 60$ V
Accuracy	$\pm(0.1\% + 25)$ mA	$\pm(0.04\% + 20)$ mV

Table 3.3: HP 6060B Electronic Load Specifications

	Current	**Voltage**
Ratings	$0 \div 60$ A	$3 \div 60$ V
Accuracy	$\pm(0.1\% + 75)$ mA	$\pm(0.1\% + 50)$ mV

Table 3.4: NI 9215 Analog Input Module Specifications

Signal levels	± 10 V
Sample rate	100 kS/s
Accuracy	$\pm(0.02\% + 1.46)$ mV
Resolution	16-bit

Table 3.5: Supercapacitor Three-branches Model Parameters

Parameter	**Unit**	**SC$_1$**	**SC$_2$**	**SC$_3$**	**SC$_4$**	**Average**
R_1	mΩ	7.01	7.03	7.00	6.99	7.00
R_2	Ω	4.54	2.19	2.07	1.62	1.96
R_3	Ω	40.96	29.07	28.59	12.73	23.46
C_1	F	73.26	75.09	76.74	86.00	79.28
C_v	F/V	23.90	22.57	22.75	11.98	19.09
C_2	F	45.91	66.12	67.51	58.14	63.92
C_3	F	58.04	64.47	64.47	61.06	63.33

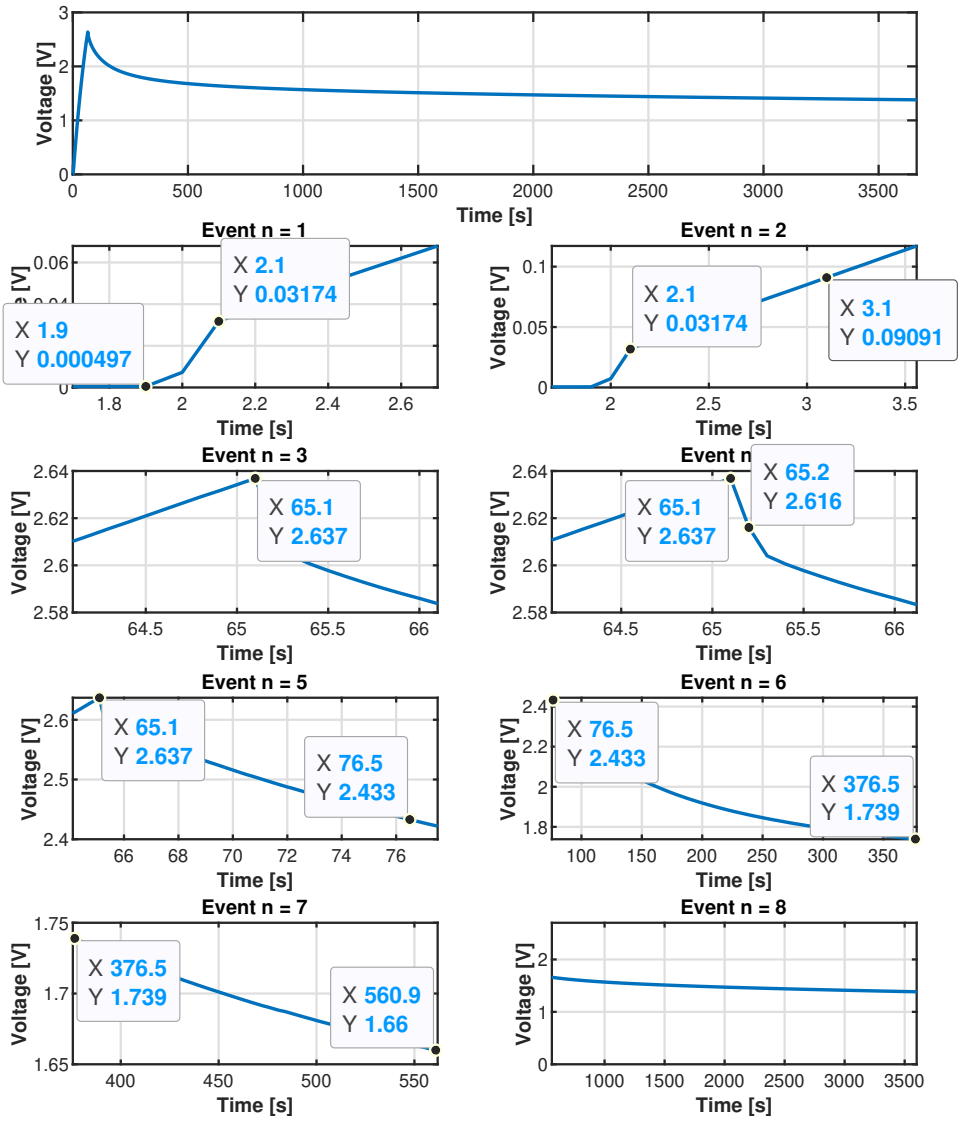

Figure 3.3: Event recognition for SC parameter estimation.

3.4 Parameter Optimization

To provide further improvement in model accuracy, a parameter optimization technique based on the non-linear least square algorithm has been applied. The parameter optimization technique was implemented in MATLAB/Simulink environment, using the Simscape Electrical Toolbox to realize the schematic reported in Fig. 3.4. The estimated parameters, in particular the average values, can be set as initial guesses for the optimization process, thereby improving the convergence chances of the method. All seven parameters ($R_1,\ R_2,\ R_3, C_1,\ C_v,\ C_2,\ C_3$) are simultaneously optimized, fitting an experimental dataset to the simulation output. The procedure is iterated until a local minimum on the residual is achieved. The optimized parameters are summarized in Table 3.6.

The results of the optimization procedure are highlighted in Fig. 3.5, where the simulated waveforms are compared to one experimental data-set. In order to have some index of the accuracy of the model, the following errors have been considered. The instantaneous error

$$Err(t_i) = A(t_i) - S(t_i), \tag{3.15}$$

where:

- $A(t_i)$ is the experimental value at the considered instant t_i,
- $S(t_i)$ is the simulated value at the considered instant t_i,

the average error

$$Err_{mean} = \frac{\sum_{i=1}^{N} [A(t_i) - S(t_i)]}{N}, \tag{3.16}$$

where N is the number of samples of the experimental and simulated data, and the maximum error

$$Err_{max} = \max(|Err(t_i)|). \tag{3.17}$$

Fig. 3.5 (a) shows the simulation results, using the estimated parameters, superimposed to the experimental SC voltage, and the instantaneous error trend. Before the optimization process, the maximum error was 186 mv and the mean error was 56.9 mV.

Fig. 3.5 (b) shows the simulation results with the optimized parameters, superimposed to the experimental SC voltage, and the instantaneous error trend. After the optimization process, the maximum error was 92.2 mv and the mean error was 1.7 mV, effectively increasing the accuracy of the model.

As further evidence of the model's accuracy, the simulated voltage response with the optimized parameters is compared with several different experimental data-sets in Fig. 3.6. It can be noticed that the model fits quite well the experimental results in all cases, with the worst case maximum and mean error respectively equal to 112 mV and 20 mV.

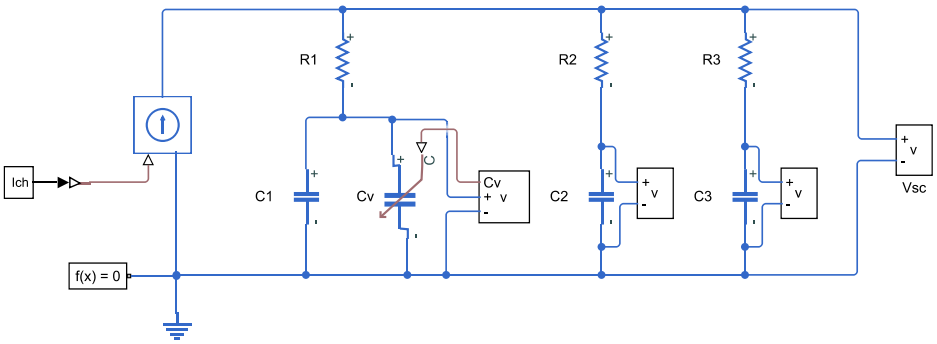

Figure 3.4: Simscape schematic of the three-branches model.

Table 3.6: Optimized parameters for the SC three-branches model

R_1 (mΩ)	R_2 (Ω)	R_3 (Ω)	C_1 (F)	C_v (F/V)	C_2 (F)	C_3 (F)
13.2	2.02	28.2	76.5	22.3	69.0	64.7

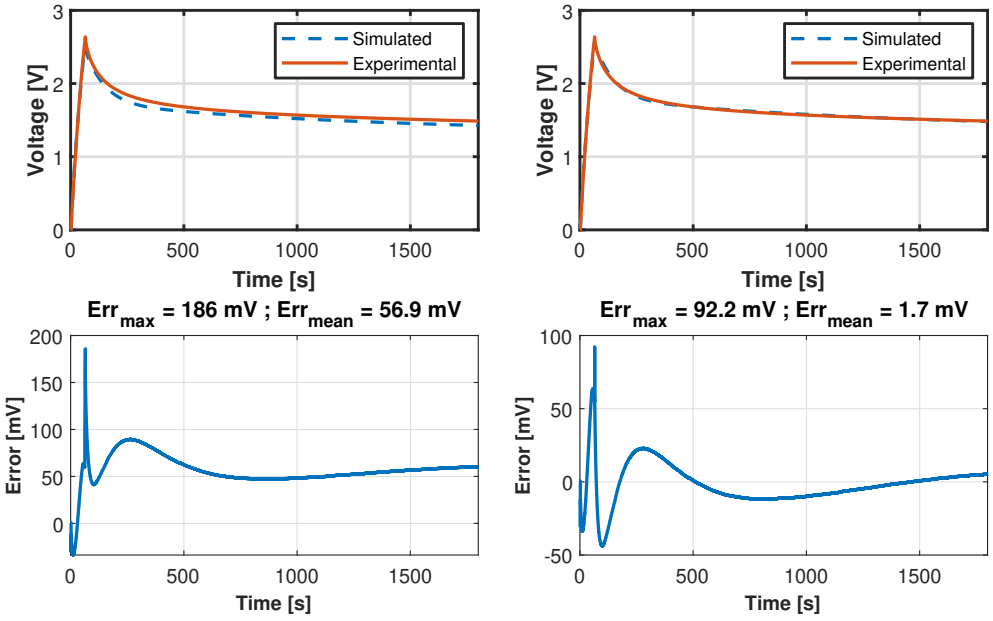

Figure 3.5: Simulated vs Experimental SC voltage response,instantaneous error trend, maximum and mean error values: (a) before the parameter optimization process; (b) after the parameter optimization process.

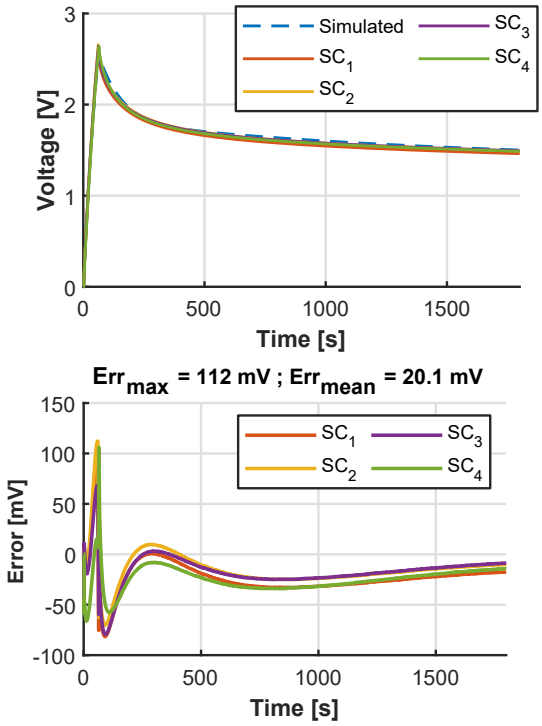

Figure 3.6: Simulated voltage response using the optimized parameters compared to the experimental voltage response of different SCs and instantaneous error trend with maximum and mean values.

3.5 Residual Charge Phenomenon

The model presented in [12] has a big drawback, that is not to take into account the residual charge phenomenon. The SCs can store energy for very long times (i.e., on the order of weeks). For this reason, they always have a residual charge, or in other word, an initial condition other than zero. This residual charge has a great influence on the SC dynamic behavior.

The residual charge phenomenon also affects the parameters estimation procedure. For proper estimation, it is essential that the model and the experimental setup start from the same initial conditions. Since knowing a SC initial conditions is practically impossible, it is necessary that the parameters estimation procedure is always applied to a brand new SC (or, at least, a SC left unloaded for several weeks).

Fig. 3.7 shows the residual charge effect on the SC voltage response. The SC was charged to the rated voltage and then totally discharged with the electronic load. Then it was left short-circuited for different amount of time and finally charged again to the rated voltage. The green curve depicts the voltage response for a brand new SC. The blue, orange, yellow and purple curves ware obtained leaving the SC short-circuited respectively for one minute, one day, one week and two weeks respectively. Two main effects can be observed: 1) the higher the residual charge, the shorter

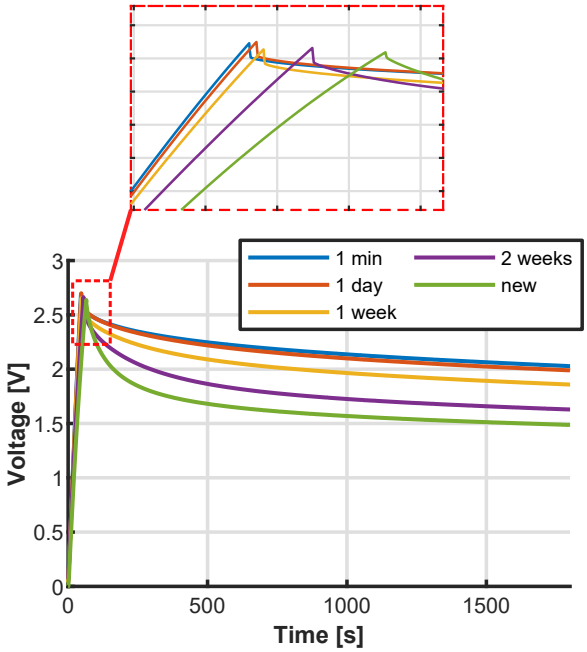

Figure 3.7: Residual charge effect on the SC voltage response for different SC resting period (different values of the residual charge).

the charging time, as can be seen from the enlargement shown in the figure; 2) the higher the residual charge, the less pronounced is the charge redistribution effect during the resting phase.

Since the only elements that can store the "history" of the SC are the capacitors present in the three branches, we can think of tying the residual charge to the initial conditions of these capacitors.

With the same approach used for the parameters estimation procedure, the initial conditions for the model can be estimated using the voltage response of a SC with a certain residual charge. Since it is not possible to measure the residual charge, it has been chosen to evaluate the initial conditions of the SC after a well defined rest period in short-circuit, preceded by several phases of charge and discharge at constant current up to the nominal voltage. The chosen rest periods are one minute (corresponding to high residual charge), one week (medium residual charge) and two weeks (low residual charge). The estimated initial voltage for the capacitors C_1, C_2 and C_3 are reported in Table 3.7. The branch with the strongest influence on the SC voltage dynamic is the second one (delayed branch) whose initial voltage goes from 2.7 V (practically the charge voltage of the SC) in the case of one minute rest to 0.9 V in the case of two weeks rest.

Fig. 3.8 shows the simulation results after the estimation of the initial conditions for three different resting periods, the instantaneous error trend and reports the maximum and mean errors value. The orange curves in Fig. 3.8 (a), (b), (c) report the simulation results, imposing all initial conditions to zero. The blue curves depict the SC experimental voltage response after (a) one minute rest, (b) 1 week rest

Table 3.7: Estimated initial conditions for different SC resting period

	V_{C_1} (V)	V_{C_2} (V)	V_{C_3} (V)
One minute	0.1385	2.6990	0.0348
One Week	0.1170	2.1830	0
Two weeks	0.9852	0.9313	0

and (c) two weeks rest. The yellow curves show the simulation results considering the estimated initial conditions. It can be noticed that the accuracy of the model is greatly improved in this way, obtaining errors comparable to the case of the simulation of brand new SC.

3.6 Model Validation of Supercapacitors Banks

A shortcoming of many of the literature articles, such as [13], [14], [12], [15] is to consider only the single SC model. In reality, SCs are assembled in banks, with multiple units connected in series and parallel to increase their voltage and current ratings.

The three-branches model can be easily updated to simulate the performances of a SCs bank considering the number of series N_s and parallel N_p connected components. Specifically, the bank voltage and current are obtained starting from the single SC voltage and current equations:

$$v_{bank} = N_s \cdot v_{sc} \tag{3.18}$$

$$i_{bank} = N_p \cdot (i_1 + i_2 + i_3 + i_b) \tag{3.19}$$

It is worth noting that in this way you are making the approximation of considering all SCs identical. In practice, SCs may have subtly different parameters. To investigate whether this approximation is acceptable, the model was validated for different SCs banks configurations: 1) single SCs bank module, 2) two parallel connected SCs banks modules, 3) two series connected SCs banks modules.

The SCs bank module characteristics [16] are reported in Table 3.8. The SCs bank modules, shown in Fig. 3.9, are composed of 24 units in series, each with a 510 Ω resistor in parallel for self-discharge and passive balancing.

To validate the model, two different experimental tests for each bank configuration were carried out.

The first test is similar to the one used for the parameter estimation, but this time the SCs bank is charged up to 48 V with 2 A constant current phase. Fig. 3.10 shows the SCs bank voltage superimposed to the simulation results, the SCs

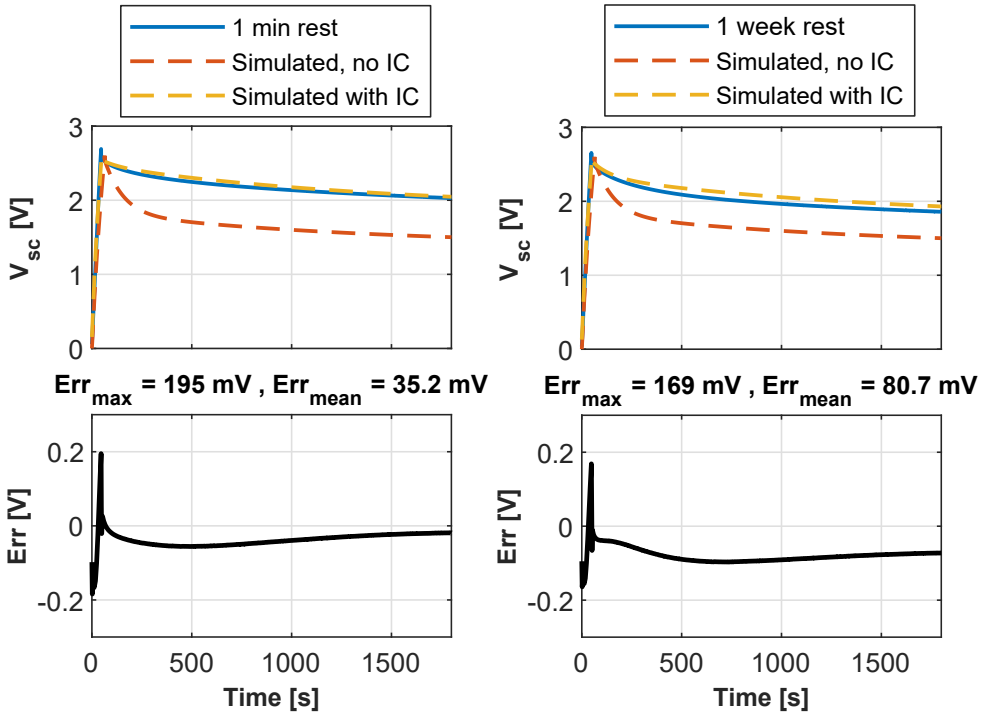

(a)

(b)

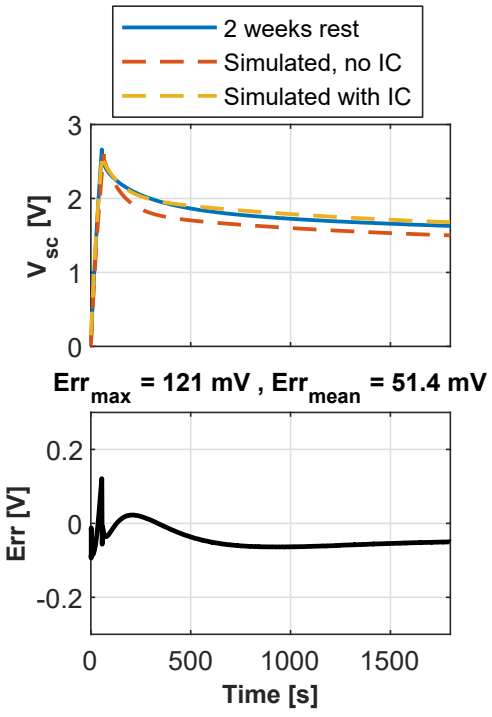

(c)

Figure 3.8: Initial conditions effects on the model accuracy for: (a) SC after one minute rest (high residual charge); (b) SC after one week rest (medium residual charge); (c) SC after two weeks rest (low residual charge.

bank current, and the instantaneous error trend for (a) the single SCs configuration (b) the parallel SCs banks configuration, (c) the series SCs banks configuration. Although the simplified approach of considering all components identical, the model estimates the SCs bank terminal voltage with sufficient accuracy, with a mean error ranging from 0.372 V for the single SCs bank to 1.28 V for the parallel SCs banks and a maximum error if 5.07 V (8.45 % of the maximum observed voltage) for the series SCs bank.

The second test is the Hybrid Pulse Power Characterization (HPPC) [17] test. It consists in alternately apply a charge and discharge current to the device under test, with a rest period in between.

Fig. 3.11 shows the voltage, current and error trends for the three different SCs bank configurations. Considering Fig. 3.11 (a), in the first phase, from $t = 0$ s to $t = 120$ s, the SCs bank is charged with a constant current up to 48 V. In the second phase, from $t = 120$ to $t = 160$ s, the SCs bank is charged with a constant voltage equal to 48 V until the current falls below 0.4 A. In the third phase, the HPPC test begins with the following settings:

- Charge current: 2 A
- Charge pulse duration: 10 s
- Rest period: 10 s
- Discharge current 3 A
- Discharge pulse duration: 10

The HPPC test is repeated until the SCs bank voltage reaches half of the initial value, i.e. 24 V. The tests on the other SCs banks configurations are performed adjusting the charge, rest and discharge duration, with the same charging and discharging current. For the series SCs banks, the maximum charging voltage was set to 60 V, that is the maximum allowable voltage for the employed test-bench. All three configurations were properly simulated, with a mean error of 0.864 V for the single SCs bank, 1.28 V for the parallel SCs banks and 0.795 V for the series SCs banks.

3.7 Conclusion

In this chapter, a comprehensive analysis of three-branches supercapacitor equivalent circuit model was presented. In particular, the three-branches model was used to model the Vinatech, 100 F, 2.7 V supercapacitor. The procedure and the instrumentation to perform the parameter estimation were thoroughly described, along with the LabVIEW and MATLAB/Simulink implementation. The model parameters were estimated using several SCs, and the averaged parameters were used as initial guesses for a parameter optimization problem.

Table 3.8: Supercapacitor Bank Specifications

Specification	Unit	Value
Series component N_s	-	24
Parallel components N_p	-	1
Nominal capacitance	F	4.17
Balancing resistor R_b	Ω	510
Nominal voltage	V	60
Nominal current	A	20
Maximum current	A	57

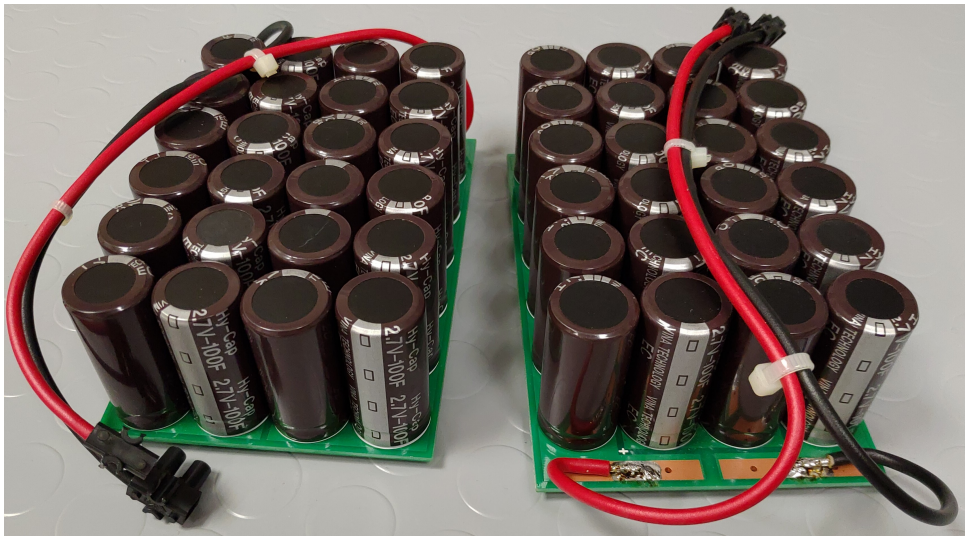

Figure 3.9: SCs banks used for experimental validation.

The residual charge phenomenon has been investigated, and a simple way to integrate it into the three-branches model, has been presented.

To verify the model applicability to a SCs bank, two SCs banks, each composed of 24 series connected component, were considered. The SCs banks were assembled in different configurations, and experimental results and simulation results have been compared and discussed. The chosen model has proven to be suitable for the simulation of SCs banks, predicting the bank terminal voltage with a mean error equal to 2-3% of the maximum observed voltage.

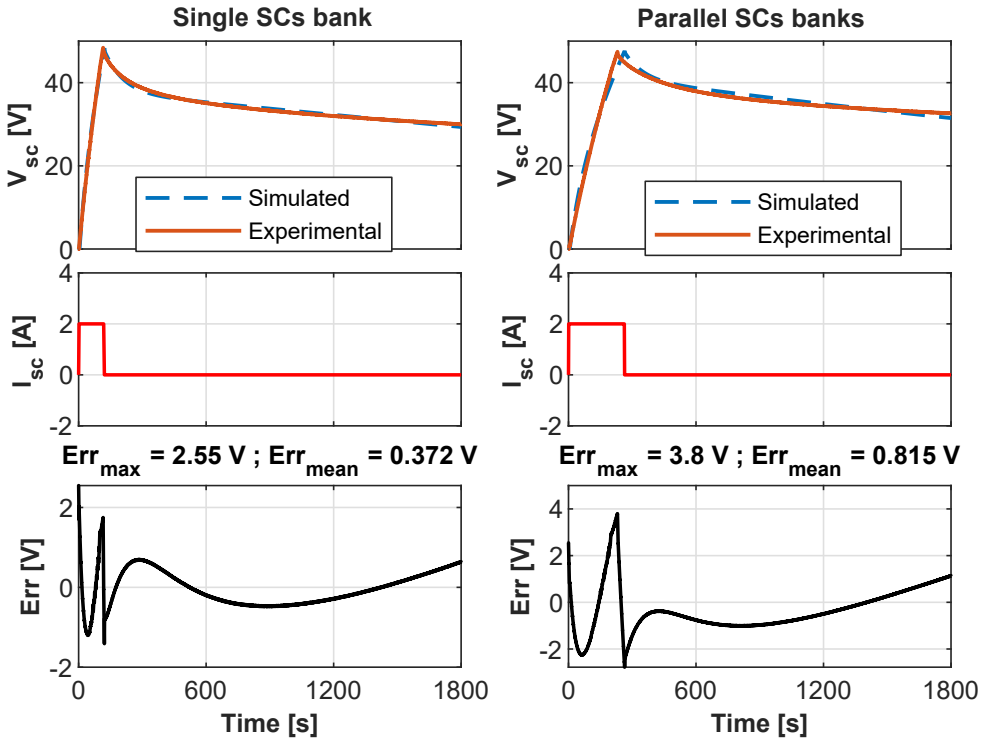

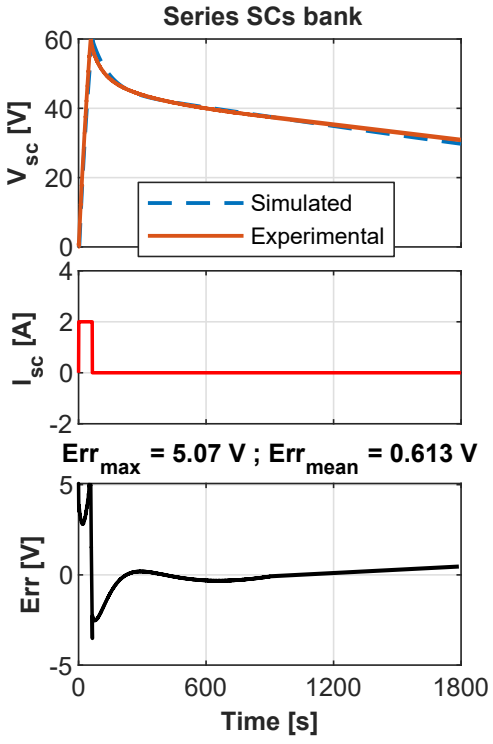

Figure 3.10: Constant current charge results with voltage, current and error trend for different banks configurations: (a) single SCs bank; (b) parallel SCs banks; (c) series SCS banks.

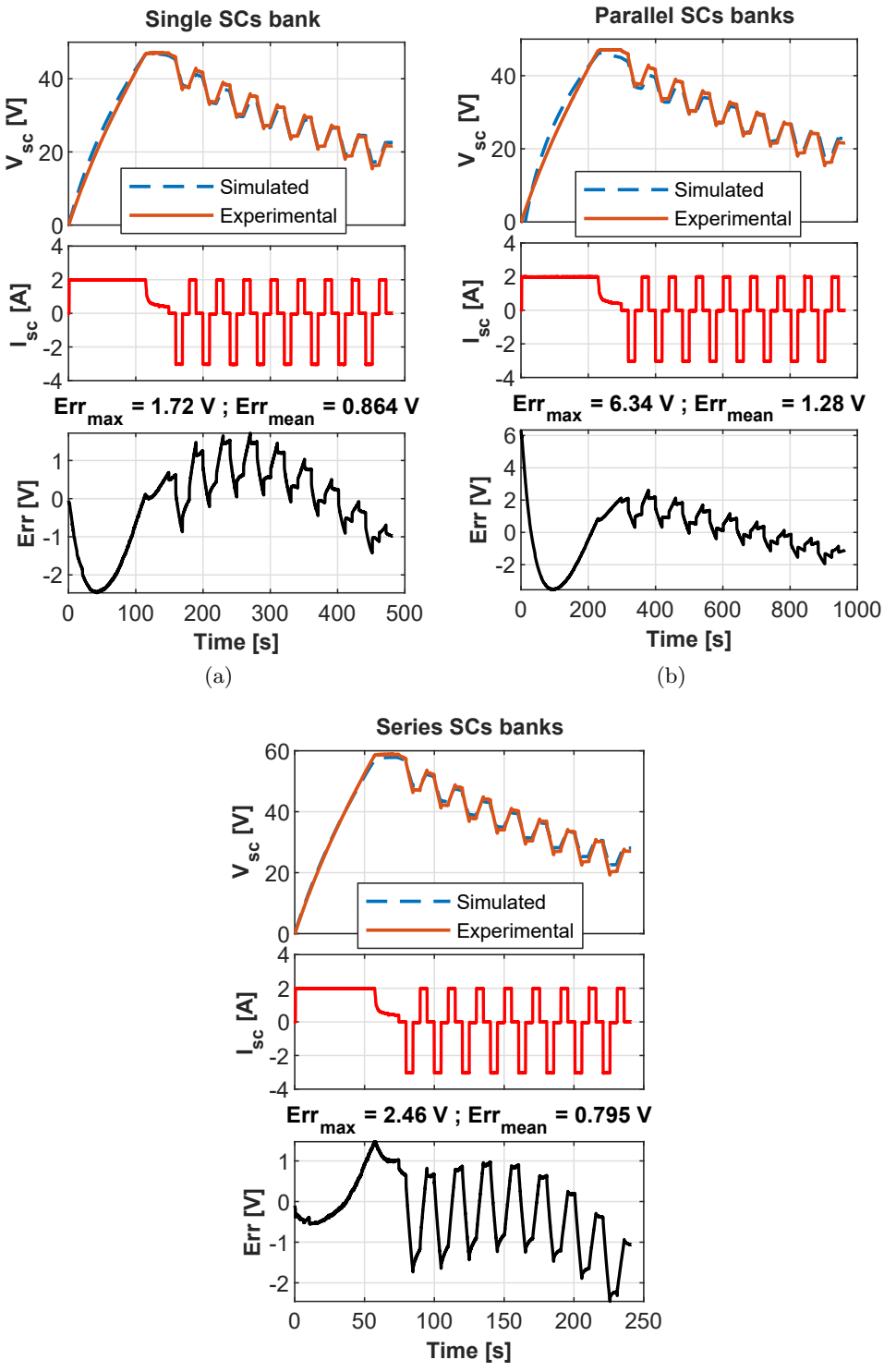

Figure 3.11: HPPC test results with voltage, current and error trend for different banks configurations: (a) single SCs bank; (b) parallel SCs banks; (c) series SCS banks.

References

[1] M. Aneke and M. Wang, "Energy storage technologies and real life applications - a state of the art review," *Applied Energy*, vol. 179, pp. 350–377, 2016. DOI: 10.1016/j.apenergy.2016.06.097.

[2] E. Chemali, M. Preindl, P. Malysz, and A. Emadi, "Electrochemical and electrostatic energy storage and management systems for electric drive vehicles: State-of-the-art review and future trends," *IEEE Journal of Emerging and Selected Topics in Power Electronics*, vol. 4, no. 3, pp. 1117–1134, 2016. DOI: 10.1109/JESTPE.2016.2566583.

[3] J. Rocabert, R. Capó-Misut, R. S. Muñoz-Aguilar, J. I. Candela, and P. Rodriguez, "Control of energy storage system integrating electrochemical batteries and supercapacitors for grid-connected applications," *IEEE Transactions on Industry Applications*, vol. 55, no. 2, pp. 1853–1862, 2019. DOI: 10.1109/TIA.2018.2873534.

[4] H. F. Habib, M. E. Hariri, A. Elsayed, and O. A. Mohammed, "Utilization of supercapacitors in protection schemes for resiliency against communication outages: A case study on size and cost optimization," *IEEE Transactions on Industry Applications*, vol. 54, no. 4, pp. 3153–3164, 2018. DOI: 10.1109/TIA.2018.2819620.

[5] A. Mamun, Z. Liu, D. M. Rizzo, and S. Onori, "An integrated design and control optimization framework for hybrid military vehicle using lithium-ion battery and supercapacitor as energy storage devices," *IEEE Transactions on Transportation Electrification*, vol. 5, no. 1, pp. 239–251, 2019. DOI: 10.1109/TTE.2018.2869038.

[6] M. Passalacqua, D. Lanzarotto, M. Repetto, L. Vaccaro, A. Bonfiglio, and M. Marchesoni, "Fuel economy and ems for a series hybrid vehicle based on supercapacitor storage," *IEEE Transactions on Power Electronics*, vol. 34, no. 10, pp. 9966–9977, 2019. DOI: 10.1109/TPEL.2019.2895209.

[7] J. Chen and Q. Song, "A decentralized dynamic load power allocation strategy for fuel cell/supercapacitor-based apu of large more electric vehicles," *IEEE Transactions on Industrial Electronics*, vol. 66, no. 2, pp. 865–875, 2019. DOI: 10.1109/TIE.2018.2833031.

[8] H. Ahmad, W. Y. Wan, and D. Isa, "Modeling the ageing effect of cycling using a supercapacitor-module under high temperature with electrochemical impedance spectroscopy test," *IEEE Transactions on Reliability*, vol. 68, no. 1, pp. 109–121, 2019. DOI: 10.1109/TR.2018.2869212.

[9] Y. Li, S. Wang, M. Zheng, and J. Liu, "Thermal behavior analysis of stacked-type supercapacitors with different cell structures," *CSEE Journal of Power and Energy Systems*, vol. 4, no. 1, pp. 112–120, 2018. DOI: 10.17775/CSEEJPES.2016.01410.

[10] P. Sharma and T. Bhatti, "A review on electrochemical double-layer capacitors," *Energy Conversion and Management*, vol. 51, no. 12, pp. 2901–2912, 2010, ISSN: 0196-8904. DOI: https://doi.org/10.1016/j.enconman.2010.06.031. [Online]. Available: https://www.sciencedirect.com/science/article/pii/S0196890410002438.

[11] L. Zubieta and R. Bonert, "Characterization of double-layer capacitors (dlcs) for power electronics applications," in *Conference Record of 1998 IEEE Industry Applications Conference. Thirty-Third IAS Annual Meeting*, vol. 2, 1998, pp. 1149–1154.

[12] ——, "Characterization of double-layer capacitors for power electronics applications," *IEEE Transactions on Industry Applications*, vol. 36, no. 1, pp. 199–205, 2000.

[13] D. Xu, L. Zhang, B. Wang, and G. Ma, "Modeling of supercapacitor behavior with an improved two-branch equivalent circuit," *IEEE Access*, vol. 7, pp. 26 379–26 390, 2019. DOI: 10.1109/ACCESS.2019.2901377.

[14] D. Torregrossa, M. Bahramipanah, E. Namor, R. Cherkaoui, and M. Paolone, "Improvement of dynamic modeling of supercapacitor by residual charge effect estimation," *IEEE Transactions on Industrial Electronics*, vol. 61, no. 3, pp. 1345–1354, 2014. DOI: 10.1109/TIE.2013.2259780.

[15] C. Quintáns, R. Iglesias, A. Lago, J. M. Acevedo, and C. Martinez-Penalver, "Methodology to obtain the voltage-dependent parameters of a fourth-order supercapacitor model with the transient response to current pulses," *IEEE Transactions on Power Electronics*, vol. 32, no. 5, pp. 3868–3878, 2017.

[16] H2planet. (), [Online]. Available: https://www.h2planet.eu/it/detail/HyCaps.

[17] J. P. Christopherson, *Battery test manual for electric vehicles*, Idaho National Laboratory.

Chapter 4

Multilevel Converters for Grid-Connected Energy Storage Systems

4.1 Introduction

In recent years Multilevel Converter (MC) have attracted a lot of attention among the researchers for many advantages that this kind of power converters presents for industrial applications where high voltage and high power are required [1]–[3]. MCs can be used also for electrical generation in PV, wind and harvesting applications. MCs are able to accomplish high quality output voltage, with low distortion, and reduce voltage and switching stress using lower switching frequency in comparison to classical two level converters [4]. When using low switching frequency, the switching angles are obtained by solving a set of non-linear transcendental equations. Several algorithms have been proposed to solve this set of equations using iterative approaches [5], optimization methods [6] and genetic algorithms [7]. These algorithms can be difficult to implement in real-time applications, where the switching angles need to be consistently calculated based on the operating conditions of the system.

In this chapter a different solution for a Single-Phase 9 Level Grid-Connected Inverter is proposed: the switching angles are computed offline just once and, instead of using the modulation index to regulate the output voltage of the inverter, a boost converter is used.

4.2 System Design

The proposed system, shown in Fig. 4.1 is composed by a first DC/DC conversion stage, with four bi-directional boost converters, and a second DC/AC conversion stage with four H-Bridge. In classical grid-connected inverter the modulator controls the output voltage of the inverter v_o varying both amplitude and phase. In this case,

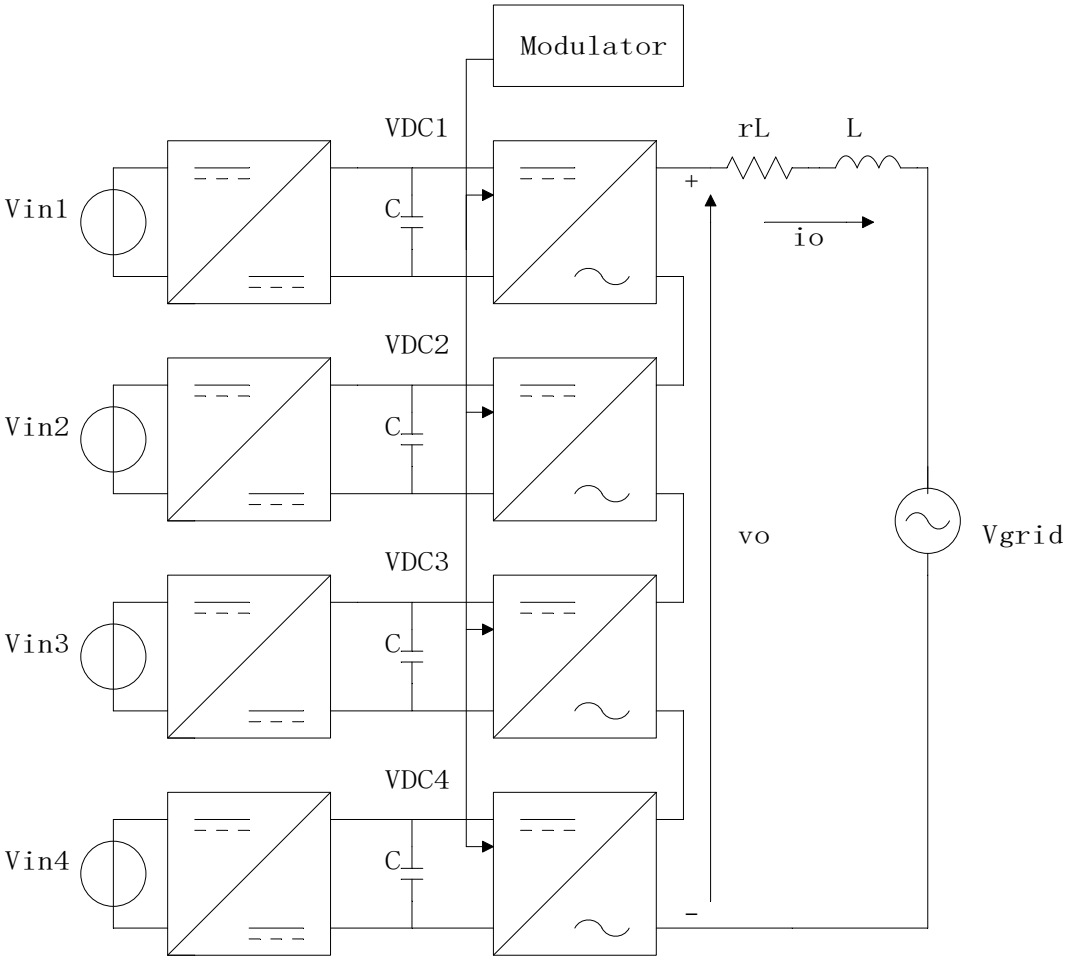

Figure 4.1: Schematic of the proposed system.

the modulator will vary only the phase of the output voltage, while the amplitude is regulated controlling the four input voltages of the H-Bridge V_{DC} acting on the boost stage. The inverter modulator's switching angles, in this way, are independent on modulation index and are computed offline with the Mixed Harmonic Elimination algorithm presented by the authors in [8].

4.2.1 Inverter Output Voltage

The output voltage of the 9-level inverter, controlled with the Mixed Harmonic Elimination technique [8], can be expressed using the Fourier Analysis as:

$$v_o(t) = \sum_{h=1,5,7...}^{\infty} [b_h sin(h\omega t)] \tag{4.1}$$

where b_h is the Fourier coefficient which represents the amplitude of the n-th voltage harmonic:

Table 4.1: Switching angles in (rad/s)

α_1	α_2	α_3	α_4
0.0992	0.3812	0.6660	1.1464

$$b_h = \frac{4}{\pi h} \sum_{n=1,2,3,4} [V_{DC} cos(h\alpha_i)] \tag{4.2}$$

where V_n are the DC input Voltages of the H-bridge. The switching angles α_i are computed from a mathematical system that:

- sets to zero the third and all odd multiple of the third harmonic
- imposes the mitigation of low order harmonic in order to minimize THD.

A procedure to solve mathematical system is given in [8]. The computed switching angles in radians are shown in Table 4.1

Assuming that all input voltages V_{DC} are equal, the fundamental component of eq. (4.1) can be written as:

$$v_{o,1}(t) = \frac{4}{\pi} [cos(\alpha_1) + cos(\alpha_2) + cos(\alpha_3) + cos(\alpha_4)] \times \\ \times V_{DC} sin(\omega t) = K V_{DC} sin(\omega t) \tag{4.3}$$

where:

$$K = \frac{4}{\pi} [cos(\alpha_1) + cos(\alpha_2) + cos(\alpha_3) + cos(\alpha_4)] \tag{4.4}$$

In order to have a fundamental component with a specific reference amplitude $V_{1,ref}$, each DC voltage must have an amplitude that can be calculated as:

$$V_{1,ref} = K V_{DC} \Rightarrow V_{DC} = \frac{V_{1,ref}}{K} \tag{4.5}$$

The output voltage in time domain can be finally obtained with eq. (4.6)

$$v_o(t) = \frac{V_{1,ref}}{K} \sum_{h=1,5,7...}^{\infty} \left\{ \frac{1}{h} sin(h\omega t) \sum_{n=1,2,3,4} cos(h\alpha_i) \right\} \tag{4.6}$$

The output voltage of one phase of the 9-level inverter, using a low switching frequency technique, is shown in Fig. 4.2. It can be noticed also that the current delivered from each level will be different. Smaller is the switching angle of the level, greater will be the current delivered. This characteristic can be used to achieve the battery balancing.

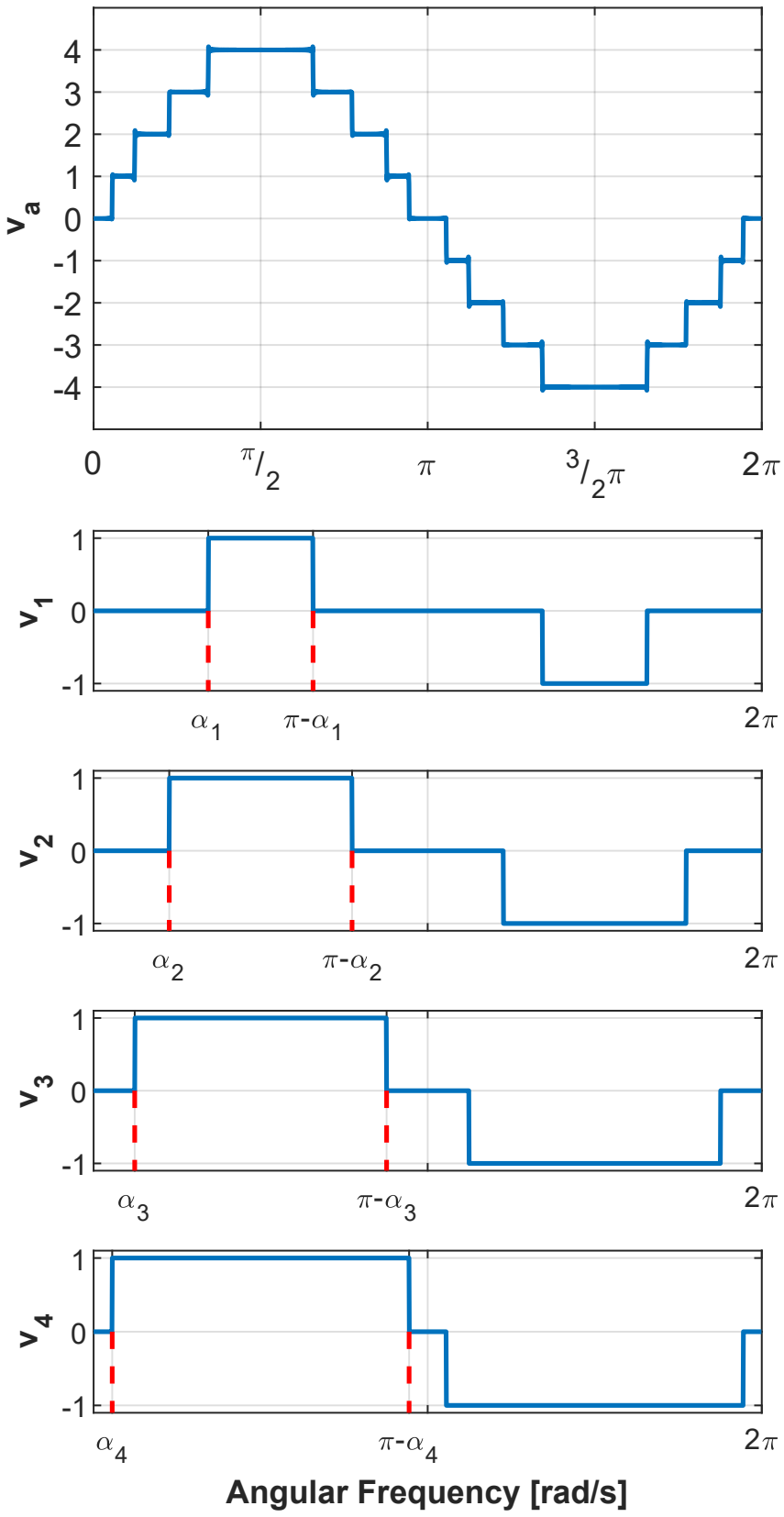

Figure 4.2: Output voltage waveform

Table 4.2: IEEE limits

(a) Maximum odd harmonic current distortion in percent of rated current I_{rated}

Individual odd harmonic order h	$h < 11$	$11 \leq h < 17$	$17 \leq h < 23$
Percent (%)	4.0	2.0	1.5
Individual odd harmonic order h	$23 \leq h < 35$	$35 \leq h < 50$	$TRD\%$
Percent (%)	0.6	0.3	5.0

(b) Maximum even harmonic current distortion in percent of rated current I_{rated}

Individual even harmonic order h	$h = 2$	$h = 4$	$h = 6$	$8 \leq h < 50$
Percent (%)	1.0	2.0	2.0	3.0

4.2.2 Filter Sizing

The output current of a grid connected inverter must comply to several limits for harmonic distortion. Recently a revision of IEEE Std 1547-2003 [9], the new IEEE 1547-2018 [10], has been published. These standards focus on the specification and the testing of interconnection and interoperability between utility electric power system and distributed energy resources. For the filter sizing, the limitations of current distortion of the latest standard are considered. The standard gives the maximum current harmonic distortion in percent of rated current I_{rated} for odd and even harmonics and the maximum value of the total rated-current distortion (TRD). The TRD can be calculated using:

$$TRD\% = \frac{\sqrt{I_{rms}^2 - I_1^2}}{I_{rated}} \times 100\% \tag{4.7}$$

where:

- $I_1$is the measured fundamental current
- I_{rated} is the rated current of the system
- I_{rms} is the root-mean-square of the output current.

The limits are reported in the following Table 4.2 (a) and (b).

For the sizing of the filter, the nominal power of the system was chosen, equal to $P_{rated} = 1\,kW$. Hence for a single-phase system with unity power factor, the rated current can be calculated as:

$$I_{rated} = \frac{P_{rated}}{V_{grid}} \tag{4.8}$$

Where V_{grid} is the rms value of the grid voltage.

In order to chose the minimum value of inductance L that allows to respects all the harmonic limits, an automatic procedure was designed.

Table 4.3: System and filter parameters

P_{rated} (W)	I_{rated} (A)	V_{grid} (V)	I_{min} (A)	r (mΩ)	f (Hz)	L (mH)
1000	4.4	230	2.2	1	50	100

The procedure begins by choosing a series resistance for the filter r, and the minimum current I_{min} at which the system must work without violating the harmonics limit. An inductance value L is then assumed and, supposing that the current is in phase with the grid voltage to have only active power, the amplitude and phase for the first harmonic of the inverter output voltage can be calculated as follows:

$$V_{1,ref} = \sqrt{(V_{grid} + I_{min} \cdot r)^2 + (\omega_0 L \cdot I_{min})^2} \tag{4.9}$$

$$\varphi_{ref} = \arctan\left(\frac{\omega_0 L \cdot I_{min}}{V_{grid} + I_{min} \cdot r}\right) \tag{4.10}$$

In the second step the instantaneous voltage applied to the filter is calculated as:

$$v_L(t) = v_o(t) - v_{grid}(t) \tag{4.11}$$

The fast Fourier transformation of $v_L(t)$ it then computed. The harmonics component of the output current can be calculated considering the transfer function of the filter and the applied voltage:

$$Z(j\omega) = \frac{1}{r + j\omega L} \tag{4.12}$$

$$I(j\omega) = \frac{V_L(j\omega)}{r + j\omega L} \tag{4.13}$$

In the last step of the design procedure, each harmonic component is compared with the respective limits as well as TRD%. If all the harmonics and the TRD are within the set limits the procedure stops, otherwise a new inductance value is assumed and the previous calculations are repeated.

Table 4.3 shows the rated parameter of the system and the resulting filter parameters.

Fig. 4.3 shows the maximum level of each harmonic in the worst case. The IEEE limits are represented with the red line. It can be seen that all the harmonics are below the limits as requested, proving that the filter design procedure correctly works.

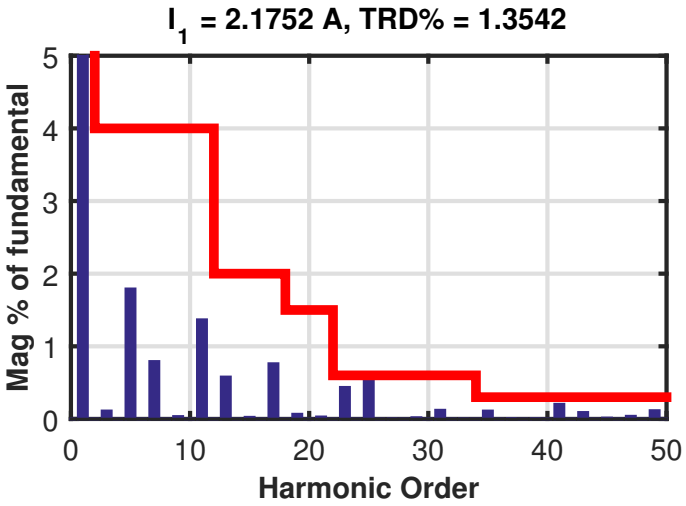

Figure 4.3: Harmonic content of the output current when the system works at 50% of the rated current

4.2.3 DC-Link Capacitor sizing

The DC-Link capacitor must supply the instantaneous current needed for the operation of the inverter, maintaining at its terminal an adequate voltage level.

Depending on the command angle α_i each boost converter supply a different mean value of current over one period of the fundamental AC voltage. In particular, the boost converter connected to the H-Bridge controlled with α_4 command angle will supply the least average current. The average current value I_{mean_4} can be calculated with the following expression

$$I_{mean_4} = \frac{2 \cdot I_{max} \cdot (\pi - 2\alpha_4)}{2\pi} \tag{4.14}$$

where I_{max} is the maximum instantaneous current supplied by the system.

When the bridge is in the ON state, the current must go from zero to the maximum value instantly. This current is supplied mostly by the capacitor, that need to be carefully sized. For a capacitor, the supplied charge ΔQ, the voltage drop across the capacitor ΔV and the capacitance C are related:

$$C \cong \gamma \frac{\Delta Q}{\Delta V} \tag{4.15}$$

In eq. (4.15), γ is a reduction factor that takes into account that not all the current is supplied by the capacitor.

The supplied charge must be calculated in the worst case, that is when the system works at the maximum operating current. Assuming that the capacitor must supply the difference between the maximum current and the mean value of current, the supplied charge can be calculated as:

Table 4.4: Parameters used for capacitor sizing

I_{max} (A)	ΔV (V)	ω (rad/s)	γ (-)	C (mF)
$\sqrt{2} \cdot I_{rated} = 6.15$	1	$2\pi f$	0.9	11

Table 4.5: Parameters used for inductor sizing

$V_{DC,max}$ (V)	Δi_L (A)	T_s (μs)	L_{boost} (mH)
95	1.5	10	0.19

$$\Delta Q = (I_{max} - I_{mean_4}) \cdot \frac{(\pi - 2\alpha_4)}{\omega} \tag{4.16}$$

Assuming a maximum acceptable ΔV, the capacitance value can be finally calculated replacing eq. (4.16) in eq. (4.15). Table 4.4 shows the parameters used for capacitor sizing and the obtained value of capacitance C.

4.2.4 Boost Inductor sizing

The inductance value for the boost stage must be sized considering the input voltage, the maximum output voltage and the switching frequency. It can be shown that the maximum ripple is when $D = 0.5$ and V_{DC} maximum.

$$D = 1 - \frac{0.5 \cdot V_{DC,max}}{V_{DC,max}} \tag{4.17}$$

The inductance value is chosen such that the desired peak-to-peak ripple Δi_L is obtained, according to the following equation:

$$L_{boost} = \frac{0.5 \cdot V_{DC,max}}{\Delta i_L} D T_s \tag{4.18}$$

Where T_s is the switching period of the boost converter. Table 4.5 shows the parameters used for inductor sizing and the obtained value of inductance L_{boost}.

4.3 System Control

4.3.1 Boost Stages control

The boost stages are designed in order to obtain the desired output voltage value $V_{DC,ref}$. A double loop controller, with Proportional-Integral regulator, is used to improve dynamic performance of the closed loop system. The inner loop regulates the inductor current while the outer loop regulates the output voltage. For the design of the PI controller the small-signal model of the boost converter is obtained.

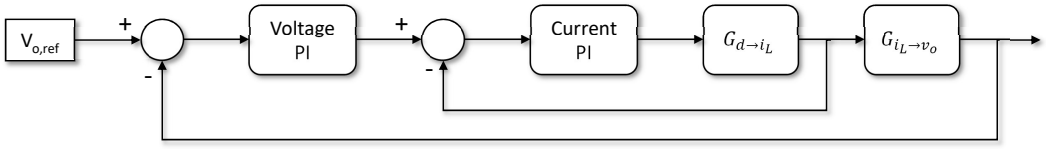

Figure 4.4: Block diagram of the double loop controller

The overall control structure of the boost stage is represented in Fig. 4.4. The converter was modelled considering as inputs of the state-space equations the input voltage of the boost converter, as state variables the inductor current and capacitor voltage and as control variable the duty cycle. The output of the model are the inductor current and the output voltage of the boost converter. The resulting small-signal transfer function of the duty to inductor current $G_{d\to i_L}$ and of the inductor current to output voltage $G_{i_L\to v_o}$ are given in (4.19), (4.20):

$$G_{d\to i_L} = \frac{4.737\cdot 10^4\cdot s + 5.678\cdot 10^{-5}}{s^2 + 6.061\cdot s + 1.361\cdot 10^4} \tag{4.19}$$

$$G_{i_L\to v_O} = \frac{G_{d\to v_o}}{G_{d\to i_L}} = \frac{-1000\cdot s + 2.297\cdot 10^6}{4.737\cdot 10^4\cdot s + 5.678\cdot 10^5} \tag{4.20}$$

The tuning of the controller is performed using the Matlab/Simulink *Control System Toolbox.* The generated controller transfer function are given in eqs. (4.21), (4.22:)

$$PI_{current} = 0.2\cdot\left(1 + 5794\frac{1}{s}\right) \tag{4.21}$$

$$PI_{voltage} = 2.73\cdot\left(1 + 46.39\frac{1}{s}\right) \tag{4.22}$$

4.3.2 Output Current Control

To regulate the output current supplied to the grid, the control acts on boost converters and inverter. In single phase converter, the Park transformation can be applied by creating a pair of orthogonal signals starting from the measured quantities. The output current and the grid voltage are sensed and sent to a *Second Order Generalized Integrator* algorithm to create two orthogonal signals i_α,i_β and e_α, e_β and to obtain the grid angular frequency ωt. Those signals are then sent to the Park transformation block to obtain the *d-q* stationary frame quantities. The DQ current controller process the error between the reference currents $i_{d,ref}$,$i_{q,ref}$ and the actual values of $i_d$and $i_q$and calculates the reference values for the $v_{d,ref}$ and $v_{q,ref}$ for the inverter output voltage in the stationary reference frame. $v_{d,ref}$ and $v_{q,ref}$ are then sent to the inverse Park transformation block to obtain the reference value in the rotating frame v_α and v_β.The information of amplitude and phase of the reference

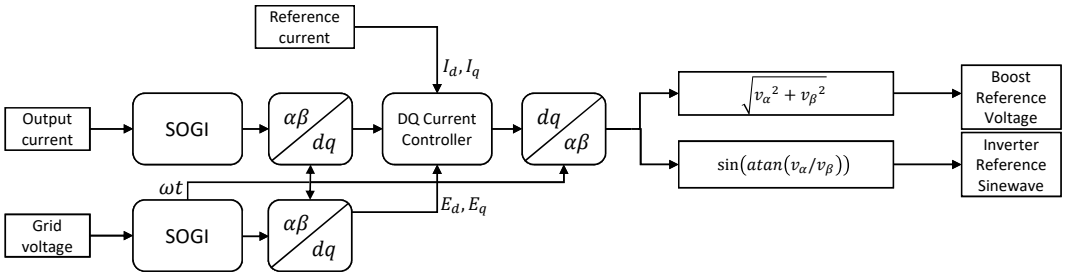

Figure 4.5: Output current control scheme

voltage are then splitted using eqs. (4.23), (4.24). The amplitude reference is used to control the output voltages of the boost stages, while the reference sinewave is sent to the inverter modulator.

$$V_{ref} = \sqrt{v_\alpha^2 + v_\beta^2} \tag{4.23}$$

$$sine_{ref} = \sin(\arctan(v_\alpha / v_\beta)) \tag{4.24}$$

The DQ current controller implements the decoupling between the two frames. In order to properly tune the dq-frame PI an equivalent model of the system was obtained, showed in Fig. 4.6.

In the d-frame model, G_{eq} is the equivalent closed loop transfer function of the Boost converters that are assumed to respond in the same way. The real closed loop transfer function is approximated by the equivalent first order transfer function G_{eq} by equating the error functions and calculating an equivalent time constant T_{eq} [11], [12]. G_f represents the output filter transfer function. The d-frame PI was tuned using the Matlab/Simulink *PID Tuner Toolbox* and the resulting transfer functions are given in eqs. (4.25), (4.26), (4.27).

$$G_{eq} = \frac{1}{11 \cdot 10^{-3} \cdot s + 1} \tag{4.25}$$

$$G_f = \frac{1}{100 \cdot 10^{-3} \cdot s + 1 \cdot 10^{-3}} \tag{4.26}$$

$$PI_d = 5.4 + 2.6\frac{1}{s} \tag{4.27}$$

In the q-frame model the Boost stages dynamics are not taken into account because the i_q component is controlled mainly by the inverter stages, by increasing or decreasing the phase shift between the grid voltage and the controlled output voltage. In this case, only the filter transfer function (4.26) is considered and the resulting tuned PI transfer function is given in eq. (4.28):

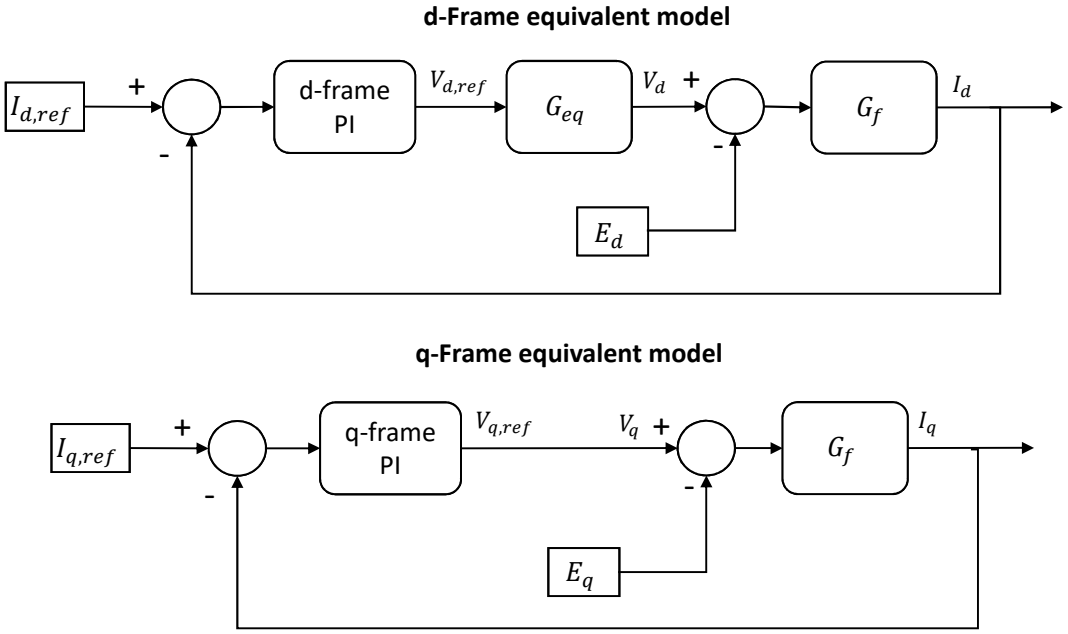

Figure 4.6: d-q frame equivalent model for PI tuning.

$$PI_q = 15 + 25\frac{1}{s} \tag{4.28}$$

4.3.3 Battery Balancing Algorithm

As said in sec.4.2.1, each level of the inverter will request different mean value of current from the connected battery. The charge removed from a battery can be expressed, considering the rms value of the output current, as:

$$Q_i = I_{rms} \cdot (\pi - 2 \cdot \alpha_i) \tag{4.29}$$

From eq. 4.29 it is clear that greater value of α_i means lower value of Q_i and vice versa. If a SoC imbalance occurs, the command angles can be swapped so that the level with the most charged battery is connected to the smaller switching angle. The SoC of each battery is estimated and then sorted from maximum to minimum:

$$SoC_{sorted} = \{SoC_1, ..., SoC_4\} \tag{4.30}$$

in which $SoC_i > SoC_{i-1}$ with $i = 1..4$. Then the command angles are associated from the greater to the smaller so that the most charged battery will have to deliver the higher mean current.

4.4 Simulation results

In order to verify the design procedure of the previous sections, a model of the complete system, depicted in Fig. , is implemented in Matlab/Simulink *SimPowerSystems™*. A total time of 1.2 s was simulated, imposing some step change of the d-frame reference current whereas the q-frame reference is always fixed to 0 to exchange only active power with the grid. The results of the simulation are showed in the following figures.

Fig. 4.8 shows the output current waveform and some magnification of the step change. The orange staircase waveform represents the d-frame reference current while the blue is the actual output current. At $t = 0.1\ s$ the synchronization switch is closed and the converter is connected to the grid. Some harmonic currents start to flow due to the residual harmonic content of the converter output voltage. At $t = 0.2 s$ a step change in $i_{d,ref}$ occurs, going from 0 to 4 Ampere. It can be seen that the settling time is less then 0.2 seconds. At $t = 0.6\ s$ another step change in $i_{d,ref}$ occurs, going from 4 to 6 Ampere. Again the settling time is less than 0.2 seconds and the performance of the system response to step changes have been validated.

Fig. 4.9 depict the steady state grid voltage (orange) and output current waveform (blue) and harmonic content . The figures on the left show the steady state conditions after the first step variation of the current and the respective harmonic content, while figures on the right show the conditions after the second variation. In both cases, voltage and current are in phase as expected, because the $i_{q,ref}$ is set to 0. It can be noted that current is almost sinusoidal and the harmonic content proves that the filter was correctly designed to comply with the IEEE limits plotted with the staircase red line.

Fig. 4.7 represents the active and reactive power trend. The orange and cyan line are respectively P_{ref} and Q_{ref} that are proportional to $i_{d,ref}$ and $i_{q,ref}$, the blue and red curve are the actual active and reactive power exchanged with the grid. At $t = 0.2\ s$ the active power steps from 0 to 650 W and the reactive power, after a short transient, is kept to zero. Similarly, at $t = 0.6\ s$ the active power steps from 650 W to the full rated power of 1000 W while keeping the reactive power to zero.

Fig. 4.10 (a) shows the state of charge of the batteries when the balancing algorithm is not active. In this case, the batteries start with the same SoC of 90 % and finish with different level of charge due to the imbalance of the current that each level deliver to the output or due the different intrinsic characteristics of the batteries. In Fig. 4.10(b) the batteries are initialized to have different SoC: Battery 1 start with 90 % SOC, Battery 2 with 86 % SOC, Battery 3 with 82% SOC and Battery 4 with 78 % SOC. It can be seen that after 40 minutes the SOC are completely balanced and are kept balanced for rest of the simulation.

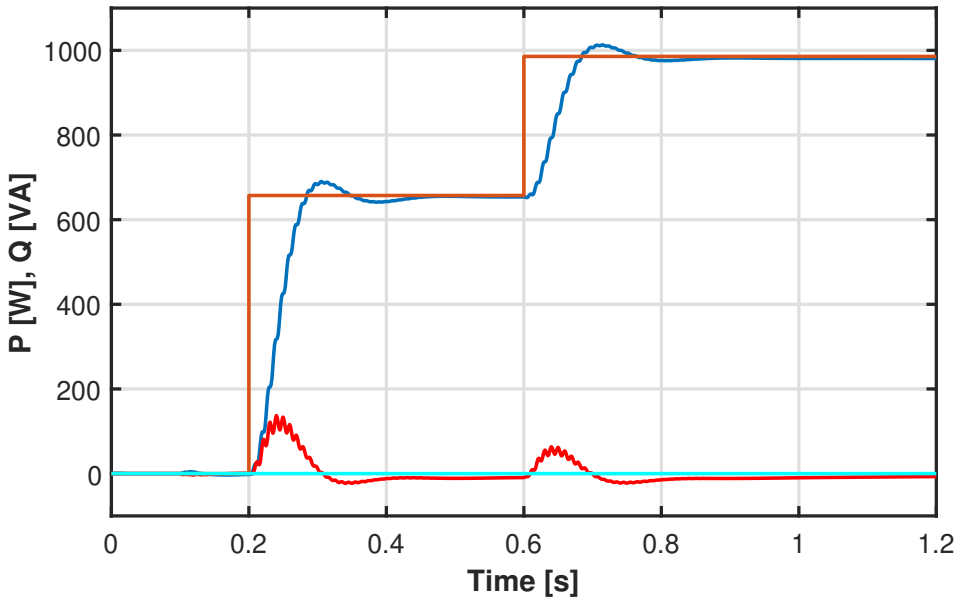

Figure 4.7: Active and reactive power trend

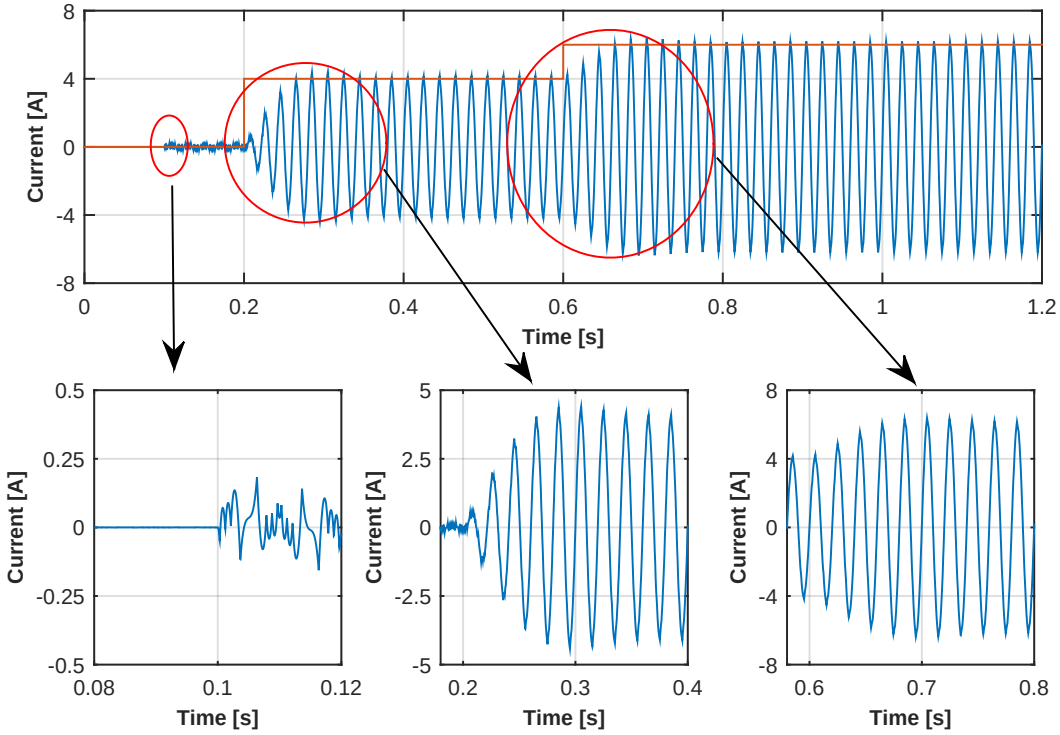

Figure 4.8: Output current waveform

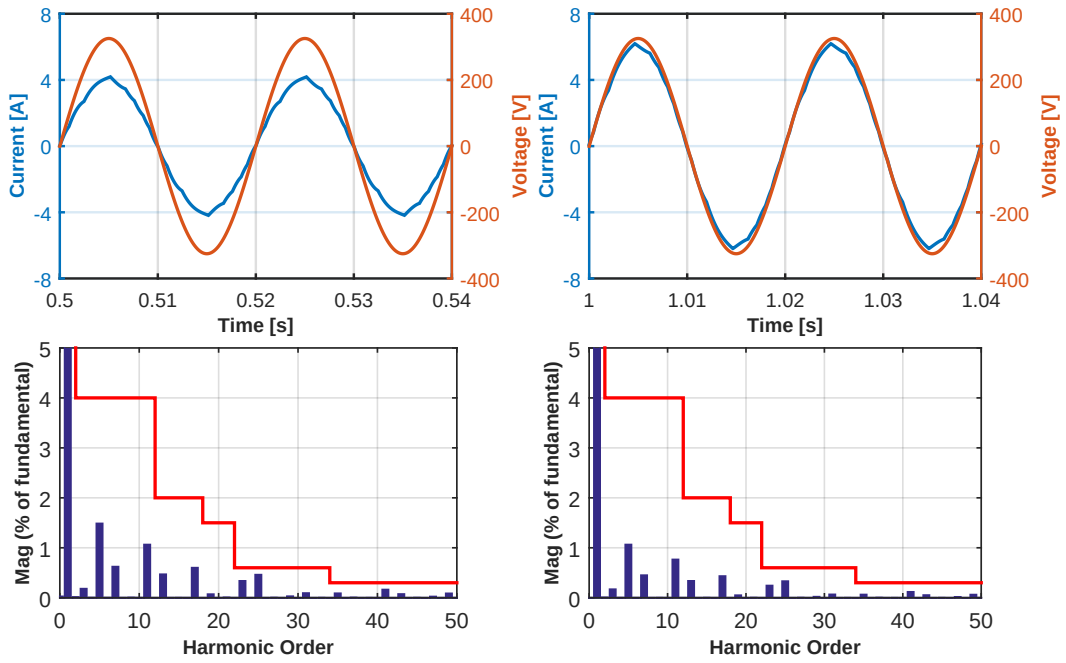

Figure 4.9: Steady state grid voltage and output current waveform and harmonic content

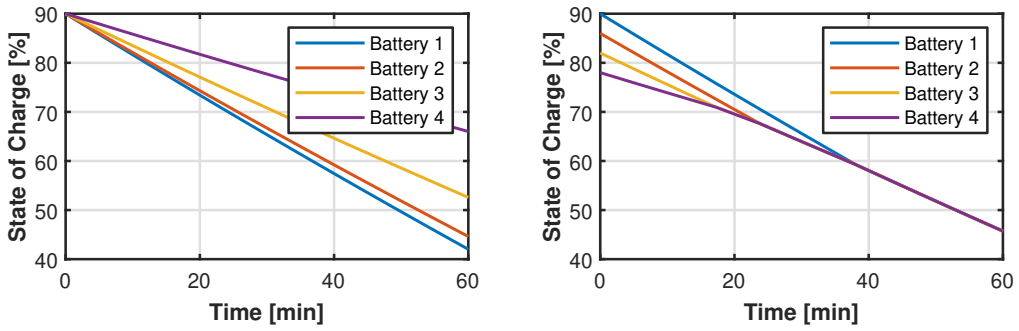

(a) (b)

Figure 4.10: State of Charge of batteries (a) without balancing algorithm (b) with balancing algorithm.

4.5 Conclusions

The possibility of using multilevel converters for grid-connected battery storage systems has been investigated, realizing simultaneously the DC/AC conversion and the balancing of battery voltages. Thanks to the multilevel converter structure, the output voltage total harmonic distortion has been considerably reduced compared to standard inverters. Moreover, the proposed low frequency modulation strategy allowed the reduction of switching losses and enabled the implementation of battery voltage balancing, without requiring additional components. Another interesting feature of the proposed structure is the possibility to use batteries with slightly different characteristics, also facilitating the use of second life batteries.

References

[1] H. Abu-Rub, J. Holtz, J. Rodriguez, and G. Baoming, "Medium-voltage multilevel converters—state of the art, challenges, and requirements in industrial applications," *IEEE Transactions on Industrial Electronics*, vol. 57, no. 8, pp. 2581–2596, 2010. DOI: 10.1109/TIE.2010.2043039.

[2] S. Ahmad, S. H. Johari, A. Ahmad, and M. F. M. A. Halim, "Grid connected multilevel inverters for pv application," in *2015 IEEE Conference on Energy Conversion (CENCON)*, 2015, pp. 181–186. DOI: 10.1109/CENCON.2015.7409536.

[3] A. K. Koshti and M. N. Rao, "A brief review on multilevel inverter topologies," in *2017 International Conference on Data Management, Analytics and Innovation (ICDMAI)*, 2017, pp. 187–193. DOI: 10.1109/ICDMAI.2017.8073508.

[4] Y. Zhang, G. P. Adam, T. C. Lim, S. J. Finney, and B. W. Williams, "Voltage source converter in high voltage applications: Multilevel versus two-level converters," in *9th IET International Conference on AC and DC Power Transmission (ACDC 2010)*, 2010, pp. 1–5. DOI: 10.1049/cp.2010.0995.

[5] A. Kumar, D. Chatterjee, and A. Dasgupta, "Harmonic mitigation of cascaded multilevel inverter with non equal dc sources using hybrid newton raphson method," in *2017 4th International Conference on Power, Control Embedded Systems (ICPCES)*, 2017, pp. 1–5. DOI: 10.1109/ICPCES.2017.8117653.

[6] S. D. Patil and S. G. Kadwane, "Application of optimization technique in she controlled multilevel inverter," in *2017 International Conference on Energy, Communication, Data Analytics and Soft Computing (ICECDS)*, 2017, pp. 26–30. DOI: 10.1109/ICECDS.2017.8390050.

[7] S. Joseph and C. A. Babu, "Performance analysis of multilevel inverter with battery balanced discharge function and harmonic optimization with genetic algorithm," in *2016 International Conference on Next Generation Intelligent Systems (ICNGIS)*, 2016, pp. 1–6. DOI: 10.1109/ICNGIS.2016.7854068.

[8] C. Buccella, M. G. Cimoroni, H. Latafat, M. Tinari, and C. Cecati, "Mixed harmonic elimination and reduction technique for single phase nine level converters," in *2017 IEEE 26th International Symposium on Industrial Electronics (ISIE)*, 2017, pp. 756–761. DOI: 10.1109/ISIE.2017.8001341.

[9] IEEE 1547-2003. "IEEE standard for interconnecting distributed resources with electric power systems." (2013), [Online]. Available: https://standards.ieee.org/standard/1547-2003.html.

[10] IEEE 1547-2018. "IEEE standard for interconnection and interoperability of distributed energy resources with associated electric power systems interfaces." (2018), [Online]. Available: https://standards.ieee.org/standard/1547-2018.html.

[11] C. Bajracharya, "Control of vsc-hvdc for wind power," 2008.

[12] C. Bajracharya, M. Molinas, J. Suul, and T. Undeland, "Understanding of tuning techniques of converter controllers for vsc-hvdc," Jun. 2008.

Chapter 5

Battery-Supercapacitor Active Hybrid Energy Storage Management System

5.1 Introduction

The worldwide energy policies aimed to reduce CO_2 emissions consider the transport sector strategic for achieving the international objectives of global warming mitigation. This is due to the great potential associated with mobility demand, as the actual state of the art of propulsion systems is fossil fuel-based. Specifically, the 2016 word CO_2 inventory assigned to the entire transport sector a share of 21.4%. As regards the automotive transport sector, multiple national action plans are already in place which aims to replace vehicles with internal combustion engines with electric vehicles, setting in 2030 as the ultimate limit for the marketing of private cars powered by fossil fuels. Considering the ambitious targets, the complete electrification of electrical vehicles represents a viable solution for improving efficiency and exploiting all the benefits of the expected transition toward renewable energy sources (RES).

One of the main problems to overcome in electric vehicles is the supply of electricity in the forms and ways required by the engines. The high power and torque densities of the electric motors make it possible to reduce the weight of the propulsion systems. However, the energy and power densities of the electrical storage systems fail to reach the levels of fossil fuels, inevitably leading to an increase in the share of weight associated with the propulsion energy. Moreover, electrical energy and power availability must be guaranteed in all possible operative conditions to satisfy the end user.

In this scenario, the usage of Hybrid Energy Storage Systems (HESS) can contribute to the overall improvement of the storage devices [1]. The sizing of HESSs has been developed to evaluate the improvement obtainable in terms of weight and

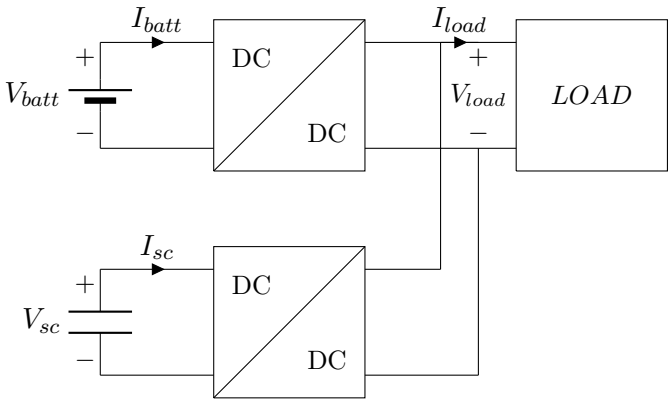

Figure 5.1: Block diagram of the HESMS.

volume reduction by using supercapacitors (SCs) for peak power smoothing and batteries as main energy buffers.

In this chapter, an active HESS is proposed. Considering a generic load power profile, the storage system sizing is first carried out. Then, the power electronics converters modeling, control and design are addressed. Finally, simulations of the complete system are performed in PLECS environment and validated through an experimental test-bench.

5.2 System Description

To effectively control the power flows between battery pack, SCs pack and load, a Hybrid Energy Storage Management System (HESMS) is needed. The chosen solution for the system proper operation is the employment of two parallel-connected DC-DC converters, as shown schematically in Fig. 5.1.

5.2.1 Power sharing

An important feature of the HESS is the capability to properly share the load request between the available storage sources [2]. Using a SCs bank in parallel with a battery pack allows for a significant reduction of the storage system weights and volumes, if compared to a traditional battery-only one. This is due to the high power density of SCs, which if used to provide high peak current, allowing the battery to be not oversized. Fig. 5.2 shows a generic power profile with high peak power demand. A rule-based algorithm [3] is chosen for the system power sharing. In the resulting hybrid storage system, the battery pack is designed to ensure, during the first phase, an increasing power up to 35 kW from $t = 0$ s to $t = 240$ s. During the central phase, the battery provides 15.5 kW constant power until the last phase at $t = 2040$ s in which the power is equal to 40 kW.

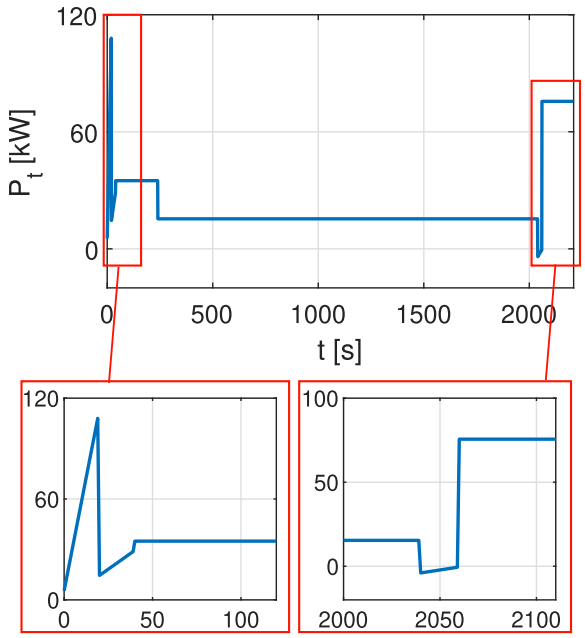

Figure 5.2: Considered Power profile.

The residual power amount required by the load is supplied by the SCs pack as

$$P_{sc} = P - P_b. \tag{5.1}$$

5.2.2 Hybrid Storage System Sizing

For the hybrid storage, the battery cell LG HG2 [4] and the TPLC-3R8 hybrid SC are chosen [5]. The datasheet parameters are reported in Table 5.1 and 5.2 respectively. To simulate the energy storage behavior, the battery *Thevenin* model and supercapacitor three-branches model, studied in Chapter 2 and 3, are considered.

The sizing procedure begins with the selection of the battery and SCs pack voltage rating. Considering commercially available voltage levels, the following nominal voltages are chosen:

$$V_{batt} = 480\,\text{V},\ V_{pack} = 400\,\text{V} \tag{5.2}$$

The number of series battery cells $N_{s,b}$ can then be obtained as the ratio of the battery pack and the battery cell nominal voltages.

$$N_{s,b} = \frac{V_{batt}}{V_{cell}} \tag{5.3}$$

The number of parallel cells $N_{p,b}$ is first obtained with an iterative method. The starting value of parallel cells is calculated considering the energy required for the considered cycle. The profile is then simulated, and it is checked whether the cells current is within the desired limits. If the cell current exceeds the limit, the number

Table 5.1: Battery datasheet specifications.

Specification	**Unit**	**Value**
Volume	ml	16.54
Weight	g	48
Nominal Voltage	V	3.7
Max Voltage	V	4.2
Min. Voltage	V	3
Standard Charge current	A	2
Fast Charge current	A	4
Nominal Discharge current (1C)	A	3
Max Discharge current (10C)	A	30
Capacity	Ah	3

Table 5.2: Supercapacitor datasheet specifications.

Specification	**Unit**	**Value**
Volume	ml	10.18
Weight	g	18
Nominal Voltage	V	3.8
Charge current	A	14.1
Discharge current	A	14.1
Capacity	F	450

of parallel cells is increased, and the procedure is reiterated.
The number of series cells SCs pack can be obtained as the ratio of the pack and the cell nominal voltages.

$$N_{s,_{sc}} = \frac{V_{pack}}{V_{sc}} \tag{5.4}$$

To ensure a proper, reliable, and efficient operation, the SCs pack is designed to be discharged between the maximum and the half of the maximum voltage [6]. Thus, the energy stored in a single SC cell is:

$$E_{sc} = \frac{1}{2} \cdot C \cdot \left[V_{max}^2 - \left(\frac{V_{max}}{2} \right)^2 \right]. \tag{5.5}$$

The SCs storage is mainly used during high power surge phases. In order to optimize the overall performances and reduce the weight of the system, the number of parallel cells for both battery $N_{p,b}$ and SCs $N_{p,sc}$ are calculated through an iterative method. The iterative method starts by considering the output of the battery-only storage system sizing algorithm. Initially, the SCs pack is composed of one parallel branch ($N_{p,sc} = 1$) and it is iteratively increased until an optimal hybrid battery-SCs configuration is found. The number of series and parallel battery cells and SCs, calculated with the above algorithm, are reported in Table 5.3 and compared to the case of the battery-only storage.

Table 5.3: Storage system sizing results.

Type	**Storage**	N_s	N_p	N_{tot}
Normal	Battery	131	40	5240
Hybrid	Battery	131	21	2751
	Supercapacitors	106	57	6042

Table 5.4: Weight and volume comparison.

Type	**Storage**	**Weight** [kg]	**Vol.** [l]	**Tot. weight** [kg]	**Tot. vol.** [l]	**Weight red.** [%]	**Vol. red.** [%]
Normal	Battery	252	87	252	87	-	-
Hybrid	Battery	132	45.5	194.25	107	22.92	18.69
	SCs	108.75	61.5				

5.3 Power Electronics Modeling and Control

The system requires bidirectional energy transfer and a non-inverting buck-boost operation. Considering these specifications the Single Inductor Four Switches (SIFoS) DC/DC power converter topology is chosen [7]. The circuit schematic of the SIFoS converter is shown in Fig. 5.3. The relationship relating the input and the output voltage is

$$V_{out} = \frac{D}{1-D} \cdot V_{in} \tag{5.6}$$

in which D is the duty cycle. The converter is controlled by closing switches Q_1 and Q_4 simultaneously while Q_2 and Q_3 are always complementary.

5.3.1 Average and small-signal model

To properly design the system controller, the dynamical model of the DC-DC converter is needed. The State Space Averaging (SSA) technique is used to obtain a

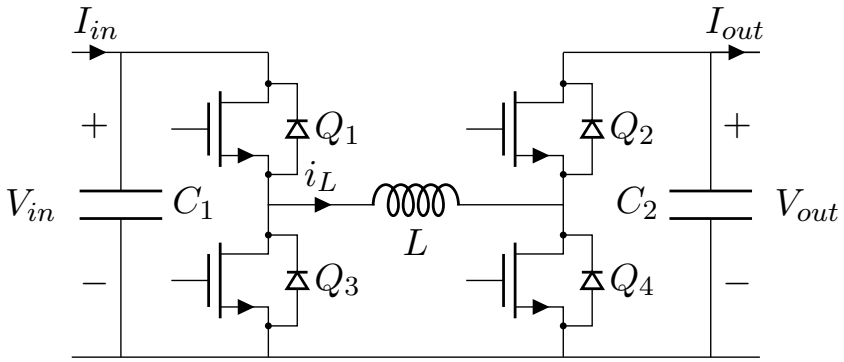

Figure 5.3: SIFoS converter schematic.

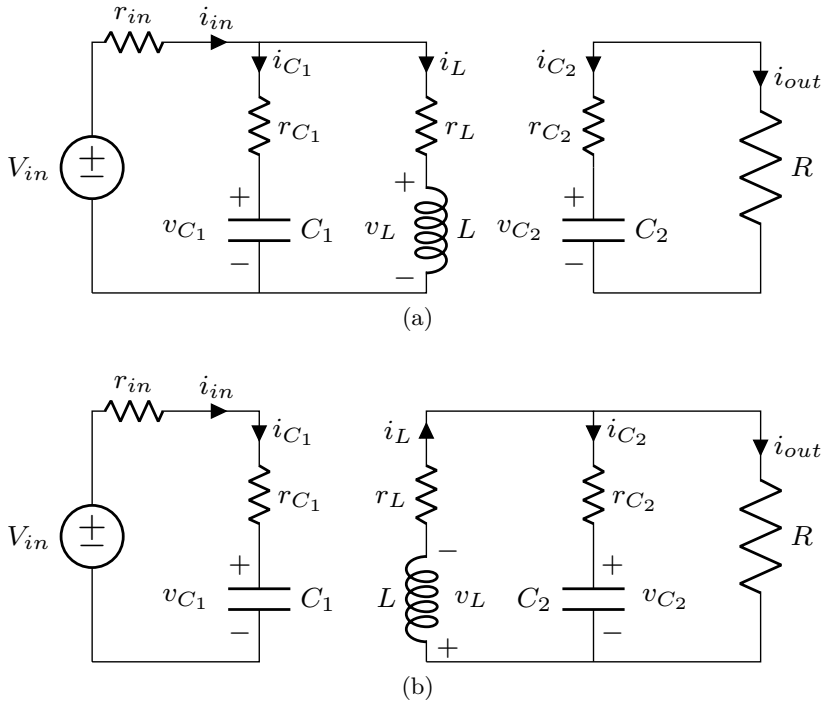

Figure 5.4: Equivalent circuit for (a) Q_1, Q_4 ON, (b) Q_1, Q_4 OFF.

linear approximation of the converter model. Based on the switches status (ON or OFF), two equivalent subcircuits can be extracted as shown in Fig. 5.4.

The inductor current i_L and the capacitors voltages v_{C1}, v_{C2} and the considered model outputs are respectively

$$x = [i_L, v_{C1}, v_{C2}]^T, \tag{5.7}$$

$$y = [i_{in}, i_{out}, i_L, v_{in}, v_{out}]^T \tag{5.8}$$

in which i_{in}, i_{out} are respectively the input and the output currents, v_{in}, v_{out} are respectively the input and the output voltages. The input of the model is the input voltage $u = [V_{in}]^T$.
The dynamical equations, considering the subcircuit represented in Fig.5.4 (a) are

$$\begin{cases} \frac{di_L}{dt} = -\frac{r_{in}r_{C1}+r_L R_1}{R_1 L} i_L + \frac{r_{in}}{R_1 L} v_{C1} + \frac{r_{C1}}{R_1 L} V_{in} \\ \frac{dv_{C1}}{dt} = -\frac{r_{in}}{R_1 C_1} i_L - \frac{1}{R_1 C_1} v_{C1} + \frac{1}{R_1 C_1} V_{in} \\ \frac{dv_{C2}}{dt} = -\frac{1}{R_2 C_2} v_{C2} \end{cases} \tag{5.9}$$

$$\begin{cases} i_{in} = \frac{r_{C1}}{R_1} i_L - \frac{1}{R_1} v_{C1} + \frac{1}{R_1} V_{in} \\ i_{out} = \frac{1}{R_2} v_{C2} \\ i_L = i_L \\ v_{in} = -\frac{r_{C1} r_{in}}{R_1} i_L + \frac{r_{in}}{R_1} v_{C1} + \frac{r_{C1}}{R_1} V_{in} \\ v_{out} = \frac{R}{R_2} v_{C2}, \end{cases} \tag{5.10}$$

in which $R_1 = r_{C1} + r_{in}$ and $R_2 = R + r_{C2}$.
The dynamical equations, considering the subcircuit represented in Fig.5.4 (b) are

$$\begin{cases} \frac{di_L}{dt} = -\frac{R}{R_2 L} v_{C2} - \frac{R_2 r_L + R r_{C2}}{R_2 L} i_L \\ \frac{dv_{C1}}{dt} = \frac{1}{R_1 C_1} V_{in} - \frac{1}{R_1 C_1} v_{C1} \\ \frac{dv_{C2}}{dt} = -\frac{1}{R_2 C_2} v_{C2} + \frac{R}{R_2 C_2} i_L \end{cases} \tag{5.11}$$

$$\begin{cases} i_{in} = -\frac{1}{R_1} v_{C1} + \frac{1}{R_1} V_{in} \\ i_{out} = \frac{r_{C2}}{R_2} i_L + \frac{1}{R_2} v_{C2} \\ i_L = i_L \\ v_{in} = \frac{r_{in}}{R_1} v_{C1} + \frac{r_{C1}}{R_1} V_{in} \\ v_{out} = \frac{R r_{C2}}{R_2} i_L + \frac{R}{R_2} v_{C2} \end{cases} \tag{5.12}$$

Equations (5.9)-(5.12) can be expressed in matrix form as:

$$\begin{cases} \dot{x} = A \cdot x + B \cdot u \\ \dot{y} = C \cdot x + D \cdot u \end{cases} \tag{5.13}$$

Then, the dynamical equations for each subcircuit are averaged over one switching period as

$$\begin{cases} A_{av} = A_{on} \cdot D + A_{off} \cdot (1 - D) \\ B_{av} = B_{on} \cdot D + B_{off} \cdot (1 - D) \\ C_{av} = C_{on} \cdot D + C_{off} \cdot (1 - D) \\ D_{av} = D_{on} \cdot D + D_{off} \cdot (1 - D) \end{cases} \tag{5.14}$$

in which A_{on}, B_{on}, C_{on}, D_{on} can be derived from eq. (5.9) and (5.10), while A_{off}, B_{off}, C_{off}, D_{off} can be derived from eq. (5.11) and (5.12).
It can be demonstrated that the linearized state-space model can be obtained as

$$\begin{cases} \dot{x} = A_{av} \cdot x + B_{sm} \cdot u \\ \dot{y} = C_{av} \cdot x + D_{sm} \cdot u \end{cases} \tag{5.15}$$

Table 5.5: System Parameters

Specification	Symbol	Unit	Value
Battery Pack			
Nominal voltage	V_{batt}	V	48
Max voltage	$V_{batt,max}$	V	54.6
Min. voltage	$V_{batt,min}$	V	39
Capacity	Q_{batt}	Ah	20
Internal resistance	r_{batt}	mΩ	20
SCs bank			
SCs Max Voltage	$V_{sc,max}$	V	60
SCs Min. Voltage	$V_{sc,min}$	V	12
SCs Capacity	C_{sc}	F	8.4
SC ESR	r_{sc}	mΩ	15
Load			
Load nominal voltage	V_{load}	V	48
Load resistor	R	Ω	12
Buck-boost converters			
Capacitors	C_1, C_2	μF	680
Capacitors ESR	r_C	mΩ	220
Inductor	L	μH	22
Inductor ESR	r_L	mΩ	1.4

where:

$$B_{sm} = [B_{av}, (A_{on} - A_{off})X + (B_{on} + B_{off})u]^T \tag{5.16}$$

$$D_{sm} = [D_{av}, (C_{on} - C_{off})X + (D_{on} + D_{off})u]^T \tag{5.17}$$

$$X = -A_{av}^{-1} \cdot B_{av} \cdot u \tag{5.18}$$

5.3.2 Parameter Design

For the experimental validation, a scaled-down (250 W) system is realized.

The battery pack is a 48 V - 20 Ah model, with fully charged voltage $V_{batt,max} = 54.6$ V and fully discharged voltage $V_{batt,min} = 39$ V. The battery internal resistance is considered constant and equal to $r_{batt} = 0.2\,\Omega$.

The SCs bank has a rated voltage of 64 V and a rated capacitance of 8.4 F. Considering that the SCs bank is never totally discharged, the maximum and minimum voltage are considered as $V_{sc,max} = 60$ V and $V_{sc,min} = 12$ V. The SCs bank internal resistance is considered constant and equal to $r_{sc} = 0.16\,\Omega$.

For the controller tuning the load is considered constant and equal to $R = 12\,\Omega$

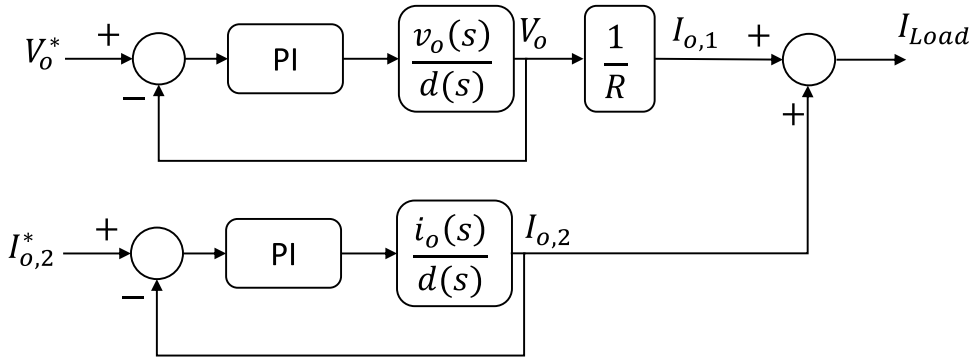

Figure 5.5: Control scheme of the proposed system.

and the load voltage is kept constant to $V_{load} = 48$ V thanks to the battery converter.

The inductance value for the converters can be chosen considering that, during the ON subcircuit, the current increases linearly as

$$L\frac{\Delta I_L}{DT_{sw}} = V_{in} \tag{5.19}$$

where ΔI_L is the desired inductor current ripple and T_{sw} is the switching period. From (5.19), the inductance can be derived as

$$L \geq V_{in}\frac{DT_{sw}}{\Delta I_L}. \tag{5.20}$$

The capacitance value can be calculated considering that, during the ON subcircuit, the capacitor supply the total output current

$$C\frac{\Delta V_C}{DT_{sw}} = \frac{V_{out}}{R} \tag{5.21}$$

where ΔV_C is the desired voltage ripple. From (5.21), the capacitance value can be derived as

$$C \geq \frac{V_{out}DT_{sw}}{R\Delta V_C}. \tag{5.22}$$

The main system parameters are summarized in Table 5.5.

5.3.3 Control scheme

The goal of the system is to provide the power required by the load and to limit the maximum power supplied by the battery pack. The SCs bank provides the possible deviations between the load power and the battery pack power. The control scheme employed is represented in Fig. 5.5.

The battery pack converter is controlled to keep the load voltage equal to the reference value V_o^*. The SCs bank converter is controlled to supply the current difference between the load and the battery converter output current $I_{o,2}^* = I_{load} - I_{o,1}$.

Battery Controller

For the battery controller design the conditions of maximum and minimum input voltage, corresponding respectively to minimum and maximum duty cycle, are considered

$$\begin{cases} D_{min} = \dfrac{V_{load}}{V_{load} + V_{batt,max}} = 0.468 \\ D_{max} = \dfrac{V_{load}}{V_{load} + V_{batt,min}} = 0.552 \end{cases} \tag{5.23}$$

The resulting transfer functions from the duty cycle to the output voltage G_{v_o} are reported in eqs. (5.24)-(5.25) and the corresponding Bode plots are represented in Fig.5.7.

$$G_{v_o,min} = \frac{-1.58s^3 + 5.02e^5 s^2 + 5.81e^9 s + 1.59e^{13}}{s^3 + 1.15e^4 s^2 + 5.19e^7 s + 8.78e^{10}} \tag{5.24}$$

$$G_{v_o,max} = \frac{-1.85s^3 + 3.43e^5 s^2 + 4.05e^9 s + 1.11e^{13}}{s^3 + 1.09e^4 s^2 + 4.46e^7 s + 6.32e^{10}} \tag{5.25}$$

Considering the minor differences between the transfer functions, a single Proportional - Integral (PI) controller with constant parameters can be used. The controller is designed to obtain a response without overshoot and a settling time less than 10 ms. The obtained PI transfer function is

$$G_{C_1} = \frac{2.864}{s}. \tag{5.26}$$

SCs Controller

For the SCs controller design, a similar approach is used. First, the duty cycles corresponding to the maximum and minimum input voltages are evaluated

$$\begin{cases} D_{min} = \dfrac{V_{load}}{V_{load} + V_{sc,max}} = 0.444 \\ D_{max} = \dfrac{V_{load}}{V_{load} + V_{sc,min}} = 0.800 \end{cases} \tag{5.27}$$

and the resulting transfer functions are reported in eqs (5.28)-(5.28) and plotted in Fig. 5.6.

$$G_{i_o,min} = \frac{-0.22s^3 + 1.18e^4 s^2 + 1.53e^8 s + 4.33e^{11}}{s^3 + 9855 + s^2 + 3.36e^7 s + 2.88e^{10}} \tag{5.28}$$

$$G_{i_o,max} = \frac{-0.13s^3 + 4.63e^4 s^2 + 5.34e^8 s + 1.46e^{12}}{s^3 + 1.16e^4 s^2 + 5.42e^7 s + 9.54e^{10}} \tag{5.29}$$

The controller transfer function is chosen as

$$G_{C_1} = 0.0142 + \frac{83.1}{s}. \tag{5.30}$$

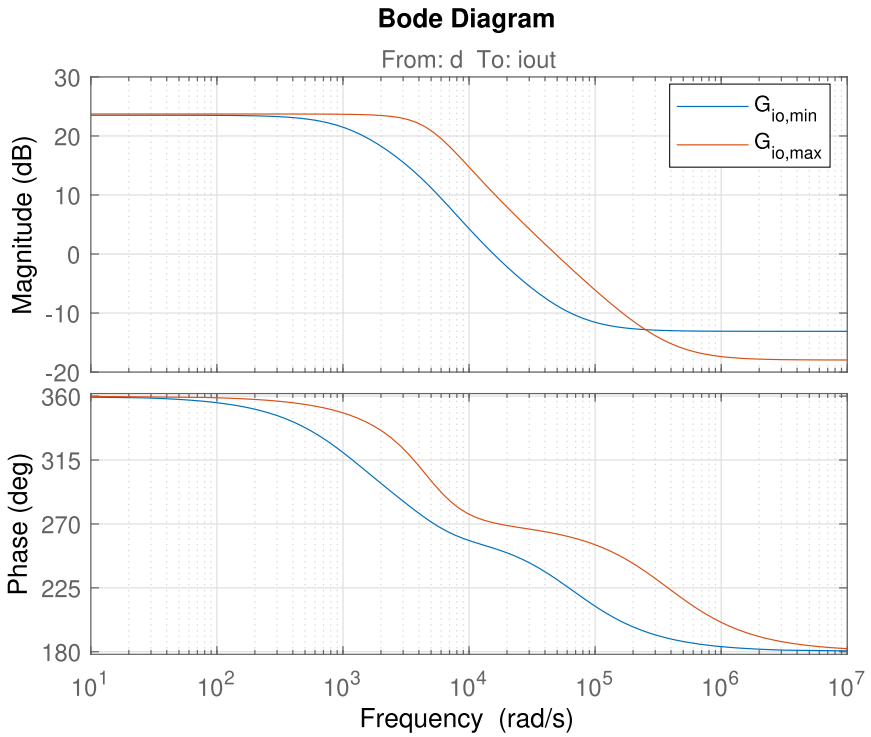

Figure 5.6: Bode diagram of the duty cycle to output current transfer function for maximum and minimum duty cycle.

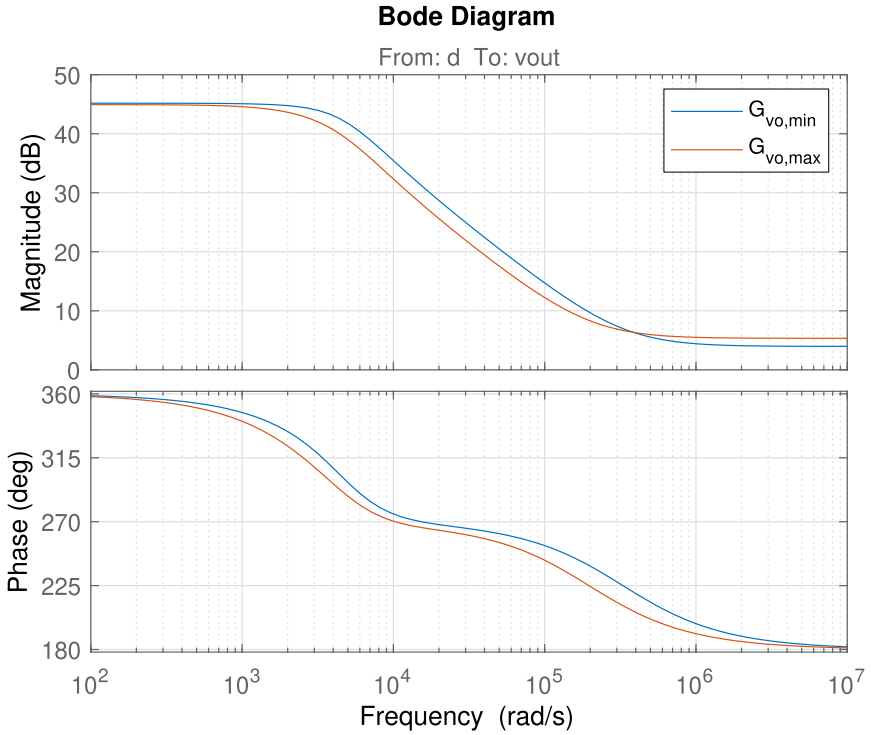

Figure 5.7: Bode diagram of the duty cycle to output voltage transfer function for maximum and minimum duty cycle.

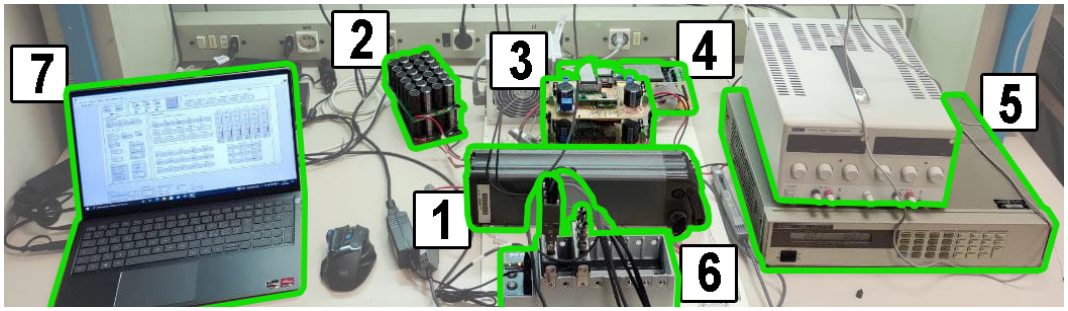

Figure 5.8: Test-bench setup for the experimental validation.

5.4 Experimental Validation

5.4.1 Test bench setup

With the aim of experimentally validate the functional suitability of the system, a low-power experimental setup, shown in Fig. 5.8, is designed and developed. It is composed of:

1. a 48 V rated Li-Ion battery pack;
2. a 64 V rated SC bank;
3. two 250 W rated non-inverting buck-boost converters (SIFoS);
4. a control-board;
5. an Agilent 6060B Single Input 300 W Electronic Load;
6. two NI 9125 16-Bit analogue input modules (placed in a NI cDAQ 9178 chassis);
7. an host PC.

For the system control, a NI sbRIO 9651-based board is used. It is equipped with 16 ADC channels 14-Bit, 8 ADC channels 8-Bit, 30 PWM output channels and 36 general purpose I/O channels. The board is used to acquire the converters' input and output voltages and currents and the switches temperatures, useful for the closed-loop control and the over-voltage, over-current and over-temperature software protections.
The electronic load, controlled via GPIB, is used to emulate the scaled-down power profile.
The NI chassis is used to continuously acquire the input battery pack and SC bank currents and voltages and the load current and voltage during the test.
The host PC is used to interface the control board, the electronic load and the NI chassis.

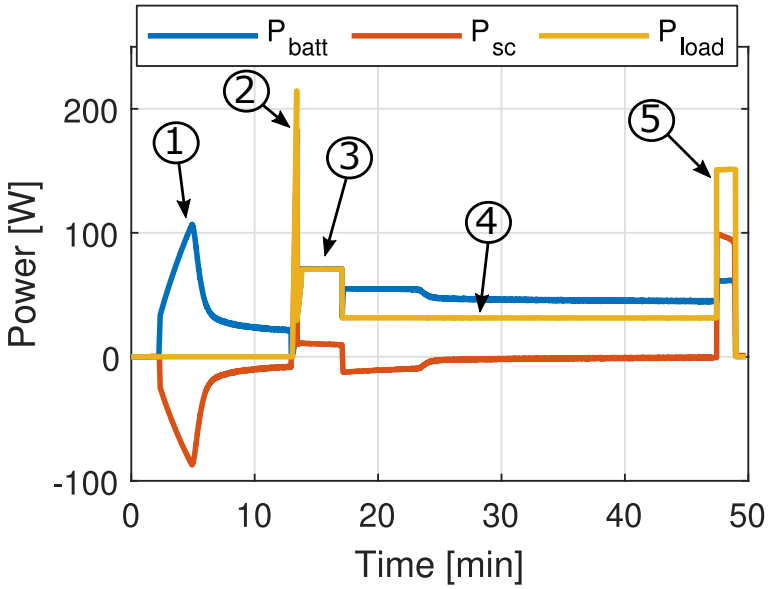

Figure 5.9: Battery pack, SCs bank, load power profiles.

5.4.2 Test description

In Fig. 5.9 the load, battery pack and SCs bank power profiles are shown. The power profile can be divided into five sections.

1. The SCs bank is charged by the battery pack in CC-CV mode up to 55 V with a maximum current equal to 2 A. The charge process is ended when the SCs current reaches 0.2 A;

2. The SCs bank gives the majority of the power required by the load, while the battery current slowly increases;

3. The power required by the load is entirely ensured by the battery pack, the SCs bank provides to compensate the system internal losses;

4. The battery provides the power to the load and additionally recharges the SCs bank in CC-CV mode;

5. the power required by the load is provided by both battery pack and SCs bank.

5.4.3 Experimental results

Fig. 5.10 shows the voltages and currents trends of battery pack, SCs bank and load. Both the simulation and experimental results are reported and compared.

At $t = 1$ min the battery pack is connected to the input of the buck-boost converter, and the control is enabled to keep the output voltage to 48 V. At $t = 2.3$ min the SC converter is enabled to perform the CC-CV charge. At $t = 13$ min the CC-CV charge stops, the electronic load is connected and the power profile starts.

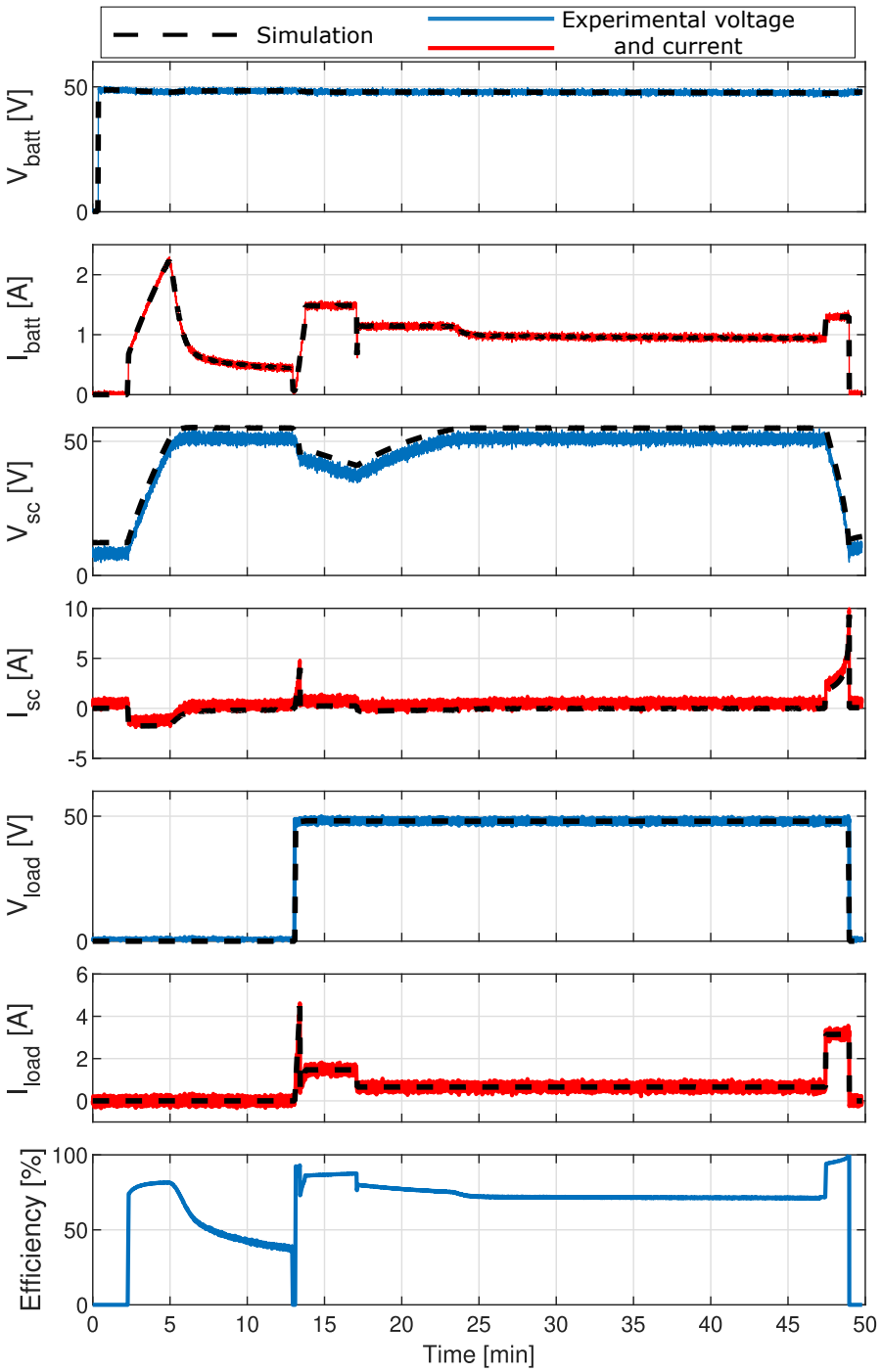

Figure 5.10: Comparison of simulated and experimental results. Battery, SCs, load voltages and currents and system efficiency.

As it can be noticed the trends observed in simulation are replicated successfully during the experimental test, thereby verifying the full functionality of the realized converters, of the control and of the whole system.

Therefore, the system efficiency can be evaluated. The power flow is different for each phase of the test. For this reason, the efficiency is calculated differently as follows.

- If the battery charges the SCs pack:

$$\eta = \frac{P_{sc}}{P_{batt}} \cdot 100 \tag{5.31}$$

- If the battery and SCs pack supply power to the load:

$$\eta = \frac{P_{load}}{P_{batt} + P_{sc}} \cdot 100 \tag{5.32}$$

- If the battery supplies power to the load and recharge the SC:

$$\eta = \frac{P_{load} + P_{SC}}{P_{batt}} \cdot 100 \tag{5.33}$$

The trend of the calculated efficiency is shown in the last plot of Fig.5.10. As it can be clearly notice, the efficiency is higher in the phases in which both the battery pack and the SCs supply power to the load, reaching peaks of 98%. In the SCs charging phases, due to the double-stage conversion, the efficiency reaches 80%. During the pre-charge phase the efficiency decreases from 80 to 40 % because in the CV phase the power is significantly low (about 10 W), becoming comparable with the converter losses.

5.5 Conclusion

In this chapter, an hybrid energy storage management system was investigated. The power and the energy required by a generic profile were considered for the sizing of the storage system. A comparison between a battery-only storage system and a hybrid storage system composed of a battery pack and a SC bank was reported. In particular, a description of the power sharing rule-based algorithm and of the iterative sizing method was provided. The comparison highlights that the hybrid configuration allows the reduction of about 20% of weight respect to the electro-chemical one and allows to cope better to the peak power request. The HESMS power electronics converters modeling, control and design was also considered. An experimental validation of the HESMS was carried out on a scaled-down laboratory prototype, confirming the effectiveness of the proposed control strategy.

References

[1] Z. Cabrane, M. Ouassaid, and M. Maaroufi, "Analysis and evaluation of battery-supercapacitor hybrid energy storage system for photovoltaic installation," *International Journal of Hydrogen Energy*, vol. 41, no. 45, pp. 20 897–20 907, 2016, ISSN: 0360-3199. DOI: https://doi.org/10.1016/j.ijhydene.2016.06.141.

[2] T. Shi, H. Liu, F. Wang, S. Zhang, H. Guo, and Z. Lin, "Accurate power sharing of hybrid energy storage system in dc shipboard power system based on quadratic programming algorithm," in *2020 IEEE 29th International Symposium on Industrial Electronics (ISIE)*, 2020, pp. 1123–1128. DOI: 10.1109/ISIE45063.2020.9152444.

[3] S. Zhou, Z. Chen, D. Huang, and T. Lin, "Model prediction and rule based energy management strategy for a plug-in hybrid electric vehicle with hybrid energy storage system," *IEEE Transactions on Power Electronics*, vol. 36, no. 5, pp. 5926–5940, 2021. DOI: 10.1109/TPEL.2020.3028154.

[4] LG. "LG HG2." (2014), [Online]. Available: https://www.nkon.nl/sk/k/hg2.pdf..

[5] Tecate Group, *TPLC-3R8*, 2020. [Online]. Available: https://www.tecategroup.com/products.

[6] Wurth. "How to Use Supercapacitors? A Brief Guide to the Design-In Process." (2019), [Online]. Available: https://www.we-online.com/catalog/media/o157040v410%20AppNote_SN009_EN.pdf.

[7] C.-W. Chang and C.-L. Wei, "Single-inductor four-switch non-inverting buck-boost dc-dc converter," in *Proceedings of 2011 International Symposium on VLSI Design, Automation and Test*, 2011, pp. 1–4. DOI: 10.1109/VDAT.2011.5783629.

Chapter 6

Quasi-Z-Source Converter Modeling and Control

6.1 Introduction

Classical Voltage Source Inverters (VSIs) are widely employed in different applications such as uninterruptible power supplies (UPS) [1], energy storage systems [2] and motor drives [3]. VSIs can only operate as buck converters, thus achieving a lower AC output voltage than the input DC voltage. For this reason, they are often paired with an additional DC/DC boost converter, which increases the complexity and cost of the system [4]. Moreover, to avoid short-circuit between the upper and the lower switches in one leg, dead–time must be added between the turn-on and turn-off signals which introduces AC output waveform distortions [4].

In order to overcome these limits, the impedance source converter was introduced [5]. The main difference with the classical VSI is the presence of an impedance network (Z-network) between the input voltage and the inverter DC-link. The Z-network makes it possible for the simultaneous regulation of the input voltage and the DC/AC conversion, realizing a single-stage DC/AC conversion with buck-boost capabilities. In addition, the converter is inherently short-circuit protected thanks to the Z-network and the dead time can be removed, improving the inverter reliability and lowering the output waveform distortion.

In the literature, many different topologies have been presented: Switched Inductor Z-Source Inverters [6], [7], Trans-Z-Source Inverters [8], LCCT-Z-Source inverters [9]. As a typical impedance source inverter, the quasi-Z-Source Inverter (qZSI) [10], shown in Fig. 6.1, inherits all the benefits of the Z-Source inverter. Moreover, it draws a continuous DC current from the input. Such characteristics make the qZSI suitable for renewable energy or energy storage system applications. However, as there are many passive components, the system order is relatively high, challenging the controller design. The commonly used approach is to derive the state-space average and small-signal model of the converter for the closed-loop controller design.

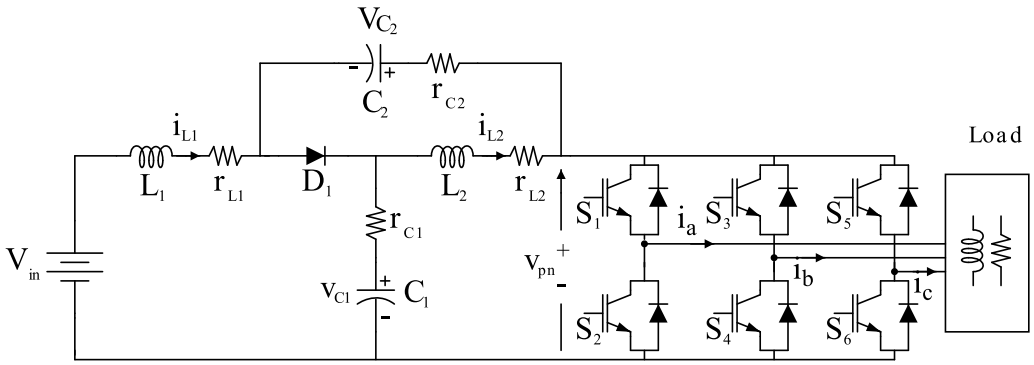

Figure 6.1: Three-phase quasi-Z-source inverter diagram.

The control approaches for the DC side can be classified mainly into Proportional Integral (PI) control or Nonlinear Control. Focusing on PI control methods, they can be further divided into single-loop and double-loop methods. In single loop methods, the controlled variables are, usually, the input voltage V_{in} [11], the capacitor voltage v_{C_1} or the DC-link peak voltage v_{pn} [12], [13]. In double loop methods, the controlled variables are the inductor current i_{L_1} for the inner loop, and the capacitor voltage v_{C_1} or DC-link voltage v_{pn} for the outer loop. For the AC side, PI regulator and Park/Clarke transformation are normally employed. In the literature, only a few articles use Proportional-Resonant (PR) regulator with the three-phase qZSI, and some present only simulation results. PR controllers have several advantages over PI controllers: at resonant frequency the PR controller does not exhibit a phase delay, it has robust reference tracking and zero steady-state error and it does not need transformation from/to rotating and stationary reference frame, thus reducing the controller complexity and computational demand.

In this chapter, a comparative study between different control schemes for the three-phase qZSI is carried out. The paper is organized as follows: in Section II, the small-signal model of the available qZSI prototype is derived. In Section III, different control schemes are considered and synthesized using the derived small-signal transfer function. Finally, in Section IV, the simulation and experimental performances of the system are compared.

6.2 Small-Signal modeling

The schematic of the analyzed system is shown in Fig. 6.1. The input voltage can be a PV generator, a battery or other energy sources. The diode D_1 can be replaced by a MOSFET to obtain a bidirectional Z-network. The other main components of the Z-network are two inductors L_1 and L_2, which can be separated or mutually coupled, and two capacitors C_1 and C_2. In order to design a closed-loop control, the small-signal model is obtained [14]-[16]. The schematic in Fig. 6.1 is divided

into two sub-circuits: the Shoot-Through State (STS), shown in Fig. 6.2, and the Non-Shoot-Through State (NSTS), shown in Fig. 6.3. During the STS, the output is short-circuited, and the diode D_1 is inversely polarized. During the NSTS, the diode D_1 is polarized and the three-phase inverter with the load are equivalent to a constant current source I_{pn}. The parasitic resistance of both inductors and capacitors, denoted by r_{L1}, r_{L2} and r_{C1}, r_{C2}, respectively, and the diode voltage drop denoted by V_{D1} are considered in the small-signal model.

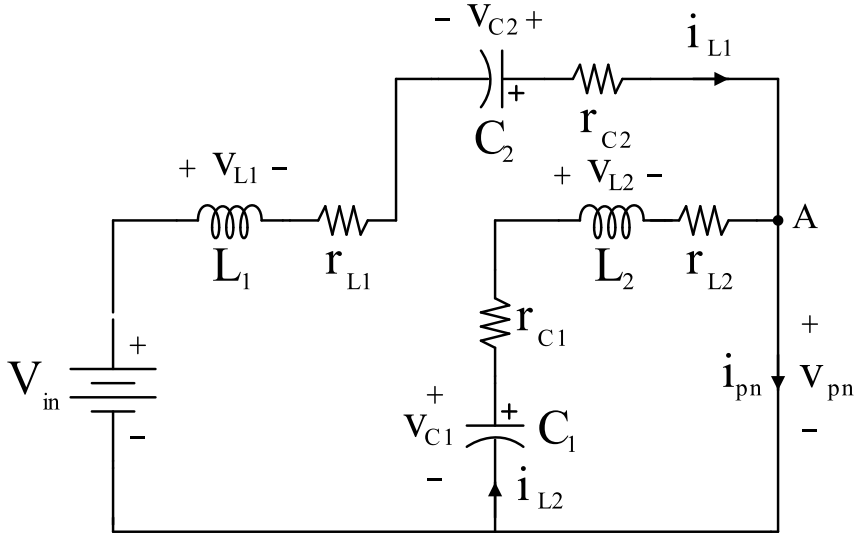

Figure 6.2: Equivalent circuit in the shoot-through state of the qZSI circuit in Fig. 6.1.

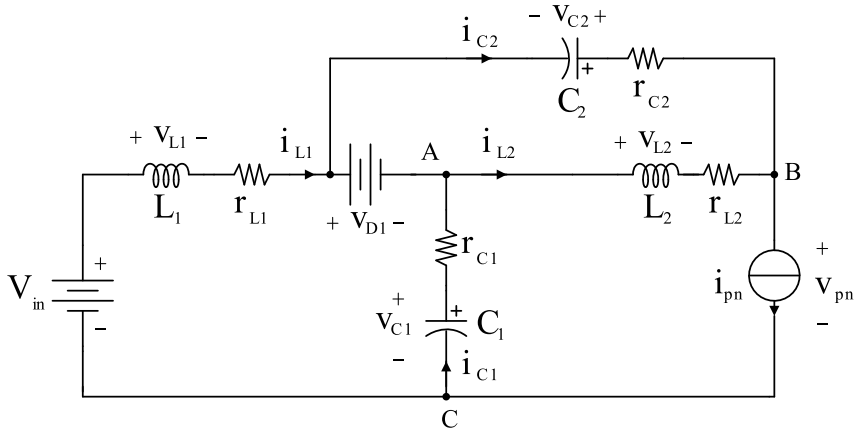

Figure 6.3: Equivalent circuit in the non-shoot-through state of the qZSI circuit in Fig. 6.1.

To apply the state-space averaging technique, a set of equations in the state-space form need to be found for each configuration of the circuit as

$$\begin{cases} \dot{x} = & A \cdot x + B \cdot u \\ y = & Q \cdot x \end{cases}. \tag{6.1}$$

Considering Fig. 6.2, the state-space equations can be written for the STS, considering the state vector as $x = [i_{L_1}, i_{L_2}, v_{C_1}, v_{C_2}]^T$, input vector as $u = [V_{in}, V_{D_1}, I_{pn}]^T$ and output vector as $y = x$

$$\begin{cases} \frac{di_{L_1}}{dt} = & -\frac{(r_{L_1}+r_{C_2})}{L_1} i_{L_1} + \frac{1}{L_1} v_{C_1} + \frac{1}{L_1} V_{in} \\ \frac{di_{L_2}}{dt} & = -\frac{(r_{C_1}+r_{L_2})}{L_2} i_{L_2} + \frac{1}{L_2} v_{C_1} \\ \frac{dv_{C_1}}{dt} & = -\frac{1}{C_1} i_{L_2} \\ \frac{dv_{C_2}}{dt} & = -\frac{1}{C_2} i_{L_1} \end{cases} \tag{6.2}$$

In a matrix form, (6.2) can be written as

$$\begin{cases} \dot{x} = & A_1 \cdot x + B_1 \cdot u \\ y = & Q_1 \cdot x \end{cases} \tag{6.3}$$

where A_1, B_1 and Q_1 are

$$A_1 = \begin{bmatrix} -\frac{(r_{L_1}+r_{C_2})}{L_1} & 0 & 0 & \frac{1}{L_1} \\ 0 & -\frac{(r_{C_1}+r_{L_2})}{L_2} & \frac{1}{L_2} & 0 \\ 0 & -\frac{1}{C_1} & 0 & 0 \\ -\frac{1}{C_2} & 0 & 0 & 0 \end{bmatrix}, \tag{6.4}$$

$$B_1 = \begin{bmatrix} \frac{1}{L_1} & 0 & 0 \\ 0 & 0 & 0 \\ 0 & 0 & 0 \\ 0 & 0 & 0 \end{bmatrix}, \tag{6.5}$$

$$Q_1 = \begin{bmatrix} 1 & 0 & 0 & 0 \\ 0 & 1 & 0 & 0 \\ 0 & 0 & 1 & 0 \\ 0 & 0 & 0 & 1 \end{bmatrix}. \tag{6.6}$$

For the NSTS, the following state-space equations can be obtained

$$\begin{cases} \frac{di_{L_1}}{dt} & = -\frac{(r_{L_1}+r_{C_1})}{L_1} i_{L_1} - \frac{1}{L_1} v_{C_1} + \frac{1}{L_1} V_{in} + \\ & -\frac{1}{L_1} v_{D_1} + \frac{r_{C_1}}{L_1} i_{pn} \\ \frac{di_{L_2}}{dt} & = -\frac{(r_{C_2}+r_{L_2})}{L_2} i_{L_2} - \frac{1}{L_2} v_{C_2} + \\ & -\frac{1}{L_2} v_{D_1} + \frac{r_{C_2}}{L_2} i_{pn} \\ \frac{di_{C_1}}{dt} & = \frac{1}{C_1} i_{L_1} - \frac{1}{C_1} i_{pn} \\ \frac{dv_{C_2}}{dt} & = \frac{1}{C_2} i_{L_2} - \frac{1}{C_2} i_{pn} \end{cases} \tag{6.7}$$

In the matrix form, (6.7) can be written as

$$\begin{cases} \dot{x} = & A_2 \cdot x + B_2 \cdot u \\ y = & Q_2 \cdot x \end{cases} \tag{6.8}$$

in which A_2, B_2 and Q_2 are

$$A_2 = \begin{bmatrix} -\frac{\left(r_{L_1}+r_{C_1}\right)}{L_1} & 0 & -\frac{1}{L_1} & 0 \\ 0 & -\frac{\left(r_{C_2}+r_{L_2}\right)}{L_2} & 0 & -\frac{1}{L_2} \\ \frac{1}{C_1} & 0 & 0 & 0 \\ 0 & \frac{1}{C_2} & 0 & 0 \end{bmatrix}, \tag{6.9}$$

$$B_2 = \begin{bmatrix} \frac{1}{L_1} & -\frac{1}{L_1} & \frac{r_{C_1}}{L_1} \\ 0 & -\frac{1}{L_2} & \frac{r_{C_2}}{L_2} \\ 0 & 0 & -\frac{1}{C_1} \\ 0 & 0 & -\frac{1}{C_2} \end{bmatrix}, \tag{6.10}$$

$$Q_2 = Q_1. \tag{6.11}$$

Subsequently, the average state-space model of the converter can be obtained by calculating the average matrices as

$$\begin{cases} A_{av} = & A_1 \cdot D + A_2 \cdot (1-D) \\ B_{av} = & B_1 \cdot D + B_2 \cdot (1-D) \\ Q_{av} = & Q_1 \cdot D + Q_2 \cdot (1-D) \end{cases} \tag{6.12}$$

where D is the shoot-through duty cycle. The resultant average matrices can be given as

$$A_{av} = \begin{bmatrix} -\frac{\left(r_{L_1}+r_{C_2}\right)}{L_1} & 0 & -\frac{(1-D)}{L_1} & \frac{D}{L_1} \\ 0 & -\frac{\left(r_{C_1}+r_{L_2}\right)}{L_2} & \frac{D}{L_2} & -\frac{(1-D)}{L_2} \\ \frac{(1-D)}{C_1} & -\frac{D}{C_1} & 0 & 0 \\ -\frac{D}{C_2} & \frac{(1-D)}{C_2} & 0 & 0 \end{bmatrix}, \tag{6.13}$$

$$B_{av} = \begin{bmatrix} \frac{1}{L_1} & -\frac{(1-D)}{L_1} & \frac{r_{C_1}}{L_1}(1-D) \\ 0 & -\frac{D}{L_2} & \frac{r_{C_2}}{L_2}(1-D) \\ 0 & 0 & -\frac{(1-D)}{C_1} \\ 0 & 0 & -\frac{(1-D)}{C_2} \end{bmatrix}, \tag{6.14}$$

$$Q_{av} = Q_1. \tag{6.15}$$

Finally, the avarage state-space model can be expressed as

$$\begin{cases} \dot{x} = & A_{av} \cdot x + B_{av} \cdot u \\ y = & Q_{av} \cdot x \end{cases}. \tag{6.16}$$

The states vector steady-state values $X = [I_{L_1}, I_{L_2}, V_{C_1}, V_{C_2}]^T$, can also be calculated as

$$X = -Q_{av} \cdot A_{av}^{-1} \cdot B_{av} \cdot u. \tag{6.17}$$

Considering a small-signal perturbation of the state variables $\tilde{x} = \begin{bmatrix} \tilde{i}_{L_1} & \tilde{i}_{L_2} & \tilde{v}_{C_1} & \tilde{v}_{C_2} \end{bmatrix}^T$, the input signals $\tilde{u} = \begin{bmatrix} \tilde{V}_{in} & \tilde{V}_{D_1} & \tilde{I}_{pn} \end{bmatrix}^T$ and the shoot-though duty cycle $\tilde{d}$, substituting those into (6.16), the following equations are obtained

$$\dot{\tilde{x}} = A_{av}\tilde{x} + B_{av}\tilde{u} + E \cdot \tilde{d} \tag{6.18}$$

$$\dot{\tilde{y}} = Q_{av}\tilde{x} \tag{6.19}$$

where $E = [(A_1 - A_2) \cdot X + (B_1 - B_2) \cdot u]$.

The small-signal duty-to-output transfer functions can be obtained with the following equation

$$y_d = Q_{av} I \left(s \cdot I - A_{av}\right)^{-1} \cdot E. \tag{6.20}$$

Considering $L_1 = L_2 = L$, $C_1 = C_2 = C$, $r_{L1} = r_{L_2} = r_L$, $r_{C_1} = r_{C_2} = r_C$, $R = r_C + r_L$ and the system parameters given in Table 6.1, the inductor current and the capacitor voltage small-signal transfer functions are given by (6.21) and (6.22), which are used to design and tune the qZSI DC-DC side controller in Section III-A.

$$G_{i_L}(s) = \frac{i_{L_1}(s)}{d(s)} = \frac{(1-2D)(I_{L_1} + I_{L_2} - I_{pn}) + (V_{C_1} + V_{C_2} + V_{D_1} - r_C I_{pn})Cs}{LCs^2 + CRs + (1-2D)^2} \tag{6.21}$$

$$G_{v_C}(s) = \frac{v_{C_1}(s)}{d(s)} = \frac{(1-2D)(V_{C_1} + V_{C_2} + V_{D_1} - I_{pn} r_C) - (Ls + R)(I_{L_1} + I_{L_2} - I_{pn})}{LCs^2 + CRs + (1-2D)^2} \tag{6.22}$$

6.3 Control System of qZSI

In the qZSI, the DC and AC sides are separately controlled. For the DC-side control, the input voltage V_{in}, the capacitor voltage V_{C_1}, the inductor current I_{L_1} or the inverter DC-link voltage V_{pn} are usually controlled through PI regulators. The PI regulator output signal is the shoot-though duty cycle D. For the AC-side control, the output current $i_{a,b,c}$ or the output voltage $v_{a,b,c}$ are commonly controlled, using the Clarke transformation and the PI regulators for the d and q frames. An alterna-

Table 6.1: System Parameters

Parameter	Unit	Symbol	Value
Input Voltage	(v)	V_{in}	50
Inductance	(μH)	L_1, L_2	275
Inducor ESR	(Ω)	r_{L_1}, r_{L_2}	0.11
Capacitance	(μF)	C_1, C_2	200
Capacitor ESR	(mΩ)	r_{C_1}, r_{C_2}	10
Diode voltage	(V)	V_{D_1}	0.6
Output current	(A)	I_{pn}	3
Duty Cycle	(-)	D	0.3
Switching Frequency	(kHz)	f_{sw}	10
Filter Inductor	(mH)	L_L	1.8
Load Resistor	(Ω)	R_L	10-80

tive solution for the AC-side control is to use PR regulators. The main advantage of PR regulators is the lack of phase delay at the resonant frequency. Moreover, they can achieve zero steady-state error, robust reference tracking and fast disturbance rejection [17], [18]. In addition, they do not need the Clarke transformation, thus simplifying the control algorithm. In the following sections, three different control schemes are described and the regulators are tuned considering the obtained small-signal model transfer functions in Section II.

6.3.1 DC-side control

Input current PI regulator

Fig. 6.4 shows the block diagram used for the input current control. The inductor current is measured and compared to the reference value. The error is sent to the PI regulator and the reference shoot-through duty cycle D is generated. In this case, the modulation index m is kept constant. From the modulation technique presented in literature [19]-[27], the Sinusoidal Pulse-Width Modulation (SPWM) for the AC stage and the Simple Boost Control (SBC) for the DC stage have been chosen. In order to tune the regulator, the small-signal transfer function (6.21) is considered. The transfer function of the regulator is given by

$$G_c = K_p + \frac{K_i}{s} \tag{6.23}$$

where K_p is the proportional gain and K_i is the integral gain. Using the Routh-Hurwitz stability criterion, the PI regulator parameters are chosen as $K_p = 9e^{-3}$ and $K_i = 19.1$. Fig. 6.5 shows the Bode plot of (6.21) and of the open loop transfer

function given by $G_{ol} = G_c \cdot G_{i_L}$. It can be noticed that the system is stable with a sufficient phase margin.

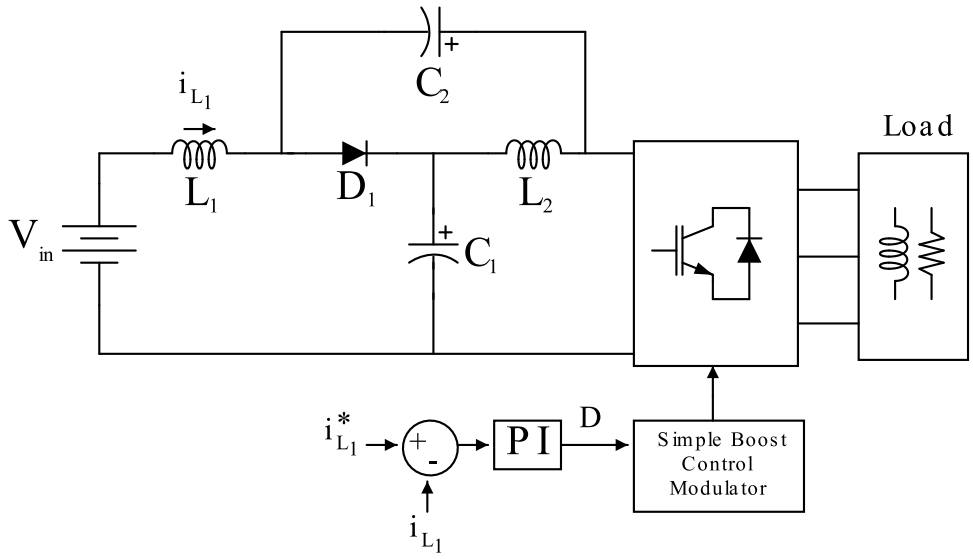

Figure 6.4: Input current control block diagram.

DC-link voltage PI regulator

Fig. 6.6 shows the block diagram used for the DC-link voltage and output current control. For the DC side control, the capacitor C_1 voltage is measured and used to calculate the DC-link peak voltage as

$$V_{pn} = \frac{1}{1 - D_{av}} v_{C_1} \tag{6.24}$$

where D_{av} is the average duty cycle, obtained with a Moving Average Filter (MAF), as shown in Fig. 6.6. The calculated DC-link peak voltage is compared to the reference value, and the error is sent to a PI regulator. The output of the controller is the shoot-though duty cycle D that is sent to the SBC modulator. To tune the regulator, the small-signal transfer function (6.22) is considered. The PI regulator parameters are chosen as $K_p = 0$ and $K_i = 0.4$. Fig. 6.7 shows the Bode plot of (6.22) and of the open loop transfer function given by $G_{ol} = G_c \cdot G_{v_C}$. In this case, the system is stable with both enough phase margin and gain margin.

6.3.2 AC-side controller

Output current PI regulator

For the AC side control, the output three-phase currents are measured and sent to the Stationary Reference Frame (SRF) transformation block. The α and β components are used to evaluate the peak current as

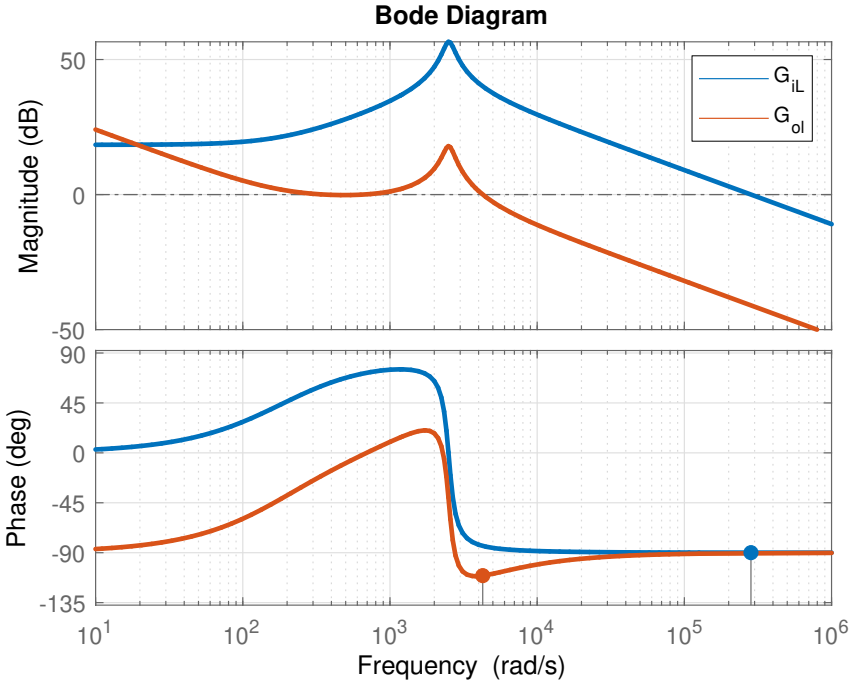

Figure 6.5: Bode plot of G_{i_L} with and without PI regulator.

$$i_p = \sqrt{i_\alpha^2 + i_\beta^2}. \tag{6.25}$$

The calculated peak current is compared to the reference value and the error is sent to a PI controller, whose output is the modulation index m sent to the SBC modulator. In order to tune the regulator parameters, the load transfer function (filter inductor and load resistor) is considered as

$$G_{load} = \frac{1}{R_L + L_L \cdot s}. \tag{6.26}$$

The PI regulator integral gain is chosen equal to the inverse of the load time constant

$$K_i = \frac{R_L}{L_L} \tag{6.27}$$

while the proportional gain can be calculated as

$$K_p = \frac{L_L}{3} f_{sw} \tag{6.28}$$

resulting in $K_p = 6$ and $K_i = 5000$.

Output current PR regulator

In order to improve the performances of the converter, a control scheme with a Proportional Resonant (PR) regulator was considered. Fig. 6.8 shows the block diagram used for the PR-based output current control. For the DC side control,

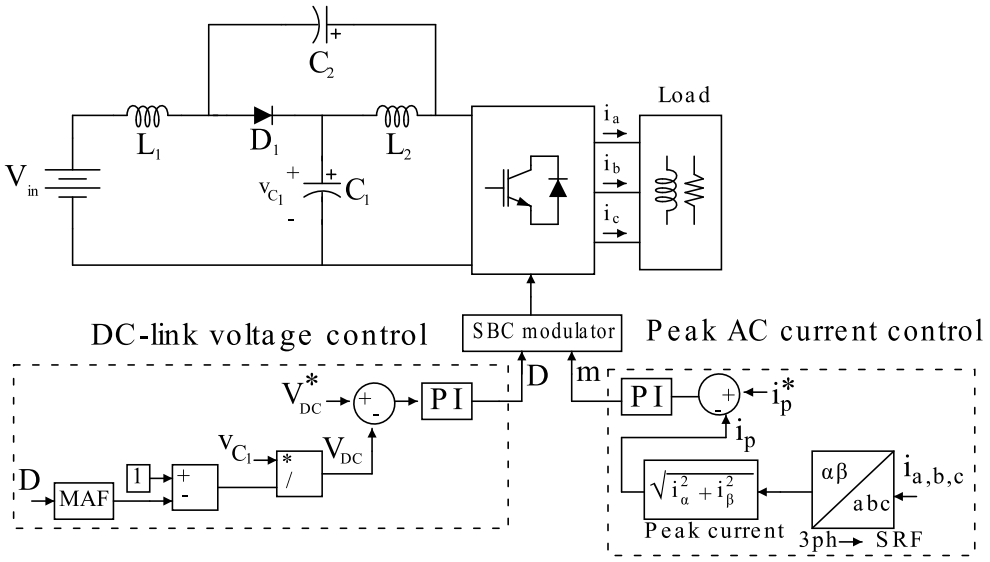

Figure 6.6: DC-link voltage and output peak current control block diagram.

the same approach presented in Section 6.4.2 was used. For the AC side control, the measured three-phase output current is compared directly to the reference three-phase current. The error is sent to the PR controller, whose output is the three-phase reference voltage sent to the SBC modulator. Ideally, the PR regulator transfer function is given by

$$G_{PR} = K_{pr} + \frac{2K_r s}{s^2 + \omega_0^2} \tag{6.29}$$

where ω_0 is the fundamental angular frequency, K_{pr} is the proportional coefficient and K_r is the resonant coefficient. The transfer function (6.29) is not feasible for practical implementation, so the non-ideal PR regulator was introduced [28], [29]

$$G'_{PR} = K_{pr} + \frac{2K_r \omega_c s}{s^2 + 2\omega_c s + \omega_0^2} \tag{6.30}$$

where ω_c is the cut-off frequency. In this form, the PR controller acts as a high-gain low-pass filter. For the PR regulator, the proportional coefficient is tuned using Eq. (6.28), the resonant coefficient is tuned using Eq. (6.27), the fundamental angular frequency ω_o is 314 rad/s and the cut-off frequency is chosen equal to 10 rad/s.

6.4 Simulation and Experimental Validation

In order to evaluate the performances of the closed-loop control of the qZSI, both simulations and experimental tests were carried out. The simulations were performed using *PLECS* software. For the experimental validation, the test-bench shown in Fig. 6.9 was used, which is composed of:

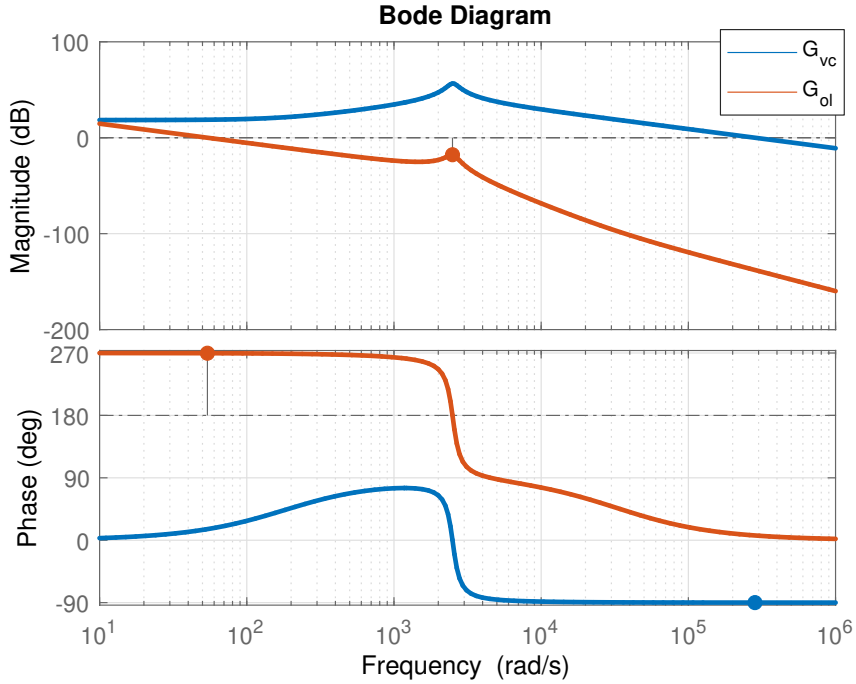

Figure 6.7: Bode plot of $G_{v_C}$with and without PI regulator.

- An FPGA Cyclone IV board, used to generate the control signals,
- A DSP 28379D control board, used to acquire voltage and current and to implement the control algorithm,
- A quasi-Z-network, composed by two inductors, two capacitors and a diode, whose parameters are reported in Table 6.1,
- A three-phase inverter realized with three PM75DSA120 IGBT module and three isolated gate-drivers,
- A variable three-phase load with a constant filter inductor L_L and a variable resistor R_L, as reported in Table 6.1,
- Voltage and current sensing and conditioning circuits.

6.4.1 Input Current Control

Fig. 6.10 compares the simulation and experimental results of the qZSI in case of the input current control. Fig. 6.10 (a) shows the simulated AC load phase current I_a and voltage V_a, the dc-link voltage V_{pn} and the inductor L_1 current I_{L_1} and Fig. 6.10 (b) shows the same quantities acquired on the experimental setup. For both simulations and experimental tests, similar conditions (input voltage, Z-network parameters, load) and same control parameters for the PI regulator were used. A step change from 1 to 2 A at 0.3 s has been imposed both in simulation and

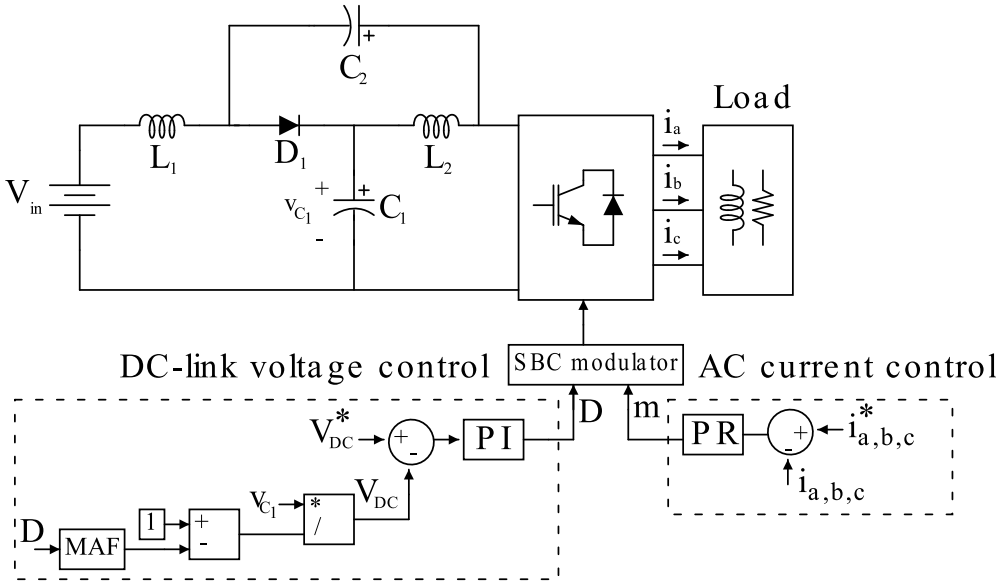

Figure 6.8: PR based output current control block diagram.

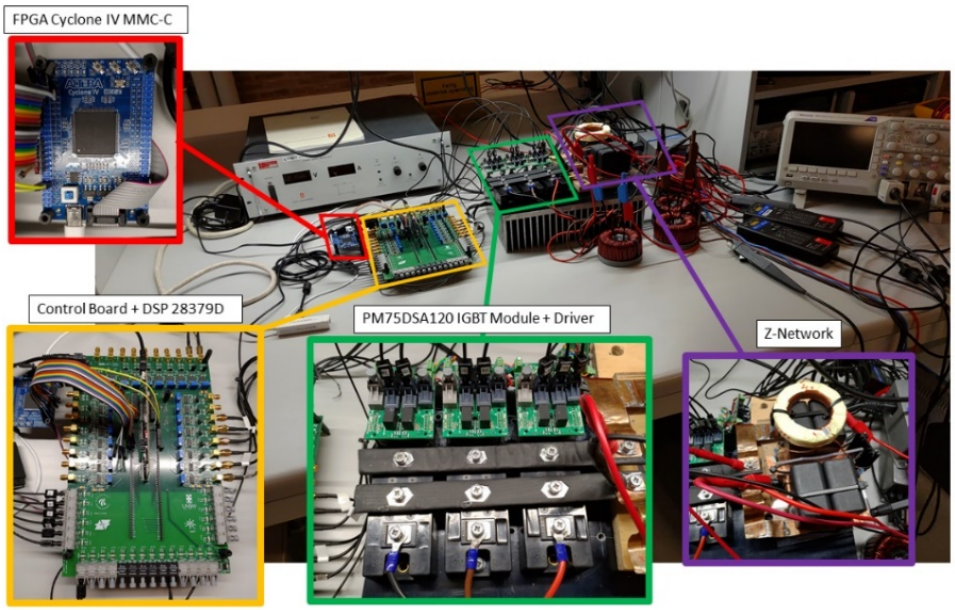

Figure 6.9: Quasi Z-source three-phase inverter test-bench.

experimental conditions. It can be noticed that almost identical dynamics in the simulation and in the experimental results are observed, with the rise time being 20 ms, the settling time being 40 ms and no overshoot.

6.4.2 PI based DC-link voltage and output current control

Figs. 6.11 and 6.12 benchmark the simulations and the experimental results of the qZSI under the step change of the controlled variables. Figs. 6.11 (a) and 6.12 (a) show the simulated ac load phase current I_a, the capacitor C_1 voltage V_{C_1}, the dc-link voltage V_{pn} and the inductor current I_{L_1} and Figs. 6.11 (b) and 6.12 (b) show the same quantities from the experimental setup in similar condition (input voltage, load) and the same control parameter for the PI regulators. In Fig. 6.11, a step change of the DC-link voltage reference from 100 to 120 V at 0.3 s is simulated, and the same step was imposed to the prototype. In Fig. 6.12, a step change of the output peak current from 2.5 to 3.5 A was given in both the simulated and experimental cases. It can be observed in Figs. 6.11 and 6.12 that both in steady state and in transient operation, stable performances are achieved, demonstrating the effectiveness of the closed-loop control. For the DC-link voltage step change, the rise time of 40 ms, the settling time of 70 ms and no overshoot were achieved. Regarding the output peak current step, the settling time of 50 ms and no overshoot were obtained.

6.4.3 Proportional Resonant (PR) based output current control

Fig. 6.13 shows the results for the qZSI with PR based controller. Fig. 6.13 (a) shows the ac load phase current I_a, the capacitor C_1 voltage V_{C_1}, the inductor L_1 current I_{L_1} and the dc-link voltage V_{pn} and Fig. 6.13 (b) shows a zoomed view of the transient change of the output current, with the red dashed line being the reference and the blue line being the ac load phase current I_a. Compared to the PI-based controller performances shown in Fig. 6.12, a faster response is achieved for the output peak current step, with the settling time being 20 ms and no overshoot. The experimental results, shown in Fig. 6.13 (c), validate the results of the simulation.

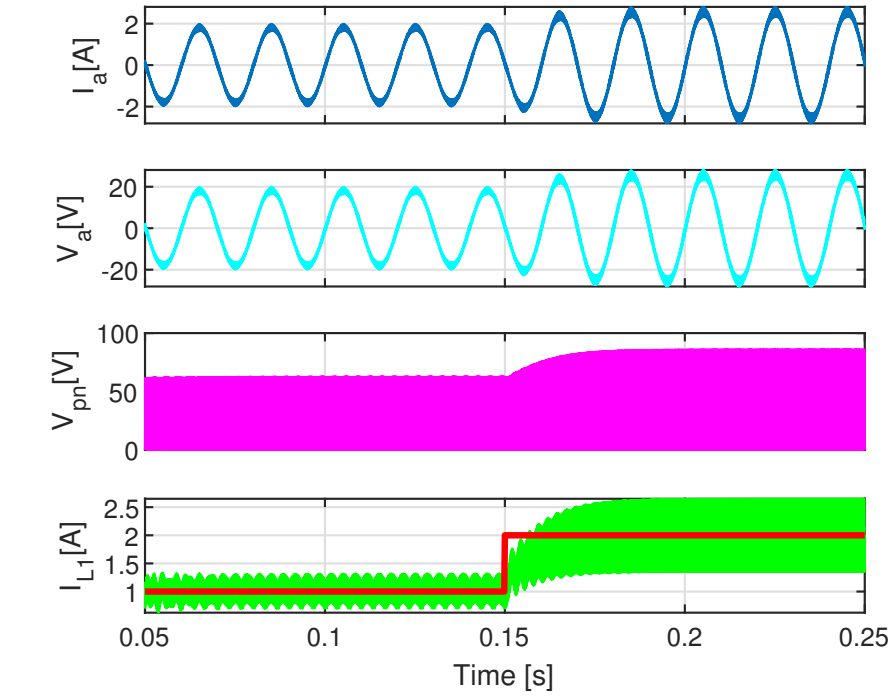

(a)

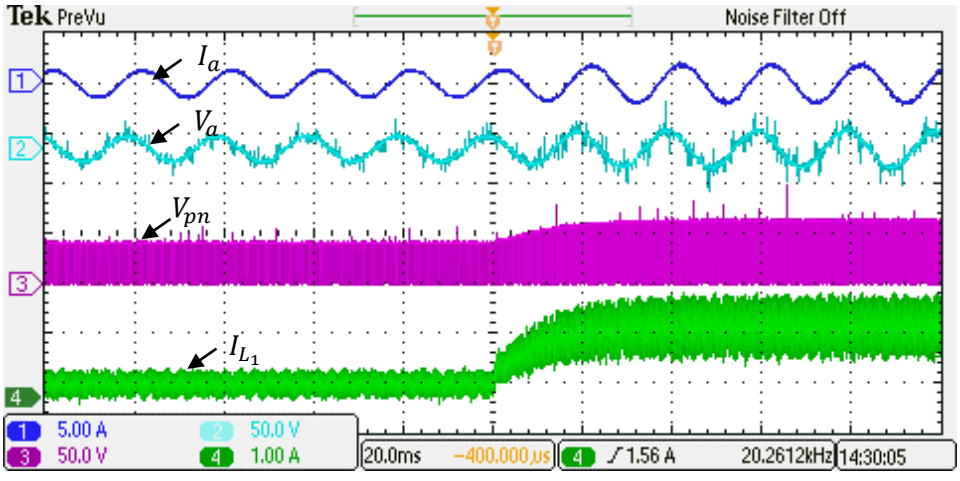

(b)

Figure 6.10: Response of the system to a step change of the reference input current. (a) Simulation results; (b) Experimental results.

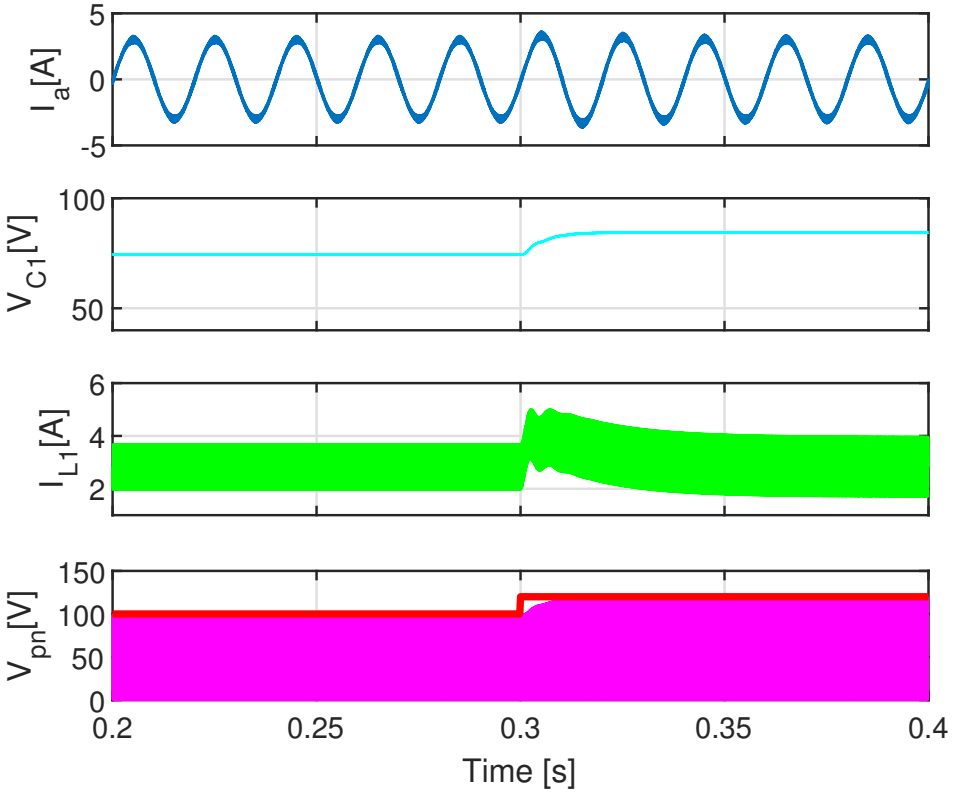

(a)

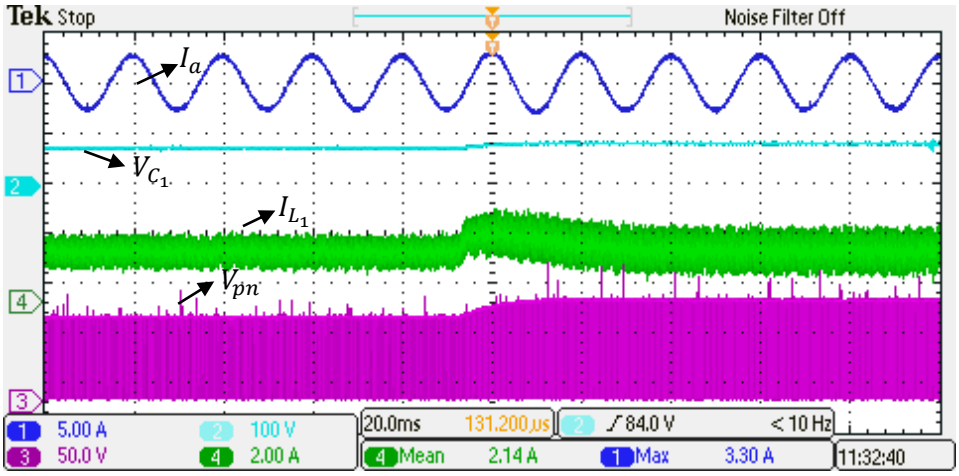

(b)

Figure 6.11: Response of the system to a step change of the reference DC-link voltage. (a) Simulation results; (b) Experimental results.

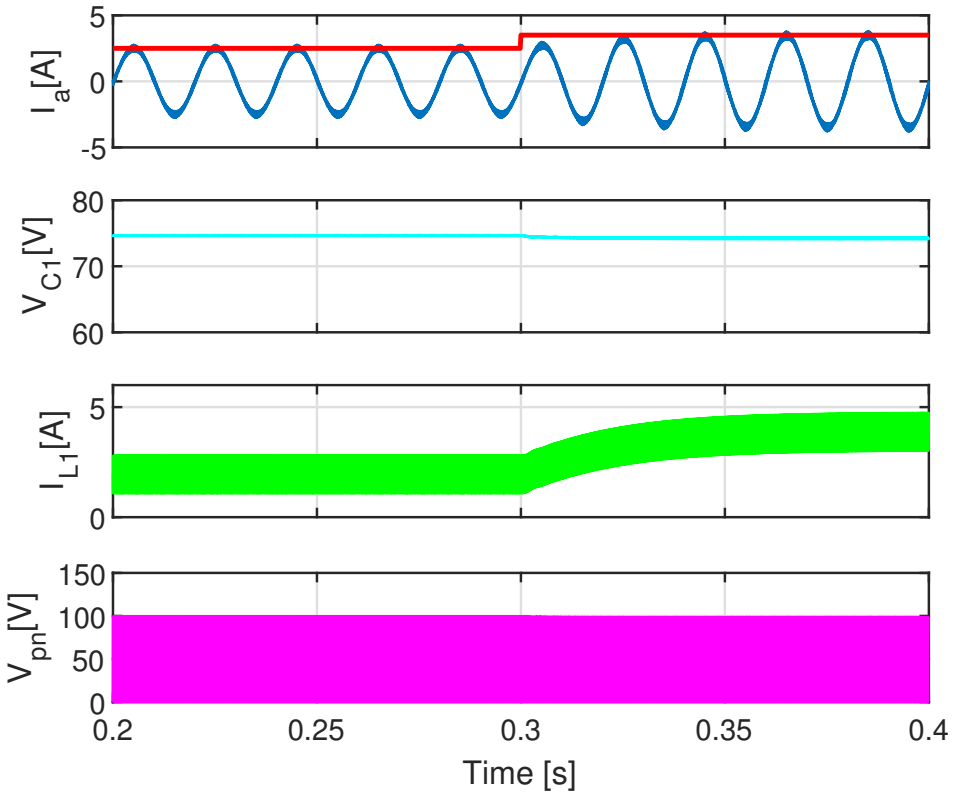

(a)

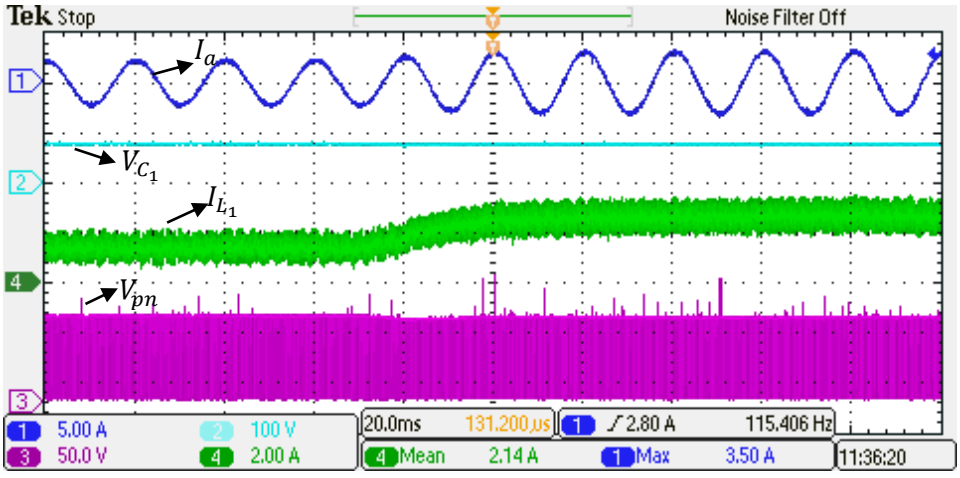

(b)

Figure 6.12: Response of the system to a step change of the reference output peak current. (a) Simulation results, (b) Experimental results.

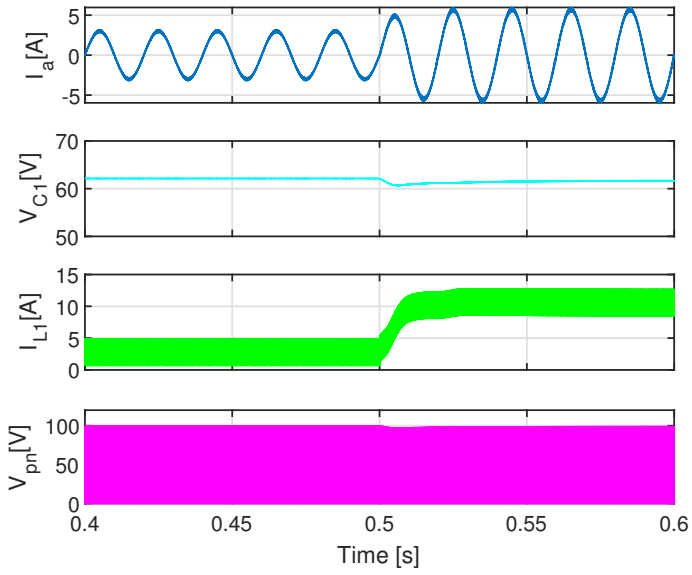

(a)

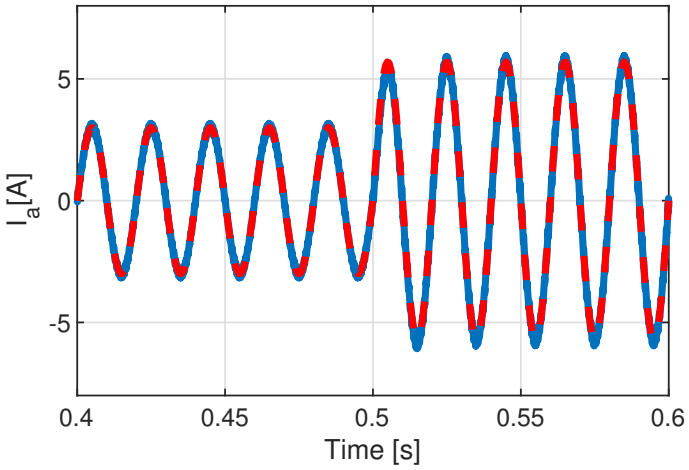

(b)

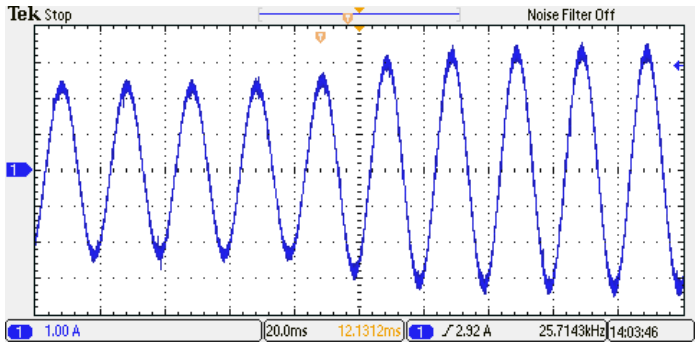

(c)

Figure 6.13: Response of the system to a step change of the reference output current. (a) Simulation results; (b) Reference current (red dashed line) and phase A current (blue line); (c) Experimental results

6.5 Conclusion

In this chapter, the experimental validation of different control schemes for the three-phase qZSI were presented. First, the small-signal model for the quasi-Z-network was obtained with the state-space averaging method. The small-signal transfer functions were used to design three control schemes: the first one for the input current control, the second one for PI based DC-link voltage and output current control and the third one for PI based DC-link voltage and PR based output current control. Simulation and experiment results have been provided to validate the controller design. The results show that the PR regulator achieves better results in terms of dynamic response, with the settling time for the output current step being 20 ms compared to 50 ms when PI regulator is used.

References

[1] J. M. Guerrero, L. Garcia De Vicuna, and J. Uceda, "Uninterruptible power supply systems provide protection," *IEEE Industrial Electronics Magazine*, vol. 1, no. 1, pp. 28–38, 2007, ISSN: 1941-0115. DOI: 10.1109/MIE.2007.357184.

[2] S. V. Giannoutsos and S. N. Manias, "A cascade control scheme for a grid connected Battery Energy Storage System (BESS)," in *Proc. of 2012 IEEE International Energy Conference and Exhibition (ENERGYCON)*, Sep. 2012, pp. 469–474. DOI: 10.1109/EnergyCon.2012.6348200.

[3] A. Hava, R. Kerkman, and T. Lipo, "Simple analytical and graphical methods for carrier-based PWM-VSI drives," *IEEE Transactions on Power Electronics*, vol. 14, no. 1, pp. 49–61, Jan. 1999, ISSN: 1941-0107. DOI: 10.1109/63.737592.

[4] Y. Liu, H. Abu-Rub, and B. Ge, "Z-Source\/Quasi-Z-Source Inverters: Derived Networks, Modulations, Controls, and Emerging Applications to Photovoltaic Conversion," *IEEE Industrial Electronics Magazine*, vol. 8, no. 4, pp. 32–44, Dec. 2014, ISSN: 1941-0115. DOI: 10.1109/MIE.2014.2307898.

[5] F. Z. Peng, "Z-source inverter," *IEEE Transactions on Industry Applications*, vol. 39, no. 2, pp. 504–510, Mar. 2003, ISSN: 1939-9367. DOI: 10.1109/TIA.2003.808920.

[6] M. Zhu, K. Yu, and F. L. Luo, "Switched Inductor Z-Source Inverter," *IEEE Transactions on Power Electronics*, vol. 25, no. 8, pp. 2150–2158, Aug. 2010, ISSN: 1941-0107. DOI: 10.1109/TPEL.2010.2046676.

[7] M.-K. Nguyen, Y.-C. Lim, and G.-B. Cho, "Switched-Inductor Quasi-Z-Source Inverter," *IEEE Transactions on Power Electronics*, vol. 26, no. 11, pp. 3183–3191, Nov. 2011, ISSN: 1941-0107. DOI: 10.1109/TPEL.2011.2141153.

[8] W. Qian, F. Z. Peng, and H. Cha, "Trans-Z-Source Inverters," *IEEE Transactions on Power Electronics*, vol. 26, no. 12, pp. 3453–3463, Dec. 2011, ISSN: 1941-0107. DOI: 10.1109/TPEL.2011.2122309.

[9] M. Adamowicz, R. Strzelecki, F. Z. Peng, J. Guzinski, and H. A. Rub, "New type LCCT-Z-source inverters," in *Proc. of the 2011 14th European Conference on Power Electronics and Applications*, Aug. 2011, pp. 1–10.

[10] J. Anderson and F. Peng, "Four quasi-Z-Source inverters," in *Proc. of 2008 IEEE Power Electronics Specialists Conference*, Jun. 2008, pp. 2743–2749. DOI: 10.1109/PESC.2008.4592360.

[11] Y. Li, S. Jiang, J. G. Cintron-Rivera, and F. Z. Peng, "Modeling and Control of Quasi-Z-Source Inverter for Distributed Generation Applications," *IEEE Transactions on Industrial Electronics*, vol. 60, no. 4, pp. 1532–1541, Apr. 2013, ISSN: 1557-9948. DOI: 10.1109/TIE.2012.2213551.

[12] X. Ding, Z. Qian, S. Yang, B. Cui, and F. Peng, "A direct DC-link boost voltage PID-like fuzzy control strategy in Z-source inverter," in *2008 IEEE Power Electronics Specialists Conference*, Jun. 2008, pp. 405–411. DOI: 10.1109/PESC.2008.4591963.

[13] Y. Tang, J. Wei, and S. Xie, "A new direct peak dc-link voltage control strategy of Z-source inverters," in *Proc. of 2010 Twenty-Fifth Annual IEEE Applied Power Electronics Conference and Exposition (APEC)*, Feb. 2010, pp. 867–872. DOI: 10.1109/APEC.2010.5433565.

[14] P. C. Loh, D. M. Vilathgamuwa, C. J. Gajanayake, Y. R. Lim, and C. W. Teo, "Transient Modeling and Analysis of Pulse-Width Modulated Z-Source Inverter," *IEEE Transactions on Power Electronics*, vol. 22, no. 2, pp. 498–507, Mar. 2007, ISSN: 1941-0107. DOI: 10.1109/TPEL.2006.889929.

[15] V. P. N and M. K. Kazimierczuk, "Small-Signal Modeling of Open-Loop PWM Z-Source Converter by Circuit-Averaging Technique," *IEEE Transactions on Power Electronics*, vol. 28, no. 3, pp. 1286–1296, Mar. 2013, ISSN: 1941-0107. DOI: 10.1109/TPEL.2012.2207437.

[16] J. Liu, J. Hu, and L. Xu, "Dynamic Modeling and Analysis of Z-Source Converter - Derivation of AC Small Signal Model and Design-Oriented Analysis," *IEEE Transactions on Power Electronics*, vol. 22, no. 5, pp. 1786–1796, Sep. 2007, ISSN: 1941-0107. DOI: 10.1109/TPEL.2007.904219.

[17] A. Ayad, M. Hashem, C. Hackl, and R. Kennel, "Proportional-resonant controller design for quasi-Z-source inverters with LC filters," in *Proc. of IECON 2016 - 42nd Annual Conference of the IEEE Industrial Electronics Society*, Oct. 2016, pp. 3558–3563. DOI: 10.1109/IECON.2016.7793282.

[18] F. Liu and X. Zha, "Research on control strategy combining pole-assignment and pr control in three-phase grid-connected inverter," in *Proc. of 2009 IEEE 6th International Power Electronics and Motion Control Conference*, May 2009, pp. 2170–2173. DOI: 10.1109/IPEMC.2009.5157761.

[19] M. Shen, J. Wang, A. Joseph, F. Z. Peng, L. Tolbert, and D. Adams, "Constant boost control of the Z-source inverter to minimize current ripple and voltage stress," *IEEE Transactions on Industry Applications*, vol. 42, no. 3, pp. 770–778, May 2006, ISSN: 1939-9367. DOI: 10.1109/TIA.2006.872927.

[20] F. Z. Peng, M. Shen, and Z. Qian, "Maximum boost control of the Z-source inverter," *IEEE Transactions on Power Electronics*, vol. 20, no. 4, pp. 833–838, Jul. 2005, ISSN: 1941-0107. DOI: 10.1109/TPEL.2005.850927.

[21] G. Schettino, N. Campagna, A. Di Tommaso, V. Castiglia, R. Miceli, and F. Viola, "Performance Comparison of modified modulation Techniques for Quasi-Z-Source Converters," in *Proc. of 2020 IEEE 20th Mediterranean Electrotechnical Conference (MELECON)*, Jun. 2020, pp. 41–45. DOI: 10.1109/MELECON48756.2020.9140513.

[22] U. S. Ali and V. Kamaraj, "A novel space vector PWM for Z-source inverter," in *Proc. of 2011 1st International Conference on Electrical Energy Systems*, Jan. 2011, pp. 82–85. DOI: 10.1109/ICEES.2011.5725307.

[23] Y. Tang, S. Xie, and J. Ding, "Pulsewidth Modulation of Z-Source Inverters With Minimum Inductor Current Ripple," *IEEE Transactions on Industrial Electronics*, vol. 61, no. 1, pp. 98–106, Jan. 2014, ISSN: 1557-9948. DOI: 10.1109/TIE.2013.2240632.

[24] G. Schettino, R. Miceli, N. Ganci, and F. Viola, "Comparative Analysis of Modified Modulation Scheme for Three-phase Voltage fed QZS Inverters," in *Proc. of 2019 8th International Conference on Renewable Energy Research and Applications (ICRERA)*, Nov. 2019, pp. 1069–1073. DOI: 10.1109/ICRERA47325.2019.8996992.

[25] Y. He, Y. Xu, and J. Chen, "Improved Space Vector Modulation of Quasi Z-Source Inverter to Suppress DC-Link Voltage Sag," *IEEE Access*, vol. 7, pp. 66 689–66 702, 2019, ISSN: 2169-3536. DOI: 10.1109/ACCESS.2019.2917765.

[26] Y. Liu, B. Ge, H. Abu-Rub, and F. Z. Peng, "Overview of Space Vector Modulations for Three-Phase Z-Source/Quasi-Z-Source Inverters," *IEEE Transactions on Power Electronics*, vol. 29, no. 4, pp. 2098–2108, Apr. 2014, ISSN: 1941-0107. DOI: 10.1109/TPEL.2013.2269539.

[27] R. Miceli, G. Schettino, F. Viola, F. Blaabjerg, and Y. Yang, "Modified Modulation Techniques for Quasi-Z-Source Cascaded H-Bridge Inverters," in *Proc. of IECON 2018 - 44th Annual Conference of the IEEE Industrial Electronics Society*, Oct. 2018, pp. 3743–3748. DOI: 10.1109/IECON.2018.8592848.

[28] A. Kuperman, "Proportional-Resonant Current Controllers Design Based on Desired Transient Performance," *IEEE Transactions on Power Electronics*, vol. 30, no. 10, pp. 5341–5345, Oct. 2015, ISSN: 1941-0107. DOI: 10.1109/TPEL.2015.2408053.

[29] R. Teodorescu, F. Blaabjerg, M. Liserre, and P. Loh, "Proportional-resonant controllers and filters for grid-connected voltage-source converters," *IEE Proceedings - Electric Power Applications*, vol. 153, no. 5, pp. 750–762, Sep. 2006, ISSN: 1350-2352. DOI: 10.1049/ip-epa:20060008.

Chapter 7

Quasi-Z-Source for Hybrid Energy Storage Management System

7.1 Introduction

Energy Storage Systems (ESS) are becoming a key element for many applications, from electric transportation to renewable energy distributed generations and storage facilities, as well as a lot of portable electronics. The main energy storage used in these applications are batteries, which may subject to high stresses due to the variable power requested e.g. by electric vehicles (EV), renewable energy sources, and also other applications. Batteries are high-energy-density devices, but they release the stored energy in a "slow" way. In the classical battery ESS, this can make the battery age faster, and then lead to poor performance in fast dynamics such as acceleration and regenerative breaking in EVs.

Accordingly, the Hybrid Energy Storage Systems (HESS) have been proposed, in which two or more energy sources are coupled to compensate each other for their disadvantages. A good match for the HESS is using a battery coupled with a bank of supercapacitors (SCs). The latter are classified as high power density and low energy density devices, behaving in a complementary way with respect to the batteries. Generally, the HESS is implemented using extra bi-directional DC/DC converters and a DC/AC converter. Obviously, this leads to an increase in the system cost, volume and control complexity. Using an impedance-source converter can possibly resolve some of the above-mentioned disadvantages. Impedance-source (Z-source) converters were first presented in [1], and since then several modulation techniques have been presented in [2]-[6]. Z-Source converters substitute the DC-link with an impedance network composed of capacitors and inductors and can be realized as a DC-DC-AC single-stage conversion. Among the topologies available in the literature, the quasi-Z-source (qZS) topology proposed in [7] and [8] presents

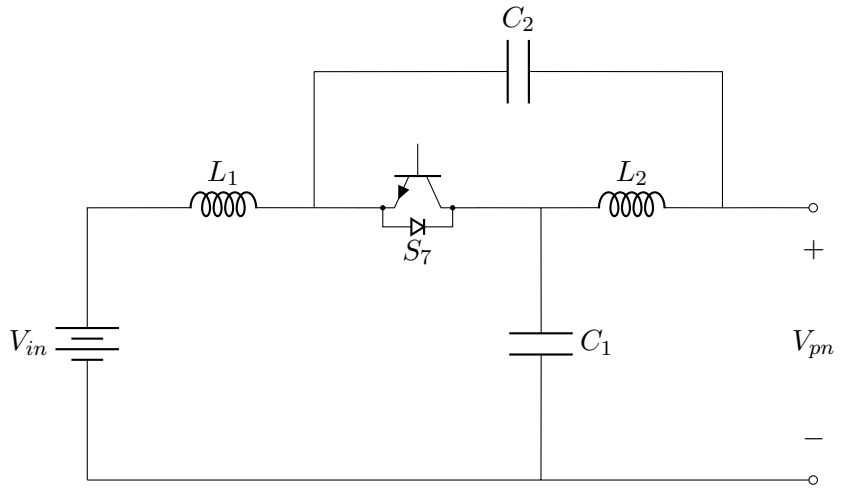

Figure 7.1: Basic qZS system diagram.

advantageous characteristics, like continuous input current, which fits well the HESS application. The basic qZS topology is shown in Fig. 7.1.

A couple of qZS-HESSs have been proposed. In [9], a qZS-HESS for an EV was proposed, integrating batteries and SCs in the Z-network. The SCs are connected at the input of the converter, while the batteries are connected in parallel to the capacitor C_2 of the basic topology. An enhanced frequency dividing coordinated control is used to share the power among the batteries and the SCs. In [10] and [11], a battery-supercapacitor qZS-HESS for an induction motor drive system was proposed. The battery is connected at the input and the SCs are connected in parallel to the capacitor C_1 of the basic topology shown in Fig. 7.1 using a bi-directional DC/DC converter. This system offers a greater power management capability at the cost of additional complexity due to the extra bi-directional DC/DC converter. In [12], an off-grid photovoltaic (PV) qZS battery-SCs HESS for a pumping system has been proposed. In this case, the PV panels are connected at the input of the Z-network. The battery is connected directly in parallel to C_1 of the basic topology and the SCs are connected in parallel to C_1 through a buck-boost converter. The switch S_7 can be replaced by a diode, but it still needs an additional power converter to handle the bi-directional power flow.

In this chapter, a new topology of qZS-HESS is investigated. The proposed system is shown in Fig. 7.2 and uses a battery at the input of the Z-network and a bank of SCs directly in parallel with C_2. The system features a single-stage DC-DC-AC conversion and also the integration of batteries and SCs without any additional converters. In Section 7.2, the small-signal model of the system is derived. The design procedure for the Z-network parameters and the battery and SCs voltage levels are provided in Section 7.3, and Section 7.4 analyses the operation of the system under different loading conditions.

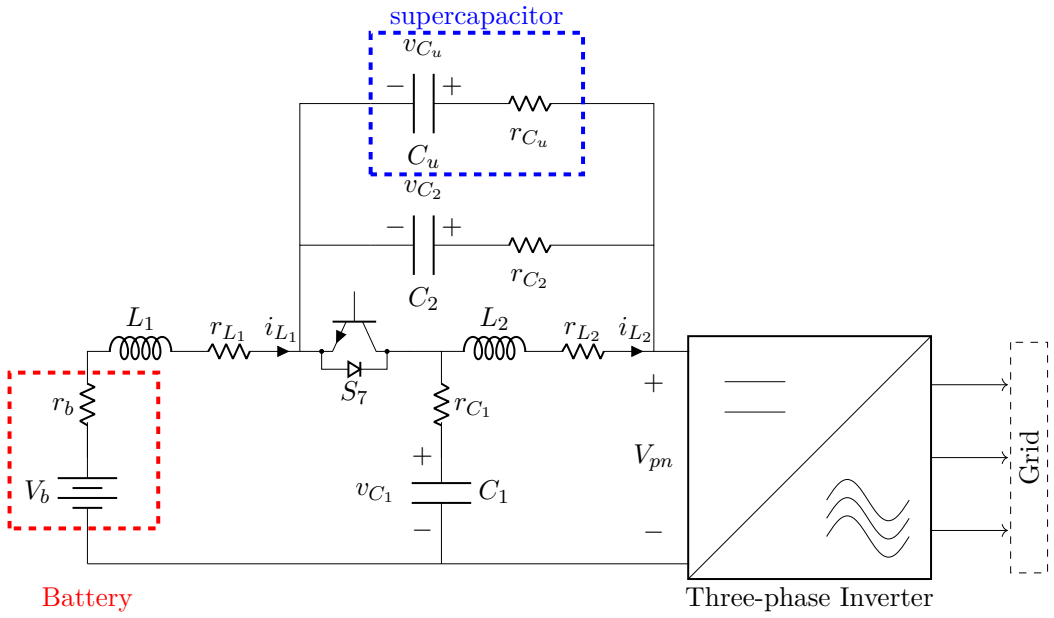

Figure 7.2: Proposed qZS-HESS topology.

7.2 System modeling

The overall schematic of the qZS-HESS is shown in Fig. 7.2. The blue dashed line depicts the battery that is modelled as a voltage source V_b and an internal resistance r_b. The red dashed line depicts the supercapacitor bank, modelled as a capacitor C_u and an internal resistance r_u. The diode in the classical Z-network is replaced with a controlled switch S_7 to allow bidirectional power flow. To design a controller for the system, a small-signal model is needed [13]. The circuit is divided into two sub-circuits: the Shoot-Through State (STS), as shown in Fig. 7.3, in which the output is short-circuited and S_7 is opened and the Non Shoot-Through State (NSTS), represented in Fig. 7.4, in which the inverter and load are replaced by a constant current source I_{pn} and S_7 is closed. The parasitics of both inductors L_1, L_2 and capacitors C_1, C_2 are considered, which are denoted by $r_{L_1}, r_{L"}, r_{C_1}, r_{C_2}$. The capacitor C_2 is chosen to have a parasitic resistance r_{C_2} which is much lower than that of the supercapacitor r_u, so that the high-frequency components are not supplied to the latter.

To apply the state-space averaging technique, a set of equations in the state-space form need to be found for each configuration of the circuit as

$$\begin{cases} \dot{x} = A \cdot x + B \cdot u \\ y = Q \cdot x \end{cases} \tag{7.1}$$

According to Fig. 7.3, the state-space equations can be written for the STS state, considering the state vector as $x = [i_{L_1}, i_{L_2}, v_{C_1}, v_{C_2}, v_{C_u}]^T$, input vector as $u =$

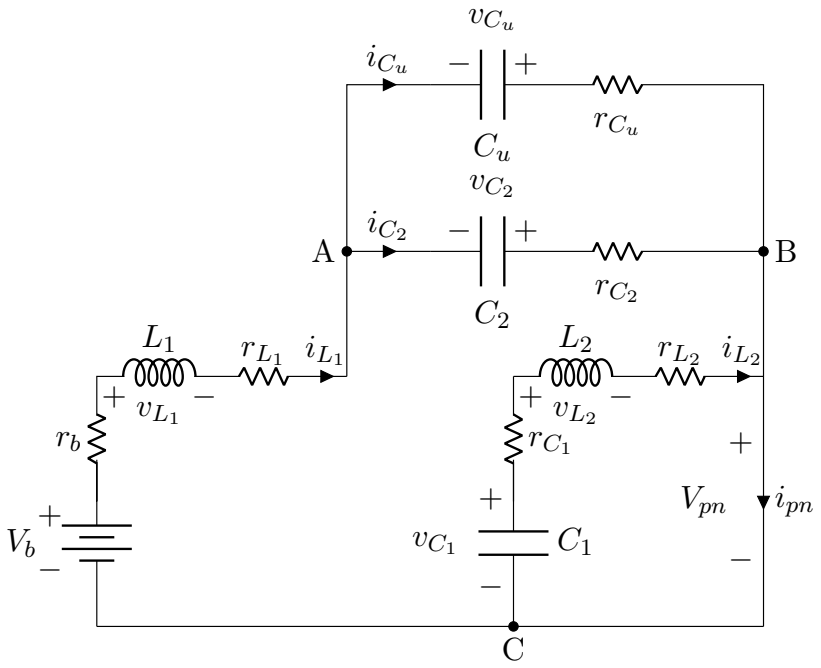

Figure 7.3: Equivalent circuit in the shoot-through state of the circuit in Fig. 7.2.

$[V_b, I_{pn}]^T$ and output vector as $y = x$:

$$\begin{cases} L_1 \frac{di_{L_1}}{dt} & = -\frac{r_u R_i + r_{C_2} R_i}{r_u + r_{C_2}} i_{L_1} + v_{C_2} + V_{ocv} \\ L_2 \frac{di_{L_2}}{dt} & = -\left(r_{C_1} + r_{L_2}\right) i_{L_2} + v_{C_1} \\ C_1 \frac{dv_{C_1}}{dt} & = -i_{L_2} \\ C_2 \frac{dv_{C_2}}{dt} & = -\frac{r_u}{r_u + r_{C_2}} i_{L_1} - \frac{1}{r_u + r_{C_2}} v_{C_2} + \frac{1}{r_u + r_{C_2}} v_{C_u} \\ C_u \frac{dv_{C_u}}{dt} & = -\frac{r_{C_2}}{r_{C_2} + r_u} i_{L_1} + \frac{1}{r_{C_2} + r_u} v_{C_2} - \frac{1}{r_{C_2} + r_u} v_{C_u} \end{cases} \tag{7.2}$$

In a matrix form, (7.2) can be written as

$$\begin{cases} \dot{x} = A_1 \cdot x + B_1 \cdot u \\ y = Q_1 \cdot x \end{cases} \tag{7.3}$$

where A_1, B_1 and Q_1 are

$$A_1 = \begin{bmatrix} -\frac{r_u R_i + r_{C_2} R_i}{L_1 (r_u + r_{C_2})} & 0 & 0 & \frac{1}{L_1} & 0 \\ 0 & -\frac{r_{C_1} + r_{L_2}}{L_2} & \frac{1}{L_2} & 0 & 0 \\ 0 & -\frac{1}{C_1} & 0 & 0 & 0 \\ -\frac{r_u}{C_2 (r_u + r_{C_2})} & 0 & 0 & \frac{-1}{C_2 (r_u + r_{C_2})} & \frac{1}{C_2 (r_u + r_{C_2})} \\ \frac{-r_{C_2}}{C_u (r_u + r_{C_2})} & 0 & 0 & \frac{1}{C_u (r_u + r_{C_2})} & \frac{-1}{C_u (r_u + r_{C_2})} \end{bmatrix}, \tag{7.4}$$

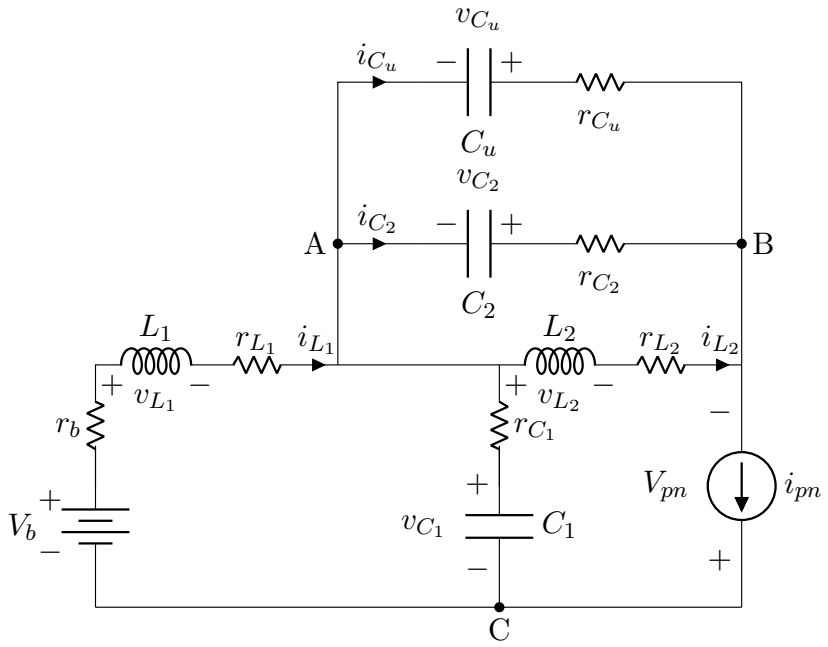

Figure 7.4: Equivalent circuit in the non-shoot-through state of the circuit in Fig. 7.2.

$$B_1 = \begin{bmatrix} \frac{1}{L_1} & 0 \\ 0 & 0 \\ 0 & 0 \\ 0 & 0 \\ 0 & 0 \end{bmatrix}, \qquad Q_1 = \begin{bmatrix} 1 & 0 & 0 & 0 & 0 \\ 0 & 1 & 0 & 0 & 0 \\ 0 & 0 & 1 & 0 & 0 \\ 0 & 0 & 0 & 1 & 0 \\ 0 & 0 & 0 & 0 & 1 \end{bmatrix} \tag{7.5}$$

For the NSTS, considering Fig. 7.4, the following state-space equations can be obtained

$$\begin{cases} L_1 \frac{di_{L_1}}{dt} & = -\left(R_i + r_{C_1} i_{L_1}\right) i_{L_1} - v_{C_1} + V_{ocv} + r_{C_1} i_{pn} \\ L_2 \frac{di_{L_2}}{dt} & = -\left(r_{L_2} - \frac{r_{C_2} r_u}{r_u + r_{C_2}}\right) i_{L_2} - \left(\frac{r_{C_2}}{r_u + r_{C_2}} + 1\right) v_{C_2} + \\ & \quad + \frac{r_{C_2}}{r_u + r_{C_2}} v_{C_u} - \frac{r_{C_2} r_u}{r_u + r_{C_2}} i_{pn} \\ C_1 \frac{di_{C_1}}{dt} & = i_{L_1} - i_{pn} \\ C_2 \frac{dv_{C_2}}{dt} & = \frac{r_u}{r_u + r_{C_2}} i_{L_2} - \frac{1}{r_u + r_{C_2}} v_{C_2} + \\ & \quad + \frac{1}{r_u + r_{C_2}} v_{C_u} - \frac{r_u}{r_u + r_{C_2}} i_{pn} \\ C_u \frac{dv_u}{dt} & = \frac{r_{C_2}}{r_u + r_{C_2}} i_{L_2} + \frac{1}{r_u + r_{C_2}} v_{C_2} + \\ & \quad - \frac{1}{r_u + r_{C_2}} v_{C_u} - \frac{r_{C_2}}{r_u + r_{C_2}} i_{pn} \end{cases} \tag{7.6}$$

In a matrix form (7.6) can be written as

$$\begin{cases} \dot{x} = A_2 \cdot x + B_2 \cdot u \\ y = Q_2 \cdot x \end{cases} \tag{7.7}$$

in which A_2, B_2 and Q_2 are

$$A_2 = \begin{bmatrix} -\frac{(R_i + r_{C_1})}{L_1} & 0 & -\frac{1}{L_1} & 0 & 0 \\ 0 & -\frac{1}{L_2}\left(r_{L_2} - \frac{r_{C_2} r_u}{r_u + r_{C_2}}\right) & 0 & -\frac{1}{L_2}\left(\frac{r_{C_2}}{r_u + r_{C_2}} + 1\right) & \frac{1}{L_2}\left(\frac{r_{C_2}}{r_u + r_{C_2}}\right) \\ \frac{1}{C_1} & 0 & 0 & 0 & 0 \\ 0 & \frac{1}{C_2}\left(\frac{r_u}{r_u + r_{C_2}}\right) & 0 & -\frac{1}{C_2}\left(\frac{1}{r_u + r_{C_2}}\right) & \frac{1}{C_2}\left(\frac{1}{r_u + r_{C_2}}\right) \\ 0 & \frac{1}{C_u}\left(\frac{r_{C_2}}{r_u + r_{C_2}}\right) & 0 & \frac{1}{C_u}\left(\frac{1}{r_u + r_{C_2}}\right) & \frac{1}{C_u}\left(\frac{-1}{r_u + r_{C_2}}\right) \end{bmatrix} \tag{7.8}$$

$$B_2 = \begin{bmatrix} \frac{1}{L_1} & r_{C_1} \\ 0 & -\frac{1}{L_2}\left(\frac{r_{C_2} r_u}{r_u + r_{C_2}}\right) \\ 0 & -\frac{1}{C_1} \\ 0 & -\frac{1}{C_2}\left(\frac{r_u}{r_u + r_{C_2}}\right) \\ 0 & \frac{1}{C_u}\left(\frac{-r_{C_2}}{r_u + r_{C_2}}\right) \end{bmatrix}, \qquad Q_2 = Q_1 \tag{7.9}$$

Subsequently, the average state-space model of the converter can be obtained by calculating the average matrix as

$$\begin{cases} A_{av} = & A_1 \cdot D + A_2 \cdot (1 - D) \\ B_{av} = & B_1 \cdot D + B_2 \cdot (1 - D) \\ Q_{av} = & Q_1 \cdot D + Q_2 \cdot \end{cases} \tag{7.10}$$

where D is the shoot-through duty cycle. The resultant average matrices can be given as

$$A_{av} = \begin{bmatrix} a_{11} & 0 & a_{13} & a_{14} & 0 \\ 0 & a_{22} & a_{23} & a_{24} & a_{25} \\ a_{31} & a_{32} & 0 & 0 & 0 \\ a_{41} & a_{42} & 0 & a_{44} & a_{45} \\ a_{51} & a_{52} & 0 & a_{54} & a_{55} \end{bmatrix} \tag{7.11}$$

$$B_{av} = \begin{bmatrix} \frac{1}{L_1} & -\frac{r_{C_1}}{L_1}(D-1) \\ 0 & \frac{r_{C_2} \cdot r_u}{L_2\left(r_{C_2} + r_u\right)}(D-1) \\ 0 & \frac{(D-1)}{C_1} \\ 0 & \frac{r_u}{C_2\left(r_{C_2} + r_u\right)}(D-1) \\ 0 & \frac{r_{C_2}}{C_u\left(r_{C_2} + r_u\right)}(D-1) \end{bmatrix}, \qquad Q_{av} = Q_1 = Q_2 \tag{7.12}$$

with:

$$
\begin{aligned}
a_{11} &= -\tfrac{R_i + r_{C_1} - D r_{C_1}}{L_1} & a_{13} &= \tfrac{D-1}{L_1} Z \\
a_{14} &= \tfrac{D}{L_1} & a_{22} &= (D-1) \cdot \left(r_{L_2} - \tfrac{r_{C_2} r_u}{r_{C_2} + r_u} \right) \tfrac{1}{L_2} - D \tfrac{r_{C_1} + r_{L_2}}{L_2} \\
a_{23} &= \tfrac{D}{L_2} & a_{24} &= \tfrac{\left(2 r_{C_2} + r_u\right)(D-1)}{L_2 \left(r_{C_2} + r_u \right)} \\
a_{25} &= \tfrac{r_{C_2}(1-D)}{L_2 \left(r_{C_2} + r_u \right)} & a_{31} &= \tfrac{1-D}{C_1} \\
a_{32} &= -\tfrac{D}{C_1} & a_{41} &= \tfrac{-D r_u}{C_2 \left(r_{C_2} + r_u \right)} \\
a_{42} &= -\tfrac{r_u (D-1)}{C_2 \left(r_{C_2} + r_u \right)} & a_{44} &= -\tfrac{1}{C_2 \left(r_{C_2} + r_u \right)} \\
a_{45} &= \tfrac{1}{C_2 \left(r_{C_2} + r_u \right)} & a_{51} &= \tfrac{-D r_{C_2}}{C_u \left(r_{C_2} + r_u \right)} \\
a_{52} &= -\tfrac{r_{C_2}(D-1)}{C_u \left(r_{C_2} + r_u \right)} & a_{54} &= \tfrac{1}{C_u \left(r_{C_2} + r_u \right)} \\
a_{55} &= -\tfrac{1}{C_u \left(r_{C_2} + r_u \right)}
\end{aligned}
$$

Finally, the average state-space model can be expressed as:

$$
\begin{cases}
\dot{x} = A_{av} x + B_{av} u \\
y = Q_{av} \cdot x
\end{cases}
\tag{7.13}
$$

The states vector steady-state values, denoted with capital letters as

$$
X = \begin{bmatrix} I_{L_1} & I_{L_2} & V_{C_1} & V_{C_2} & V_{C_u} \end{bmatrix}^T \tag{7.14}
$$

can also be calculated as

$$
X = -Q_{av} \cdot A_{av}^{-} 1 \cdot Bav \cdot u \tag{7.15}
$$

In order to verify the average model, a comparison with the switching circuit simulation was carried out, as shown in Fig. 7.5. The system parameters for this simulation are given in Table 7.1.

Considering a small-signal perturbation of the state variables and the input signals, defined as

$$
\tilde{x} = \begin{bmatrix} \tilde{i}_{L_1} & \tilde{i}_{L_2} & \tilde{v}_{C_1} & \tilde{v}_{C_2} & \tilde{v}_{C_u} \end{bmatrix}^T, \qquad \tilde{u} = \begin{bmatrix} \tilde{V}_b & \tilde{I}_{pn} \end{bmatrix}^T \tag{7.16}
$$

and the shoot-though duty cycle $\tilde{d}$, substituting those into (7.13) gives

$$
\dot{x} = A_{av} x + B_{av} u + \left[(A_1 - A_2) \cdot X + (B_1 - B_2) \cdot U \right] \cdot \tilde{d}. \tag{7.17}
$$

Let

$$
E = \left[(A_1 - A_2) \cdot X + (B_1 - B_2) \cdot U \right], \tag{7.18}
$$

$$
B_{sm} = \begin{bmatrix} B_{av} & E \end{bmatrix}, \qquad \tilde{u}_{sm} = \begin{bmatrix} \tilde{V}_{ocv} & \tilde{I}_{pn} & \tilde{d} \end{bmatrix} \tag{7.19}
$$

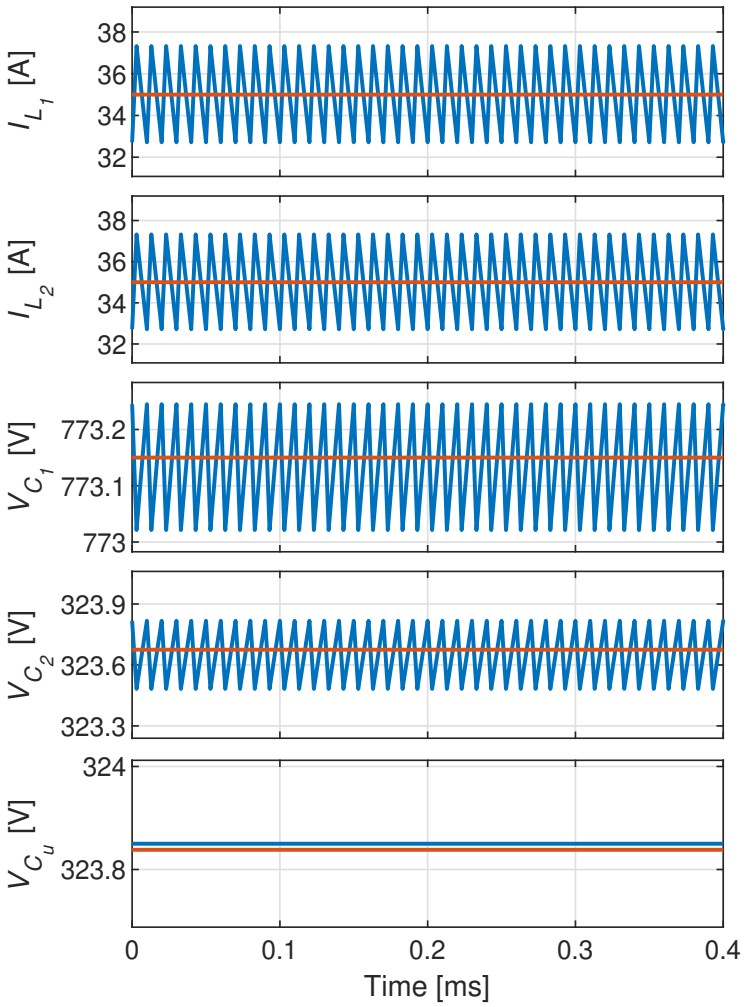

Figure 7.5: Comparison of the switching circuit model and the average model.

Table 7.1: System Parameters

Parameter	**Unit**	**Symbol**	**Value**
Battery Voltage	(v)	V_b	450
Battery internal resistance	$m\Omega$	r_b	20
Inductance	(μH)	L_1, L_2	5000
Inductor ESR	(Ω)	r_{L_1}, r_{L_2}	0.15
Capacitance	(μF)	C_1, C_2	4700
Capacitor ESR	(mΩ)	r_{C_1}, r_{C_2}	10
Supercapacitor	F	C_u	2
Supercapacitor ESR	Ω	r_u	0.5
Output current	(A)	I_{pn}	20
Duty Cycle	(-)	D	0.3
Switching Frequency	(kHz)	f_{sw}	10

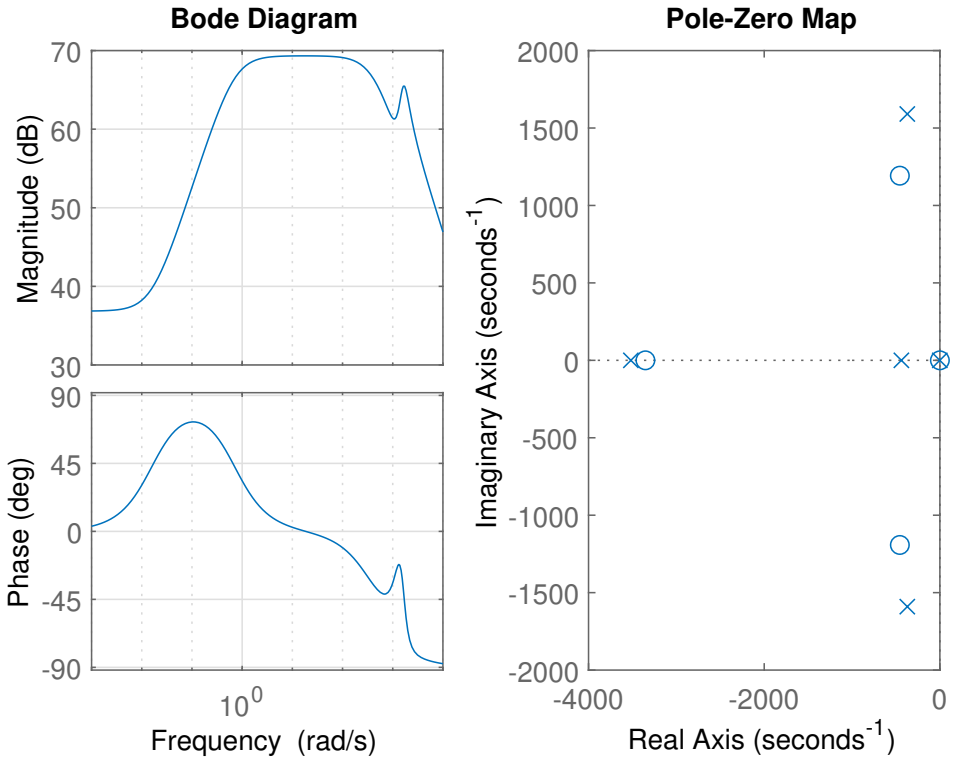

Figure 7.6: Bode diagram and pole-zero map of the duty cycle-to-inductor current transfer function using the parameters in Table 7.1.

With the previous assumptions, eq. (7.17) can be rewritten as

$$\begin{cases} \dot{\tilde{x}} = A_{av}\tilde{x} + B_{sm}\tilde{u}_{sm} \\ \dot{\tilde{y}} = Q_{av}\tilde{x} \end{cases} \tag{7.20}$$

The small-signal duty-to-output transfer functions can be obtained using Matlab/Simulink by implementing the following

$$y_d = Q_{av} I \left(s \cdot I - A_{av}\right)^{-1} \cdot E. \tag{7.21}$$

To control the battery current i_b which coincides with the inductor current i_{L_1}, the transfer function to be considered is:

$$G_{i_b d}(s) = \frac{i_b(s)}{d(s)} = \frac{2.2e06s^4 + 9.9e09s^3 + 1.2e13s^2 + 1.2e16s + 2e14}{s^5 + 4819s^4 + 7.8e06s^3 + 1.2e10s^2 + 6.1e12s + 2.8e12}. \tag{7.22}$$

Fig. 7.6 shows the Bode diagram and pole-zero map of the above transfer function, which will be used to design and tune the qZSI controller.

7.3 System Design

7.3.1 Power Balance

For the proposed system, neglecting all power losses and considering the average power over a switching cycle, the following power balance can be obtained as

$$\bar{P}_b + \bar{P}_u = \bar{P}_{pn} \tag{7.23}$$

where $\bar{P}_b$ is the average power from the battery, $\bar{P}_{uc}$ is the average power supplied by the SCs and $\bar{P}_{pn}$ is the average power on the DC-link. Eq. (7.23) can be rewritten as

$$\bar{I}_b\bar{V}_b + \bar{I}_u\bar{V}_u = \bar{I}_{pn}\bar{V}_{pn} \tag{7.24}$$

$\bar{V}_u$ and $\bar{V}_{pn}$ can then be expressed as functions of the duty cycle D:

$$\begin{cases} \bar{V}_u & = \frac{D}{1-2D}\bar{V}_b \\ \bar{V}_{pn} & = \hat{V}_{pn}(1-D) + 0 \cdot D = \frac{1-D}{1-2D}\bar{V}_b. \end{cases} \tag{7.25}$$

Accordingly, it can be obtained that

$$\bar{I}_b + \bar{I}_u\frac{D}{1-2D} = \bar{I}_{pn}\frac{1-D}{1-2D} \tag{7.26}$$

which implies that the battery average current can be regulated using the duty cycle. The DC-link current will be regulated by using the modulation index m. The SCs will automatically supply the rest of the current.

7.3.2 Battery and DC-Link Voltages

The system in Fig. 7.2 will work as a support interface to the grid, supplying or absorbing current according to the grid conditions. The nominal power of the system is $P_n = 10\ kW$, the nominal RMS grid voltage is $V_g = 230\ V$.
For a three-phase inverter, the first harmonic will have an amplitude $\hat{V}_{a(1)}$ given as

$$\hat{V}_{a(1)} = \frac{\hat{V}_{pn} \cdot m}{2}. \tag{7.27}$$

The DC-link voltage $\hat{V}_{pn}$ can be calculated with the same equation as in the classical qZSI topology, if we neglect all the power losses:

$$\hat{V}_{pn} = \frac{1}{1-2D}V_b. \tag{7.28}$$

Based on the modulation technique used to control the qZSI, the modulation index m and the duty cycle D have different relationship and limits. In this case, the *Simple*

Boost Control (SBC) method [1] is used. The relationship between the modulation index and the duty cycle is:

$$m_{max} \leq 1 - D. \tag{7.29}$$

Combining Eqs. (7.27)-(7.29), we can obtain:

$$\hat{V}_{a(1)} = \frac{1}{1-2D}\frac{(1-D)}{2}V_b \tag{7.30}$$

which indicates that the nominal battery voltage can be obtained, by fixing the duty cycle D. For this system, $D = 0.3$ was chosen. To have a first harmonic amplitude equal to the grid voltage amplitude, the battery voltage should be:

$$V_b = V_g 2\sqrt{2}\frac{(1-2D)}{(1-D)} = 370\ V.$$

The steady-state voltage on the SCs will become:

$$V_{C_u} = \frac{D}{1-2D}V_b = 277\ V.$$

To effectively use the SCs as an energy buffer, the voltage will be maintained between 280 V to 300 V.

7.3.3 Z-Network Parameters

The inductance for the Z-network can be calculated considering that during the STS the current increases linearly as

$$V_L = L_1\frac{\Delta i_L}{D}f_{sw}. \tag{7.31}$$

During the STS, the voltage applied to the inductor is:

$$V_L = V_b - (-V_{C_2}) \tag{7.32}$$

$$V_{C_2} = \frac{D}{1-2D}V_b \tag{7.33}$$

$$V_L = V_b + \frac{D}{1-2D}V_b = \frac{1-D}{1-2D}V_b. \tag{7.34}$$

Substituting (7.31) into (7.34) and rearranging (7.34), we have

$$L_1 \geq \frac{D-D^2}{1-2D}\frac{V_b}{\Delta i_L f_{sw}}. \tag{7.35}$$

Assuming that the desired value of the current ripple is Δi_L, the inductance value can be calculated. Using the parameters given in Table 7.1 and a maximum current ripple of $\Delta i_L = 3\,A$, the designed inductor will be:

$$L_1 \geq 4725\ \mu H.$$

Thus, $L_1 = L_2 = 5000\,\mu H$ is selected in the system.

The capacitor value can be calculated considering that during the NSTS, the capacitors C_1 and C_2 are in series and they limit the voltage ripple on the DC-link. The capacitors also supply a portion of the current, I_{pn}.

$$I_{pn} = \frac{C_1}{2} \frac{\Delta\left(V_{C_1} + V_{C_2}\right)}{(1-D)} f_{sw}. \tag{7.36}$$

Assuming that the desired value of the voltage ripple is $\Delta\left(V_{C_1} + V_{C_2}\right)$, the capacitance can be calculated. Using the parameters in Table 7.1 and a maximum voltage ripple of $\Delta\left(V_{C_1} + V_{C_2}\right) = 0.7\,V$, the capacitance is determined as

$$C_1 = C_2 = I_{pn} \frac{2(1-D)}{\Delta\left(V_{C_1} + V_{C_2}\right) f_{sw}} \tag{7.37}$$

$$C_1 \geq 4000\ \mu F.$$

Accordingly, $C_1 = C_2 = 4700\,\mu F$ is selected.

7.4 Simulation Results

The system can work in different modes, depending on the conditions of the battery, the SCs and the grid. Fig. 7.7 shows several modes of operation that are explained below. The modes are identified with the corresponding number in Fig. 7.7 (c).

7.4.1 Battery Discharging

1. **Battery to SCs:** Considering Fig. 7.7, from $t = 0$ to $t = 0.1$ s, the power requested by the grid is zero (blue curve). The battery power (red curve) is set to 10 kW and it is used to recharge the SCs (negative power, yellow curve), raising the SCs voltage, as shown in Fig. 7.7.

2. **Battery to Grid:** From $t = 0.1$ to $t = 0.2$ s, the grid requests the nominal power of 10 kW. All of the battery power is supplied to the grid, and the SCs keep the same voltage.

3. **Battery and SCs to Grid:** From $t = 0.2$ to $t = 0.3$ s, the grid suddenly requests more power, but the battery is already supplying the maximum power. The SCs will start to discharge, so that the battery power plus the SCs power equals to the grid power.

4. **Battery to SCs and grid:** From $t = 0.3$ to $t = 0.4$ s, the grid requests lower power than the battery nominal power. The difference can be used to recharge

the SCs.

5. **Battery and grid to SCs:** From $t = 0.4$ to $t = 0.5$ s, the grid requests negative power, for example when renewable sources produce more energy than the loads require. Both the grid and the battery supply power to the SCs and recharging them.

7.4.2 Battery Recharging

6. **SCs to Battery:** From $t = 0.5$ to $t = 0.6$ s, the grid requests no power. The battery can be set in recharge mode, recovering energy from the SCs.

7. **SCs and Grid to Battery:** From $t = 0.6$ to $t = 0.7$ s, the grid requests negative power. The battery is recharged by both the SCs and the grid.

8. **Grid to Battery:** From $t = 0.7$ to $t = 0.8$ s, the grid requests more negative power. All the grid power is used to recharge the battery, while the SCs are kept at the same voltage.

9. **Grid to Battery and SCs:** From $t = 0.8$ to $t = 0.9$ s, the grid supplies more power than the nominal recharge power of the battery. The difference can be used to recharge the SCs.

7.5 Conclusion

In this chapter, a new topology for the qZS-HESS has been presented. The proposed topology uses a battery and a bank of supercapacitors as energy sources. The system features a single-stage DC-DC-AC conversion and the integration of battery and SCs without additional converters. The system modeling and design have been considered. The power balance between the battery, the SCs and the grid was achieved by controlling the shoot-through duty cycle D and the modulation index m. The operation of the system under several different conditions were simulated using PLECS. The simulation results confirm the correct operation of the system and the possibility to use this topology in HESS applications. Future works will address in more details the control of the system and the smart management of the energy sources, considering the voltage limits for the supercapacitors and the battery state of charge.

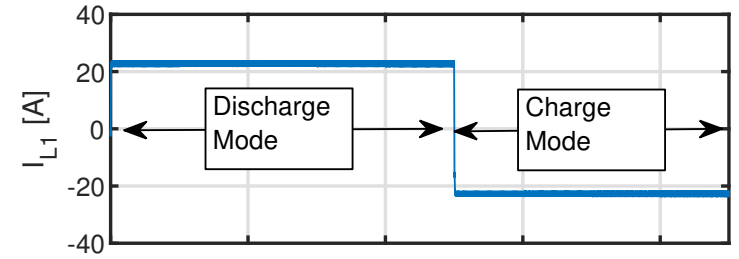

(a)

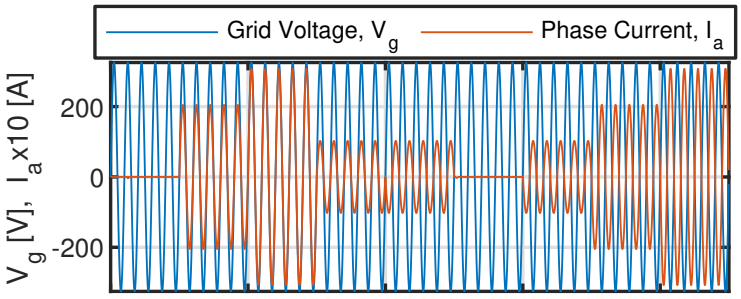

(b)

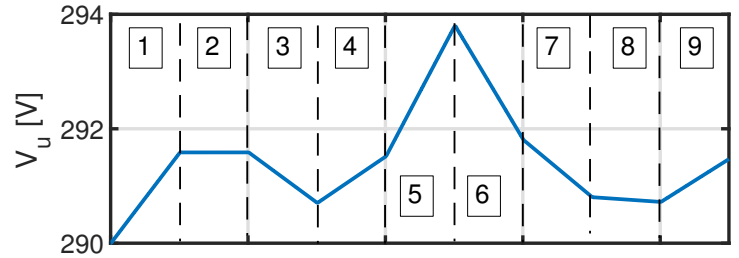

(c)

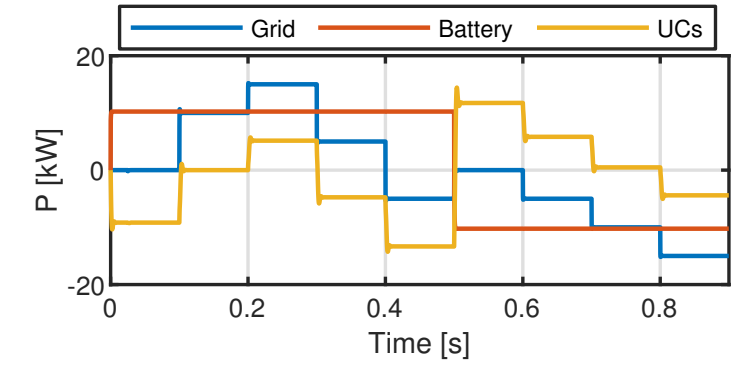

(d)

Figure 7.7: Simulation results of the system under different operation modes. (a) Inductor (battery) current (b) Grid voltage and phase current (c) Ultracapacitor voltage and modes of operation identifier (d) Power trends.

References

[1] F. Z. Peng, "Z-source inverters," *Wiley Encyclopedia of Electrical and Electronics Engineering*, pp. 1–11, 1999.

[2] F. Z. Peng, M. Shen, and Z. Qian, "Maximum boost control of the z-source inverter," *IEEE Transactions on Power Electronics*, vol. 20, no. 4, pp. 833–838, Jul. 2005. DOI: 10.1109/TPEL.2005.850927.

[3] M. Shen, J. Wang, A. Joseph, F. Z. Peng, L. M. Tolbert, and D. J. Adams, "Maximum constant boost control of the z-source inverter," in *Conference Record of the 2004 IEEE Industry Applications Conference, 2004. 39th IAS Annual Meeting.*, vol. 1, Oct. 2004. DOI: 10.1109/IAS.2004.1348400.

[4] A. Abdelhakim, P. Davari, F. Blaabjerg, and P. Mattavelli, "Switching loss reduction in the three-phase quasi-z-source inverters utilizing modified space vector modulation strategies," *IEEE Transactions on Power Electronics*, vol. 33, no. 5, pp. 4045–4060, May 2018. DOI: 10.1109/TPEL.2017.2721402.

[5] R. Miceli, G. Schettino, F. Viola, F. Blaabjerg, and Y. Yang, "Modified modulation techniques for quasi-z-source cascaded h-bridge inverters," in *IECON 2018 - 44th Annual Conference of the IEEE Industrial Electronics Society*, Oct. 2018, pp. 3743–3748. DOI: 10.1109/IECON.2018.8592848.

[6] Y. Liu, B. Ge, F. J. T. E. Ferreira, A. T. de Almeida, and H. Abu-Rub, "Modeling and svpwm control of quasi-z-source inverter," in *11th International Conference on Electrical Power Quality and Utilisation*, Oct. 2011, pp. 1–6. DOI: 10.1109/EPQU.2011.6128914.

[7] J. Anderson and F. Z. Peng, "Four quasi-z-source inverters," in *2008 IEEE Power Electronics Specialists Conference*, Jun. 2008, pp. 2743–2749. DOI: 10.1109/PESC.2008.4592360.

[8] Y. Li, J. Anderson, F. Z. Peng, and D. Liu, "Quasi-z-source inverter for photovoltaic power generation systems," in *2009 Twenty-Fourth Annual IEEE Applied Power Electronics Conference and Exposition*, Feb. 2009, pp. 918–924. DOI: 10.1109/APEC.2009.4802772.

[9] S. Hu, Z. Liang, D. Fan, and X. He, "Hybrid ultracapacitor/battery energy storage system based on quasi-z-source topology and enhanced frequency dividing coordinated control for EV," *IEEE Transactions on Power Electronics*, vol. 31, no. 11, pp. 7598–7610, Nov. 2016, ISSN: 0885-8993.

[10] M. Muhammad, Z. Rasin, and A. Jidin, "Bidirectional quasi-z-source inverter with hybrid energy storage for im drive system," in *2019 IEEE 9th Symposium on Computer Applications Industrial Electronics (ISCAIE)*, Apr. 2019, pp. 75–80. DOI: 10.1109/ISCAIE.2019.8743869.

[11] M. Muhammad, Z. Rasin, A. Jidin, A. M. Razali, and N. A. Yusoff, "Investigation on quasi-z-source inverter with hybrid energy storage for pmsm drive system," in *5th IET International Conference on Clean Energy and Technology (CEAT2018)*, Jan. 2018, pp. 1–7. DOI: 10.1049/cp.2018.1349.

[12] S. E. Boukebbous, D. Kerdoun, N. Benbaha, H. Ammar, and A. Bouchakour, "Performance enhancement of grid-off photovoltaic pumping system-quasi z source inverter by hybrid battery-supercapacitor energy storage," in *2018 6th International Renewable and Sustainable Energy Conference (IRSEC)*, Dec. 2018, pp. 1–6. DOI: 10.1109/IRSEC.2018.8702898.

[13] Y. Li and F. Z. Peng, "Ac small signal modeling, analysis and control of quasi-z-source converter," in *Proceedings of The 7th International Power Electronics and Motion Control Conference*, vol. 3, Jun. 2012, pp. 1848–1854. DOI: 10.1109/IPEMC.2012.6259119.

Chapter 8

Quasi-Z-Source Based Inductive Power Transfer

8.1 Introduction

The increasing need to reduce pollutant emissions has led, in recent years, to the rapid spread of Electric Vehicles (EVs) [1]. Thanks to high-performance electric motors and the use of "clean" energy sources for recharging EVs, the contribution of polluting gases caused by transportation could be drastically reduced. One of the most discussed topics in this area is the EVs charging mode [2]-[5]. Two different connection methods have been proposed for recharging the EVs: the classic one, which provides a cable connection (conductive or wired charging) [6], and the innovative one involving wireless power transmission (wireless charging)[7]. Wireless Power Transfer (WPT) systems use the electric field (Capacitive Power Transfer, CPT) [8]-[10] or magnetic field (Inductive Power Transfer, IPT) [11] to transfer power from a primary side to a secondary side. By removing the connection cable between the charging station and EV, the electrocution hazard is eliminated, the risk of short circuits and sparks is reduced, contact resistors are eliminated and the possibility of contact failures or breakage is then eliminated. Moreover, WPT systems are also unaffected by dirt, dust, and water. Thus, compared to wired systems, improved reliability, safety and less environmental impact are achieved [12].

IPT systems have been preferred over CPT systems and have been developed and commercialized rapidly [13], [14]. The general architecture of an IPT system for EV charging applications is shown in Figure 8.1 [15]-[16]. It consists of two sides, respectively, the transmitter side located in the charging station and the receiving side located in the vehicle. The charging station can be supplied by the grid, as shown in Fig. 8.1, or by a DC power source such as Photovoltaic (PV) or Fuel Cells (FC). A detailed schematic of a typical IPT system is shown in Fig. 8.2 (a). The input voltage is usually regulated by a boost DC/DC converter. To increase the coupling between the two coils, the DC/AC in the primary side and the AC/DC converter in

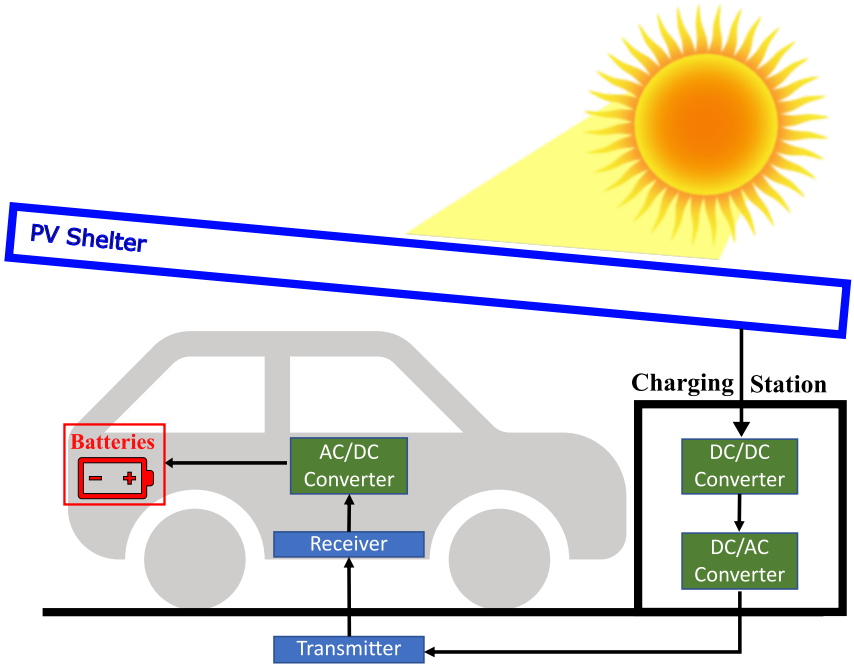

Figure 8.1: IPT system architecture for EV charging applications.

the secondary side must work at high frequencies, in the order of hundreds of kHz. On the other hand, to keep the system efficient, switching losses limit the operating frequencies [17].

In order to overcome this problem, a second possible configuration has been proposed using Impedance Source (Z-Source) converters [18]-[25]. The main advantage of using these converters is the single-stage DC/AC conversion with a smaller number of switches [26]. In fact, it is possible to obtain the DC voltage boost and AC conversion simultaneously [27]-[28]. Moreover, the input impedance network (Z-network) ensures short circuit protection.

Another key element in IPT systems is the battery charging method [29]-[30]. Lithium-ion (Li-ion) batteries are currently the most widely used in EV storage systems due to their high energy density [31]-[32]. The best Li-ion batteries charging method, which ensures efficient charging and long service life, is the constant current-constant voltage (CC/CV) [12] method. Different solutions have been adopted for the CC/CV charge implementation [33]. In [34], two different control loop are used to achieve the CC mode and the CV mode, measuring the battery voltage and current and controlling only the primary side inverter. In [35], a load identification approach is used to avoid the battery voltage and current sensing and the data communication between the primary and secondary side. In [36], the CC and CV modes are implemented using a reconfigurable IPT system. In [37], a decoupled control method is proposed, which enhances the transient response and the overall system performance compared to the traditional closed-loop control. It should be noted that

the articles reviewed so far are all preferred for the classic IPT configuration, while there are still few works that consider the implementation of the CC/CV charging mode on Z-source converters-based IPT systems.

In [20] and [24], a Z-source converter with integrated Power Factor Correction (PFC) and load regulation for sinusoidal charging of batteries is proposed. The main problem of the Z-source converter is the discontinuous input current, which is not very suitable for renewable energy sources like PV and FCs. To achieve a continuous input current, the quasi-Z-source (qZS) converter is used in [18], [25]. In [18], the performance comparison of the qZS and Z-source converters is carried out. In [25], the sliding mode predictive control is applied to the qZS converter, but the charging process of batteries is not taken into account. In [19], the qZS converter is controlled in the CC/CV mode to recharge the batteries, using two separated control schemes and a buck converter in the receiver side.

With the above, the main motivation of this chapter is to investigate impedance source converters in IPT systems for CC/CV charging of EV batteries. Among the different Z-source converter topologies, the qZS was chosen because of the continuous input current feature. The detailed schematic of the proposed qZS based inductive power transfer system (qZS-IPT) is shown in Fig. 8.2 (b). Differently from the one proposed in [18], [19], [25], the Z-network diode is replaced by a switch to ensure the Continuous Conduction Mode (CCM) operation. The inductive coupling is realized by means of the series-series (SS) topology, which features a load independent characteristic during the CC mode. To achieve the CC/CV charging method, the control acts on the primary side qZS converter and with a proper modulation scheme, the converter can increase (boost mode) or decrease (buck mode) the voltage on the primary side. To summarize, the main contributions of this work, compared to what is found in the literature, are underlined in the following:

- Unlike [19], the receiver side buck converter is removed to keep the design as simple as possible,
- Use of a single control scheme for the implementation of CC/CV phases, achieving a smooth transition between the two modes,
- Implementation of an innovative modulation scheme that allows the qZS converter to easily change between boost and buck modes.

This chapter has been divided into five sections. Section II describes the operating principle of the system and the basic theoretical analysis. Section III presents the CC/CV charge implementation. Section IV describes the system operation with simulations in PLECS. A small-scale prototype is presented in Section V and the acquired waveforms and recorded CC/CV charging curves are provided, validating the proposed system with experimental results.

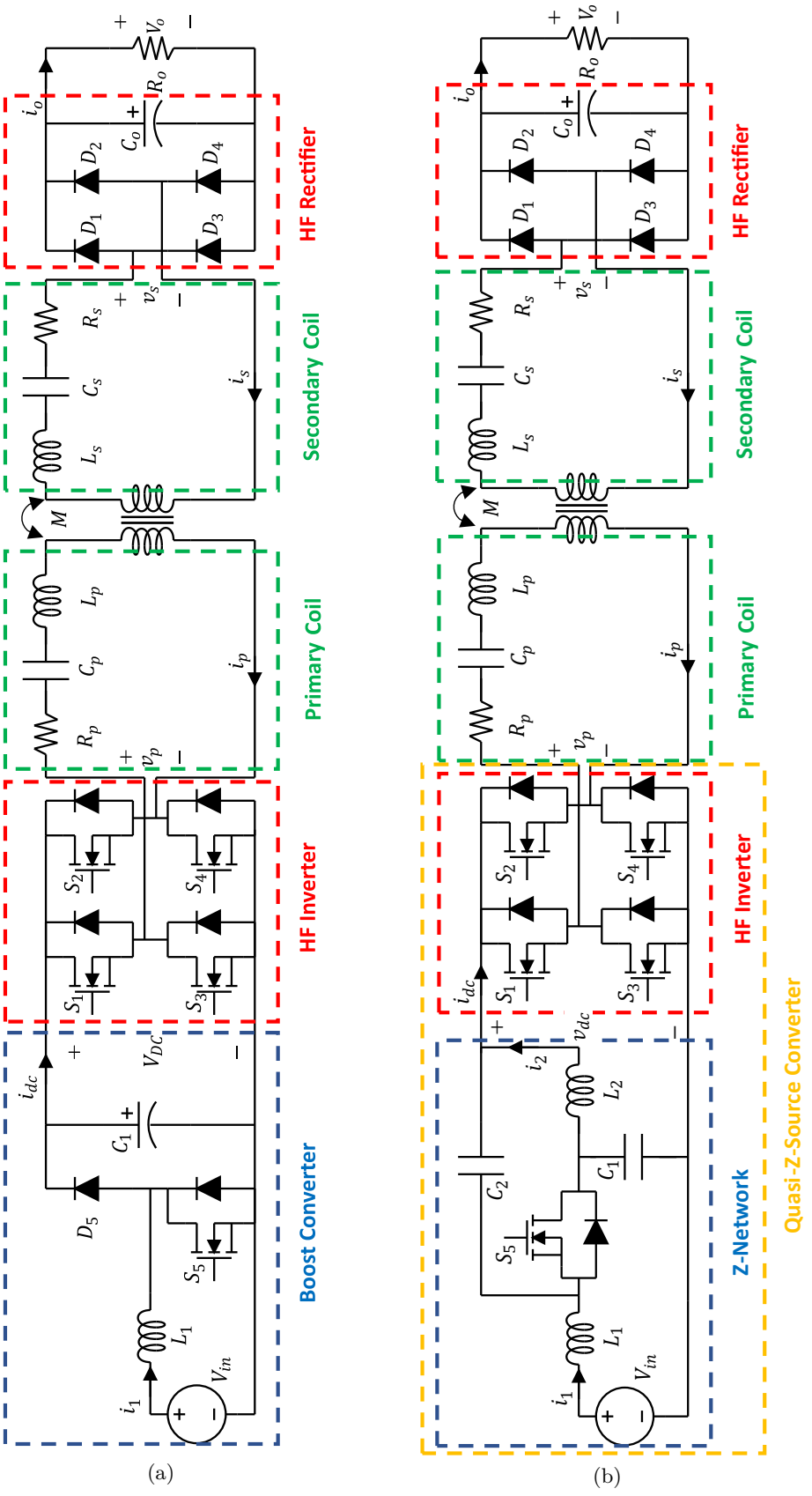

Figure 8.2: Circuit schematic of a classical IPT system.

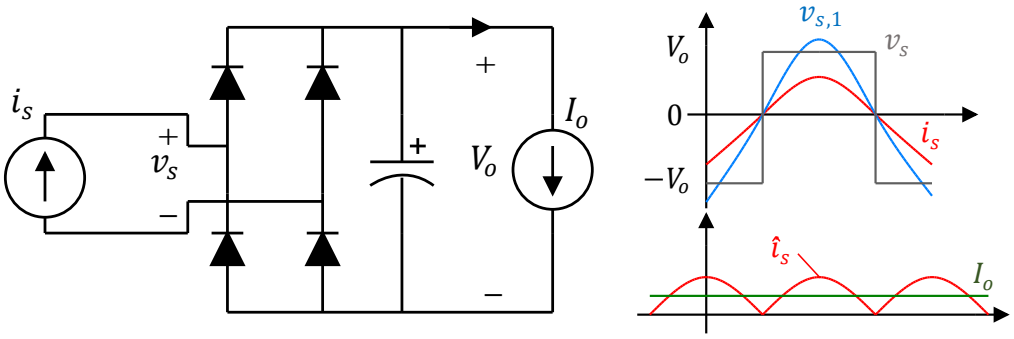

Figure 8.3: Simplified circuit for the equivalent resistance derivation.

8.2 System Analysis and Modeling

Fig. 8.2 (b) shows the proposed qZS-based inductive power transfer system, including a Z-network, a High Frequency (HF) full-bridge inverter, an inductive coupling in SS configuration, an HF Rectifier, and the load.

8.2.1 HF Rectifier and Load Modeling

Using the fundamental harmonic approximation (FHA), the secondary side HF rectifier along with the load can be replaced by an equivalent resistor R_{eq}. Considering Fig. 8.3, i_s (red curve) is the secondary side current, v_s (grey curve) is the rectifier input voltage which swings between V_o and $-V_o$, $\hat{v}_{s,1}$ is the peak value of the fundamental component of v_s, $\hat{i}_s$ is the peak value of the rectified current and I_o (green curve) is the DC output current. The fundamental component $\hat{v}_{s,1}$ and the peak value $\hat{i}_s$ can be expressed, respectively, as

$$\hat{v}_{s,1} = \frac{4}{\pi} V_o, \quad \hat{i}_s = \frac{\pi}{2} I_o. \tag{8.1}$$

The equivalent resistance R_{eq} can be then calculated as

$$R_{eq} = \frac{\hat{v}_{s,1}}{\hat{i}_s} \approx \frac{\frac{4}{\pi} V_o}{\frac{\pi}{2} I_o} = \frac{8}{\pi^2} \frac{V_o}{I_o}. \tag{8.2}$$

8.2.2 Inductive Coupling Modeling

Using the FHA, the inductive coupling can be simplified as represented in the equivalent circuit model of Fig. 8.4. Accordingly, it can be derived that

$$\begin{cases} \bar{v}_{p,1} = \left(R_p + j\omega L_p + \dfrac{1}{j\omega C_p} \right) \bar{i}_{p,1} - j\omega M \bar{i}_{s,1} \\ j\omega M \bar{i}_{p,1} = \left(R_s + j\omega L_s + \dfrac{1}{j\omega C_s} \right) \bar{i}_{s,1} + \bar{v}_{s,1} \end{cases}. \tag{8.3}$$

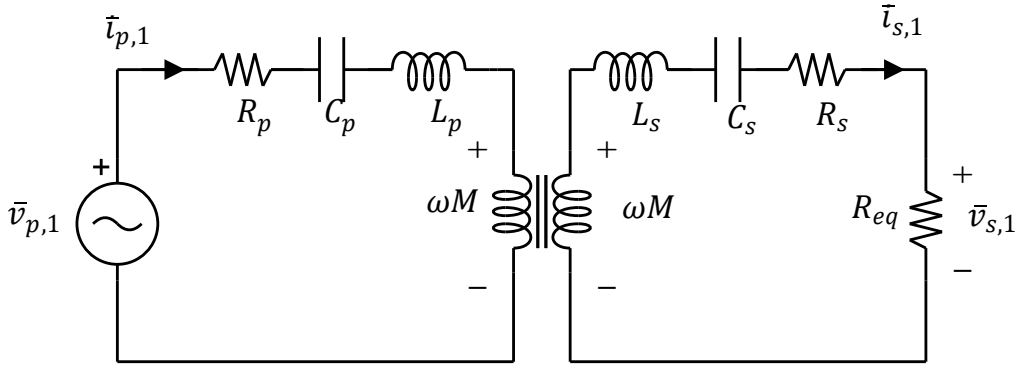

Figure 8.4: FHA of the IPT system.

Subsequently, the input impedance Z_{in} can be obtained as

$$Z_{in} = \left(R_p + \frac{1}{j\omega C_p} + j\omega L_p\right) + \frac{j\omega^2 M^2}{\left(R_s + R_{eq} + \frac{1}{j\omega C_s} + j\omega L_s\right)}. \tag{8.4}$$

To have a null input impedance, the reactive term of the input impedance must be zero , i.e.,

$$\left(\frac{1}{j\omega C_p} + j\omega L_p\right) = imag\left[\frac{j\omega^2 M^2}{\left(R_s + R_{eq} + \frac{1}{j\omega C_s} + j\omega L_s\right)}\right] \tag{8.5}$$

and after developing (8.5), we obtain:

$$\omega L_p - \frac{1}{\omega C_p} = \frac{\omega^2 M^2 \left(\omega L_s - \frac{1}{\omega C_s}\right)}{\left(R_s + R_{eq}\right)^2 + j\left(j\omega L_s - \frac{1}{\omega C_s}\right)^2}. \tag{8.6}$$

Equation (8.6) is assessed, when the coil inductance and the compensation capacitors form a resonant tank with the resonance frequency ω_0 being

$$\omega_0 = \frac{1}{\sqrt{L_p C_P}} = \frac{1}{\sqrt{L_s C_s}}. \tag{8.7}$$

Considering (8.3) and substituting (8.7), we obtain:

$$\begin{cases} \bar{v}_{p,1} = R_p \bar{i}_{p,1} - j\omega_0 M \bar{i}_{s,1} \\ j\omega_0 M \bar{i}_{p,1} = R_s \bar{i}_{s,1} + R_{eq} \bar{i}_{s,1} \end{cases} \tag{8.8}$$

The primary current can be obtained from the first equation of (8.8)

$$\bar{i}_{p,1} = \frac{\bar{v}_{p,1}}{R_p} + \frac{j\omega_0 M \bar{i}_{s,1}}{R_p} \tag{8.9}$$

and the secondary current is obtained by replacing (8.9) in the second equation of

(8.8) as

$$\bar{i}_{s,1} = \frac{j\omega_0 M}{R_p\left(R_s + R_{eq}\right) + \omega_0^2 M^2}\bar{v}_{p,1}. \tag{8.10}$$

Since R_p and R_s are generally small compared to R_{eq}, the secondary current can be expressed as

$$\bar{i}_{s,1} \approx j\frac{1}{\omega_0 M}\bar{v}_{p,1}. \tag{8.11}$$

From (8.11), we can infer that the secondary current is independent from the load and can be regulated to increase or decrease the HF inverter output voltage.

8.2.3 QZS Converter Modeling

The qZS converter has different states based on which switch is turned ON or OFF. In addition to the Active State (AS) and Zero State (ZS), normally used in traditional inverters, the Shoot-Through (ST) state is introduced. All the possible configurations of the converter are shown in Fig. 8.5 and are described below.

1. *Active State*: During the AS, see Fig. 8.5 (a) and (b), the diagonal switches (S_1 and S_4 or S_2 and S_3) are ON and the switch S_5 is ON. The capacitors C_1 and C_2 are connected in series through S_5 and supply current to the load along with the DC source.

2. *Zero State*: During the ZS, see Fig. 8.5 (c) and (d), the upper (S_1 and S_2) or lower (S_3 and S_4) switches are ON and the switch S_5 is ON. The transmitter current is freewheeling, the Z-network inductors and the source charge the Z-network capacitors.

3. *Shoot-Through State*: During the ST state, see Fig. 8.5 (e), the switches S_1 to S_4 are ON and S_5 is OFF. The inductors are charged both by the DC source and the Z-network capacitors. Thanks to this ST state, the Z-network output voltage is boosted. Using the voltage-second balance across one of the Z-network inductors, the DC-link peak voltage can be obtained as

$$\hat{v}_{DC} = \frac{1}{1-2D}V_{in} \tag{8.12}$$

   where D is the duty cycle.

Combining the previous three states, different operating modes can be achieved. In particular, the system can operate both in boost mode, increasing the DC-link voltage with respect to the input voltage, in buck mode, decreasing the AC output voltage or in buck-boost mode.

Buck Mode

In buck mode operation, only the AS and ZS are used. Fig. 8.6 (a) shows the control signals generation and waveforms and the inverter output voltage waveform.

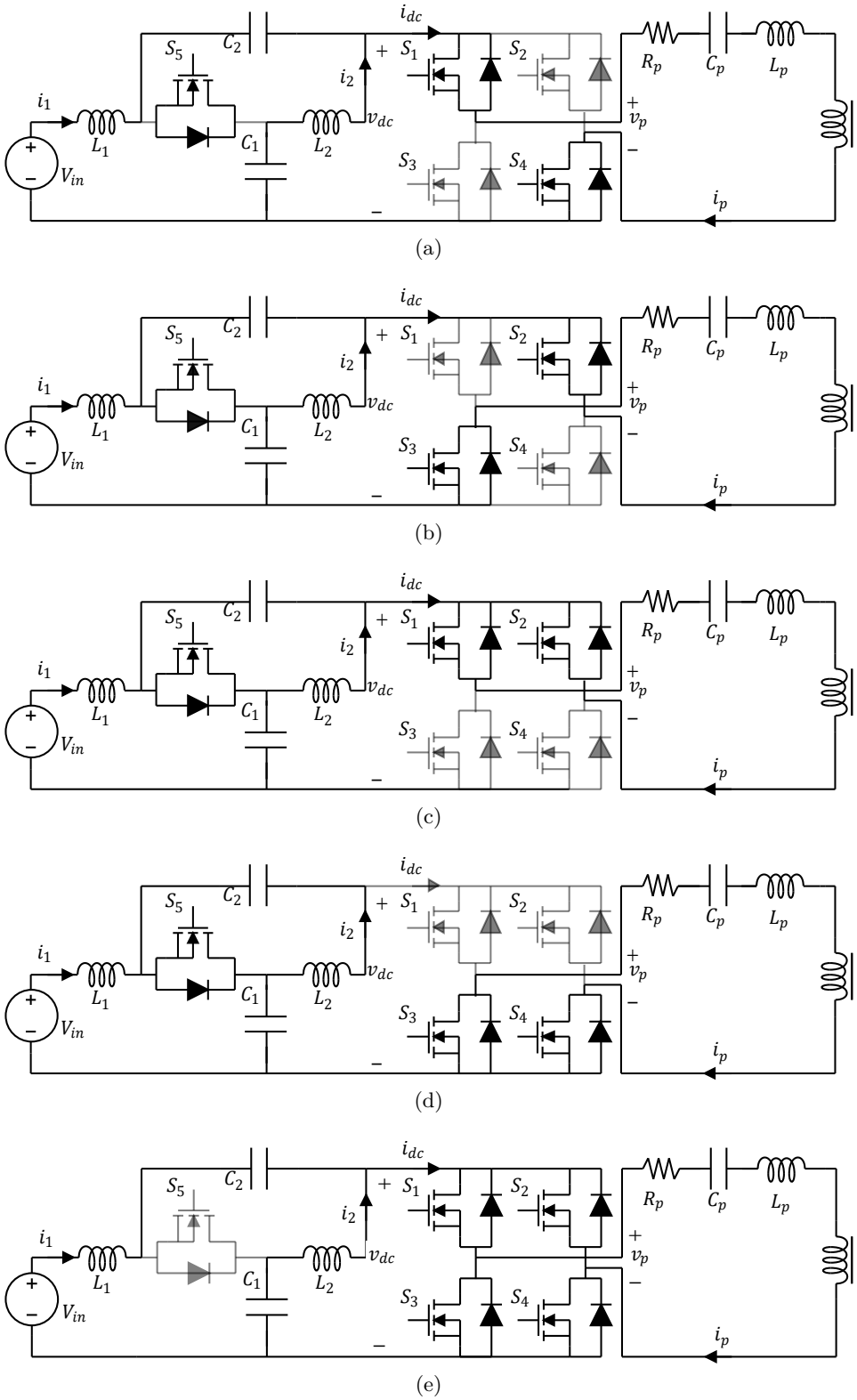

Figure 8.5: Circuit schematic of the qZS-IPT system in different states. (a) Active state S_1, S_4. (b) Active state S_2, S_3. (c) Zero state S_1, S_2. (d) Zero state S_3, S_4. (e) Shoot-through state.

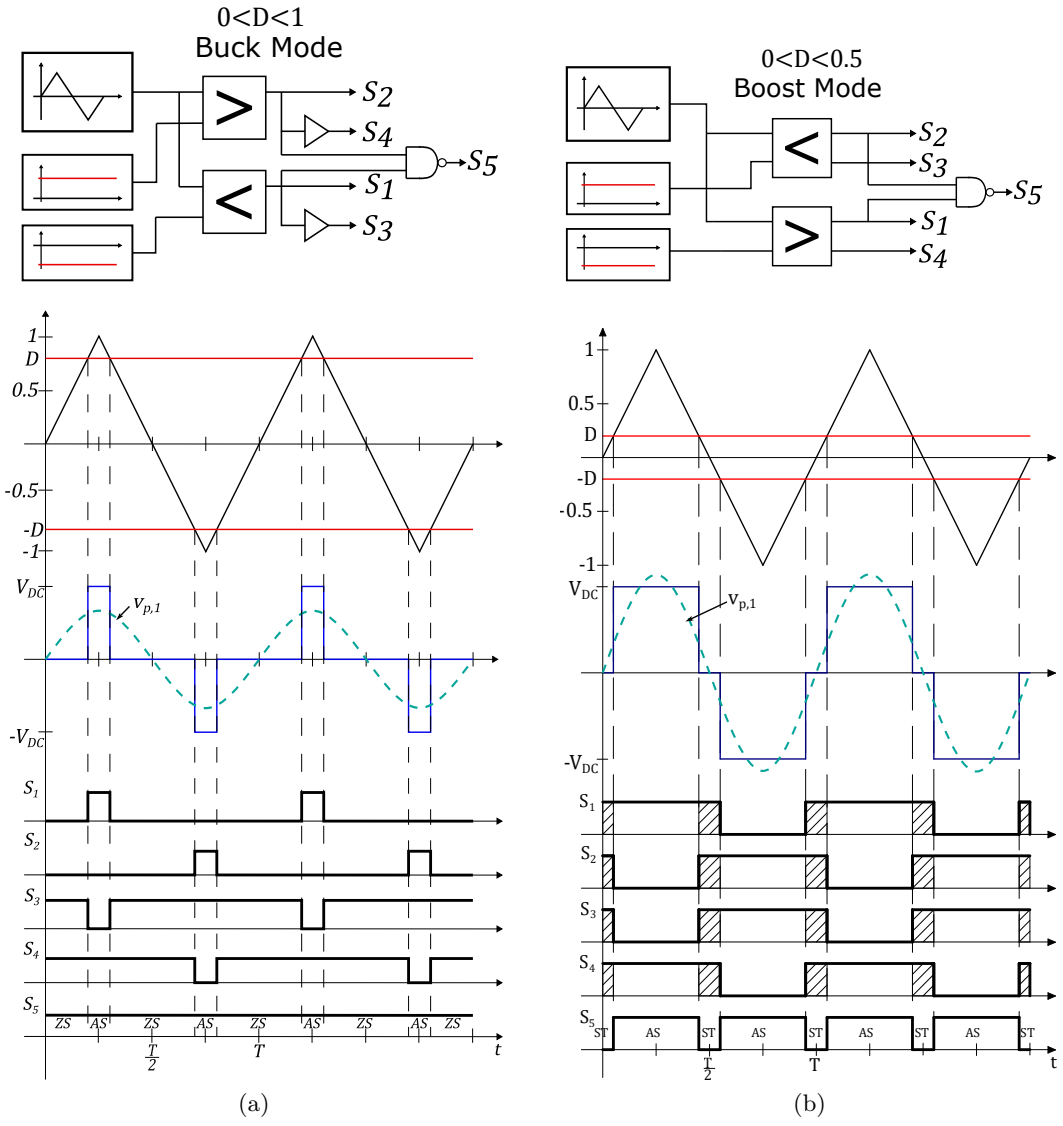

Figure 8.6: Logic circuit for control signal generation and relative time domain waveforms. (a) Buck mode. (b) Boost mode.

The first harmonic of the inverter output voltage , denoted with $v_{p,1}$ in Fig. 8.6 (a), can be expressed as follows

$$v_{p,1} = \frac{4V_{DC}}{\pi} \cos\left(\frac{\pi}{2}D\right) \sin\left(\omega_0 t\right). \tag{8.13}$$

The DC-link voltage V_{DC} during the buck mode operation is equal, neglecting the voltage drops across the Z-network components, to

$$V_{DC} \cong V_{in} \tag{8.14}$$

thus, the amplitude of the first harmonic is

$$\hat{v}_{p,1} = \frac{4V_{in}}{\pi} \cos\left(\frac{\pi}{2}D\right) \tag{8.15}$$

and it will be maximum when the duty cycle is 0 and minimum when the duty cycle is 1. The output current in this operation mode can be calculated combining (8.15), (8.11), and the second equation in (8.1):

$$I_o = \frac{8}{\omega_0 M} \frac{V_{in}}{\pi^2} \cos\left(\frac{\pi}{2}D\right). \tag{8.16}$$

Boost Mode

In boost mode operation, only the AS and the ST state are used. Fig. 8.6 (b) shows the control signal generation and waveforms and the inverter output voltage waveform for this operation mode. The inverter output voltage first harmonic expression is the same in (8.13). However, thanks to the boosting action during the ST state, the DC-link peak voltage will be increased as reported in (8.12). Thus, the amplitude of the first harmonic during the boost mode can be calculated replacing (8.12) in (8.13), as

$$\hat{v}_{p,1} = \frac{4V_{in}}{\pi} \frac{1}{1-2D} \cos\left(\frac{\pi}{2}D\right) \tag{8.17}$$

and it will be minimum for D equal to 0 and theoretically infinite for D equal to 0.5.

The output current in this operation mode can be calculated combining (8.17), (8.11), and the second equation in (8.1):

$$I_o = \frac{8V_{in}}{\omega_0 M \pi^2 (1-2D)} \cos\left(\frac{\pi}{2}D\right). \tag{8.18}$$

Buck-Boost Mode

In order to achieve a smooth transition between buck and boost mode and to use a single modulator for both operation modes, a new control logic was implemented. In particular, the duty cycle has been allowed to vary not between 0 and 1 for the

Table 8.1: Thruth tables of (a) S_3 control signal, (b) S_4 control signal

(a)

T	S_1	S_2	S_3
0	**0**	**1**	**1**
0	**1**	**1**	**1**
0	0	0	0
0	1	0	0
1	**0**	**1**	**1**
1	1	1	0
1	**0**	**0**	**1**
1	1	0	0

(b)

T	S_1	S_2	S_3
0	0	1	0
0	**1**	**1**	**1**
0	0	0	0
0	**1**	**0**	**1**
1	0	1	0
1	1	1	0
1	**0**	**0**	**1**
1	**1**	**0**	**1**

buck mode and between 0 and 0.5 for the boost mode, as normally happens, but between -1 and 0 for buck mode and between 0 and 0.5 for boost mode. In this way, when the control circuit tries to decrease the current, the duty cycle may become negative by switching to buck operation. Considering the control signal generation shown in Fig 8.6 (a), this means that the two relational operators can be changed by becoming the same as in the boost mode shown in Fig. 8.6 (b). Thus, the control signals S_1, S_2 and S_5 are generated in the same way for both operation modes. The S_3 and S_4 signals remain to be generated differently, so we introduce a variable T that indicates whether the duty cycle is greater ($T = 0$) or smaller ($T = 1$) than 0. Thus, the following relationship and truth table can be written:

$$S_3 = \begin{cases} S_2, & D > 0 \ \rightarrow T = 0 \\ \bar{S_1}, & D < 0 \ \rightarrow T = 1 \end{cases}, \tag{8.19}$$

$$S_4 = \begin{cases} S_1, & D > 0 \ \rightarrow T = 0 \\ \bar{S_2}, & D < 0 \rightarrow T = 1 \end{cases}. \tag{8.20}$$

Considering all the minterms in the truth tables, the following combinatorial expressions are obtained.

$$\begin{gathered} \bar{T}\bar{S_1}S_2 + \bar{T}S_1S_2 + T\bar{S_1}S_2 + T\bar{S_1}\bar{S_2} = \\ \bar{T}\bar{S_1}S_2 + \bar{T}S_1S_2 + T\bar{S_1}S_2 + T\bar{S_1}\bar{S_2} = \\ \bar{S_1}S_2 + \bar{T}S_1S_2 + T\bar{S_1}\bar{S_2} \end{gathered} \tag{8.21}$$

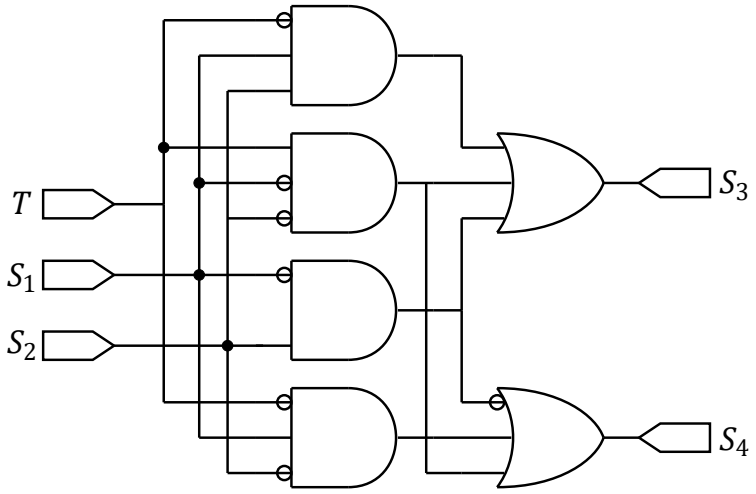

Figure 8.7: Combinatorial logic circuit for the proposed modulator.

$$\begin{aligned} &\bar{T}S_1S_2 + \bar{T}S_1\bar{S}_2 + T\bar{S}_1\bar{S}_2 + TS_1\bar{S}_2 = \\ &\left(\bar{T}+T\right)\left(S_1\bar{S}_2\right) + \bar{T}S_1\bar{S}_2 + T\bar{S}_1\bar{S}_2 = \\ &S_1\bar{S}_2 + \bar{T}S_1\bar{S}_2 + T\bar{S}_1\bar{S}_2 \end{aligned} \tag{8.22}$$

The combinational logic circuit associated to (8.21) and (8.22) is shown in Fig. 8.7.

8.3 CC/CV Charging Implementation

In order to ensure fast and safe charging of the battery, the CC/CV charging method was considered. This well-known method, whose typical waveforms are reported in Fig. 8.8, consists in two phases: in the CC phase, the battery charging current is kept constant and equal to I_{max} until the battery voltage reaches its maximum allowable valueV_{max}.

In the CV phase, the battery voltage is kept constant to V_{max} until the battery charge current reaches a minimum value I_{min}.

The CC/CV charge was implemented using a double-loop control scheme: the external loop, which controls the battery voltage V_o, and the internal loop which controls the battery current I_o. An interesting feature of the proposed control method is the possibility to achieve a smooth transition between CC and CV charging modes, with no need to reconfigure the controller. The complete control scheme is shown in Fig. 8.9.

The battery voltage V_o is measured and compared to the reference value V_o^*, set to the maximum allowable voltage for the battery. The error is sent to a Proportional-Integral (PI) controller to generate the reference charging current I_o^*, which is compared to the actual battery current I_o and processed by the second PI controller to generate the reference duty cycle D^*. To the first PI controller output, a saturation block is added. The upper limit of the saturation block is set to be equal to the

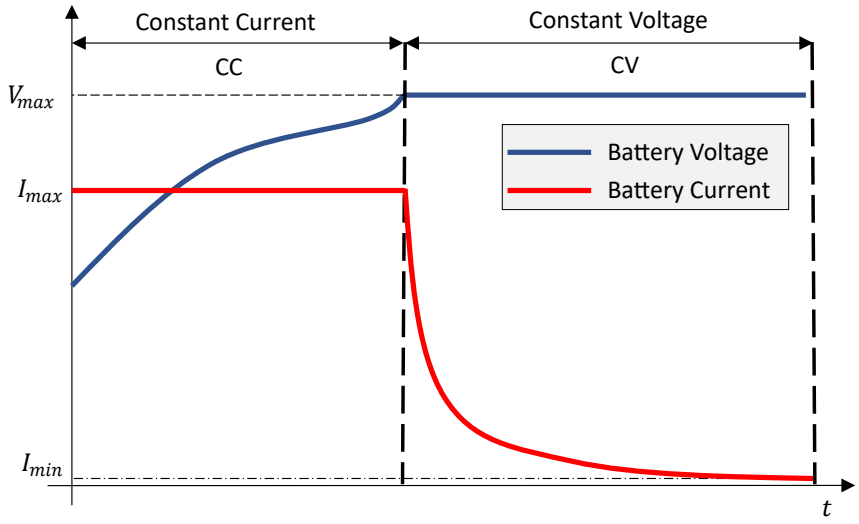

Figure 8.8: CC/CV charging typical waveforms.

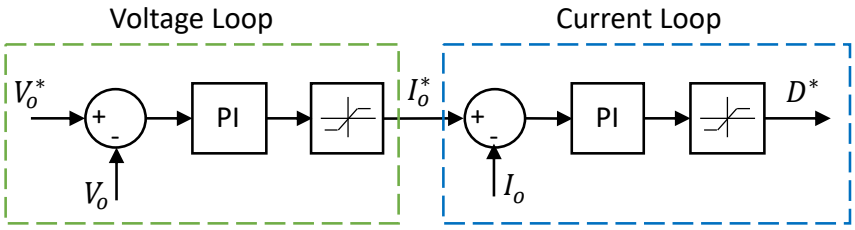

Figure 8.9: Closed-loop control scheme for CC/CV charging implementation.

maximum battery charging current, while the lower limit is set to 0.

To the second PI controller output, another saturation block is added to limit the duty cycle, with the upper saturation limit set to 0.4 and the lower saturation limit set to -1. In this way, when the battery voltage is low, the PI controller tries to increase the charging current, which will be saturated to the maximum permissible value by the battery. During the CC phase, the converter usually works in boost mode, with duty cycle in the range of 0 to 0.4. As the battery charges, the charging current will be kept constant until the maximum voltage is reached. At this point, the system automatically switches to the CV phase, during which the charging current is reduced to a minimum value. In this phase, the converter will switch to the buck mode when the duty cycle becomes negative in the range of 0 to -1. When the charging current reaches the minimum value, the charging process is completed.

8.4 Simulation Results

The proposed system was designed and simulated in PLECS. The simulation parameters are summarized in Table 8.2. The simulation is carried out to demonstrate the system behaviour during the CC-CV charge. Fig. 8.10 shows the steady-state

Table 8.2: Simulation Parameters

Parameter	**Unit**	**Symbol**	**Value**
Output power	(kW)	P_o	25
Input DC Voltage	(V)	V_{in}	330
Nominal Battery Voltage	(V)	V_o	200
Maximum Battery Voltage	(V)	$V_{o,max}$	225
Maximum Battery Current	(A)	$I_{o,max}$	125
Minimum Battery Current	(A)	$I_{o,min}$	5
Coil Inductance	(μH)	L_s, L_p	13.6
Compensation Capacitance	(nF)	C_s, C_p	286
Coil ESR	(Ω)	r_p, r_s	0.1
Z-Network Inductance	(μH)	L_1, L_2	100
Z-network Capacitance	(mF)	C_s, C_p	1.5
Output Capacitance	(mF)	C_o	2
Duty Cycle	(-)	D	-1 to 0.4
Switching Frequency	(kHz)	f_0	85

voltage and current waveforms during boost mode (a) and buck mode (b) operation of each stage of the proposed system. From top to bottom the input voltage V_{in} and current i_1, the DC-link voltage v_{DC} and current i_{DC}, the primary side voltage v_p and current i_p, the secondary side voltage v_s and current i_s and the battery voltage V_o and current I_o are represented.

Fig. 8.10 (a) shows the waveforms during boost mode and CC phase. The battery charging current reference is set to 125 A (red dashed line), corresponding to a duty cycle of 0.18. During the shoot-though state, the DC-link current reaches almost 200 A, charging the Z-network inductors. It can be noticed that the DC-link voltage is boosted from 330 V to almost 500 V.

Fig. 8.10 (b) shows the waveforms during buck mode and CV phase. The battery maximum voltage reference is set to 225 V, corresponding to a duty cycle of -0.57 . It can be noticed that the DC-link voltage in this case is practically constant and equal to the input voltage apart from voltage drops on components.

In CC phase, the closed-loop control maintains the battery charging current to 125 A while the battery voltage is increasing. As the battery voltage reaches the maximum value $V_{o,max} = 225$ V, the CV phase is activated. To maintain a constant voltage, the charging current is proportionally decreased until its value reaches the minimum battery charging current $I_{o,min} = 5$ A. Thanks to the improved control algorithm, no voltage and current transients are observed during the transition from CC to CV phase.

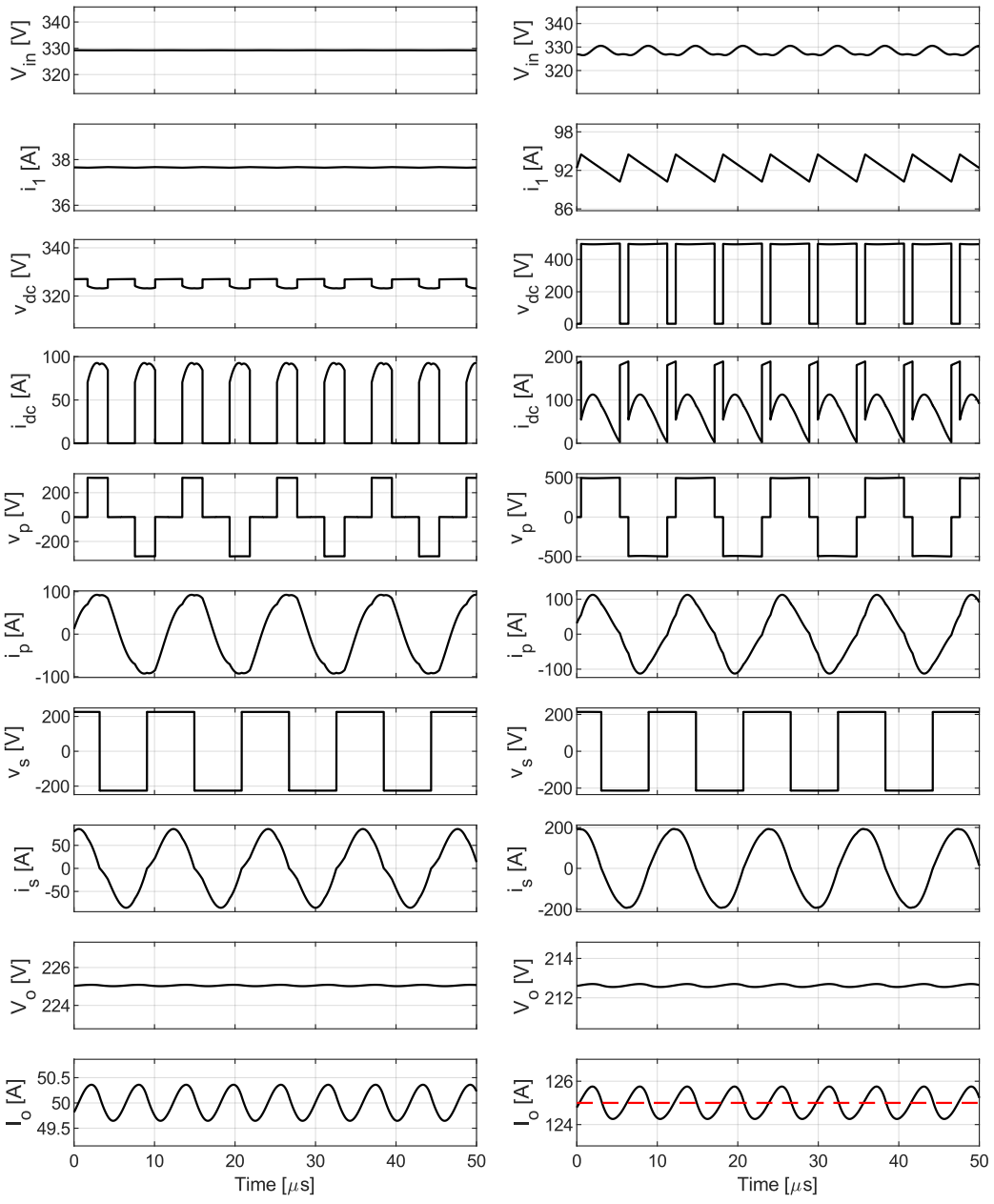

(a) (b)

Figure 8.10: Steady-state voltage and current waveforms for (a) boost mode operation ($D = 0.18$) and (b) buck mode operation ($D = -0.57$).

Table 8.3: Laboratory Prototype Parameters

Parameter	**Unit**	**Symbol**	**Value**
Output power	(W)	P_o	250
Input DC voltage	(V)	V_{in}	20
Coil inductance	(μH)	L_s, L_p	13.6
Compensation capacitance	(nF)	C_s, C_p	286
Coil ESR	(Ω)	r_p, r_s	0.1
Z-Network inductance	(μH)	L_1, L_2	10
Z-network capacitance	(mF)	C_s, C_p	150
Output capacitance	(μF)	C_o	200
Duty cycle	(-)	D	$-1 \div 0.4$
Switching frequency	(kHz)	f_0	85

8.5 Experimental Results

Experimental tests have been performed on a scaled-down prototype to validate the simulation results and prove that the system achieves the CC-CV charge. The test-bench, shown in Fig. 8.11, is composed of:

- A PED-board, used to acquire voltages and currents, implement the control algorithm and generate the control signals for the inverter.
- The proposed qZS-IPT system, whose parameters are summarized in Table 8.3.
- An Agilent 6672A DC Power Supply (0-20 V/0-100 A, 2 kW), used as the input source.
- An Agilent 6060B Single Input Electronic Load (3-60 V/0–60 A, 300 W), used as a load in voltage mode for open-loop tests.
- A lithium-ion battery, whose parameters are reported in Table 8.4, used for the CC-CV charging demonstration,
- A Lecroy WavePro 7200A oscilloscope with 2 differential voltage probe and 2 current probe.

Fig. 8.12 shows the key waveforms of the proposed system in open-loop configuration with the electronic load, in voltage mode, set to 12 V. Fig. 8.12 (a)-(c) show the waveforms obtained with $D = 0.1$, whereas Fig. 8.12 (d)-(f) show the waveforms obtained with $D = 0.2$ in boost mode. Fig. 8.12 (a) and (d) show the Z-network input and output voltage and current. The theoretical DC-link peak voltage can

Table 8.4: Battery Parameters

Configuration	4S2P
Cell brand	LGHG2
Format	186520

Parameter	Unit	Symbol	Value
Nominal battery voltage	(V)	V_o	14.8
Maximum battery voltage	(V)	$V_{o,max}$	16.8
Maximum battery current	(A)	$I_{o,max}$	8
Minimum battery current	(A)	$I_{o,min}$	0.2
Maximum capacity	(Ah)	Q_{max}	6

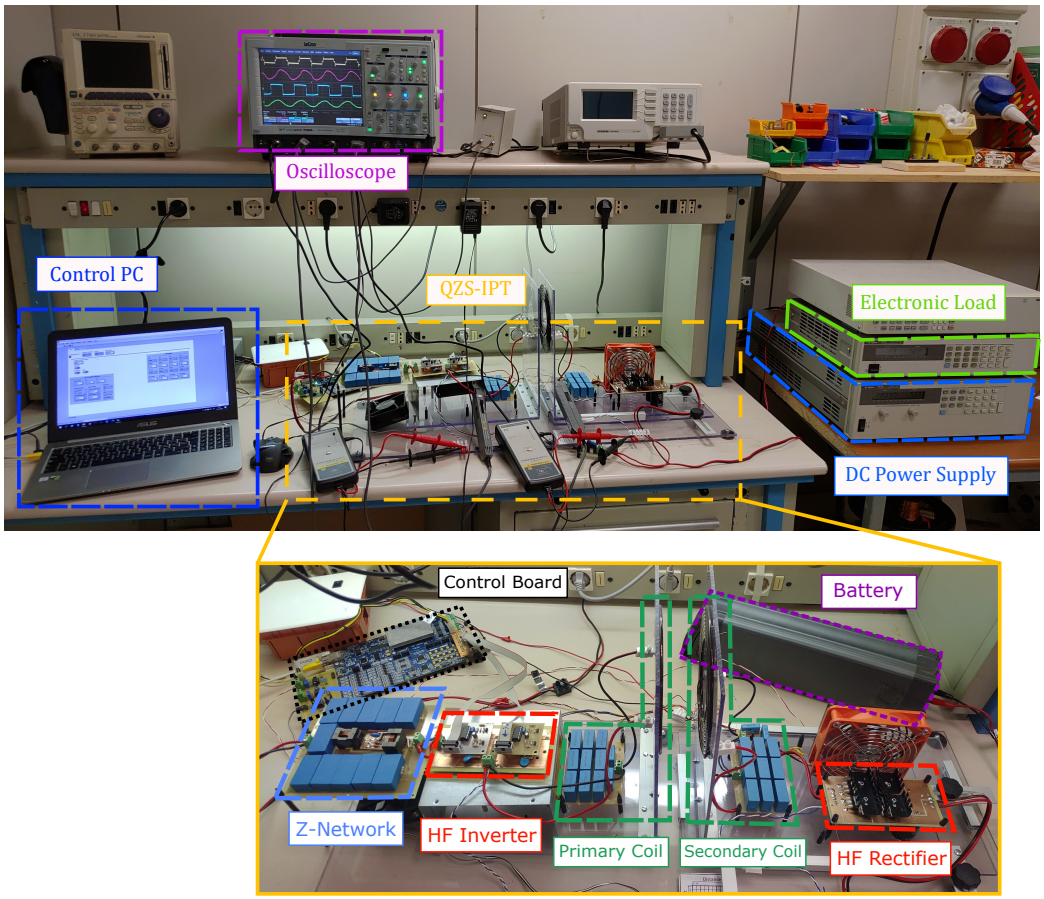

Figure 8.11: Setup of the laboratory prototype for the proposed qZS-IPT system.

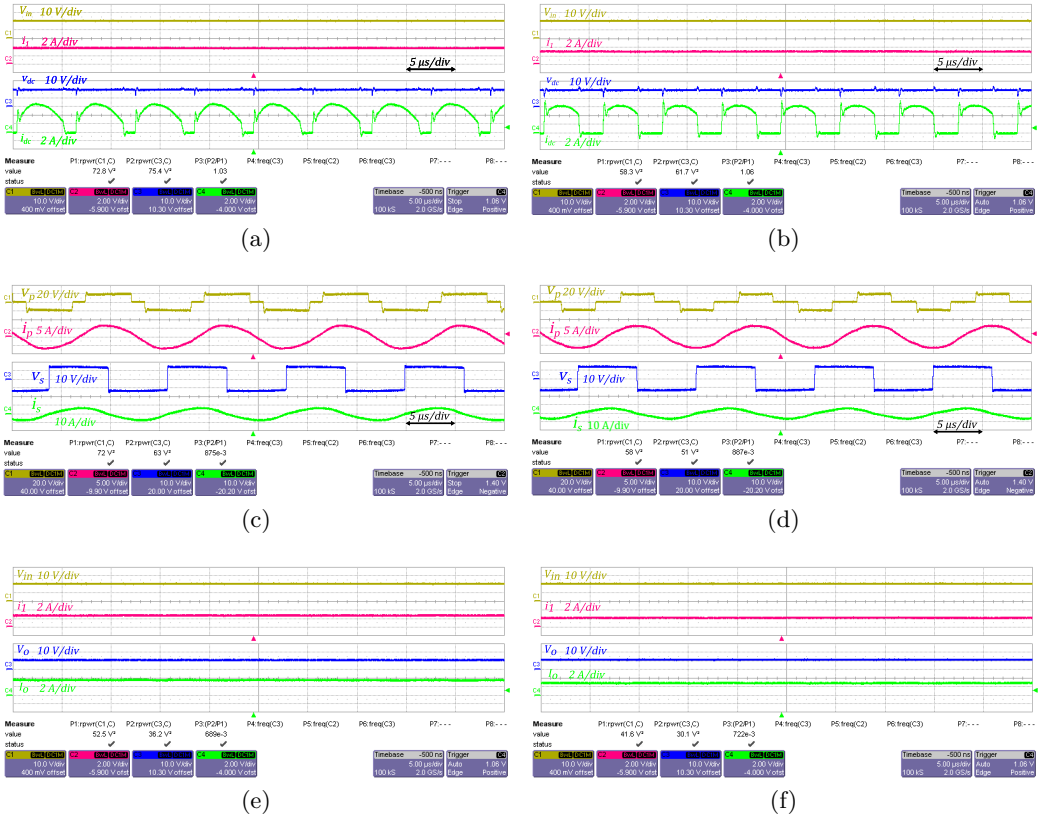

Figure 8.12: Experimental waveforms of the qZS-IPT system in boost mode with $D = 0.1$ (left side) and $D = 0.2$ (right side). (a) and (d) Input voltage V_{in} and current i_1, DC-link voltage v_{pn} and current i_{pn}. (b) and (e) primary side voltage v_p and current i_p, secondary side voltage v_s and current i_s. (c) and (f) input voltage V_{in} and current i_1, output voltage V_o and current I_o.

be calculated using (8.12), obtaining 25 V for $D = 0.1$ and 33 V for $D = 0.2$. The practical DC-link peak voltage was 22 V and 30 V respectively due to the component voltage drops. Fig. 8.12 (b) and (e) show the inverter output voltage and current and the rectifier input voltage and current. The theoretical secondary current amplitude can be calculated combining (8.11) and (8.17), as 9.8 A for $D = 0.1$ and 12.6 A for $D = 0.2$. The practical secondary current amplitude was 9.2 A and 12 A. Fig. 8.12 (c) and (f) show the input and output voltage and current. The theoretical output current value can be calculated by using (8.18) to be 6.25 A for $D = 0.1$ and 8 A for $D = 0.2$. The measured value was 5.9 A and 7.6 A, respectively.

Fig. 8.13 reports the key waveforms of the system in buck mode operation. Fig. 8.13 (a)-(c) show the waveforms obtained with $D = -0.2$, whereas Fig. 8.13 (d)-(f) show the waveforms obtained with $D = -0.4$. Fig. 8.13 (a) and (d) show the Z-network input and output voltage and current. As expected, the DC-link voltage in this case is constant and equal to the input voltage. Fig. 8.13 (b) and (e) show the inverter output voltage and current and the rectifier input voltage and current. The theoretical secondary current amplitude can be calculated combining (8.11) and

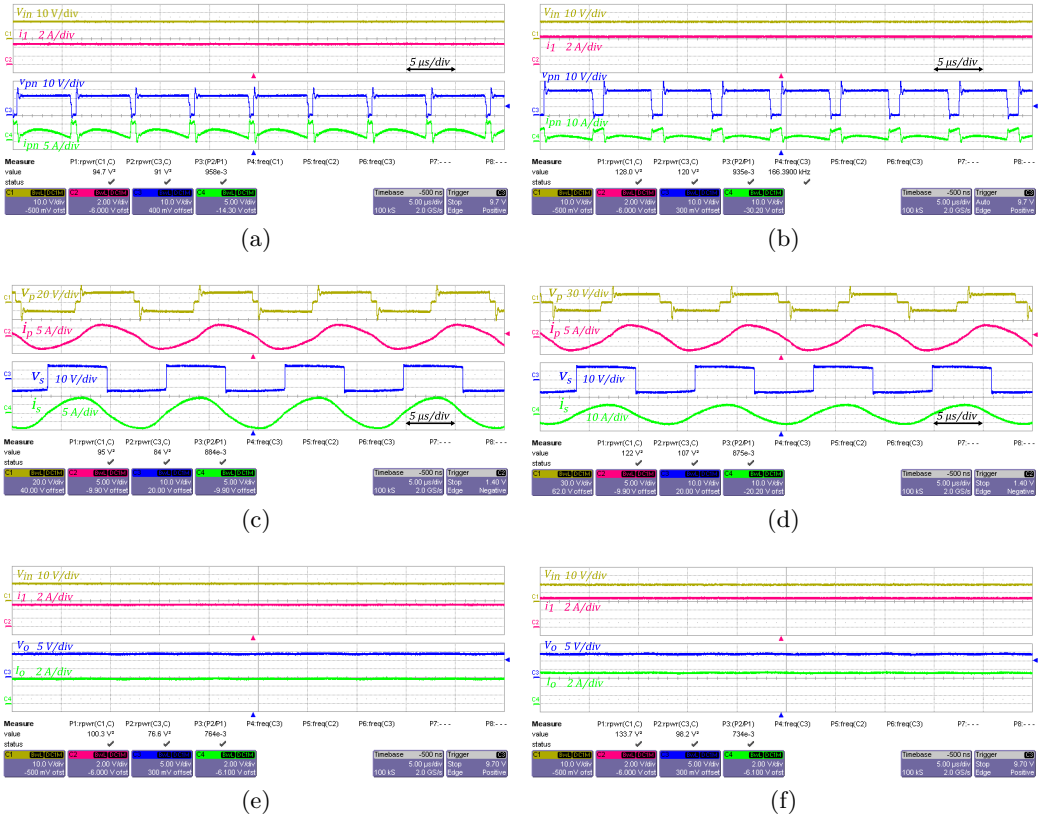

Figure 8.13: Experimental waveforms of the qZS-IPT system in buck mode with $D = -0.2$ (left side) and $D = -0.4$ (right side). (a) and (d) Input voltage V_{in} and current i_1, DC-link voltage v_{pn} and current i_{pn}. (b) and (e) primary side voltage v_p and current i_p, secondary side voltage v_s and current i_s. (c) and (f) input voltage V_{in} and current i_1, output voltage V_o and current I_o.

(8.15), as 7.5 A for $D = -0.2$ and 6.4 A for $D = -0.4$. The practical secondary current amplitude was 7 A and 6 A. Fig. 8.13 (c) and (f) show the input and output voltage and current. The theoretical output current value can be calculated by using (8.15) to be 4.4 A for $D = -0.2$ and 3.77 A for $D = -0.4$. The measured value was 3.9 A and 3.2 A, respectively.

The experimental results are in accordance with the mathematical analysis carried out in Section II, demonstrating the correct operation of the modulator by switching from boost operation, for positive duty cycle values, to buck operation, for negative duty cycle values. Moreover, the measured values of voltages and currents in the various stages of the system agree with the theoretical ones, demonstrating the correct operation of the prototype.

To demonstrate the CC/CV charge process for the proposed system, the control scheme shown in Fig. 8.9 was implemented in the control board, using LabVIEW. The control board interfaces with a control PC, on which a graphic interface has been realized to control the various parameters of the system. The battery was first discharged to the minimum voltage $V_{o,min} = 12$ V and was then connected to the

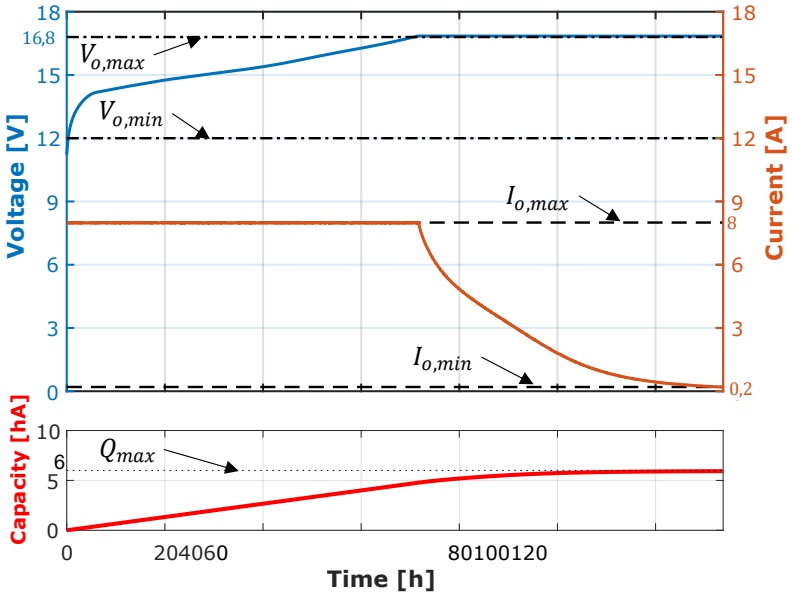

Figure 8.14: Experimental battery voltage and current during a complete CC/CV charge cycle.

qZS-IPT system. The maximum current for the CC phase was set to $I_{o,max} = 8$ A, the maximum voltage for the CV phase was set to $V_{o,max} = 16.8$ V and the minimum current to stop the charging process was set to $I_{o,min} = 0.2$ A. Fig. 8.14 shows the acquired battery voltage and current during the entire process and the estimated capacity using the Coulomb counting method. As predicted by the simulations, the system was able to perform CC/CV charging, without transients during the transition between the two phases.

8.6 Conclusion

This chapter has presented a quasi-Z-source-based IPT system for EV battery charging applications. Thanks to the Z-network the qZS-IPT system is immune to short-circuiting and taking advantage of the shoot-through states the simultaneous DC voltage regulation and DC/AC conversion is possible. A new modulator has been proposed, capable of making the transition between buck and boost modes in a simple and effective way. Among the different charging methods, the CC/CV charge was chosen. Unlike many other papers that propose two separate control loops, one for the CC phase and one for the CV phase, a single double-loop control was proposed improving the transition between the two phases. This chapter validated the theoretical analysis by means of simulations and experimental results, verifying proper system operation in both buck and boost modes, and ensuring the system ability to perform CC/CV charging.

References

[1] Y.-T. Liao and C.-N. Lu, "Dispatch of ev charging station energy resources for sustainable mobility," *IEEE Transactions on Transportation Electrification*, vol. 1, no. 1, pp. 86–93, 2015. DOI: 10.1109/TTE.2015.2430287.

[2] A. Khaligh and Z. Li, "Battery, ultracapacitor, fuel cell, and hybrid energy storage systems for electric, hybrid electric, fuel cell, and plug-in hybrid electric vehicles: State of the art," *IEEE Transactions on Vehicular Technology*, vol. 59, no. 6, pp. 2806–2814, 2010. DOI: 10.1109/TVT.2010.2047877.

[3] S. Li and C. C. Mi, "Wireless power transfer for electric vehicle applications," *IEEE Journal of Emerging and Selected Topics in Power Electronics*, vol. 3, no. 1, pp. 4–17, 2015. DOI: 10.1109/JESTPE.2014.2319453.

[4] F. J. Márquez-Fernández, J. Bischoff, G. Domingues-Olavarría, and M. Alaküla, "Assessment of future ev charging infrastructure scenarios for long-distance transport in sweden," *IEEE Transactions on Transportation Electrification*, pp. 1–1, 2021. DOI: 10.1109/TTE.2021.3065144.

[5] C. C. Chan, "The state of the art of electric, hybrid, and fuel cell vehicles," *Proceedings of the IEEE*, vol. 95, no. 4, pp. 704–718, 2007. DOI: 10.1109/JPROC.2007.892489.

[6] P. He and A. Khaligh, "Comprehensive analyses and comparison of 1 kw isolated dc–dc converters for bidirectional ev charging systems," *IEEE Transactions on Transportation Electrification*, vol. 3, no. 1, pp. 147–156, 2017. DOI: 10.1109/TTE.2016.2630927.

[7] D. Patil, M. K. McDonough, J. M. Miller, B. Fahimi, and P. T. Balsara, "Wireless power transfer for vehicular applications: Overview and challenges," *IEEE Transactions on Transportation Electrification*, vol. 4, no. 1, pp. 3–37, 2018. DOI: 10.1109/TTE.2017.2780627.

[8] D. Vincent, P. S. Huynh, N. A. Azeez, L. Patnaik, and S. S. Williamson, "Evolution of hybrid inductive and capacitive ac links for wireless ev charging—a comparative overview," *IEEE Transactions on Transportation Electrification*, vol. 5, no. 4, pp. 1060–1077, 2019. DOI: 10.1109/TTE.2019.2923883.

[9] F. Lu, H. Zhang, H. Hofmann, and C. Mi, "A double-sided lclc-compensated capacitive power transfer system for electric vehicle charging," *IEEE Transactions on Power Electronics*, vol. 30, no. 11, pp. 6011–6014, 2015. DOI: 10.1109/TPEL.2015.2446891.

[10] M. P. Theodoridis, "Effective capacitive power transfer," *IEEE Transactions on Power Electronics*, vol. 27, no. 12, pp. 4906–4913, 2012. DOI: 10.1109/TPEL.2012.2192502.

[11] W. Zhong and S. Y. R. Hui, "Maximum energy efficiency operation of series-series resonant wireless power transfer systems using on-off keying modulation," *IEEE Transactions on Power Electronics*, vol. 33, no. 4, pp. 3595–3603, 2018. DOI: 10.1109/TPEL.2017.2709341.

[12] M. Yilmaz and P. T. Krein, "Review of battery charger topologies, charging power levels, and infrastructure for plug-in electric and hybrid vehicles," *IEEE Transactions on Power Electronics*, vol. 28, no. 5, pp. 2151–2169, 2013. DOI: 10.1109/TPEL.2012.2212917.

[13] B. Esteban, M. Sid-Ahmed, and N. C. Kar, "A comparative study of power supply architectures in wireless ev charging systems," *IEEE Transactions on Power Electronics*, vol. 30, no. 11, pp. 6408–6422, 2015. DOI: 10.1109/TPEL.2015.2440256.

[14] A. Ahmad, M. S. Alam, and R. Chabaan, "A comprehensive review of wireless charging technologies for electric vehicles," *IEEE Transactions on Transportation Electrification*, vol. 4, no. 1, pp. 38–63, 2018. DOI: 10.1109/TTE.2017.2771619.

[15] H. Feng, R. Tavakoli, O. C. Onar, and Z. Pantic, "Advances in high-power wireless charging systems: Overview and design considerations," *IEEE Transactions on Transportation Electrification*, vol. 6, no. 3, pp. 886–919, 2020. DOI: 10.1109/TTE.2020.3012543.

[16] M. Mohammad, O. C. Onar, G.-J. Su, *et al.*, "Bidirectional lcc-lcc compensated 20 kw wireless power transfer system for medium-duty vehicle charging," *IEEE Transactions on Transportation Electrification*, pp. 1–1, 2021. DOI: 10.1109/TTE.2021.3049138.

[17] Chwei-Sen Wang, O. H. Stielau, and G. A. Covic, "Design considerations for a contactless electric vehicle battery charger," *IEEE Transactions on Industrial Electronics*, vol. 52, no. 5, pp. 1308–1314, 2005. DOI: 10.1109/TIE.2005.855672.

[18] M. S. Mahdavi and G. B. Gharehpetian, "A new wireless power transfer topology based on quasi-z-source and llc resonant network with low input current thd," in *2019 10th International Power Electronics, Drive Systems and Technologies Conference (PEDSTC)*, 2019, pp. 373–376. DOI: 10.1109/PEDSTC.2019.8697230.

[19] A. Iqbal, M. A. Al-Hitmi, P. K. Maroti, M. Daula, M. Meraj, and S. Rahman, "A quasi impedance source inverter based wireless power transfer system for battery charging applications for electric vehicle," in *2019 International Conference on Electrical, Electronics and Computer Engineering (UPCON)*, 2019, pp. 1–6. DOI: 10.1109/UPCON47278.2019.8980231.

[20] H. Zeng, X. Wang, and F. Z. Peng, "High power density z-source resonant wireless charger with line frequency sinusoidal charging," *IEEE Transactions on Power Electronics*, vol. 33, no. 12, pp. 10 148–10 156, 2018. DOI: 10.1109/TPEL.2018.2806919.

[21] T. Wang, X. Liu, H. Tang, and M. Ali, "Modification of the wireless power transfer system with z-source inverter," *Electronics Letters*, vol. 53, Nov. 2016. DOI: 10.1049/el.2016.3986.

[22] B. Pakhaliuk, O. Husev, R. Strzelecki, K. Tytelmaier, J. Zakis, and D. Stepins, "Optimal multivariable control for modified z-source based ipt," in *2018 IEEE 59th International Scientific Conference on Power and Electrical Engineering of Riga Technical University (RTUCON)*, 2018, pp. 1–6. DOI: 10.1109/RTUCON.2018.8659817.

[23] H. Zeng and F. Z. Peng, "Sic-based z-source resonant converter with constant frequency and load regulation for ev wireless charger," *IEEE Transactions on Power Electronics*, vol. 32, no. 11, pp. 8813–8822, 2017. DOI: 10.1109/TPEL.2016.2642050.

[24] N. S. González-Santini, H. Zeng, Y. Yu, and F. Z. Peng, "Z-source resonant converter with power factor correction for wireless power transfer applications," *IEEE Transactions on Power Electronics*, vol. 31, no. 11, pp. 7691–7700, 2016. DOI: 10.1109/TPEL.2016.2560174.

[25] B. Kim and O. Lavrova, "Quasi-z-source resonant full bridge converter for wireless power transfer with sliding mode model predictive control," in *2020 IEEE Power and Energy Conference at Illinois (PECI)*, 2020, pp. 1–6. DOI: 10.1109/PECI48348.2020.9064661.

[26] V. Castiglia, R. Miceli, F. Blaabjerg, and Y. Yang, "A quasi-z-source based hybrid energy storage system with battery and ultracapacitor integration," in *2020 IEEE 9th International Power Electronics and Motion Control Conference (IPEMC2020-ECCE Asia)*, 2020, pp. 768–773. DOI: 10.1109/IPEMC-ECCEAsia48364.2020.9367629.

[27] A. Battiston, E.-H. Miliani, S. Pierfederici, and F. Meibody-Tabar, "Efficiency improvement of a quasi-z-source inverter-fed permanent-magnet synchronous machine-based electric vehicle," *IEEE Transactions on Transportation Electrification*, vol. 2, no. 1, pp. 14–23, 2016. DOI: 10.1109/TTE.2016.2519349.

[28] J. Cuenot, S. Zaim, B. Nahid-Mobarakeh, *et al.*, "Overall size optimization of a high-speed starter using a quasi-z-source inverter," *IEEE Transactions on Transportation Electrification*, vol. 3, no. 4, pp. 891–900, 2017. DOI: 10.1109/TTE.2017.2738022.

[29] Z. Moghaddam, I. Ahmad, D. Habibi, and Q. V. Phung, "Smart charging strategy for electric vehicle charging stations," *IEEE Transactions on Transportation Electrification*, vol. 4, no. 1, pp. 76–88, 2018. DOI: 10.1109/TTE.2017.2753403.

[30] C.-H. Chung, S. Jangra, Q. Lai, and X. Lin, "Optimization of electric vehicle charging for battery maintenance and degradation management," *IEEE Transactions on Transportation Electrification*, vol. 6, no. 3, pp. 958–969, 2020. DOI: 10.1109/TTE.2020.3000181.

[31] R. Stocker, A. Mumtaz, Paramjeet, M. Braglia, and N. Lophitis, "Universal li-ion cell electrothermal model," *IEEE Transactions on Transportation Electrification*, vol. 7, no. 1, pp. 6–15, 2021. DOI: 10.1109/TTE.2020.2986606.

[32] X. Hu, W. Liu, X. Lin, and Y. Xie, "A comparative study of control-oriented thermal models for cylindrical li-ion batteries," *IEEE Transactions on Transportation Electrification*, vol. 5, no. 4, pp. 1237–1253, 2019. DOI: 10.1109/TTE.2019.2953606.

[33] H. Tu, H. Feng, S. Srdic, and S. Lukic, "Extreme fast charging of electric vehicles: A technology overview," *IEEE Transactions on Transportation Electrification*, vol. 5, no. 4, pp. 861–878, 2019. DOI: 10.1109/TTE.2019.2958709.

[34] V. Vu, D. Tran, and W. Choi, "Implementation of the constant current and constant voltage charge of inductive power transfer systems with the double-sided lcc compensation topology for electric vehicle battery charge applications," *IEEE Transactions on Power Electronics*, vol. 33, no. 9, pp. 7398–7410, 2018. DOI: 10.1109/TPEL.2017.2766605.

[35] K. Song, Z. Li, J. Jiang, and C. Zhu, "Constant current/voltage charging operation for series–series and series–parallel compensated wireless power transfer systems employing primary-side controller," *IEEE Transactions on Power Electronics*, vol. 33, no. 9, pp. 8065–8080, 2018. DOI: 10.1109/TPEL.2017.2767099.

[36] Y. Chen, B. Yang, Z. Kou, Z. He, G. Cao, and R. Mai, "Hybrid and reconfigurable ipt systems with high-misalignment tolerance for constant-current and constant-voltage battery charging," *IEEE Transactions on Power Electronics*, vol. 33, no. 10, pp. 8259–8269, 2018. DOI: 10.1109/TPEL.2018.2809785.

[37] C. Chen, H. Zhou, Q. Deng, *et al.*, "Modeling and decoupled control of inductive power transfer to implement constant current/voltage charging and zvs operating for electric vehicles," *IEEE Access*, vol. 6, pp. 59 917–59 928, 2018. DOI: 10.1109/ACCESS.2018.2875413.

Conclusions

In this PhD thesis, different issues concerning the use of hybrid energy storage management systems have been discussed. Contributions to storage systems modeling and parametrization, power converter modeling and control and storage system sizing and management have been provided.

In the first part of the thesis, the issues in modeling energy storage sources have been addressed, particularly referring to batteries and supercapacitors. For the batteries modeling, the main contribution was the comparison of different state of the art models to evaluate the achievable accuracy compared to the model complexity. In particular, three models were compared: the *Rint*, the *Sheperd* and the *Thevenin* models. Furthermore the implementation of an automatic measurement system to test, parametrize and validate the analyzed model was carried out. The models were experimentally validated testing a 3 Ah LGHG2 battery cell. The comparison between the experimental results and the simulations at different charging conditions have highlighted a good accuracy, even at high C-rates, of the *Thevenin* model. On the other hand, the *Rint* model parameters can be obtained from the manufacturers' datasheet, making it suitable for early design stages when it is necessary to compare different cell types without performing experimental tests. As for supercapacitors modeling, the three-branches model from literature was analyzed and improved to take into account the residual charge phenomenon. Again, an automatic measurement system to test, parametrize and validate the analyzed model was implemented. The model was experimentally validated testing several 2.7 V, 100 F supercapacitor cell. The model was then extended to simulate the behavior of different configurations of supercapacitors packs. The comparison between the experimental results and the simulations with different current profiles have highlighted that the three-branches model can achieve excellent accuracy for both the single supercapacitor and the pack.

In the second part of the thesis, innovative solutions for energy storage and hybrid energy storage management systems have been proposed.
The possibility of using multilevel converters for grid-connected battery storage systems has been investigated, realizing simultaneously the DC/AC conversion and the balancing of battery voltages. Thanks to the multilevel converter structure, the output voltage total harmonic distortion has been considerably reduced compared

to standard inverters. Moreover, the proposed low frequency modulation strategy allowed the reduction of switching losses and enabled the implementation of battery voltage balancing, without requiring additional components. Another interesting feature of the proposed structure is the possibility to use batteries with slightly different characteristics, also facilitating the use of second life batteries.

The employment of a new kind of power converter topology, the Impedance Source (Z-Source) converters, for hybrid energy storage systems have been investigated. The use of the Z-source inverters allows overcoming the typical issues of the traditional inverters as the AC output voltage is limited by DC input voltage and the components of the same leg cannot be gated simultaneously because a shoot-through would occur and destroy the devices. In Z-source inverters, the shoot-through states are introduced in order to boost the DC voltage across the inverter, thus realizing a single DC/AC conversion with both buck and boost capabilities. A particular topology, called quasi-Z-source inverter, has been studied and applied to two different solutions of energy storage management systems. The first proposed solution is a novel battery/supercapacitor quasi-Z-Source-based hybrid energy storage system. The proposed topology uses a battery as primary energy source and a supercapacitors pack as secondary energy source. The system features a single-stage DC-DC-AC conversion and the integration of hybrid energy storage without additional converters. The power balance between the battery, the supercapacitors and the grid is achieved by controlling the shoot-through duty cycle and the modulation index. The operation of the system under several different conditions has been simulated using PLECS. The simulation results confirm the technical feasibility and the correct operation of the system and the possibility to use this topology in hybrid energy storage management system applications. The second proposed solution is a quasi-Z-source-based inductive power transfer system for electrical vehicle battery charging. Taking advantage of the shoot-through states the simultaneous DC voltage regulation and DC/AC conversion is possible. Moreover, thanks to the Z-network, the quasi-Z-source-based inductive power transfer system is immune to short-circuits. A new modulator is proposed, capable of making the transition between buck and boost modes in a simple and effective way. The theoretical analysis has been validated by means of simulations and experimental results, verifying proper system operation in both buck and boost modes, and ensuring the system ability to perform the battery charging.

Finally, a battery/supercapacitor based active hybrid energy storage system has been investigated. The power and energy required by a generic profile have been considered for the sizing of the storage system. A comparison between a battery-only storage system and a hybrid storage system composed of a battery pack and a supercapacitors bank has been reported. In particular, a description of the power sharing rule-based algorithm and of the iterative sizing method has been provided. The comparison has pointed out that the hybrid configuration allows the reduction

of about 20% of weight respect to the electrochemical one and allows to cope better to the peak power request. The hybrid energy storage system power electronics converters modeling, control and design has been also considered. The system requires two DC/DC buck-boost converters, whose input are the storage sources and whose output are connected in parallel to the load. An experimental validation of the hybrid energy storage management system has been carried out on laboratory prototype, confirming the effectiveness of the proposed control strategy.

List of pubblications

Journal articles:

1. G. Ala, G. di Filippo, F. Viola, G. Giglia, A. Imburgia, P. Romano, V. Castiglia, F. Pellitteri, G. Schettino e R. Miceli, «Different scenarios of electric mobility: Current situation and possible future developments of fuel cell vehicles in Italy,» Sustainability (Switzerland), vol. 12, 2020.

2. G. Schettino, G. Ala, M. Caruso, V. Castiglia, F. Pellitteri, M. Trapanese, F. Viola e R. Miceli, «Experimental study on B-spline-based modulation schemes applied in multilevel inverters for electric drive applications», Energies, vol. 12, 2019.

3. Pellitteri, F., Campagna, N., Castiglia, V., Damiano, A., Miceli, R. «Design, implementation and experimental results of an inductive power transfer system for electric bicycle wireless charging» (2020) IET Renewable Power Generation, 14 (15), pp. 2908-2915.

4. Campagna, N., Castiglia, V., Miceli, R., Mastromauro, R.A., Spataro, C., Trapanese, M., Viola, F. «Battery models for battery powered applications: A comparative study» (2020) Energies, 13 (15), art. no. 4085.

International Conference Articles:

1. Damiano, M. Porru, A. Salimbeni, A. Serpi, V. Castiglia, A. O. Di Tommaso, R. Miceli e G. Schettino, "Batteries for Aerospace: a Brief Review," 2018 AEIT International Annual Conference, Bari, 2018, pp. 1-6.

2. G. Schettino, V. Castiglia, P. Livreri, R. Miceli, F. Viola e R. Rizzo, «Novel Computational Method for Harmonic Mitigation for Three-phase Five-level Cascaded H-Bridge Inverter» 2018, International Conference on Smart Grid (icSmartGrid), Nagasaki, Japan, 2018, pp. 299-306.

3. V. Castiglia, R. Miceli, G. Schettino, F. Viola, C. Buccella, C. Cecati e M. C. Cimoroni, «Mixed Harmonic Elimination Control for a Single-Phase 9 Level

Grid-Connected Inverter» 2018, International Conference on Smart Grid (icSmartGrid), Nagasaki, Japan, 2018, pp. 240-245.

4. F. Pellitteri, V. Castiglia, P. Livreri e R. Miceli, «Analysis and design of bidirectional DC-DC converters for ultracapacitors management in EVs» 2018, Thirteenth International Conference on Ecological Vehicles and Renewable Energies (EVER), Monte-Carlo, 2018, pp. 1-6.

5. P. Livreri, V. Castiglia, F. Pellitteri e R. Miceli, «Design of a Battery / Ultracapacitor Energy Storage System for Electric Vehicle Applications» 2018, IEEE 4th International Forum on Research and Technology for Society and Industry (RTSI), Palermo, 2018, pp. 1-5.

6. V. Castiglia, R. Miceli, G. Schettino, M. G. Cimoroni, C. Buccella e C. Cecati, «Selective harmonic elimination in a 5-Level single phase converter with FPGA based controller» 2018, 5th International Symposium on Environment-Friendly Energies and Applications (EFEA), Rome, 2018, pp. 1-6.

7. P. Livreri, M. Caruso, V. Castiglia, F. Pellitteri e G. Schettino, «Dynamic reconfiguration of electrical connections for partially shaded PV modules: Technical and economical performances of an Arduino-based prototype» International Journal of Renewable Energy Research, vol. 8, pp. 336-344, 2018.

8. V. Castiglia, P. Ciotta, A. O. Di Tommaso, R. Miceli e C. Nevoloso, «High Performance FOC for Induction Motors with Low Cost ATSAM3X8E Microcontroller» 2018, 7th International Conference on Renewable Energy Research and Applications (ICRERA), Paris, 2018, pp. 1495-1500.

9. V. Castiglia, R. Miceli, G. Ala, P. Romano, F. Viola, G. Giglia, A. Imburgia e G. Schettino, «Modelling, simulation and characterization of Li-Ion battery cell», in 5th International Forum on Research and Technologies for Society and Industry: Innovation to Shape the Future, RTSI, 2019.

10. C. Buccella, C. Cecati, M. G. Cimoroni, R. Miceli, G. Schettino, V. Castiglia e F. Pellitteri, «Harmonic reduction in CHB 13-level inverters by PAM fundamental-frequency strategy», in 8th International Conference on Renewable Energy Research and Applications, ICRERA, 2019.

11. F. Viola, D. Zaninelli, G. Ala, G. Schettino, V. Castiglia e R. Miceli, «Forecasting the diffusion of hydrogen EV refuelling infrastructures in Italy», in 14th International Conference on Ecological Vehicles and Renewable Energies, EVER, 2019.

12. G. Giglia, G. Ala, V. Castiglia, A. Imburgia, R. Miceli, G. Rizzo, P. Romano, G. Schettino e F. Viola, «Electromagnetic Full-Wave Simulation of Partial

Discharge Detection in High Voltage AC Cables», in 5th International Forum on Research and Technologies for Society and Industry: Innovation to Shape the Future, RTSI, 2019.

13. F. Pellitteri, N. Campagna, V. Castiglia, A. Damiano e R. Miceli, «Design, implementation and experimental results of a wireless charger for E-bikes», in 7th International Conference on Clean Electrical Power: Renewable Energy Resources Impact, ICCEP, 2019.

14. N. Campagna, V. Castiglia, R. Miceli e F. Pellitteri, «A bidirectional IPT system for electrical bicycle contactless energy transfer», in 8th International Conference on Renewable Energy Research and Applications, ICRERA, 2019.

15. V. Castiglia, A. O. Di Tommaso, R. Miceli, F. Pellitteri e G. Vassallo, «Investigation on Cascode Devices for High Frequency Electrical Drives Applications», in International Annual Conference, AEIT, 2019.

16. Campagna, N., Castiglia, V., Miceli, R., "Fuel Cell Based Inductive Power Transfer System for Supercapacitors Constant Current Charging", (2021) 2021 16th International Conference on Ecological Vehicles and Renewable Energies, EVER 2021, art. no. 9456620.

17. Castiglia, V., Miceli, R., Blaabjerg, F., Yang, Y. "A Quasi-Z-Source based Hybrid Energy Storage System with Battery and Ultracapacitor Integration", (2020) 2020 IEEE 9th International Power Electronics and Motion Control Conference, IPEMC 2020 ECCE Asia, art. no. 9367629, pp. 768-773.

18. Schettino, G., Miceli, R., Castiglia, V., Viola, F., Blaabjerg, F., Yang, Y., "A Novel Symmetrical Boost Modulation Method for qZS-based CHB Inverters", (2020) 2020 IEEE 21st Workshop on Control and Modeling for Power Electronics, COMPEL 2020, art. no. 9265660.

19. Castiglia, V., Miceli, R., Blaabjerg, F., Yang, Y. "Small-Signal Modeling and Experimental Validation of the Three-phase Quasi-Z-Source Inverter", (2020) 2020 IEEE 21st Workshop on Control and Modeling for Power Electronics, COMPEL 2020, art. no. 9265716.

20. Nevoloso, C., Campagna, N., Caruso, M., Castiglia, V., Di Tommaso, A.O., Miceli, R., "Interior Permanent Magnet Synchronous Machine Drive Powered by Fuel Cell for Automotive Applications", (2020) 9th International Conference on Renewable Energy Research and Applications, ICRERA 2020, art. no. 9242773, pp. 499-504.

21. Campagna, N., Castiglia, V., Di Tommaso, A.O., Miceli, R., Pellitteri, F., Viola, F., "Experimental Characterization of a Double Receiver Dynamic Wire-

less Charging System", (2020) 9th International Conference on Renewable Energy Research and Applications, ICRERA 2020, art. no. 9242731, pp. 494-498.

22. Castiglia, V., Campagna, N., Di Tommaso, A.O., Miceli, R., Pellitteri, F., Puccio, C., Viola, F., "Modelling, Simulation and Characterization of a Supercapacitor in Automotive Applications", (2020) 2020 15th International Conference on Ecological Vehicles and Renewable Energies, EVER 2020, art. no. 9243065.

23. Campagna, N., Di Tommaso, A.O., Castiglia, V., Pellitteri, F., Miceli, R., Schettino, G., "Hydrogen Supplied Wireless Charging System for Electric Vehicles", (2020) 2020 15th International Conference on Ecological Vehicles and Renewable Energies, EVER 2020, art. no. 9242925.

24. Pellitteri, F., Castiglia, V., Di Tommaso, A.O., Miceli, R., Vassallo, G., Schirone, L., "Preliminary test on a cascode switch for high-frequency applications", (2020) Proceedings - 2020 2nd IEEE International Conference on Industrial Electronics for Sustainable Energy Systems, IESES 2020, art. no. 9210672, pp. 377-382.

25. Castiglia, V., Miceli, R., Blaabjerg, F., Yang, Y. "A Comparison of Two-Stage Inverter and Quasi-Z-Source Inverter for Hybrid Energy Storage Applications", (2020) 2020 22nd European Conference on Power Electronics and Applications, EPE 2020 ECCE Europe, art. no. 9215934.

26. Campagna, N., Caruso, M., Castiglia, V., Miceli, Viola, F. "Energy Management Concepts for the Evolution of Smart Grids", (2020) 8th International Conference on Smart Grid, icSmartGrid 2020, art. no. 9144909, pp. 208-213.

27. Castiglia, V., Campagna, N., Spataro, C., Nevoloso, C., Viola, F., Miceli, R., "Modelling, simulation and characterization of a supercapacitor", (2020) 20th IEEE Mediterranean Electrotechnical Conference, MELECON 2020 - Proceedings, art. no. 9140474, pp. 46-51.

28. Ala, G., Castiglia, V., Di Filippo, G., Miceli, R., Romano, P., Viola, F. "From electric mobility to hydrogen mobility: Current state and possible future expansions", (2020) 20th IEEE Mediterranean Electrotechnical Conference, MELECON 2020 - Proceedings, art. no. 9140482, pp. 1-6.

29. Schettino, G., Campagna, N., Di Tommaso, A.O., Castiglia, V., Miceli, R., Viola, F., "Performance Comparison of modified modulation Techniques for Quasi-Z-Source Converters", (2020) 20th IEEE Mediterranean Electrotechnical Conference, MELECON 2020 - Proceedings, art. no. 9140513, pp. 41-45.

La borsa di dottorato è stata cofinanziata con risorse del
Programma Operativo Nazionale Ricerca e Innovazione 2014-2020 (CCI 2014IT16M2OP005),
Fondo Sociale Europeo, Azione I.1 “Dottorati Innovativi con caratterizzazione Industriale”

UNIONE EUROPEA
Fondo Sociale Europeo